Friedrich-Alexander-Universität
Faculty of Engineering

Dissertation

2025

Arun Babu

Condition Monitoring of Road Traffic Infrastructure by Using Synthetic Aperture Radar

Condition Monitoring of Road Traffic Infrastructure by Using Synthetic Aperture Radar

Zustandsüberwachung der Straßeninfrastruktur durch Radar mit synthetischer Apertur

Der Technischen Fakultät
der Friedrich-Alexander-Universität
Erlangen-Nürnberg

zur
Erlangung des Doktorgrades Dr.-Ing.

vorgelegt von

Arun Babu

aus Thodiyoor, Indien

Als Dissertation genehmigt
von der Technischen Fakultät
der Friedrich-Alexander-Universität Erlangen-Nürnberg

Tag der mündlichen Prüfung: 11.11.2025

Gutachter: Prof. Dr.-Ing. Gerhard Krieger
Prof. Dr.-Ing. Stefan Hinz

Acknowledgments

This doctoral research, carried out at the Microwaves and Radar Institute of the German Aerospace Center (DLR), would not have been possible without the assistance and support of many individuals. I am deeply thankful to everyone who has guided and supported me throughout this scientific journey.

First and foremost, I would like to express my heartfelt thanks to my supervisor Dr. Stefan V. Baumgartner, for sharing his extensive knowledge of SAR concepts, data processing, and analysis. His consistent technical and moral support, coupled with regular meetings, innovative ideas, and valuable insights, were crucial in guiding me through the challenges I encountered during the research phase. I am also grateful to him for reviewing my conference papers, journal articles, and this dissertation, which significantly improved their quality.

I am sincerely grateful to my PhD advisor and department head, Prof. Dr. Gerhard Krieger, for providing me with the opportunity to register as a PhD student at the Faculty of Engineering, Friedrich-Alexander-Universität Erlangen-Nürnberg. His ideas and suggestions during the PhD status meetings were helpful in refining my results and encouraged me to look at the research problems from different perspectives. I am also thankful to him for reviewing my journal articles and this dissertation, offering constructive feedback that greatly enhanced their clarity and overall quality.

I also wish to thank my group leader, Prof. Dr. Marwan Younis, for allowing me to carry out my research within his team.

Furthermore, my sincere thanks go to the director of the Microwaves and Radar Institute Prof. Dr. Alberto Moreira for providing me the opportunity to conduct this doctoral research at the institute and also for having regular PhD status meetings.

I am grateful to my colleagues at DLR for their efforts in acquiring and providing the experimental SAR datasets and ground truth data necessary for this research, as well as for their assistance with administrative tasks both within DLR and at the foreigner's office.

Finally, I would like to extend my deepest thanks to my parents and my beloved wife Arya for their constant support and encouragement, which motivated me to strive for greater achievements.

Oberpfaffenhofen, January 2025

Arun Babu

Abstract

Roads play a crucial role in the development of a country. Therefore, it is essential to carry out periodic inspections to assess the road surface conditions and carry out necessary maintenance activities for ensuring the efficient and safe movement of people and goods. The most important factors affecting the quality of road surfaces include surface roughness, cracks, potholes as well as unevenness. Nowadays, specialised survey vehicles equipped with numerous sensors are used globally to monitor road conditions, however, this activity is mainly concentrated on major roads and only once in every few years, as this is a very resource-intensive task. However, as road conditions deteriorate rapidly, particularly in winter due to freeze-thaw cycles, more frequent monitoring is essential to detect problems early and take preventative actions. The utilisation of airborne and spaceborne synthetic aperture radar (SAR) systems is a promising avenue for road condition monitoring as it offers cost-effective and large-scale monitoring capabilities, enabling predictive road maintenance strategies.

This doctoral thesis focuses on the development of methods and processing chains for accurate road surface roughness estimation, detection and orientation estimation of cracks as well as road width estimation using high-resolution fully focused SAR data. The road surface roughness estimation methods were developed and tested for both airborne and spaceborne X-band SAR systems, while the processing chains for crack detection, orientation estimation and road width estimation were specifically tailored and tested for airborne X-band SAR systems.

A new semi-empirical roughness estimation model and machine learning-based support vector regression (SVR), random forest regression (RFR) and artificial neural network (ANN)-based regression models were developed, trained and tested specifically for road surface roughness estimation using fully polarimetric airborne X-band SAR data. The new semi-empirical roughness estimation model and processing chain were adapted for road surface roughness estimation using single-polarised X-band spaceborne SAR data. Since both the airborne and spaceborne SAR data have a low signal-to-noise ratio (SNR) due to the lower backscatter from smooth road surfaces, additive noise estimation and minimisation techniques were integrated into the processing chains as a pre-processing step to improve the reliability of the road surface roughness estimation. Similarly, after generating the road surface roughness values, upper sigma nought (σ^o) and lower SNR thresholding techniques were implemented to further eliminate the invalid and noisy results. Multi-dataset fusion approaches were also developed to fuse the surface roughness estimates from multiple SAR datasets with different data acquisition geometries to minimise the errors introduced in road surface roughness estimation due to incidence angle variations, low SNR and shadow regions.

Furthermore, a novel method based on the combined use of an adaptive thresholding algorithm and the Radon transform has been proposed in this thesis for cracks detection, severity and orientation estimation. In this method, the cracks detection is performed using the adaptive threshold algorithm, while the severity of the cracks is expressed in terms of the maximum Radon magnitude values obtained from the sinogram and the orientation of the detected cracks is represented as bearing angles. The road width is measured by detecting abrupt changes in road surface roughness at the road boundaries.

All processing chains, including those for road surface roughness, cracks detection, orientation estimation and road width measurements, generate keyhole markup language (KML) files to visualise the results in Google Earth (GE) for enhanced interpretation.

Validation of these methods and processing chains was conducted using DLR's airborne F-SAR system and Germany's spaceborne TerraSAR-X system, demonstrating close agreement with ground truth measurements, which were acquired with sub-millimetre level accuracy by using a 3D laser scanner. Overall, this research contributes to advancing road condition monitoring techniques, with implications for predictive maintenance strategies and infrastructure management.

Zusammenfassung

Straßen spielen eine entscheidende Rolle in der Entwicklung eines Landes. Daher ist es unerlässlich, regelmäßige Inspektionen durchzuführen, um die Zustände der Fahrbahnoberflächen zu bewerten und notwendige Instandhaltungsmaßnahmen durchzuführen, um eine effiziente und sichere Bewegung von Menschen und Gütern zu gewährleisten. Die wichtigsten Faktoren, die die Qualität der Fahrbahnoberflächen beeinflussen, sind Oberflächenrauheit, Risse, Schlaglöcher sowie Unebenheiten. Heutzutage werden weltweit spezialisierte Vermessungsfahrzeuge mit zahlreichen Sensoren eingesetzt, um Straßenbedingungen zu überwachen, jedoch hauptsächlich auf Hauptstraßen und nur alle paar Jahre, da dies eine sehr ressourcenintensive Aufgabe ist. Da sich Straßenbedingungen jedoch insbesondere im Winter aufgrund von Frost-Tau-Zyklen schnell verschlechtern, ist eine häufigere Überwachung erforderlich, um Probleme frühzeitig zu erkennen und präventive Maßnahmen zu ergreifen. Die Nutzung von luft und raumgestützten Radarsystemen mit synthetischer Apertur (SAR) bietet sich als vielversprechender Ansatz für die Überwachung von Straßenbedingungen an, da sie kostengünstige und großflächige Überwachungsmöglichkeiten bieten und die Entwicklung prädiktiver Straßeninstandhaltungsstrategien ermöglichen.

Diese Doktorarbeit konzentriert sich auf die Entwicklung von Methoden und Verarbeitungsketten zur genauen Schätzung der Fahrbahnoberflächenrauheit, zur Erkennung und Orientierungsschätzung von Rissen sowie zur Schätzung der Straßenbreite unter Verwendung hochauflösender voll fokussierter SAR-Daten. Die Methoden zur Abschätzung der Straßenoberflächenrauheit wurden sowohl für luft- als auch weltraumgestützte X-Band-SAR-Systeme entwickelt und getestet, während die Verarbeitungsketten für Rissdetektion, Orientierungsabschätzung und Straßenbreitenabschätzung speziell für luftgestützte X-Band-SAR-Systeme maßgeschneidert und getestet wurden.

Ein neues semi-empirisches Rauheitsschätzungsmodell und auf maschinellem Lernen basierende Modelle wie Support-Vektor-Regression (SVR), Random-Forest-Regression (RFR) und künstliche neuronale Netze (ANN) wurden speziell für die Rauheitsschätzung von Fahrbahnoberflächen unter Verwendung vollständig polarimetrischer luftgestützter SAR-Daten entwickelt, trainiert und getestet. Das neue semi-empirische Rauheitsschätzungsmodell und die Verarbeitungskette wurden für die Schätzung der Fahrbahnoberflächenrauheit mit weltraumgestützten X-Band-SAR-Daten für die Verwendung von nur einer Polarisation angepasst. Da sowohl luft- als auch weltraumgestützte SAR-Daten aufgrund der geringeren Rückstreuung von glatten Fahrbahnoberflächen ein niedriges Signal-Rausch-Verhältnis (SNR) aufweisen, wurden additive

Rauschschätzungs-und Minimierungstechniken als Vorverarbeitungsschritt in die Verarbeitungsketten integriert, um die Zuverlässigkeit der Fahrbahnoberflächenrauhigkeitsschätzung zu verbessern. Nach der Schätzung der Fahrbahnoberflächenrauheitswerte wurden außerdem obere Sigma-Nought- (σ^o) und untere SNR-Schwellenwerttechniken implementiert, um ungültige und verrauschte Ergebnisse weiter zu eliminieren. Es wurden auch Ansätze zur Fusion mehrerer Datensätze entwickelt, um die Rauheitsschätzungen aus mehreren SAR-Datensätzen mit unterschiedlichen Datenerfassungsgeometrien zu fusionieren, um Fehler bei der Schätzung der Fahrbahnoberflächenrauheit aufgrund von Einfallswinkelvariationen, niedrigem SNR und Schattenbereichen zu minimieren.

Darüber hinaus wurde in dieser Doktorarbeit eine neuartige Methode zur Detektion, Bewertung der Schwere und Orientierung von Rissen vorgeschlagen, die auf der kombinierten Verwendung eines adaptiven Schwellenwertalgorithmus und der Radon-Transformation basiert. Bei dieser Methode erfolgt die Rissdetektion mithilfe des adaptiven Schwellenwertalgorithmus, während die Schwere der Risse durch die maximalen Radon-Magnitudenwerte aus dem Sinogramm ausgedrückt wird und die Orientierung der detektierten Risse als Himmelsrichtung angegeben wird. Die Straßenbreite wird durch die Erkennung abrupter Änderungen der Fahrbahnoberflächenrauheit an den Straßengrenzen gemessen.

Um die Ergebnisse besser interpretieren zu können, haben die entwickelten Verarbeitungsketten für die Schätzung der Fahrbahnoberflächenrauheit, Rissentdeckung, Orientierungsschätzung und Straßenbreitenmessungen Keyhole Markup Language (KML)-Dateien generiert. Diese Dateien werden verwendet, um die Ergebnisse in Google Earth (GE) zu visualisieren und ermöglichen Vergleiche mit GE-Optikbildern.

Die Validierung dieser Methoden und Verarbeitungsketten wurde mit dem luftgestützten F-SAR-System des DLR und dem deutschen weltraumgestützten TerraSAR-X-System durchgeführt. Sie zeigen eine gute Übereinstimmung mit den aktuellen Bodenmessungen. Insgesamt trägt diese Forschung zur Weiterentwicklung von Techniken zur Überwachung des Straßenzustands bei und hat Auswirkungen auf vorausschauende Instandhaltungsstrategien und das Infrastrukturmanagement.

Contents

List of Symbols and Abbreviations

List of Abbreviations

Abbreviation	Description
AIEM	Advanced Integral Equation Model
ANN	Artificial Neural Network
ATI	Along-Track Interferometry
BASt	Bundesanstalt für Straßenwesen
CSAR	Circular SAR
CT	Computer Tomography
DEM	Digital Elevation Model
DLR	Deutsches Zentrum für Luft- und Raumfahrt (German Aerospace Center)
duraBASt	Demonstrations- Untersuchungs- und Referenzareal der BASt
E-SAR	Experimental-SAR of DLR
ELU	Exponential Linear Unit
EM	Electromagnetic
F-SAR	Flugzeug-SAR of DLR
GCE	Geocoded Cracks Enhanced Image
GE	Google Earth
GeoTIFF	Geographic Tagged Image File Format
GIS	Geographic Information System
GLCM	Grey Level Co-occurrence Matrix
GO	Geometric Optics
GPR	Ground Penetrating Radar
GPS	Global Positioning System
GT	Ground Truth
HH	Horizontal polarisation transmitted - horizontal polarisation received

Abbreviation	Description
HS	High-resolution spotlight SAR mode
HV	Horizontal polarisation transmitted - vertical polarisation received
IEM	Integral Equation Model
IRI	International Roughness Index
KML	Keyhole Markup Language
LCMS	Laser Crack Measurement System
LFM	Linear Frequency Modulation
MAE	Mean Absolute Error
MLP	Multilayer Perceptron
MSE	Mean Square Error
NEBN	Noise Equivalent Beta Nought
NESZ	Noise Equivalent Sigma Zero
NMR	Nuclear Magnetic Resonance
OSM	Open Street Map
PO	Physical Optics
PolSAR	Polarimetric Synthetic Aperture Radar
PPP	Public Private Partnership
PRF	Pulse Repetition Frequency
RAR	Real Aperture Radar
RBF	Radial Basis Function
RCMC	Range Cell Migration Correction
RCS	Radar Cross Section
ReLU	Rectified Linear Unit
RF	Random Forest
RFR	Random Forest Regression
RMS	Root Mean Square
RMSE	Root Mean Square Error
SAR	Synthetic Aperture Radar
SC	ScanSAR

Abbreviation	Description
SELU	Scaled Exponential Linear Unit
SL	Spotlight SAR mode
SLAR	Side Looking Airborne Radar
SM	StripMap
SNR	Signal to Noise Ratio
SPM	Small Perturbation Model
ST	Staring Spotlight
SVM	Support Vector Machine
SVR	Support Vector Regression
SWT	Stationary Wavelet Transform
TD-X	TanDEM-X
TS-X	TerraSAR-X
VH	Vertical polarisation transmitted - horizontal polarisation received
VV	Vertical polarisation transmitted - vertical polarisation received
WS	Wide ScanSAR
XTI	Cross-Track Interferometry

List of Symbols

Symbol	Unit	Description
A		Anisotropy parameter
α_{wn}		Losses due to windowing applied during range compression
$\sigma(v)$		ANN activation function
β_k		Weights for the ANN hidden layers
α_m		Weights for the ANN input layers
$g_k(T)$		ANN output function
B		Number of training sets for bagging

Symbol	Unit	Description
B_{r}	Hz	Bandwidth of the chirp signal
$\hat{f}_{\mathrm{avg}}(x)$		Low-variance statistical learning model for bagging technique
θ_{b}	°	Bearing angle
c	$\mathrm{m\,s^{-1}}$	Speed of light in vacuum
$\boldsymbol{C}_3$		3x3 covariance matrix
$\boldsymbol{C}_4$		4x4 covariance matrix
α , β		Parameters obtained from the Cloude-Pottier polarimetric decomposition
coeff		Coefficients of the TS-X noise polynomial
*		Complex conjugate operator
$\cos(\theta)$		Cosine function
deg		Degree of the TS-X noise polynomial
δ_{az}	m	Azimuth resolution of the SAR system
$\delta_{\mathrm{az,raw}}$	m	Azimuth resolution of the RAR system
δ_{r}	m	Slant range resolution after pulse compression
δ_{rg}	m	Ground range resolution
$\delta_{\mathrm{r,raw}}$	m	Slant range resolution without pulse compression
DN		Pixel intensity values of the TS-X data
E_1, E_2		EM fields representing the effects of small surface irregularities
E_{o}		EM field over a perfectly flat surface
$\langle\cdot\rangle$		Local averaging operator over a set of neighbouring pixels
ϵ'		Dielectric constant
F		Noise figure of the SAR system
f_2		Contrast of a GLCM
f_3		Correlation of a GLCM
f_4		Homogeneity of a GLCM
f_7		Dissimilarity of a GLCM

Symbol	Unit	Description
$\boldsymbol{x}$, $\boldsymbol{x}$'		Feature vectors for radial basis function
G	dB	Gain of the SAR antenna
Γ^{o}		Fresnel reflectivity
$\boldsymbol{P}$		Co-occurrence probability matrix
$p(i, j)$		Elements of the co-occurrence probability matrix ($\boldsymbol{P}$)
σ_x		Standard deviation of the marginal-probability matrix obtained by summing the rows of $\boldsymbol{P}$
σ_y		Standard deviation of the marginal-probability matrix obtained by summing the columns of $\boldsymbol{P}$
μ_x		Mean of the marginal-probability matrix obtained by summing the rows of $\boldsymbol{P}$
μ_y		Mean of the marginal-probability matrix obtained by summing the columns of $\boldsymbol{P}$
GT h_{rms}	m	Ground truth surface roughness
GT h_{rms_i}	m	Ground truth surface roughness value for each GT spot
H		Entropy
h	m	Altitude of the SAR system above the ground
h_i	m	Height of the i^{th} sample of the road surface undulation
h_{rms}	m	Road surface roughness (root mean square height of the vertical undulations on the road surface)
$h(t)$		Reference function for pulse compression
$\psi(t)$		Haar wavelet function
h_{rms_i}		Model estimated surface roughness value for each GT spot
$f(x, y)$		2D image function
j		Imaginary unit, $\mathrm{j} = \sqrt{-1}$
K		Number of ANN output units
k	J K^{-1}	Boltzmann constant
$\boldsymbol{k}_{\mathrm{l}}$		Lexicographic feature vector
$\boldsymbol{k}_{\mathrm{p}}$		Pauli feature vector
kl		Correlation length

Symbol	Unit	Description
ks		Effective vertical surface roughness
ks_{HH}		Effective vertical surface roughness estimated for the HH polarisation
ks_{VV}		Effective vertical surface roughness estimated for the VV polarisation
L	dB	Combined losses in the SAR system
l_{a}	m	Length of the physical antenna
L_{sa}	m	Length of the synthetic aperture
λ	m	Wavelength of the SAR system
λ_2		Second eigenvalue of the $\boldsymbol{T}_3$ matrix
λ_3		Third eigenvalue of the $\boldsymbol{T}_3$ matrix
λ_4		Fourth eigenvalue of the $\boldsymbol{T}_4$ matrix
$Lat1$, $Lat2$		Latitude values
$Lon1$, $Lon2$		Longitude values
M		Number of ANN hidden units
Max_1		Element-wise maximum operation output obtained from SWT for scale 1
Max_2		Element-wise maximum operation output obtained from SWT for scale 2
Max_3		Element-wise maximum operation output obtained from SWT for scale 3
Max_i		Element-wise maximum operation output obtained from SWT for the i^{th} scale
$\overline{h}$	m	Mean height over all the road surface undulation samples
δ, β, and ϵ		Coefficients of the new semi-empirical model
mv		Surface moisture
N		Additive noise
n		Number of road surface undulation samples
$n_{\mathrm{GT\ spots}}$		Number of ground truth spots
$\boldsymbol{N}$		Additive noise matrix

Symbol	Unit	Description
P		Number of ANN input units
p		Co-polarisation ratio
P_{avg}	W	Average transmit power
$\boldsymbol{k}_{\text{4p noisy}}$		Additive noise affected 4x1 Pauli basis vector
$\boldsymbol{k}_{\text{3p noisy}}$		Additive noise affected 3x1 Pauli basis vector
$\lvert r \rvert$		Pearson correlation coefficient
π		Pi (ratio of the circumference of a circle to its diameter)
θ_{r}	°	Radon projection/rotation angle
q		Cross-polarisation ratio
R	m	Slant range distance
R_{o}	m	Minimum slant range distance
$R(\theta_{\text{p}}, s)$		Radon transform function
$K(x, x')$		Radial basis function kernel
γ		Radial basis function coefficient
$Re\{\cdot\}$		Real part of a complex number
θ_{road}	°	Road angle
s		Distance from orgin in Radon transform
$\boldsymbol{S}$		Scattering matrix
$\boldsymbol{S}'$		Additive noise affected scattering matrix
$s_{\text{out}}(t)$		Pulse compressed signal
$s(t)$		Uncompressed received signal
σ^o	dB	Radar backscatter coefficient
σ^o_{pq}	dB	Radar backscatter coefficient for p transmitted and q received polarisation
$\sin(\theta)$		Sine function
SNR_{pq}		SNR estimated for the p transmitted and q received polarisation
$\lvert \rho \rvert$		Spearman correlation coefficient
C		SVR regularisation parameter
T		Set of outputs of the ANN hidden layer

Symbol	Unit	Description
$\boldsymbol{T}_{3\,\text{noisy}}$		Additive noise affected 3x3 coherency matrix
$\boldsymbol{T}_{4\,\text{noisy}}$		Additive noise affected 4x4 coherency matrix
$\boldsymbol{T}_3$		3x3 coherency matrix
$\boldsymbol{T}_4$		4x4 coherency matrix
T_{CPI}	s	Coherent processing interval
τ_{max}		Maximum validity range point for NEBN estimation
τ_{min}		Minimum validity range point for NEBN estimation
τ_{p}	s	Transmitted pulse duration
τ_{ref}		Reference point for NEBN estimation in range direction
T_{s}	K	System noise temperature
T_{sa}	s	Synthetic aperture time
θ	°	Incidence angle
Θ_{az}	°	Azimuth beamwidth of the SAR antenna
θ_{d}	°	Depression angle
Θ_{rg}	°	Range beamwidth of the SAR antenna
t	s	Time
k_{s}		TS-X calibration and processor scaling factor
v_{p}	$\text{m}\,\text{s}^{-1}$	Velocity of the SAR platform
σ^2		Variance
w		Straight line along which the Radon line intergation is performed
X		Set of ANN input features
Y		ANN target variable (prediction output)
Z		Set of derived features of ANN

1 Introduction

1.1 Background and Motivation

Road infrastructure plays a vital role in facilitating the movement of people and goods, making it crucial for a country's development [92]. Consequently, regular inspection and maintenance of roads are essential for both economic progress and safety considerations [P2, 69]. Several factors can affect the quality of road surfaces, with road surface roughness, cracks, potholes, and unevenness being the most significant ones [3, 33, 68, 82].

Road surface roughness plays a crucial role in determining the friction between the road and vehicle tyres [56, 143], thereby significantly affecting a vehicle's skid resistance [53, 85]. Figure 1.1(a) illustrates the interaction between a rough road surface and a vehicle tyre [P4]. The weight on the tyre and the road's vertical profile cause the tyre's rubber to be penetrated by the road's vertical rough points. Due to the tyre rubber's flexibility, it conforms to the shape of the rough points, resulting in an increased contact surface area between the road and the tyre [2]. This behaviour enhances the grip and reduces the likelihood of tyre skidding [96]. On the other hand, Figure 1.1(b) portrays the contact between a very smooth road surface and a tyre. In this scenario, there are not enough vertical rough points on the road, leading to a smaller contact surface area compared to Figure 1.1(a). Consequently, less friction is generated, increasing the chances of skidding [2, 96]. The observations from both figures emphasise the importance of an optimal level of skid resistance for safe acceleration, braking, and steering manoeuvres. However, excessively high road surface roughness can adversely affect driving comfort, fuel consumption, and generate increased noise levels [83]. Achieving the right balance of skid resistance is crucial to ensure both safety and driving quality.

Road surfaces with cracks and potholes pose significant safety risks to road users, leading to accidents and premature wear and tear of vehicles [5, 106]. Cracks typically develop on the road surface due to the expansion and contraction caused by temperature variations. During the day, the sun's heat causes the road to expand, while at night, the temperature drop causes contraction. This repetitive cycle of expansion and contraction weakens certain areas on the road, and regular vehicular movement over these weakened spots eventually results in the formation of cracks [12, 13]. Over time, these cracks can worsen and lead to the emergence of potholes, which are particularly prevalent during winter. In the winter season, freezing and thawing cycles play a key role in pothole formation (cf. Figure 1.2) [11]. When the temperature is above zero degrees Celsius, snow on the road surface melts, and the water seeps into the cracks present on the road. As the temperature drops below zero degrees Celsius, this water freezes and expands, exerting

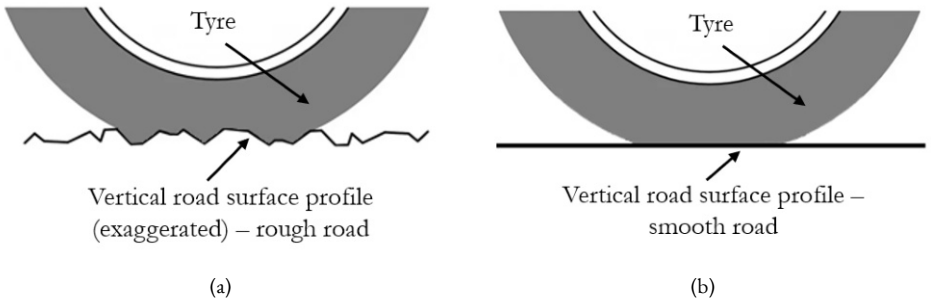

Figure 1.1: Road surface roughness visualisation. (a) The contact area between a rough road surface and a tyre (road vertical profile is exaggerated for better visualisation). (b) The contact area between a very smooth road surface and a tyre [P4].

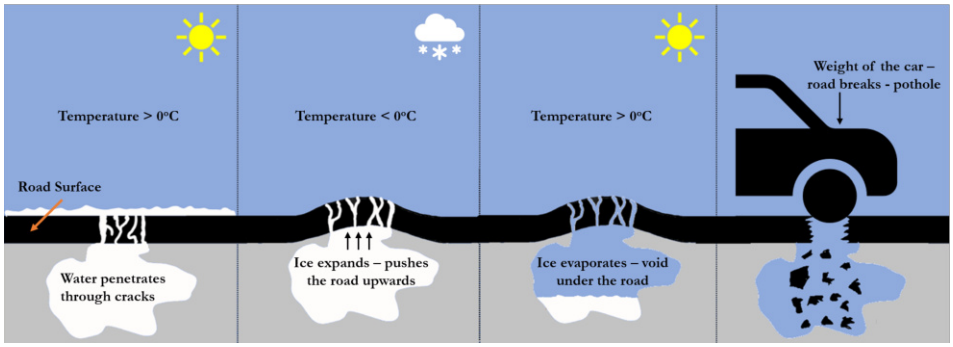

Figure 1.2: Cracks deterioration and pothole formation due to freeze-thaw cycles in the winter season.

pressure on the road surface, causing the cracks to widen. When the temperature rises again, the ice beneath the road surface melts and evaporates, leaving behind a void under the road surface. When a vehicle passes over these weakened points, the road surface breaks, leading to the creation of potholes [67]. The continuous freezing and thawing process during winter exacerbates the pothole problem, making it a significant concern for road maintenance and safety.

Road surface unevenness refers to the smoothness of the road surface in both longitudinal and transverse directions (cf. Figure 1.3) [87]. Factors affecting it include construction methods, equipment used, compaction level, construction quality control measures, and material choice. Deficiencies in these aspects can lead to variations, resulting in an uneven road surface [86]. The consequences are impactful, directly affecting vehicle performance, comfort, and stability. Uneven surfaces reduce acceleration, braking, and cornering efficiency, posing safety risks. They also increase vehicle operating costs due to accelerated wear on tyres, suspension systems, and other components, necessitating frequent maintenance. Moreover, an uneven road has a shorter lifespan due

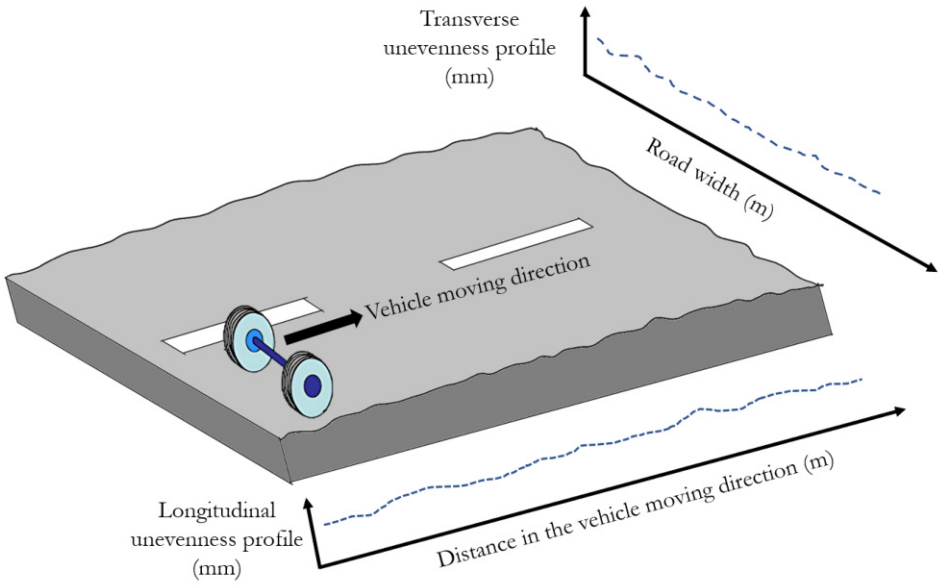

Figure 1.3: Road surface unevenness.

to constant traffic impact and environmental factors, requiring more frequent repairs [146]. Addressing road surface unevenness is crucial during both the construction and maintenance phases.

In summary, ensuring the regular and systematic monitoring of road surfaces is of prime importance for maintaining acceptable quality levels and promptly addressing adverse factors. Proactively identifying and rectifying road surface issues, such as roughness, cracks, potholes, and unevenness, enhances road safety, improves driving comfort, and prolongs the lifespan of roads. The following section will delve into the state-of-the-art road condition monitoring techniques used for this purpose.

1.2 State-of-the-art Road Condition Monitoring Techniques

The strategies employed for road condition monitoring differ across various countries, involving both wide-scale data collection for major roads and localised approaches that target specific road sections of interest [91]. The information gathered from reports published by transportation departments in different countries are discussed in [16, 43, 128, 144].

For nationwide road condition monitoring, several countries utilise specialised survey vehicles equipped with various sensors. A fully automated Laser Crack Measurement

System (LCMS) is mounted on these vehicles to detect different types of cracks, such as longitudinal cracks, transverse cracks, pavement edge cracking, and alligator cracking [81]. Laser profilers or multi-sensor profilers are employed to estimate rutting, which refers to longitudinal depressions on the road surface often caused by heavy trucks' wheel paths. These profilers are also used to measure the road surface roughness and international roughness index (IRI) which is widely used as a measure of road surface unevenness [79]. Additionally, high-resolution digital cameras are installed on these survey vehicles to inspect road signs, structures, lane dividers, and guardrails. Some transportation departments also equip these vehicles with ground-penetrating radar (GPR) systems. These GPR systems serve various purposes, including the detection of subsurface changes beneath the road surface, the demarcation of homogeneous zones, the estimation of asphalt or concrete layer thicknesses, and the identification of voids or buried utilities [62]. Differential GPS systems are integrated into the vehicles to precisely locate and determine the orientation of the road defects identified by the sensors [110]. However, these advanced survey vehicles come with significant costs and require substantial time and manpower to operate throughout the country. Consequently, such comprehensive surveys are conducted only once every few years [P4]. For instance, in Germany, they are performed approximately every four years, primarily focusing only on major motorways [107].

Localised approaches for road condition assessment involve accredited surveyors inspecting the road sections either by walking or driving. The defects identified by the surveyors are analysed, and a priority rating for maintenance is assigned. Based on this rating, the defects are repaired, and a report is uploaded to a central database, which includes images of the defects, surveyor findings, and information about the maintenance work performed. However, this approach is highly inefficient and demands considerable time and effort [91, 110].

Considering that road deterioration happens much faster, especially during the winter season [24], there is a growing need for more frequent road condition monitoring, ideally on an annual basis. To address this need, researchers are exploring novel approaches using remote sensing techniques for wide-scale road condition monitoring to improve efficiency and cost-effectiveness [120]. The next section will delve into state-of-the-art road condition monitoring using synthetic aperture radar remote sensing techniques.

1.3 State-of-the-art SAR-based Road Condition Monitoring

Synthetic Aperture Radar (SAR) has the potential to be used as an alternative technology for wide-area road condition monitoring due to its sensitivity to changes in dielectric properties and surface roughness [137]. Only a few studies can be found in the open literature that have utilised SAR data to estimate road surface quality.

In one such study [129], L-band SAR data from the ALOS-PALSAR satellite of Japan, with a 7-meter spatial resolution, were used to establish a correlation between SAR backscatter signal and the International Roughness Index (IRI) values for the road surfaces in Thailand. The findings revealed that as road conditions deteriorated, the SAR backscatter values increased, suggesting a potential relationship between the two parameters.

Another study took place in the Commonwealth of Virginia, employing X-band SAR data from the Cosmo-SkyMed satellite of Italy, with a 3-meter spatial resolution to estimate IRI values. This study achieved an overall accuracy of 92.6% in estimating IRI values from the SAR data [95].

These studies demonstrate the feasibility of SAR-based approaches for estimating road defects, highlighting the potential of SAR technology as a valuable tool for road condition monitoring and maintenance assessment.

1.4 Main Objectives and Thesis Contributions

Although studies in the literature have explored the use of SAR for monitoring road surface quality, as mentioned in the previous section, it is crucial to highlight that these studies were preliminary and limited in scope. They primarily focused on estimating the International Roughness Index (IRI), which represents road unevenness, but this is just one parameter for road condition monitoring. Furthermore, the SAR data used in these studies were of medium resolution (3 to 7 meters), which posed limitations in generating high-quality road condition maps. Consequently, interpreting the results of these studies might be challenging for a road maintenance engineer without expertise in SAR data analysis.

This thesis aims to expand the scope and assess multiple parameters critical to road condition monitoring. The main objectives of this study are as follows:

1. **Road Surface Roughness Estimation:** The first objective is to evaluate the potential of state-of-the-art roughness estimation models for road surface roughness estimation using high-resolution airborne SAR data. Additionally, the study will develop a new semi-empirical road surface roughness estimation model tailored to airborne SAR, offering enhanced accuracy and applicability.
2. **Machine Learning Applications:** Building upon the roughness estimation efforts, the second objective is to investigate the effectiveness of machine learning-based algorithms for estimating road surface roughness using high-resolution airborne SAR data. These algorithms have the potential to further refine roughness estimates and streamline the monitoring process.

3. **Spaceborne SAR Application:** The third objective focuses on exploring the possibility of utilising high-resolution spaceborne SAR data for road surface roughness estimation. This study aims to expand road condition monitoring capabilities to a global scale.
4. **Cracks Detection and Road Width Estimation:** The fourth objective involves the development of algorithms for crack detection and road width estimation using high-resolution airborne SAR data. These algorithms will enable the identification of road surface defects, such as cracks, and provide valuable data for road width assessment.

This thesis introduces a novel and comprehensive approach to road condition monitoring through the application of SAR technology. By estimating multiple parameters that influence road conditions and leveraging high-resolution SAR data with sub-meter spatial resolution, this research aims to bridge the gap between current monitoring techniques and the requirements of modern road infrastructure management.

The key novelties and contributions of this thesis are outlined below:

- Detailed analysis has been carried out to assess the applicability of state-of-the-art roughness estimation models, initially designed for estimating soil roughness in agricultural fields, for the estimation of road surface roughness (cf. Chapters 2 and 3) [P1, P2, P3, P4].
- A new semi-empirical model and processing chain have been specifically developed for accurately estimating road surface roughness using high-resolution airborne SAR data. The model has been developed to overcome the shortcomings of the state-of-the-art roughness estimation models and to improve the accuracy of road surface roughness estimation. To achieve the best possible results, the model is trained using high-resolution airborne SAR data with 25 cm spatial resolution, along with ground truth surface roughness data of micrometre accuracy (cf. Chapter 3) [P4, P5].

  The functionalities of the processing chain include:

  - Estimation and minimisation of additive noise in the polarimetric SAR (PolSAR) data to enhance the reliability of road surface roughness estimation.
  - Upper sigma nought thresholding to remove pixels with high backscattering from lane dividers, overhead signboards, flyover walls, and other similar structures, which can lead to invalid surface roughness estimates.

  - Lower signal-to-noise-ratio (SNR) thresholding to eliminate the noise-dominated pixels, avoiding invalid surface roughness values from low SNR regions and radar shadow regions.
  - Multi-dataset fusion to combine road surface roughness results from various SAR datasets with different acquisition geometries and incidence angles, improving the overall accuracy of the results.
  - Geocoding of road surface roughness images, extraction of roads of interest using Open Street Map (OSM) data, and visualisation of the road surface roughness results in Google Earth.

- Machine learning-based artificial neural network (ANN), random forest (RF), and Support Vector Regression (SVR) models were trained and evaluated for road surface roughness estimation utilising high-resolution airborne SAR data. These models can learn and adapt to data variations and different environmental conditions, making them valuable for estimating road surface roughness even when the SAR data characteristics fall outside the validity conditions of the conventional roughness estimation models (cf. Chapter 4) [P5, P8].
- The newly developed semi-empirical road surface roughness estimation model and processing chain, originally designed for airborne SAR applications, have been adapted for spaceborne SAR scenarios. This adaptation allows for consistent monitoring of road conditions worldwide, using high-resolution spaceborne SAR data (cf. Chapter 5) [P6].

  The modifications introduced to enable this adaptation comprise:

  - Estimating a new set of coefficients for the semi-empirical model.
  - Estimating and subtracting the noise-equivalent beta nought (NEBN) from the sigma nought backscatter image to reduce additive noise.
  - Employing multilooking of the SAR data, enhancing the signal-to-noise ratio (SNR), and generating approximately square pixels, which facilitates easier image interpretation.

- Algorithms were developed to detect cracks on the road surface, estimate their orientation with respect to the true north direction, and determine the road width using high-resolution airborne SAR data (cf. Chapter 6).

  The key investigations include:

  - Analysis of the flight heading angle dependency on the visibility of cracks in airborne SAR data.

- Investigations on the possibility of cracks detection from airborne SAR data using methods based on Canny edge detector [30], stationary wavelet transform (SWT) [41] and Radon transform [9].
- Development of a novel method for cracks detection and orientation estimation based on the combined use of an adaptive thresholding algorithm and the Radon transform.
- Combining the geocoded road surface roughness images with the OSM data for road width estimation.

Moreover, this research's findings hold significant promise for predictive maintenance in road infrastructure management. By harnessing SAR technology to periodically monitor road conditions, it enables the early detection of potential issues and facilitates proactive maintenance efforts. This proactive approach can significantly extend the lifespan of road networks, reduce maintenance costs, and enhance overall transportation safety and efficiency. Thus, this research not only establishes SAR as a valuable tool for road condition assessment but also paves the way for the integration of predictive maintenance practices into road infrastructure management, ensuring the long-term sustainability and resilience of road networks.

1.5 Structure of the Thesis

This thesis is structured into seven chapters, each dedicated to addressing various aspects of road condition monitoring using SAR data. The remaining chapters are organised as follows:

Chapter 2 covers the principles of SAR, data acquisition geometry, SAR image generation, and information about distortions in SAR images and radar backscatter coefficients. Additionally, this chapter explores state-of-the-art roughness estimation models.

In **Chapter 3**, a new semi-empirical road surface roughness model for airborne SAR is introduced. The chapter details the processing chain used to estimate road surface roughness and presents the experimental results. Furthermore, it includes a comparative analysis between the results obtained using state-of-the-art roughness estimation models and the newly developed semi-empirical model.

Chapter 4 discusses the application of machine learning-based algorithms for road surface roughness estimation using airborne SAR data. The chapter covers the structure of the processing chain and presents the experimental results obtained from this approach.

The estimation of road surface roughness using high-resolution spaceborne SAR data is presented in **Chapter 5**. This chapter discusses the adaptation of the newly developed

semi-empirical road surface roughness estimation model for spaceborne SAR scenarios and outlines the processing chain's structure. Additionally, the chapter presents and compares the experimental road surface roughness results obtained from the spaceborne SAR data with those from the airborne SAR data.

Chapter 6 focuses on the algorithms developed for detecting cracks and estimating road width using airborne SAR. The chapter deals with different approaches for crack detection and a method for road width estimation is also explained. The chapter concludes by presenting the experimental results obtained using these algorithms.

The thesis concludes with **Chapter 7**, which offers a comprehensive summary and discussion. Additionally, this chapter presents future work and outlook for further advancements in SAR-based road condition monitoring.

2 Synthetic Aperture Radar and Classical Roughness Estimation Models

2.1 SAR Concepts

Synthetic Aperture Radar (SAR) is an active remote sensing technology that has the capability to produce high-resolution two-dimensional images of the Earth's surface. Unlike passive sensors that detect naturally occurring electromagnetic (EM) radiation, SAR operates by transmitting its own EM pulses towards the ground and then capturing the signals that bounce back after interacting with the terrain and objects on the Earth's surface [4]. This interaction provides information about the properties and structure of the objects and surfaces under observation. SAR systems typically operate in the microwave portion of the EM spectrum, encompassing various frequency bands such as P, L, S, C, X, and Ka [136]. SAR is evolved from the side-looking airborne radar (SLAR) [77] and it differs in operation from SLAR by harnessing the motion of platforms such as satellites, aircraft, or drones, on which it is mounted, to synthesize a larger antenna aperture or "virtual antenna" which is larger than the physical antenna size [99, 138]. This is achieved by the application of phase-coherent signal processing techniques that integrate multiple transmitted pulses [132]. The larger antenna aperture, combined with advanced processing techniques, results in SAR's unique ability to generate high-resolution images [99].

A SAR system functions by transmitting precisely timed microwave pulses towards the Earth's surface. These pulses interact with various features such as landforms, vegetation, buildings, water bodies, etc. and produce backscattered signals [134]. These backscattered signals are received by the SAR system between the pulse transmission events [47], and the system records both their amplitude and phase values which contain information about the observed surface [23]. The phase data can be used to determine the distance between the SAR system and ground targets, while the amplitude data can be used to quantify the backscattered signal that returns to the radar, revealing details about the surface roughness, terrain slope and dielectric properties [89]. These amplitude and phase data, often referred to as 'raw data', undergo further processing which involves complex motion compensation and SAR focusing techniques to generate the SAR image [114]. Since SAR has its own pulse transmission capability, parameters like frequency, look angle and polarisation can be chosen according to the intended applications [136]. Modern SAR systems can transmit and receive EM pulses in various polarisation states, such as linear (horizontal and vertical) or circular polarisations, enabling the generation of dual- and quad-polarised SAR images that provide diverse perspectives of the same scene [49]. Quad-polarised SAR, known as fully polarimetric

SAR (PolSAR) [90], captures various structural and physical information and facilitates the detection of different scattering mechanisms. The operating frequency, look angle, polarisation and illuminated area dimensions of a SAR dataset determine its suitability for different remote sensing applications [136].

Furthermore, SAR's active nature means it can operate independently of external factors like weather conditions and daylight. Microwave wavelengths can penetrate through clouds and rain, enabling SAR to provide consistent imaging capabilities regardless of environmental conditions [99, 142]. This attribute distinguishes SAR as an all-weather, all-time imaging technology, making it invaluable for a wide array of applications, including agriculture (for crop monitoring and yield prediction) [93, 108], forestry (for assessing forest health and deforestation) [78, 130], infrastructure monitoring (for detecting changes and deformations) [58, 105], disaster management (for assessing post-disaster damage) [17, 71], and military surveillance (for intelligence gathering and target identification) [57, 112], among others. The following sub-sections discuss SAR concepts in more detail and address the data acquisition geometry, SAR image generation, distortions in SAR images and the importance of the backscatter coefficient in SAR remote sensing.

2.1.1 Data Acquisition Geometry

This subsection explains the data acquisition geometry for an airborne SAR system, assuming a flat earth geometry, disregarding the effects of Earth's curvature [46, 104]. SAR systems can operate in various imaging modes, depending on the desired spatial resolution and the extent of the region that needs to be imaged. The most frequently employed imaging modes for both airborne and spaceborne SAR systems are the spotlight, stripmap, and scansar modes [99]. Figure 2.1 illustrates the data acquisition geometry of the stripmap data acquisition mode.

In Figure 2.1, the SAR antenna is affixed to the side of a moving platform, such as an aircraft, which maintains a constant velocity (v_{p}) and a constant altitude (h) above the ground. The antenna observes the terrain in a side-looking configuration. The SAR captures images of the region orthogonal to the aircraft's flight path, known as the range direction. The direction of the aircraft movement is termed as the azimuth direction. The extent of the region that the SAR system can image in a specific mode is referred to as the swath. The area of the swath closest to the SAR antenna is called the near range, while the area farthest from the SAR antenna is known as the far range. The slant range direction is the path in which the antenna transmits the radar pulses to the ground. Consequently, the slant range distance increases from the near range to the far range [73, 99, 137]. The projection of the slant range on the ground from the nadir is known as the ground range. The antenna is tilted downwards from the horizontal plane by a

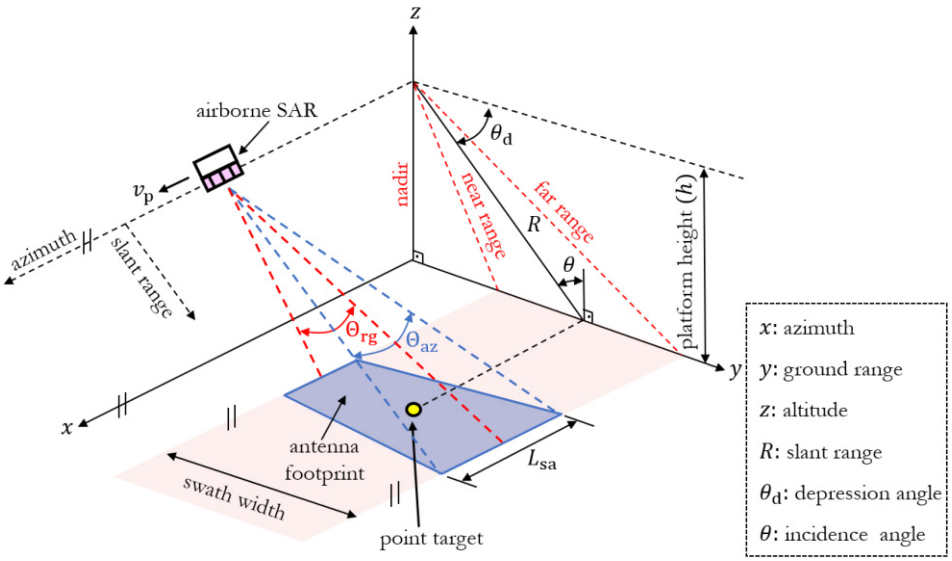

Figure 2.1: SAR data acquisition geometry in stripmap mode.

depression angle (θ_d), which is complementary to the incidence angle (θ) for the case of a flat Earth Cartesian geometry as with airborne SAR. In the stripmap mode, the SAR antenna maintains a fixed boresight and transmits radar pulses at a rate known as the pulse repetition frequency (PRF) [47].

The imaging characteristics of the SAR system are determined by the 3 dB half-power beamwidth of the antenna. In the range direction, the range beamwidth (Θ_{rg}) defines the maximum width of the swath, while in the azimuth direction, the azimuth beamwidth (Θ_{az}) determines the synthetic aperture length (L_{sa}). The synthetic aperture length, which is dependent on the slant range, can be expressed as [38]:

$$L_{sa} = 2R_o \tan\left(\frac{\Theta_{az}}{2}\right) , \tag{2.1}$$

where R_o represents the slant range distance to the center of the swath. The time required to create this synthetic aperture, known as the synthetic aperture time (T_{sa}), is given by [38]:

$$T_{sa} = \frac{L_{sa}}{v_p} . \tag{2.2}$$

In real-world scenarios, the SAR antenna footprint includes multiple targets. For two targets to be distinguished in the slant range direction without applying any pulse

compression, their backscattered signals must not overlap in time. Assuming the SAR transmits rectangular pulses of duration (τ_{p}), the minimum slant range distance (slant range resolution) required to separate two neighbouring targets can be expressed as [38]:

$$\delta_{\mathrm{r,raw}} = \frac{\mathrm{c}\tau_{\mathrm{p}}}{2} \ , \tag{2.3}$$

where c denotes the speed of light in a vacuum. This equation indicates that slant range resolution improves with shorter pulse durations. However, shorter pulses demand higher transmission power to maintain a strong signal-to-noise ratio (SNR) in the backscattered signals. The trade-off between pulse duration and slant range resolution can be resolved by using pulse compression techniques with matched filters (cf. section 2.1.2). These techniques enable high-resolution imaging while maintaining lower peak transmission power, significantly improving both the slant range resolution and the SNR for point targets.

In the azimuth direction, the backscattered signals from the targets overlap within the azimuth footprint. For real aperture radars (RAR) with a narrow azimuth beamwidth (Θ_{az}), the azimuth resolution can be approximated as [38]:

$$\delta_{\mathrm{az,raw}} \approx \Theta_{\mathrm{az}} R_{\mathrm{o}} = \frac{\lambda R_{\mathrm{o}}}{l_{\mathrm{a}}} \ , \tag{2.4}$$

where λ is the radar wavelength, and l_{a} is the physical antenna length. This formula shows that the azimuth resolution degrades as the slant range (R_{o}) increases. At a given frequency, a longer antenna improves azimuth resolution for RAR systems.

In SAR, instead of using a longer antenna, signal processing techniques can be used to coherently combine backscatter signals received over the illumination period of a particular target to create a very large synthetic aperture in the azimuth direction. This method achieves a higher azimuth resolution (δ_{az}) without requiring a physically larger antenna. The azimuth resolution, based on the coherent processing interval time (T_{CPI}), can be expressed as [25]:

$$\delta_{\mathrm{az}} \approx \frac{\lambda R_{\mathrm{o}}}{2 v_{\mathrm{p}} T_{\mathrm{CPI}}} \ . \tag{2.5}$$

From the above equation, it is evident that the azimuth resolution can be improved by increasing the T_{CPI}. If the complete synthetic aperture time is used as the coherent processing interval ($T_{\mathrm{CPI}} = T_{\mathrm{sa}}$), then the best possible azimuth resolution for the SAR system can be obtained and can be written as [38]:

$$\delta_{az} \approx \frac{l_a}{2} . \tag{2.6}$$

This equation highlights that SAR systems provide azimuth resolution independent of range, depending only on the physical length of the antenna. Therefore, even spaceborne SAR systems can achieve high azimuth resolution by designing antennas with shorter lengths to widen the azimuth beamwidth, allowing for extended coherent integration times.

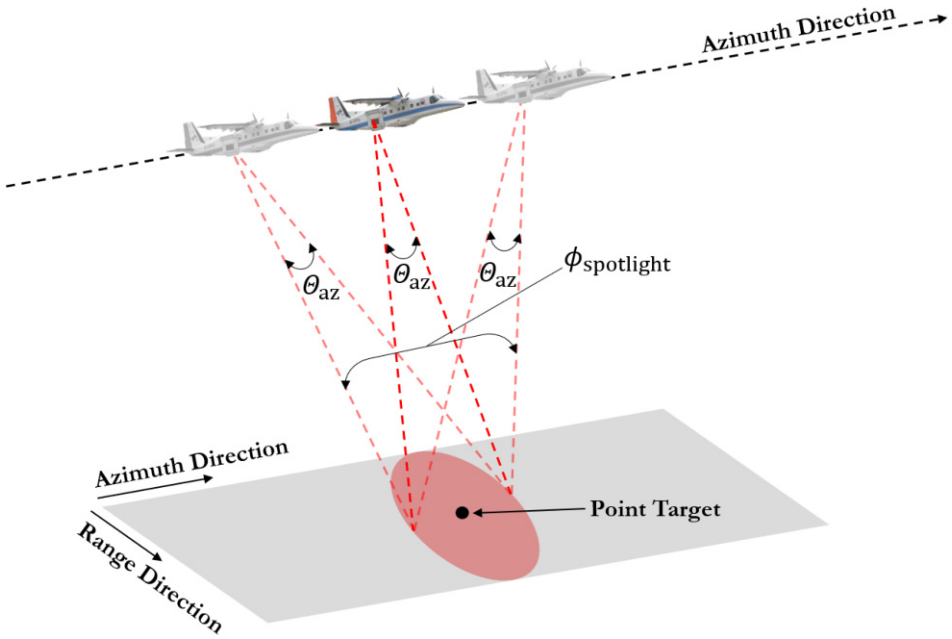

Figure 2.2: SAR data acquisition geometry in staring spotlight mode.

As mentioned at the beginning of this sub-section, the SAR system can be operated in other imaging modes such as the spotlight mode to increase the azimuth resolution. Figure 2.2 shows the data acquisition geometry for the staring spotlight mode, which is the most advanced variant of the spotlight technique capable of providing the best possible azimuth resolution. In this mode, the antenna pattern is electronically steered in the azimuth direction to focus on a fixed area for an extended duration. This prolonged illumination time increases the synthetic aperture length (L_{sa}), consequently enhancing azimuth resolution. However, a drawback of this technique lies in the reduced coverage area due to the extended observation time required for a small area, resulting in a narrower swath compared to the stripmap mode [97].

2.1.2 Pulse Compression and Range Resolution

Pulse compression techniques enhance the slant range resolution and SNR in SAR systems by employing long, modulated transmit pulses instead of short, high-power ones. This approach uses linear frequency modulated (LFM) signals, commonly referred to as "chirp" signals. When these chirp signals are transmitted and their backscattered signals are received, matched filtering is applied during signal processing. This process compresses the spread-out backscattered signals in the range direction, achieving the fine slant-range resolution of a short pulse while retaining the high energy of a long pulse [39].

Pulse compression is performed by convolving an uncompressed received signal $s(t)$ with a proper reference function $h(t)$. The pulse compressed signal $s_{\text{out}}(t)$ is given as:

$$s_{\text{out}}(t) = s(t) * h(t) = \int_{-\infty}^{\infty} s(\tau)h(t-\tau)\,d\tau\,, \tag{2.7}$$

where $*$ denotes the convolution operator. The reference function $h(t)$ is the time-reversed complex conjugate of the expected received signal $s(t)$.

After performing the pulse compression using matched filters, the slant range resolution (δ_{r}) for a LFM transmitted pulse is given by [38]:

$$\delta_{\text{r}} = \alpha_{\text{wn}} \frac{\text{c}}{2B_{\text{r}}}\,, \tag{2.8}$$

where B_{r} is the bandwidth of the chirp signal and α_{wn} accounts for windowing losses (e.g., $\alpha_{\text{wn}} \cong 0.89$ for a rectangular window). This equation highlights that large chirp bandwidths should be used for achieving high slant range resolution.

Since the ability of a SAR system to distinguish objects in the ground range direction is more critical than in the slant range direction, the ground range resolution (δ_{rg}) can be approximated by modifying the slant range resolution equation as follows [116]:

$$\delta_{\text{rg}} = \alpha_{\text{wn}} \frac{\text{c}}{2B_{\text{r}} \sin\theta}\,, \tag{2.9}$$

where θ is the local incidence angle at the point of incidence of the transmitted chirp signal on the ground.

2.1.3 SAR Image Generation

To convert the raw data, i.e. the backscattered signals recorded by the SAR system, into a SAR image, several signal processing steps are required, collectively referred to as SAR image focusing [114]. The important signal-processing steps involved in this process include range compression, range cell migration correction (RCMC), and azimuth compression [34]. Figure 2.3 illustrates a simplified block diagram outlining the progression from raw SAR data to the focused image, specifically for a single-point target imaged by the SAR system. Brief descriptions for each of the steps are as follows:

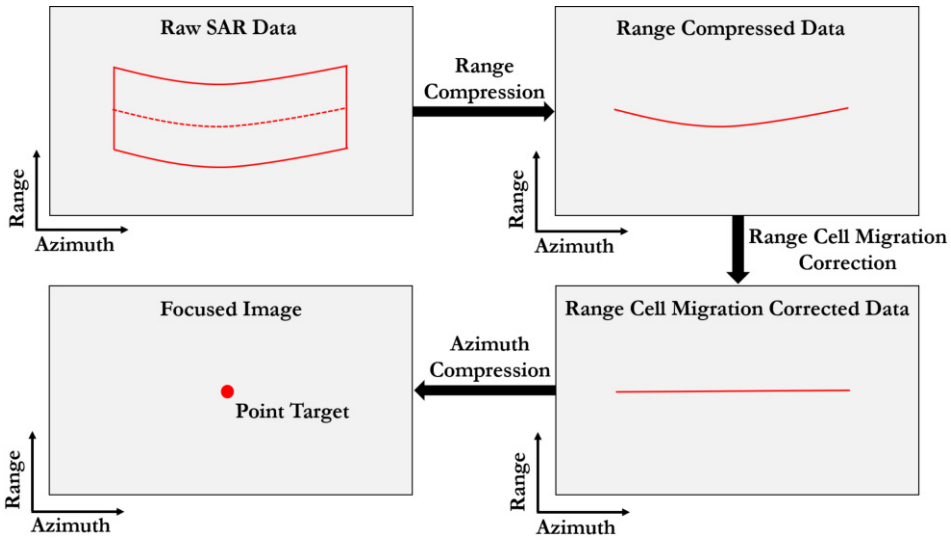

Figure 2.3: Major steps in focused SAR image generation from raw data.

Range Compression: Pulse compression is performed along the range direction of the received raw SAR data (cf. top right image in Figure 2.3) [34].

Range Cell Migration Correction (RCMC): This is a crucial correction step in the SAR image generation procedure that addresses the motion-induced range walk, particularly in the range direction, known as range cell migration (RCM). RCM happens because the radar pulse illuminates different ground areas at different times due to the movement of the SAR platform. This leads to different Doppler shifts in the backscattered signals from various ground locations, causing phase errors. These errors result in the displacement of the SAR image in the range direction, causing blurring. The RCM is mitigated by correcting the curvature of the target range history (cf. bottom right image in Figure 2.3) [34, 38].

Azimuth Compression: It is the final step in the SAR image generation process. It involves focusing the radar echoes in the azimuth direction to generate the final SAR

image. This process compensates for the Doppler shift caused by the motion of the SAR platform and ensures that the backscattered signals from different ground points are correctly aligned along the azimuth direction. The result is a focused SAR image with high azimuth resolution [99].

By sequentially performing these signal processing steps, raw radar measurements can be converted into high-quality and high-resolution SAR images suitable for various remote sensing applications.

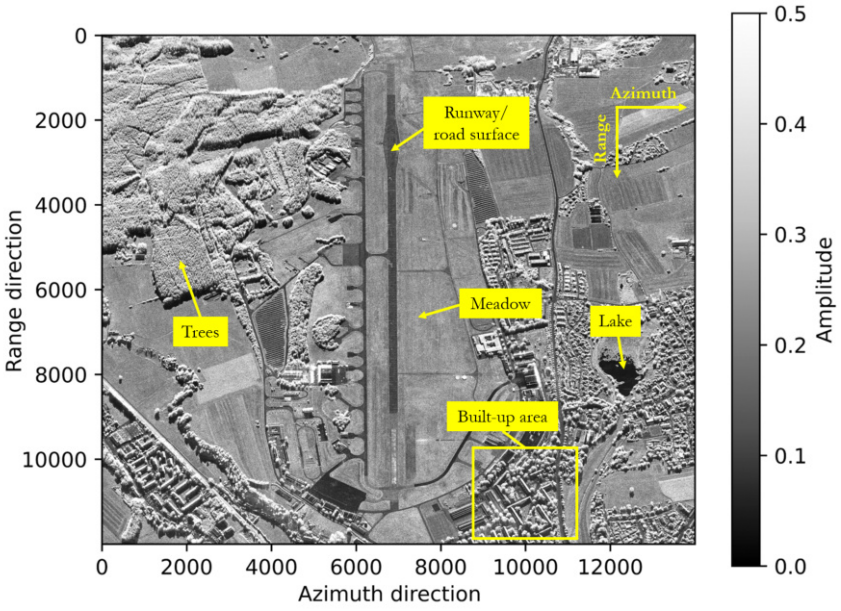

Figure 2.4: SAR image acquired by the airborne X-band F-SAR system.

The fully focused SAR data obtained after performing the above-described SAR image generation steps are in a complex form, where each pixel is represented by real and imaginary values. By calculating the pixel-wise amplitude values of these complex numbers, a visual representation of the SAR data can be created, an example of which is shown in Figure 2.4. This image was created using the airborne X-band F-SAR system with an azimuth and range resolution of 25 x 25 cm (see also Appendix A). The yellow directional arrows indicate the azimuth and range direction. When visually analysing the image, different ground targets can be identified based on the differences in amplitude values. Lakes appear very dark due to the low backscatter from calm water surfaces, while roads also have a relatively low brightness due to the low backscatter from smooth surfaces. Meadows in the vicinity of roads appear brighter because of increased backscatter from comparatively rough land surfaces, whereas trees and built-up areas appear bright due to strong backscatter. So, as with optical images, a thorough examination of fully focused

SAR images can also provide valuable insights into ground features and targets within the imaged regions.

2.1.4 Distortions in SAR Image

SAR images are susceptible to various types of distortions, primarily occurring due to the side-looking geometry of the SAR system. This configuration causes SAR systems to measure distances to objects on the ground in the slant range rather than directly in the ground range from the nadir point. Consequently, SAR images display variation in ground range resolution (δ_{rg}) from the near range to the far range. The distortions commonly encountered in SAR images due to this side-looking geometry are foreshortening, layover, and radar shadow.

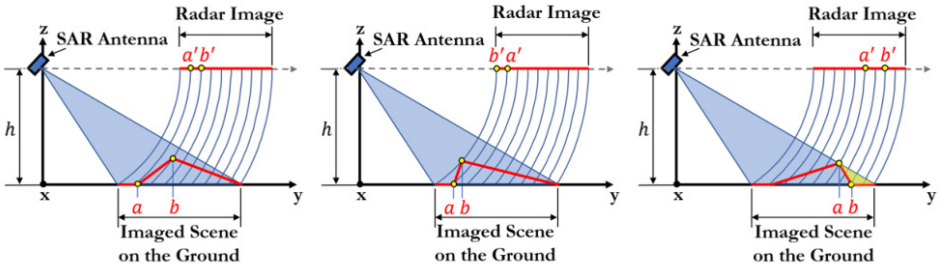

Figure 2.5: Distortions in SAR image. (a) Foreshortening. (b) Layover. (c) Radar shadow.

Foreshortening is observed when the radar beam encounters an inclined tall feature, such as a mountain or skyscraper (cf. Figure 2.5(a)). In such cases, the radar wavefront reaches the feature's base at point a before it reaches the top at point b. Since SAR systems measure distances in the slant range, this inclination causes the slope of the feature, spanning from point a to point b, to appear compressed. Consequently, the length of the slope is misrepresented as being shorter (from point a' to point b') in the (slant range) radar image [142].

Layover, as illustrated in Figure 2.5(b), occurs when the radar beam first encounters the top of a tall feature (point b) before reaching its base (point a). Consequently, the backscattered signal from the top of the feature arrives before the signal from the bottom. This results in the top of the feature being displaced toward the SAR sensor, creating a "layover" effect over the base of the feature, as shown by points b' to a'. Layover is most prominent at smaller incidence angles, particularly in the near range, and is frequently observed in rugged, mountainous terrain [142].

Radar shadowing arises when the radar beam is unable to illuminate a specific portion of the ground surface. These shadows predominantly occur behind vertical features or steep slopes, extending towards the far range (yellow region shown in Figure 2.5(c)). In regions where the radar beam cannot reach, shadowed areas appear dark in the SAR image, as there is no radar energy available for backscattering. As the incidence angle increases from the near range to the far range, the shadow effects become more pronounced, as the radar beam approaches the surface at a shallow angle [116].

SAR images also exhibit a form of distortion called speckle, which is a granular or grainy noise-like pattern that appears as a result of the interference of radar waves. It is characterized by random variations in brightness or intensity across the image pixels. Speckle can obscure fine details in the image and reduce its visual clarity [99, 125].

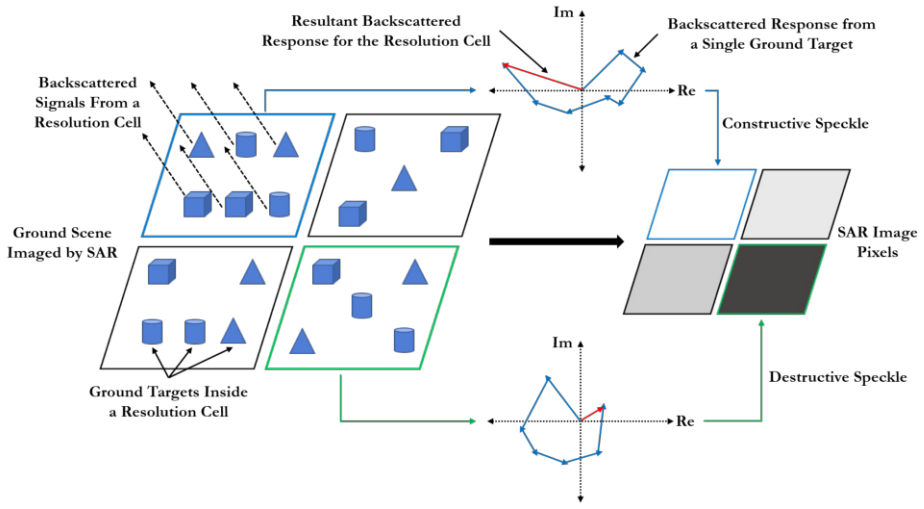

Figure 2.6: Speckle formation in a SAR image.

The formation of speckle can be primarily attributed to the interference of multiple radar waves returning from a resolution cell. A resolution cell in SAR represents the smallest distinguishable area on the ground, determined by the system's spatial resolution and it encompasses a finite number of scattering centres or reflectors on the ground. Each of these scattering centres contributes to the backscattered signal. Speckle arises due to the constructive and destructive summation of radar waves reflected from these scattering centres within the resolution cell (cf. Figure 2.6). When radar waves return in phase, they constructively interfere, leading to pixels of high intensity or brightness in the image. Conversely, when waves return out of phase, destructive interference occurs, resulting in pixels of low intensity or darkness. The random distribution and phase relationships of scattering centres within the resolution cell collectively give rise to the speckle pattern

[99, 125]. To address the issue of speckle, various techniques are employed, including multilooking [141] and speckle filtering [133].

2.1.5 Signal-to-Noise Ratio and Backscattering Coefficient

The signal-to-noise ratio (SNR) is a measure of the strength of the backscattered signal compared to the background noise received by the SAR system. SNR is an important parameter in SAR because it indicates how well the radar can distinguish between the target signal (desired information) and unwanted noise. The higher the SNR, the better the SAR system's ability to detect and distinguish features on the ground [45]. The SNR of a monostatic SAR system after coherent integration can be calculated as follows:

$$SNR = \frac{P_{\text{avg}} G^2 \lambda^3 \text{c}}{4^4 \pi^3 R^3 B_{\text{r}} \sin\theta v k T_{\text{s}} F L} \sigma^o \ , \tag{2.10}$$

where P_{avg} is the average transmit power, G is the gain of the SAR antenna, λ is the wavelength of the SAR system, c is the speed of light, σ^o is the radar backscattering coefficient, R is the slant range distance, B_{r} is the bandwidth of the chirp signal, θ is the local incidence angle, v is the SAR platform velocity, k is the Boltzmann constant, T_{s} is the system noise temperature, F is the noise figure of the SAR system and L accounts for combined losses in the SAR system.

The radar backscatter coefficient (σ^o) is a normalised measure of how much radar energy is scattered back in the direction of the radar. It is the radar cross section (RCS) per unit area and is given in square metres per square metre (m^2/m^2) or decibels (dB). The radar backscatter coefficient is independent of the size of the target and is more related to the intrinsic scattering properties of the target material. The σ^o values are influenced by several factors, including the material composition, dielectric constant, surface roughness, slope, moisture content and other characteristics of the imaged ground surface [123]. As a result, it is an important parameter for evaluating the structural and physical properties of the imaged area, which justifies its wide applicability in remote sensing applications, including road condition monitoring.

2.2 State-of-the-Art Roughness Estimation Models

The vertical profile of a road surface, as shown in Figure 2.7, illustrates the millimeter-level undulations present on the road's surface [P4]. The variability within this profile plays a pivotal role in determining the road surface roughness [44]. To quantitatively assess road surface roughness, one commonly used metric is the root mean square (RMS) height (h_{rms}) of these vertical undulations, which can be computed as follows [64, 74]:

$$h_{\text{rms}} = \sqrt{\frac{\sum_{i=1}^{n}(h_i - \overline{h})^2}{n-1}}\ , \tag{2.11}$$

where h_i is the height of the i^{th} sample, $\overline{h}$ is the mean height over all the samples and n is the number of samples considered.

However, it is important to note that h_{rms} cannot be directly estimated from SAR data. Instead, the effective vertical roughness parameter (ks), a dimensionless parameter, can be estimated from SAR data. Subsequently, h_{rms} can be calculated using the following equation [64, 74]:

$$h_{\text{rms}} = \frac{ks}{2\pi/\lambda}\ , \tag{2.12}$$

where λ denotes the wavelength of the SAR system.

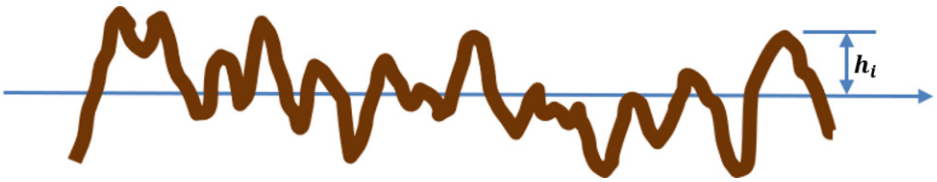

Figure 2.7: Vertical road surface profile.

The following sub-sections offer an overview of existing surface roughness estimation models in the literature that utilise SAR data to assess surface roughness values (ks parameters) within the imaged region. While these models were primarily designed for assessing surface roughness of agricultural fields, their applicability to road surface roughness estimation is explored later in chapter 3. The models are categorized into three groups: SAR polarimetry-based models, physical roughness estimation models, and semi-empirical roughness estimation models [74].

2.2.1 SAR Polarimetry-based Models

As mentioned in section 2.1, a PolSAR system employs four transmit-receive polarisation combinations: HH (horizontal transmit, horizontal receive), HV (horizontal transmit, vertical receive), VH (vertical transmit, horizontal receive), and VV (vertical transmit, vertical receive). These measurements are represented by a scattering matrix ($\boldsymbol{S}$) as follows [P4, 88, 142]:

$$\boldsymbol{S} = \begin{bmatrix} S_{\mathrm{HH}} & S_{\mathrm{HV}} \\ S_{\mathrm{VH}} & S_{\mathrm{VV}} \end{bmatrix} . \tag{2.13}$$

This 2x2 scattering matrix offers valuable insights into radar return polarisation properties, facilitating a comprehensive characterisation of ground target scattering behaviour [32]. Targets on the ground can be classified or decomposed based on their scattering mechanisms using coherence and covariance matrices, which are second-order representations derived from the scattering matrix [99]. Two common target vector representations in the literature are the Pauli feature vector ($\boldsymbol{k}_{\mathrm{p}}$) and the lexicographic feature vector ($\boldsymbol{k}_{\mathrm{l}}$), which are described as [88, 115]:

$$\boldsymbol{k}_{\mathrm{p}} = \frac{1}{\sqrt{2}} \begin{bmatrix} S_{\mathrm{HH}} + S_{\mathrm{VV}} \\ S_{\mathrm{HH}} - S_{\mathrm{VV}} \\ S_{\mathrm{HV}} + S_{\mathrm{VH}} \\ \mathrm{j}(S_{\mathrm{HV}} - S_{\mathrm{VH}}) \end{bmatrix}, \boldsymbol{k}_{\mathrm{l}} = \begin{bmatrix} S_{\mathrm{HH}} \\ S_{\mathrm{HV}} \\ S_{\mathrm{VH}} \\ S_{\mathrm{VV}} \end{bmatrix} . \tag{2.14}$$

The 4x4 covariance matrix $\boldsymbol{C}_4$ is computed by multiplying the lexicographic feature vector with its transpose conjugate [88]:

$$\boldsymbol{C}_4 = \langle \boldsymbol{k}_{\mathrm{l}} \boldsymbol{k}_{\mathrm{l}}^{\mathrm{T}*} \rangle = \begin{bmatrix} |S_{\mathrm{HH}}|^2 & S_{\mathrm{HH}} S_{\mathrm{HV}}^* & S_{\mathrm{HH}} S_{\mathrm{VH}}^* & S_{\mathrm{HH}} S_{\mathrm{VV}}^* \\ S_{\mathrm{HV}} S_{\mathrm{HH}}^* & |S_{\mathrm{HV}}|^2 & S_{\mathrm{HV}} S_{\mathrm{VH}}^* & S_{\mathrm{HV}} S_{\mathrm{VV}}^* \\ S_{\mathrm{VH}} S_{\mathrm{HH}}^* & S_{\mathrm{VH}} S_{\mathrm{HV}}^* & |S_{\mathrm{VH}}|^2 & S_{\mathrm{VH}} S_{\mathrm{VV}}^* \\ S_{\mathrm{VV}} S_{\mathrm{HH}}^* & S_{\mathrm{VV}} S_{\mathrm{HV}}^* & S_{\mathrm{VV}} S_{\mathrm{VH}}^* & |S_{\mathrm{VV}}|^2 \end{bmatrix} , \tag{2.15}$$

where $\langle \cdot \rangle$ represents local averaging over a set of neighbouring pixels [142].

Similarly, the 4x4 coherency matrix ($\boldsymbol{T}_4$), resulting from the product of the Pauli feature vector with its conjugate transpose, is represented as [88]:

$$
\boldsymbol{T}_4 = \left\langle \boldsymbol{k}_\mathrm{p} \boldsymbol{k}_\mathrm{p}^{\mathrm{T}*} \right\rangle =
\begin{bmatrix}
|S_{\mathrm{HH}} + S_{\mathrm{VV}}|^2 & (S_{\mathrm{HH}} + S_{\mathrm{VV}})(S_{\mathrm{HH}} - S_{\mathrm{VV}})^* & (S_{\mathrm{HH}} + S_{\mathrm{VV}})(S_{\mathrm{HV}} + S_{\mathrm{VH}})^* & (S_{\mathrm{HH}} + S_{\mathrm{VV}})(\mathrm{j}(S_{\mathrm{HV}} - S_{\mathrm{VH}}))^* \\
(S_{\mathrm{HH}} - S_{\mathrm{VV}})(S_{\mathrm{HH}} + S_{\mathrm{VV}})^* & |S_{\mathrm{HH}} - S_{\mathrm{VV}}|^2 & (S_{\mathrm{HH}} - S_{\mathrm{VV}})(S_{\mathrm{HV}} + S_{\mathrm{VH}})^* & (S_{\mathrm{HH}} - S_{\mathrm{VV}})(\mathrm{j}(S_{\mathrm{HV}} - S_{\mathrm{VH}}))^* \\
(S_{\mathrm{HV}} + S_{\mathrm{VH}})(S_{\mathrm{HH}} + S_{\mathrm{VV}})^* & (S_{\mathrm{HV}} + S_{\mathrm{VH}})(S_{\mathrm{HH}} - S_{\mathrm{VV}})^* & |S_{\mathrm{HV}} + S_{\mathrm{VH}}|^2 & (S_{\mathrm{HV}} + S_{\mathrm{VH}})(\mathrm{j}(S_{\mathrm{HV}} - S_{\mathrm{VH}}))^* \\
\mathrm{j}(S_{\mathrm{HV}} - S_{\mathrm{VH}})(S_{\mathrm{HH}} + S_{\mathrm{VV}})^* & \mathrm{j}(S_{\mathrm{HV}} - S_{\mathrm{VH}})(S_{\mathrm{HH}} - S_{\mathrm{VV}})^* & \mathrm{j}(S_{\mathrm{HV}} - S_{\mathrm{VH}})(S_{\mathrm{HV}} + S_{\mathrm{VH}})^* & |S_{\mathrm{HV}} - S_{\mathrm{VH}}|^2
\end{bmatrix}. \tag{2.16}
$$

For monostatic SAR systems (where the same radar antenna is used for both transmission and reception), the scattering reciprocity principle holds: $S_{\mathrm{HV}} = S_{\mathrm{VH}}$ [99]. Consequently, the 4x4 coherency and covariance matrices simplify into 3x3 matrices, denoted as $\boldsymbol{T}_3$ and $\boldsymbol{C}_3$, respectively [88, 142]:

$$\boldsymbol{T}_3 = \begin{bmatrix} |S_{\mathrm{HH}} + S_{\mathrm{VV}}|^2 & (S_{\mathrm{HH}} + S_{\mathrm{VV}})(S_{\mathrm{HH}} - S_{\mathrm{VV}})^* & 2(S_{\mathrm{HH}} + S_{\mathrm{VV}})S_{\mathrm{HV}}^* \\ (S_{\mathrm{HH}} - S_{\mathrm{VV}})(S_{\mathrm{HH}} + S_{\mathrm{VV}})^* & |S_{\mathrm{HH}} - S_{\mathrm{VV}}|^2 & 2(S_{\mathrm{HH}} - S_{\mathrm{VV}})S_{\mathrm{HV}}^* \\ 2S_{\mathrm{HV}}(S_{\mathrm{HH}} + S_{\mathrm{VV}})^* & 2S_{\mathrm{HV}}(S_{\mathrm{HH}} - S_{\mathrm{VV}})^* & 4|S_{\mathrm{HV}}|^2 \end{bmatrix} , \tag{2.17}$$

$$\boldsymbol{C}_3 = \begin{bmatrix} |S_{\mathrm{HH}}|^2 & \sqrt{2}S_{\mathrm{HH}}S_{\mathrm{HV}}^* & S_{\mathrm{HH}}S_{\mathrm{VV}}^* \\ \sqrt{2}S_{\mathrm{HV}}S_{\mathrm{HH}}^* & |S_{\mathrm{HV}}|^2 & \sqrt{2}S_{\mathrm{HV}}S_{\mathrm{VV}}^* \\ S_{\mathrm{VV}}S_{\mathrm{HH}}^* & \sqrt{2}S_{\mathrm{VV}}S_{\mathrm{HV}}^* & |S_{\mathrm{VV}}|^2 \end{bmatrix} . \tag{2.18}$$

The first SAR polarimetry-based method to estimate the ks parameter is based on the anisotropy parameter (A), which gives information about the secondary scattering mechanisms and is derived from the minor eigenvalues of the 3x3 coherency matrix ($\boldsymbol{T}_3$) as shown below [21, 88]:

$$A = \frac{\lambda_2 - \lambda_3}{\lambda_2 + \lambda_3} , \tag{2.19}$$

where λ_2 and λ_3 represent the second and third eigenvalues of the T_3 matrix.

The ks parameter can then be estimated using the anisotropy parameter with the following equation [64, 74]:

$$ks = 1 - A . \tag{2.20}$$

The second method, based on the coherency matrix, uses the T_{22} and T_{33} elements of the $\boldsymbol{T}_3$ matrix to estimate ks [64, 74]:

$$ks = 1 - \frac{T_{22} - T_{33}}{T_{22} + T_{33}} , \tag{2.21}$$

where $T_{22} = |S_{\mathrm{HH}} - S_{\mathrm{VV}}|^2$ and $T_{33} = 4|S_{\mathrm{HV}}|^2$.

2.2.2 Physical Roughness Estimation Models

Physical roughness estimation models are mathematical approximations that rely primarily on electromagnetic scattering theory to estimate surface roughness values. These models are based on the physical principles that govern the interaction of radar waves with ground surfaces. Physical models attempt to relate SAR observables (such as σ^{o} values) to surface roughness values [52, 139]. Since randomly rough surfaces do not have a direct solution, several approximations are considered in the development of these models, which limits their use within a certain validity range [74]. Some of the commonly used physical models/approximations for estimating surface roughness from SAR data are:

1. **Kirchoff Approximation Method:** This method is also known as the tangent plane approximation and assumes that the reflection from a point on the ground is locally specular, i.e., it is mainly directed towards a single scattering angle. It models the reflection from each ground point by approximating the local terrain profile around that point with a tangent plane. In other words, the complex surface geometry is simplified by assuming that the terrain is locally flat [122]. This approach is particularly effective when the surface undulations are larger than the wavelength of the SAR system and is therefore suitable for SAR systems with smaller wavelengths (e.g. X-band) [64]. The Geometric Optics (GO) and Physical Optics (PO) methods are derived from the Kirchoff approximation. The GO method uses a stationary-phase approximation and is suitable for surfaces with large-scale undulations and steep variations [131]. For surfaces with smaller slopes and moderate undulation heights, a scalar approximation is required, which is included in the PO model [131]. The Kirchhoff approximation method is valid when the surface correlation length (kl), which is a measure of the spatial extent over which the surface height variations are statistically correlated, satisfies the condition $kl > 6$. The GO model has validity conditions $ks > \sqrt{10}/(2\cos\theta)$ and $kl > 6$, and the PO model has validity conditions $ks < 1/(4/\sqrt{2}) \cdot kl$ and $kl = 4/\sqrt{2} \cdot ks$. Here θ is the local incidence angle [74].

2. **Small Perturbation Model (SPM):** In this model, the scattering of the EM waves at the ground surface is considered as a boundary value problem defined by partial differential equations [54]. The central idea is to find a plane wave solution that matches the boundary conditions of the surface and ensures the continuity of the tangential component of the EM field across the boundary [122]. The estimation of the surface roughness is done by expanding the EM field scattered from the surface into a Taylor series in which each term reflects a different order of the perturbation. The initial term (E_{o}) within this Taylor series characterises the field over a perfectly flat surface, while subsequent terms (E_{1}, E_{2}, etc.) detail the effects of small surface irregularities. To model the roughness,

the concept of effective surface currents is introduced, which are characterised by the small-scale roughness on a mean surface. By finding a solution that is consistent with the boundary conditions and takes into account the influence of the effective surface currents and perturbation terms, the surface roughness values can be estimated [131]. SPM assumes that these roughness variations are small relative to the wavelength of the incident EM waves and are therefore suitable for SAR systems operating at longer wavelengths (e.g. L-band) [64]. The SPM has a validity range of $ks < 0.3$ and $kl > \sqrt{(2)}/0.3 \cdot ks$ [74].

3. **Integral Equation Model (IEM):** This model was developed to account for multiple scattering from a ground point and to provide a more accurate representation of the interaction of radar waves. This is achieved by introducing an additional complementary term to the Kirchhoff tangent plane approximation [131]. This extended approach allows the modelling of the expected backscatter coefficient (σ^o) from the ground surface as a function of several key parameters, including the dielectric constant (ϵ'), the surface roughness parameter (ks), the correlation function (e.g. Gaussian or exponential) and the correlation length (kl). It is important to note that the IEM provides a more detailed and comprehensive understanding of surface scattering effects [36]. The Advanced Integral Equation Model (AIEM) is an improved and updated version of the IEM that extends its applicability to a wider range of scenarios and surface types [35]. IEM has the validity conditions of $ks < 1.2\sqrt{\epsilon'}/kl$, $kl < 1.2\sqrt{\epsilon'}/ks$, and $\epsilon' < ks^2 \cdot kl^2/1.44$ [74].

2.2.3 Semi-Empirical Roughness Estimation Models

The semi-empirical roughness estimation models are mathematical models that combine theoretical radar scattering principles with observed properties of the ground surface to estimate roughness values. Unlike purely physical models, which rely solely on electromagnetic scattering theory to estimate roughness, and purely empirical models, which rely solely on observed relationships with no theoretical basis, semi-empirical models strike a balance between the two approaches [72]. They take into account both the underlying physics of radar scattering and the empirical knowledge gained from ground truth data collected at the test sites to improve the accuracy of roughness estimates [74]. The Oh models and the Dubois model are the most widely used semi-empirical roughness estimation models.

The original Oh model [102], developed in 1992, necessitates the calculation of the Fresnel reflectivity (Γ^o) parameter to estimate the ks. The non-linear equation used to estimate Γ^o is:

$$\left(\frac{2\theta}{\pi}\right)^{\frac{1}{\Gamma^{o}}}\left[1-\frac{q}{0.23\sqrt{\Gamma^{o}}}\right]+\sqrt{p}-1=0\ , \tag{2.22}$$

where p is the co-polarisation ratio given by $p=\frac{\sigma^{o}_{HH}}{\sigma^{o}_{VV}}$, q is the cross-polarisation ratio given by $q=\frac{\sigma^{o}_{HV}}{\sigma^{o}_{VV}}$, and θ is the local incidence angle. This equation requires an iterative root-finding algorithm to estimate Γ^{o} values. Once Γ^{o} is obtained, the ks parameter can be calculated using:

$$ks=\ln\left(\frac{\sqrt{p}+1}{\left(\frac{2\theta}{\pi}\right)^{\frac{1}{3\Gamma^{o}}}}\right)\ . \tag{2.23}$$

The updated version of the Oh model [103], published in 2004, estimates the surface moisture (mv) parameter instead of Γ^{o} to determine ks. The mv parameter is derived by finding the solution for the following equation using an iterative root-finding algorithm:

$$\begin{aligned}&1-\left(\frac{\theta}{90}\right)^{0.35mv^{-0.65}}e^{-0.65}\\&\times\left[\left[-3.125\ln\left\{1-\frac{\sigma^{o}_{VH}}{0.11mv^{0.7}\cos^{2.2}\theta}\right\}\right]^{0.556}\right]^{1.4}-p=0\ .\end{aligned} \tag{2.24}$$

Subsequently, ks can be estimated as:

$$ks=\left[-3.125\ln\left\{1-\frac{\sigma^{o}_{VH}}{0.11mv^{0.7}\cos^{2.2}\theta}\right\}\right]^{0.556}\ . \tag{2.25}$$

Similar to the physical roughness estimation models, the semi-empirical models are also developed for use within certain validity ranges. Both versions of the Oh model have a validity range of $0.1<ks<6.0$ and the accuracy of the ks values outside this validity range cannot be guaranteed and should therefore be discarded.

The semi-empirical Dubois model [48], introduced in 1995 for soil roughness and moisture estimation, determines the ks parameter in a two-step non-iterative process. First, it estimates the dielectric constant ($\epsilon^{'}$) using the equation:

$$\epsilon^{'}=\frac{\log_{10}\left(\frac{(\sigma^{o}_{HH})^{0.7857}}{\sigma^{o}_{VV}}\right)10^{-0.19}\cos^{1.82}\theta\sin^{0.93}\theta\lambda^{0.15}}{-0.024\tan\theta}\ . \tag{2.26}$$

Then, ks is estimated in the second step:

$$ks = \sigma^{\circ}_{\mathrm{HH}}{}^{\frac{1}{1.4}} 10^{\frac{2.75}{1.4}} \frac{\sin^{2.57}\theta}{\cos^{1.07}\theta} 10^{-0.02\epsilon' \tan\theta} \lambda^{-0.5} \ , \tag{2.27}$$

where λ is the wavelength of the SAR system.

The Dubois model has validity conditions of $ks < 2.5$ and $\theta > 30^{\circ}$, and ks values not meeting both conditions should be discarded.

2.3 Chapter Summary

This chapter provided a thorough exploration of SAR technology, highlighting its ability to generate high-resolution images regardless of weather conditions. It discussed SAR data acquisition geometry, including concepts like synthetic aperture formation, imaging modes and spatial resolution calculations in stripmap mode. Furthermore, it delves into SAR image generation processes such as range compression, range cell migration correction and azimuth compression, essential for converting raw data into usable SAR images.

Distortions in SAR images, such as foreshortening and speckle, are discussed and their effects on image interpretation are highlighted. The importance of the signal-to-noise ratio (SNR) and the SAR backscatter coefficient (σ°) for the evaluation of image quality and for applications such as road condition monitoring are also explained.

The chapter then explored various models for estimating the surface roughness from SAR data, categorised into SAR polarimetry-based, physical, and semi-empirical models. Each model category is thoroughly examined, detailing its principles, validity conditions, and limitations.

Overall, this chapter provides an essential foundation for understanding SAR technology and its associated applications. It equips the reader with the knowledge necessary to go into depth in subsequent chapters, which will focus on the practical applications of these state-of-the-art roughness estimation models and also on the development of new models/methods for road surface roughness estimation and also for road condition assessment.

3 Novel Semi-Empirical Road Surface Roughness Estimation Model for Airborne SAR

This chapter introduces a novel semi-empirical model specifically developed for road surface roughness estimation with airborne SAR. A comparative analysis is also performed between the experimental results derived from this model and the results of the state-of-the-art roughness estimation models described in section 2.2. The experimental road surface roughness results were generated for the Kaufbeuren, duraBASt and Braunschweig test sites using high-resolution airborne X-Band SAR data from the German Aerospace Center's (DLR) F-SAR system. Further information on the test sites and the F-SAR data acquisition is available in Appendix A. Contents of this chapter were already published in [P1, P2, P3, P4, P5].

3.1 Development of a New Semi-Empirical Model

To assess the reliability of polarisation channels for road surface roughness estimation, particularly for very smooth road surfaces with low backscattering, an investigation was conducted on the co-polarisation (HH & VV) and cross-polarisation (HV & VH) channels. In this context, a comparison was made between the sigma nought (σ^o) backscattering coefficient (see section 2.1.5 on page 21) and the noise equivalent sigma zero (NESZ) parameter. The NESZ represents the noise floor of a SAR system and any σ^o values below the NESZ for that particular SAR system can be considered as noise and unreliable for subsequent investigations [P4, 51].

Figure 3.1 illustrates σ^o versus NESZ plots for the Kaufbeuren runway, covering the entire runway length. These plots display σ^o values for different polarisations alongside the NESZ plot, utilising two F-SAR datasets (PS04 and PS12) with parallel flight tracks to the runway. The PS04 dataset, acquired at an altitude of approximately 2.2 km with a 39° incidence angle (cf. Table A.3 on page 175), and the PS12 dataset, acquired from an altitude of about 3 km with a 40° incidence angle (cf. Table A.2 on page 174), reveal an increase in σ^o values at the runway ends due to rougher concrete and lower σ^o values in the smoother asphalt middle region (refer to Figure 3.1 for the Google Earth image of the Kaufbeuren runway highlighting these regions). Co-polarisation σ^o values are consistently above the NESZ of the F-SAR system, indicating their reliability for road surface roughness estimation. However, cross-polarisation σ^o values fall below the NESZ for asphalt areas, indicating noise dominance. Since SAR polarimetry-based models and semi-empirical Oh models require cross-polarisation channels (see section 2.2 on page 21), they are therefore unsuitable for reliable road surface roughness estimation,

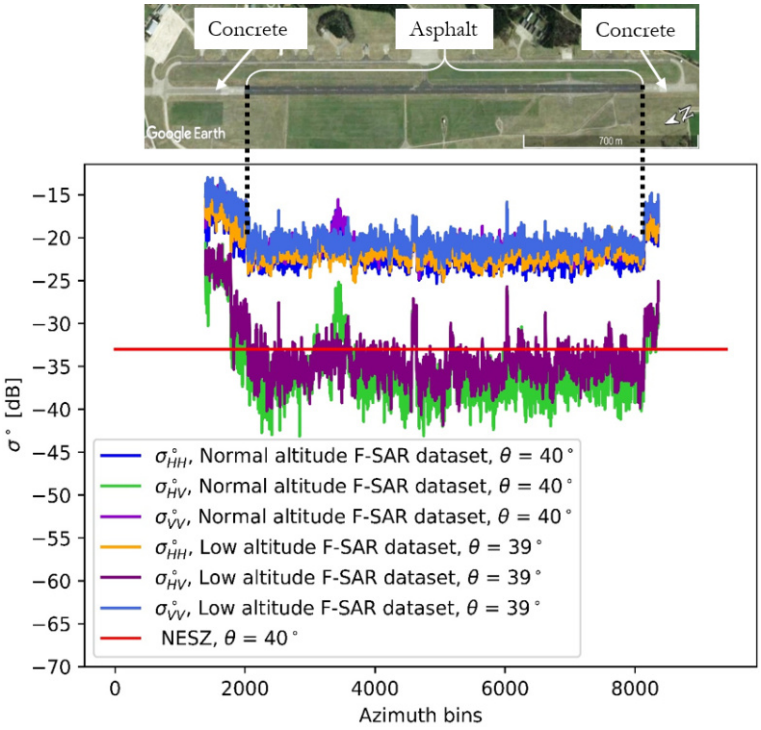

Figure 3.1: σ^{o} vs NESZ plots for the Kaufbeuren runway. The Google Earth image shown at the top highlights the asphalt and concrete regions of the runway.

at least for the radar data investigated in this thesis. In addition, the physical models described in section 2.2 are also not suitable for estimating road surface roughness, as the scattering mechanisms considered in the development of these models apply to rough soil surfaces and are not suitable for road surfaces.

The Dubois model is the only state-of-the-art roughness estimation model requiring only co-polarisation channels. However, early investigations revealed an incidence angle dependency in the Dubois model, resulting in a gradient change in surface roughness values from near to far range [P4]. Consequently, a new semi-empirical road surface roughness estimation model was developed based on Dubois model assumptions, aiming to minimise incidence angle dependency and enhance overall accuracy.

The scattering assumptions from the Dubois model assert that the backscattered signal (σ^{o}_{pq}) for a p transmitted and q received polarisation can be modelled as a function of surface roughness (ks), surface moisture, and local incidence angle (θ) [137]. If it can be ensured that the road surface is dry, then the surface moisture component in the backscattered signal can be neglected. The new semi-empirical model is formulated as a function of the surface roughness (ks) and the local incidence angle (θ) as follows [P4]:

$$\sigma^{o}_{\mathrm{pq}} = \delta(\cos(\theta))^{\beta}(ks)^{\epsilon \sin(\theta)} \,. \tag{3.1}$$

In (3.1), the term $\delta(\cos(\theta))^{\beta}$ denotes the relationship between σ^{o}_{pq} and the local incidence angle (θ). From this relationship, it can be understood that the σ^{o}_{pq} decreases as the incidence angle (θ) increases and this decrease in σ^{o}_{pq} is higher at low incidence angles and lower at high incidence angles [19, 20, 27].

The second term $(ks)^{\varepsilon \sin(\theta)}$ indicates the relationship between σ^{o}_{pq} and the effective surface roughness (ks). σ^{o}_{pq} and ks have a power law relationship and the sensitivity of σ^{o}_{pq} to ks is higher at high incidence angles than at low incidence angles [20, 22, 117]. The sin (θ) term is added to the relationship to minimise this incidence angle dependency.

The equation in (3.1) can be inverted to estimate ks as a function of σ^{o}_{pq} and incidence angle (θ) as follows:

$$ks = 10^{\left\lceil \frac{\log(\sigma^{o}_{\mathrm{pq}}) - \log(\delta(\cos(\theta))^{\beta})}{\epsilon \sin(\theta)} \right\rceil} \,, \tag{3.2}$$

where δ, β, and ϵ are the unknown coefficients that need to be estimated to solve the equation. The coefficients can be estimated using the ground truth (GT) surface roughness (GT h_{rms}) values, σ^{o}_{pq} values and the known incidence angle values (θ) at the GT spots using the method of least square-based curve fitting. Details about the GT data collection process and the GT h_{rms} can be found in Appendix A on page 178.

Three F-SAR datasets (PS04, PS05, and PS12) acquired over the Kaufbeuren test site (cf. Table A.2 on page 174) were used to estimate the δ, β, and ϵ coefficients. These datasets were acquired from distinct sides of the runway (cf. Figure 3.2). Table A.2 provides information on the flight heading direction, aspect angle, and incidence angle values at the runway. The aspect angle represents the SAR look direction towards the runway relative to the north direction. Notably, these three datasets exhibit diverse aspect and incidence angles for the runway, facilitating an unbiased model coefficients estimation.

Figure 3.3(a) depicts the GT h_{rms} plot for GT spots 1-8. Figures 3.3(b-d) present the σ^{o}_{HH} and σ^{o}_{VV} plots for the PS04, PS05, and PS12 datasets, respectively, corresponding to GT spots 1-8. The similarity in trends between Figure 3.3(a) and Figures 3.3(b-d) suggests a correlation between changes in h_{rms} and magnitude changes in σ^{o}_{HH} and σ^{o}_{VV}. This correlation was leveraged in estimating the coefficients for the new model using a least square-based curve fitting algorithm, employing the GT h_{rms}, σ^{o}_{HH}, σ^{o}_{VV}, and incidence angle (θ) values for GT spots 1-8 from these datasets as inputs [P4].

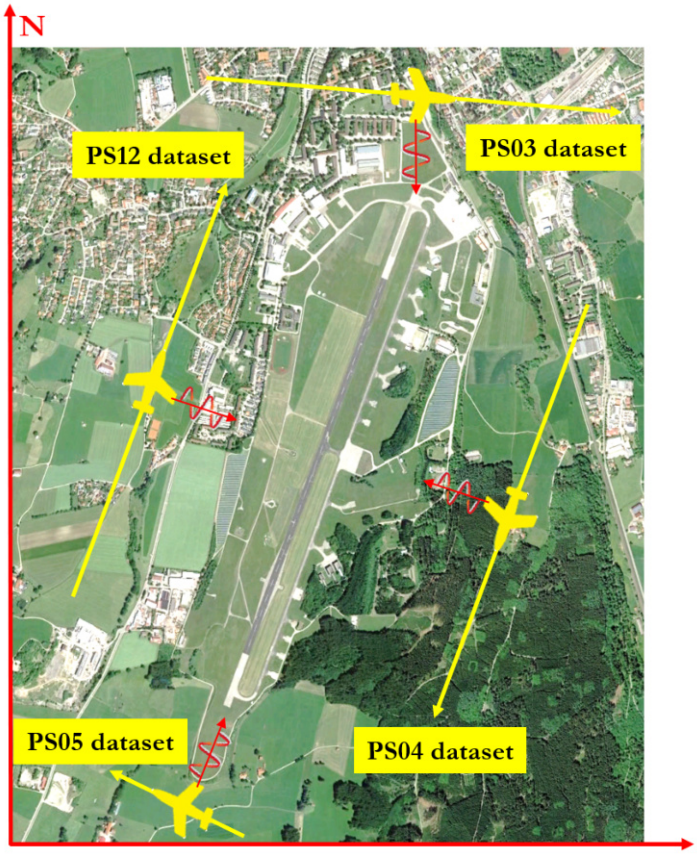

Figure 3.2: Flight tracks for acquiring the F-SAR datasets used for estimating and testing the new model coefficients.

Table 3.1: Coefficients estimated for the new semi-empirical model.

Model Coefficients	Polarisation	
	HH	VV
δ	0.06782502	0.06792563
β	-0.9301637	-2.46489793
ε	2.23988886	2.27478606

The model coefficients were estimated for the HH and VV polarisations separately and the values are shown in Table 3.1. Using this model coefficient values, (3.2) can be written as:

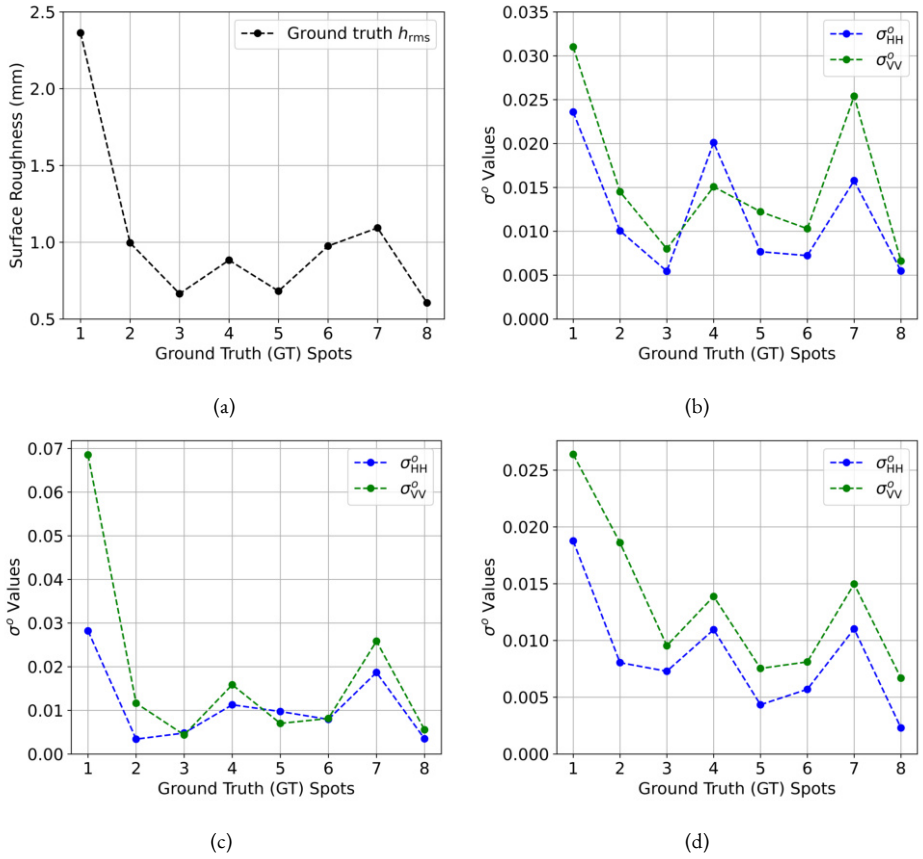

Figure 3.3: Correlation between ground truth (GT) h_{rms} and σ^o values. (a) GT h_{rms} plot. σ^o_{HH} and σ^o_{VV} plots for (b) PS04 dataset, (c) PS05 dataset, (d) PS12 dataset.

$$ks_{\text{HH}} = 10^{\left[\frac{\log(\sigma^o_{pq}) - \log(0.06782502(\cos\theta)^{-0.9301637})}{2.23988886\sin\theta}\right]}, \tag{3.3}$$

$$ks_{\text{VV}} = 10^{\left[\frac{\log(\sigma^o_{pq}) - \log(0.06792563(\cos\theta)^{-2.46489793})}{2.27478606\sin\theta}\right]}, \tag{3.4}$$

where ks_{HH} is the ks value estimated for the HH polarisation and ks_{VV} is the ks value estimated for the VV polarisation. The final ks value can be calculated by taking the mean of the ks_{HH} and ks_{VV} values.

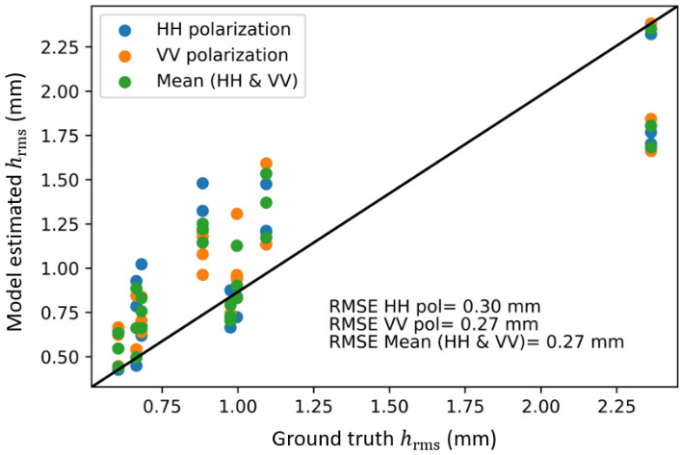

Figure 3.4: Ground truth (GT) h_{rms} vs. model estimated surface roughness.

Figure 3.4 shows the GT h_{rms} vs. model-estimated surface roughness plots generated using the ks_{HH} values, ks_{VV} values and the mean ks values after estimating the model coefficients using the least square-based curve fitting method. By analysing Figure 3.4, it can be understood that the deviation between the GT h_{rms} and the model-estimated surface roughness is not so high, the Root Mean Square Error (RMSE) obtained for the HH polarisation is 0.30 mm, for the VV polarisation the RMSE is 0.27 mm and for the HH-VV average, the RMSE obtained is also 0.27 mm. This low RMSE indicates that the model coefficients given in Table 3.1 are reliable and can be used in the new model to accurately estimate the road surface roughness. From Figure 3.4, it can also be observed that the RMSE obtained for the VV polarisation is slightly better compared to the RMSE obtained for the HH polarisation. Also, the RMSE obtained from the HH-VV average is the same as the RMSE obtained for the VV polarisation alone (0.27 mm). So, averaging the ks values obtained from the HH and VV polarisations does not provide a better RMSE than using the VV polarisation alone. For a more robust performance analysis of the new model, surface roughness estimates were generated using several X-band airborne F-SAR datasets acquired from multiple test sites with different data acquisition geometries, which are discussed later in this chapter.

Figure 3.5(a) and Figure 3.5(b) show the model dynamics of the new model for HH and VV polarisation, respectively. The change in surface roughness (h_{rms}) values with respect to different incidence angles (θ) and sigma nought (σ^o) combinations can be observed in the plots. In both Figure 3.5(a) and Figure 3.3(b), each surface roughness line represents the change in surface roughness with respect to the incidence angle variations when the sigma nought remains constant. From both the plots, it can be observed the changes in surface roughness are small with respect to the incidence angle when the σ^o magnitudes are small (for, e.g., -27 dB and -32 dB). The change in surface roughness is higher as

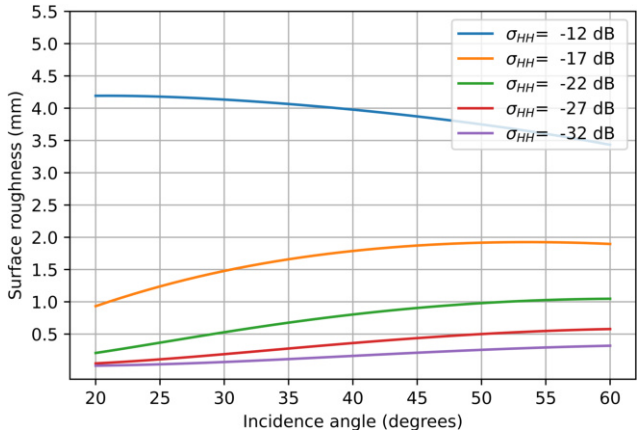

(a)

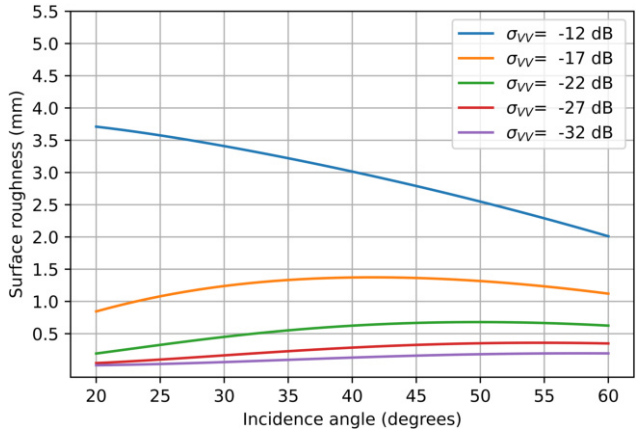

(b)

Figure 3.5: Model dynamics of the new model. (a) HH polarisation. (b) VV polarisation.

the incidence angle changes when the σ^o magnitude is larger (e.g., -12 dB). Given that road surfaces typically have low σ^o values, this suggests that the surface roughness values estimated using the new model for road surfaces are less affected by changes in incidence angle, leading to more consistent estimates even under different geometric conditions.

3.2 Algorithm and Processing Chain

The estimation of road surface roughness using fully polarimetric (PolSAR) airborne X-band F-SAR datasets using the previously discussed state-of-the-art roughness estimation models (refer to section 2.2 on page 21) and the newly developed semi-empirical model (refer to section 3.1 on page 31) involves several key steps. The PolSAR datasets are

pre-processed before feeding them to the surface roughness estimation models. Also, post-processing steps are applied to the model-estimated surface roughness (h_{rms}) values before generating the final surface roughness image. The flowchart illustrating the processing chain for road surface roughness estimation is shown in Figure 3.6.

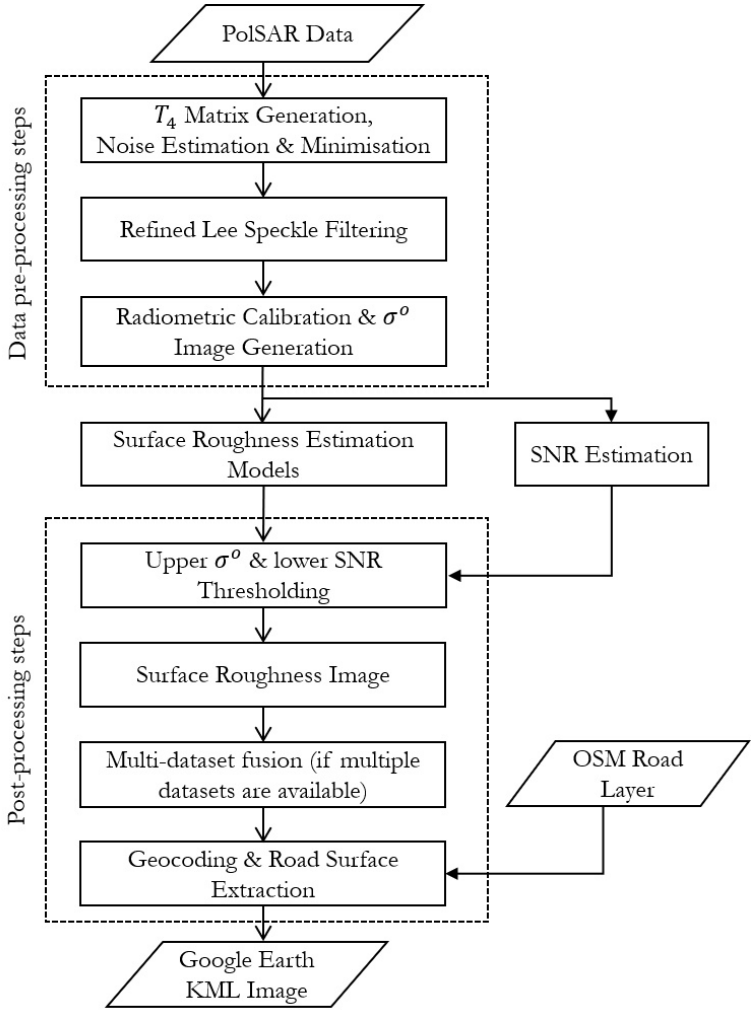

Figure 3.6: Flowchart of the processing chain for road surface roughness estimation using airborne F-SAR data.

3.2.1 Data Pre-processing Steps

The data pre-processing steps are aimed at preparing the fully polarimetric SAR (PolSAR) datasets for using them effectively as input to the roughness estimation models for

accurate and reliable road surface roughness (h_{rms}) assessment. These procedures include estimating and minimising additive and multiplicative noise and applying radiometric calibration to generate sigma nought (σ^o) backscatter images.

Since the SAR backscatter received from the road surfaces is very low, the additive and multiplicative noise present in the airborne PolSAR data needs to be minimised for low SNR applications such as road surface roughness estimation [50]. The additive noise N present in the PolSAR data is caused by the thermal/system noise of the SAR system and it affects each of the polarisation channels [63]. Therefore the measured scattering matrix $\boldsymbol{S}^{'}$ by the SAR system can be written as a sum of the ideal scattering matrix $\boldsymbol{S}$ and additive noise matrix $\boldsymbol{N}$ as follows [63]:

$$\boldsymbol{S}^{'} = \boldsymbol{S} + \boldsymbol{N}\,, \tag{3.5}$$

where $\boldsymbol{N} = \begin{bmatrix} n_{\text{HH}} & n_{\text{HV}} \\ n_{\text{VH}} & n_{\text{VV}} \end{bmatrix}$.

The additive noise present in the data can be considered as a zero-mean Gaussian white noise process and the additive noise power N can be modelled as [63]:

$$\left\langle n_{ij} n_{ij}^{*} \right\rangle = \left\langle n_{mn} n_{mn}^{*} \right\rangle = N \text{ and } \left\langle n_{ij} n_{mn}^{*} \right\rangle = 0\,, \tag{3.6}$$

where * is the complex conjugate operator.

The additive noise affected Pauli basis vector $\boldsymbol{k}_{\text{3p noisy}}$ corresponding to the measured scattering matrix $\boldsymbol{S}^{'}$ can be written as [63]:

$$\boldsymbol{k}_{\text{3p noisy}} = \frac{1}{\sqrt{2}} \begin{bmatrix} S_{\text{HH}} + S_{\text{VV}} + (n_{\text{HH}} + n_{\text{VV}}) \\ S_{\text{HH}} - S_{\text{VV}} + (n_{\text{HH}} - n_{\text{VV}}) \\ S_{\text{HV}} + S_{\text{VH}} + (n_{\text{HV}} - n_{\text{VH}}) \end{bmatrix}\,. \tag{3.7}$$

The additive noise affected 3x3 coherency matrix $\boldsymbol{T}_{\text{3 noisy}}$ corresponding to the measured scattering matrix $\boldsymbol{S}^{'}$ can be estimated by the spatially averaged multiplication of the Pauli basis vector $\boldsymbol{k}_{\text{3p noisy}}$ with the transpose of its complex conjugate as follows [63]:

$$\boldsymbol{T}_{\text{3 noisy}} = \frac{1}{2} \begin{bmatrix} T_{11} + 2N & T_{12} & T_{13} \\ T_{21} & T_{22} + 2N & T_{23} \\ T_{31} & T_{32} & T_{33} + 2N \end{bmatrix}\,. \tag{3.8}$$

For a monostatic SAR system, the cross-polarised channels are completely correlated in the absence of additive noise, i.e., $S_{\mathrm{HV}} = S_{\mathrm{VH}}$ [63]. This is because a monostatic SAR follows the scattering reciprocity condition. Since the two cross-polarised channels are measured independently by the SAR system the additive noise level present in the two cross-polarised channels will be different. So, as the additive noise level increases the correlation between the cross-polarised channels decreases. This decorrelation between the cross-polarisation channels can be utilised to estimate the additive noise power N. Since the scattering reciprocity condition is not valid for noisy data, the 4-dimensional Pauli basis vector $\boldsymbol{k}_{\mathrm{4p\ noisy}}$ is required and it can be written as shown in (3.9) [63].

$$\boldsymbol{k}_{\mathrm{4p\ noisy}} = \frac{1}{\sqrt{2}} \begin{bmatrix} S_{\mathrm{HH}} + S_{\mathrm{VV}} + (n_{\mathrm{HH}} + n_{\mathrm{VV}}) \\ S_{\mathrm{HH}} - S_{\mathrm{VV}} + (n_{\mathrm{HH}} - n_{\mathrm{VV}}) \\ S_{\mathrm{HV}} + S_{\mathrm{VH}} + (n_{\mathrm{HV}} - n_{\mathrm{VH}}) \\ \mathrm{j}(S_{\mathrm{HV}} - S_{\mathrm{VH}}) + (n_{\mathrm{HV}} - n_{\mathrm{VH}}) \end{bmatrix} . \tag{3.9}$$

This $\boldsymbol{k}_{\mathrm{4p\ noisy}}$ vector can be used to estimate the noise-affected 4x4 coherency matrix $\boldsymbol{T}_{\mathrm{4\ noisy}}$ as [63]:

$$\boldsymbol{T}_{\mathrm{4\ noisy}} = \left\langle \boldsymbol{k}_{\mathrm{4p\ noisy}} \cdot \boldsymbol{k}^{*}_{\mathrm{4p\ noisy}} \right\rangle . \tag{3.10}$$

The diagonalisation of the $\boldsymbol{T}_{\mathrm{4\ noisy}}$ matrix leads to the following form [63]:

$$\boldsymbol{D}_4 = \begin{bmatrix} \lambda_1 + N & 0 & 0 & 0 \\ 0 & \lambda_2 + N & 0 & 0 \\ 0 & 0 & \lambda_3 + N & 0 \\ 0 & 0 & 0 & N \end{bmatrix} , \tag{3.11}$$

where λ_1, λ_2, λ_3 are the first three eigenvalues of the additive noise-free 4x4 coherency matrix and N is the additive noise present in the data.

In the absence of additive noise, the 4x4 coherency matrix has a rank of 3, and only the first three eigenvalues λ_1, λ_2, λ_3 have non-zero values. But, the presence of noise makes the 4x4 coherency matrix be of rank 4 and the 4^{th} eigenvalue λ_4 represents the additive noise present in the data ($\lambda_4 = N$). So, the additive noise can be filtered out by subtracting the additive noise power N from the first three eigenvalues of the coherency matrix or by subtracting N from the diagonal elements of the $\boldsymbol{T}_{\mathrm{3\ noisy}}$ as follows [63]:

$$\boldsymbol{T}_3 = \boldsymbol{T}_{3\,\text{noisy}} - N \begin{bmatrix} 1 & 0 & 0 \\ 0 & 1 & 0 \\ 0 & 0 & 1 \end{bmatrix} , \tag{3.12}$$

where $\boldsymbol{T}_3$ is the additive-noise filtered 3x3 coherency matrix.

The next data pre-processing step is the estimation and minimisation of multiplicative noise present in the PolSAR data. Speckle is the dominant multiplicative noise present in the SAR data [14]. It appears as a granular disturbance and occurs due to the coherent imaging of the SAR systems. For this study, the speckle present in the PolSAR data was minimised by speckle filtering using a refined-Lee speckle filter with a 3x3 window [145].

After minimising the additive and multiplicative noise present in the data, the noise-minimised scattering matrix elements can be estimated from $\boldsymbol{T}_3$ as given below [P4].

$$|S_{\text{HH}}|^2 = \frac{T_{11} + 2Re\{T_{12}\} + T_{22}}{2} \tag{3.13}$$

$$|S_{\text{HV}}|^2 = \frac{T_{33}}{2} \tag{3.14}$$

$$|S_{\text{VV}}|^2 = \frac{T_{11} - 2Re\{T_{12}\} + T_{22}}{2} \tag{3.15}$$

The final step in the data pre-processing procedure involves performing radiometric calibration to generate calibrated backscatter images (σ^o). This calibration is carried out as follows [75]:

$$\sigma^o_{\text{HH}} = \sin\theta \cdot |S_{\text{HH}}|^2 , \tag{3.16}$$

$$\sigma^o_{\text{HV}} = \sin\theta \cdot |S_{\text{HV}}|^2 , \tag{3.17}$$

$$\sigma^o_{\text{VV}} = \sin\theta \cdot |S_{\text{VV}}|^2 , \tag{3.18}$$

where θ is the local incidence angle.

These noise-minimised, radiometrically calibrated σ^o images enable the comparison of backscatter measurements between surfaces and facilitate the estimation of surface properties such as roughness [P6]. Consequently, these images, along with the local incidence angle image (θ), serve as input for road surface roughness estimation models.

3.2.2 Post-processing of the Road Surface Roughness Results

After estimating the road surface roughness values using different roughness estimation models, several post-processing steps are required to increase the reliability of the h_{rms} estimation and to facilitate better visualisation and interpretation of the final road surface roughness image. These post-processing steps include σ^o and SNR masking, multi-dataset fusion, as well as geocoding and visualisation on Google Earth (GE).

1. **σ^o and SNR masking:** High sigma nought (σ^o) values not originating from the road surface can cause errors in the road surface roughness estimation. Figure 3.7(a) shows the σ^o_{VV} image for the Cologne motorway intersection. By analysing the image, it can be observed that the strong reflection from the lane dividers present in between the roads and also the strong reflection from the flyover walls are visible in yellow colour. These strong reflections cause invalid high surface roughness values which need to be eliminated. For this purpose, an upper σ^o threshold masking technique was implemented.

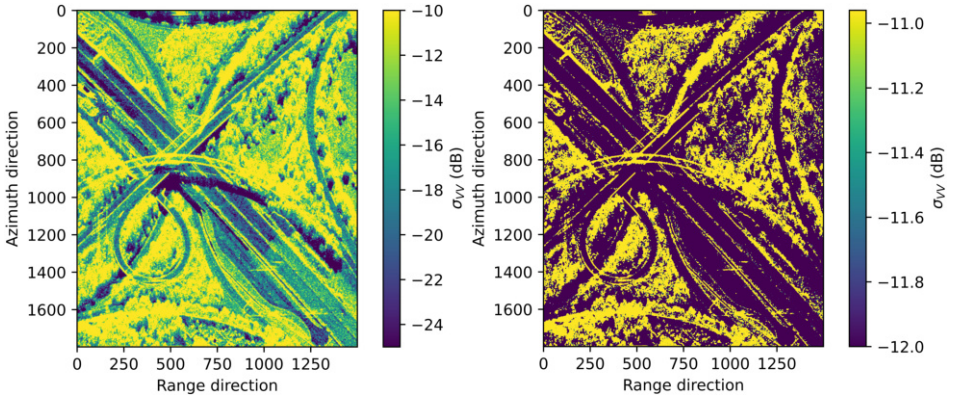

Figure 3.7: σ^o_{VV} images. (a) σ^o_{VV} image for Cologne motorway intersection. (b) σ^o_{VV} image showing primarily reflections from lane divider and flyover walls.

Figure 3.7(b) shows the σ^o_{VV} image with sigma nought values higher than -10.96 dB. This threshold value was determined empirically using a trial-and-error procedure. From Figure 3.7(b), it can be understood that all the pixels on the road surface with σ^o_{VV} higher than -10.96 dB correspond to strong reflections from

lane dividers and flyover walls. So, all the pixels with σ^o_{VV} greater than -10.96 dB were masked out from the final surface roughness image.

Similar to the high sigma nought values not corresponding to the road surface, the very low signal-to-noise ratio (SNR) pixels can also result in unreliable surface roughness estimation. The sigma nought values obtained from the low SNR pixels are more dominated by the noise than the actual radar signal. The surface roughness values obtained from these pixels are unreliable and do not correspond to the actual ground truth surface roughness. Therefore, the surface roughness values obtained from the low SNR pixels should be discarded. The SNR of the dataset can be estimated as follows [51]:

$$SNR_{\mathrm{pq}} = \frac{\sigma^o_{\mathrm{pq}} - \lambda_4}{\lambda_4} \ , \tag{3.19}$$

where SNR_{pq} is the SNR estimated for the p transmitted and q received polarisation, σ^o_{pq} is the sigma nought value for the pq polarisation and λ_4 is the 4^{th} eigenvalue of the 4x4 coherency matrix which is used for the additive noise removal.

An SNR vs. surface roughness analysis was carried out to estimate the changes in the model-estimated surface roughness as the SNR decreases. For this purpose, a region with high SNR was selected on the runway surface at the Kaufbeuren test site. The actual SNR and the surface roughness values for that region were computed using different surface roughness models from the PS04 dataset (cf. Table A.2 on page 174). After that, simulated complex random Gaussian noise was added to the four polarisation channels independently and the SNR was varied from the actual value to lower values and the corresponding changes in the surface roughness were plotted.

In Figure 3.8(a), the red plot illustrates the relationship between SNR and surface roughness for the anisotropy-based roughness estimation method. Notably, for SNR above 8.45 dB, the estimated surface roughness exhibits minimal variations, while below this threshold, the roughness increases. The green plot in the same figure presents the SNR vs. surface roughness plot for the coherency matrix-based method, indicating nearly constant roughness (around 2.78 mm) for SNR above 9.45 dB. Figure 3.8(b) displays the SNR vs. surface roughness plot for the Dubois model, with stable roughness (around 0.3 mm) for SNR over 7.7 dB and then increasing as SNR falls below this value. In Figure 3.8(c), a similar analysis for the new semi-empirical model reveals constant roughness (1.45 mm) for SNR equal to or greater than 8.43 dB, with minimal surface roughness deviations for SNR higher than 5.98 dB. These slight variations in surface roughness values while decreasing the SNR up to 5.98 dB are typically insignificant and can be neglected

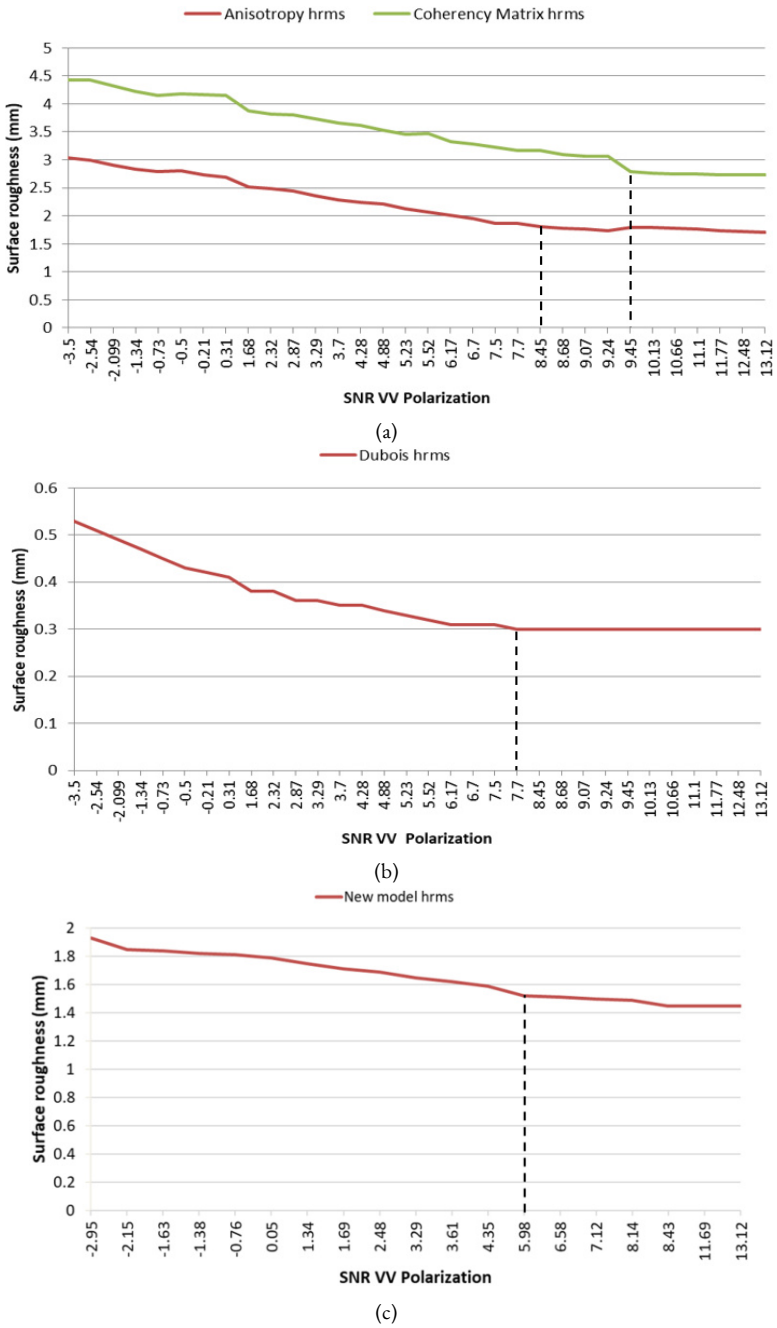

Figure 3.8: Surface roughness vs. SNR plots. For (a) anisotropy and coherency matrix methods, (b) the Dubois model and (c) the new semi-empirical model.

in most of the cases. It is important to note that the plots in Figure 3.8 have different scales on the y-axis due to the large variations in surface roughness values estimated by the different models. Using different scales appropriate for each model allows for better identification of small variations in surface roughness values as the SNR decreases. From this analysis, it can be generalised that the lowest SNR that ensures constant roughness is the minimum SNR required for reliable and unbiased surface roughness estimation. Therefore, surface roughness values where the SNR falls below these model-specific SNR thresholds are considered invalid and can be neglected to minimise measurement errors.

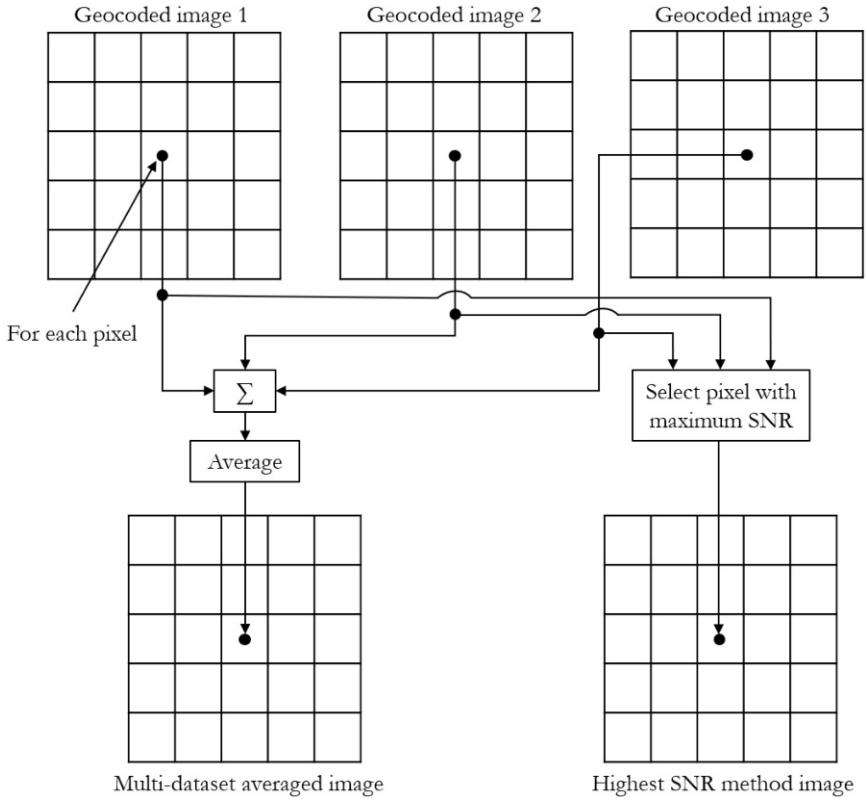

Figure 3.9: "Multi-Dataset Averaging Method" (left) and "Highest SNR Method" (right).

2. **Multi-dataset fusion:** When multiple datasets with different incidence angles and viewing directions contribute surface roughness images, fusing them into a single surface roughness image enhances the overall accuracy of h_{rms} estimates. This fusion process effectively mitigates errors in h_{rms} estimation arising from challenges like low SNR, speckle, and shallow incidence angles. Two novel multi-dataset fusion approaches were employed in this study: the "Highest SNR Method" and the "Multi-Dataset Averaging Method".

The "Highest SNR Method" assumes that the most accurate h_{rms} estimate is derived from the dataset with the highest SNR. Consequently, a pixel-wise SNR search is conducted across all pixels in the available datasets, and for each pixel, the h_{rms} value is extracted from the dataset with the highest SNR for that specific pixel (cf. Figure 3.9 right).

On the other hand, the "Multi-Dataset Averaging Method" assumes that all h_{rms} values from the various available datasets are accurate and valid. This is ensured by applying upper σ^o and lower SNR thresholds in advance to eliminate invalid h_{rms} estimates in all individual surface roughness images. As a result, the fused surface roughness image is generated by pixel-wise averaging of the h_{rms} values from all available surface roughness images (cf. Figure 3.9 left).

3. **Geocoding, road extraction and Google Earth visualisation:** The analysis of the road surface conditions can be better evaluated by visualising the surface roughness estimates, for instance in Google Earth (GE). This can help to compare the surface roughness values with the recent high-resolution optical views of the same regions (if available). To visualise the surface roughness in GE, the generated surface roughness images were geocoded from the slant-range coordinate system to a geographic coordinate system with a grid spacing of 0.25m.

   For extracting the roads from the geocoded road surface roughness image, the Open Street Map (OSM) road layers are used [98]. The road layers within the boundaries of the geocoded road surface roughness image were extracted using the OSMnx Python package [28]. However, the road layers from the OSM only contain the road centrelines without information about the road width, as shown by the black lines in Figure 3.10. Knowledge of the road width is required for the extraction of roads from the geocoded road surface roughness image. For this purpose, a "buffer" operation [61] was performed on these road centrelines to create polygons around these centrelines with a specific width, as shown by the red polygons in Figure 3.10. Depending on the type of road, the width of these polygons was set to match the expected road boundaries, which were measured using Google Earth. For example, for the roads considered in the Braunschweig test site (see section A.1.3 on page 170), the width of these polygons was set to 12 m for motorways and 6 m for motorway link roads. For the runway at the Kaufbeuren test site (see section A.1.1 on page 169), the polygon width was set to 30 metres. If these preset road widths are not suitable for the roads of interest, a manual road width input can be entered into the processing chain to adjust the width of these polygons to that of the road boundaries. The processing chain also has the functionality to extract the road layers and create the road width polygons only for the roads of interest. For example, by specifying the OSM

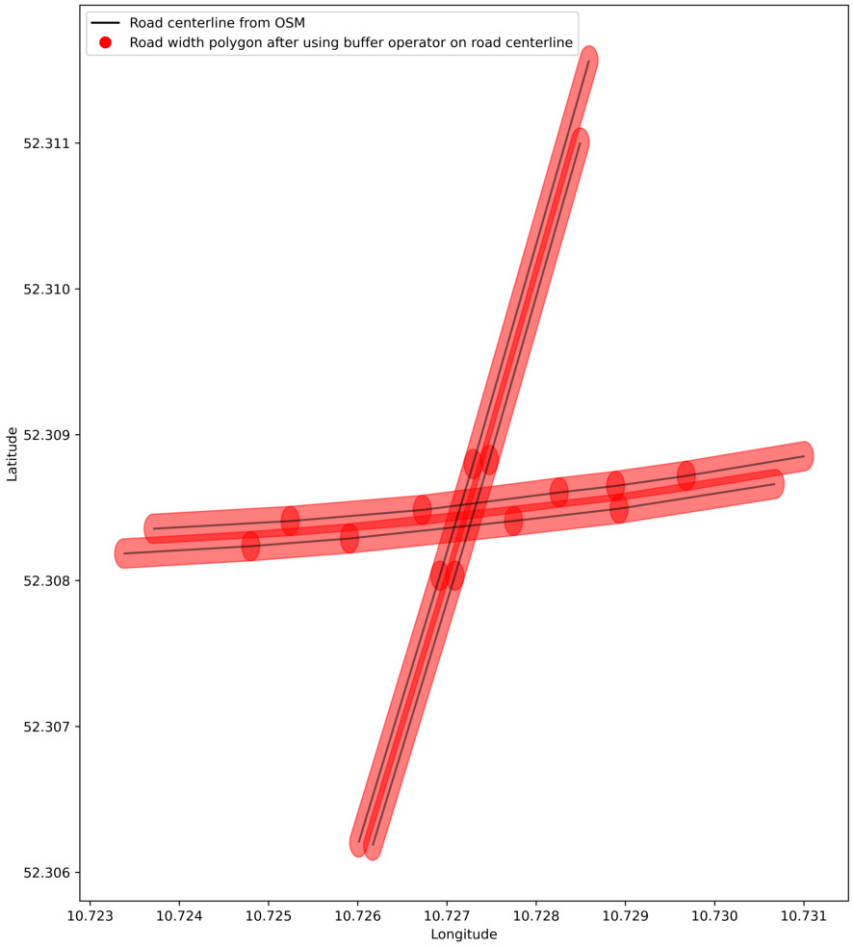

Figure 3.10: OSM road layer (black) and buffered road width polygon (red) visualisation. The buffered road width polygon represents the most likely road width for the known road type.

filter key ”Motorway A4”, the road width polygons are only generated for the motorway A4 within the extent of the geocoded road surface roughness image.

In the next step, all surface roughness values in the geocoded road surface roughness image outside of these road width polygons are masked out from the final surface roughness image, so that only the surface roughness values of the roads of interest are retained. KML files are then created overlaying only the road surface roughness results in GE. This approach is intended to make it easier for road maintainers without SAR expertise to interpret the results and enable them to carry out maintenance measures efficiently. In addition to the KML file, a Geographic tagged image file format (GeoTIFF) file is also created that contains the

extracted road surface roughness images to ensure compatibility with state-of-the-art geographic information system (GIS) software. An example is shown in Figure 3.22 on page 63.

3.3 Experimental Results and Discussion

3.3.1 Comparison of Different Roughness Estimation Models

This sub-section presents road surface roughness (h_{rms}) results for the duraBASt and Kaufbeuren test sites obtained from the anisotropy method, coherency matrix method, Dubois model, Oh model, and the new semi-empirical model.

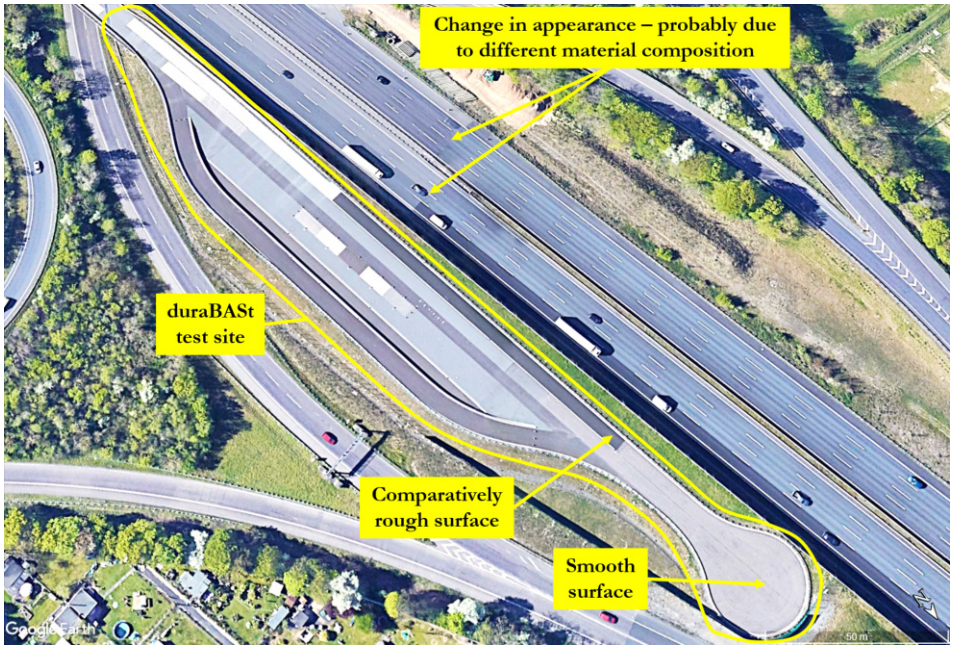

Figure 3.11: Google Earth image of duraBASt test site (yellow polygon) and nearby motorway showing smooth and rough road surfaces.

Figure 3.11 displays the Google Earth (GE) image of the duraBASt test site, which is outlined with the yellow border near the Cologne motorway intersection and shows distinct road materials with varying surface roughness. The smooth and rough regions identified at the duraBASt test site are shown in Figure 3.11. Also, a change in road surface colour can be observed on the motorway near the duraBASt test site in the GE image. This may be due to maintenance work done in that region. Further details about this test site can be found in Appendix A on page 170.

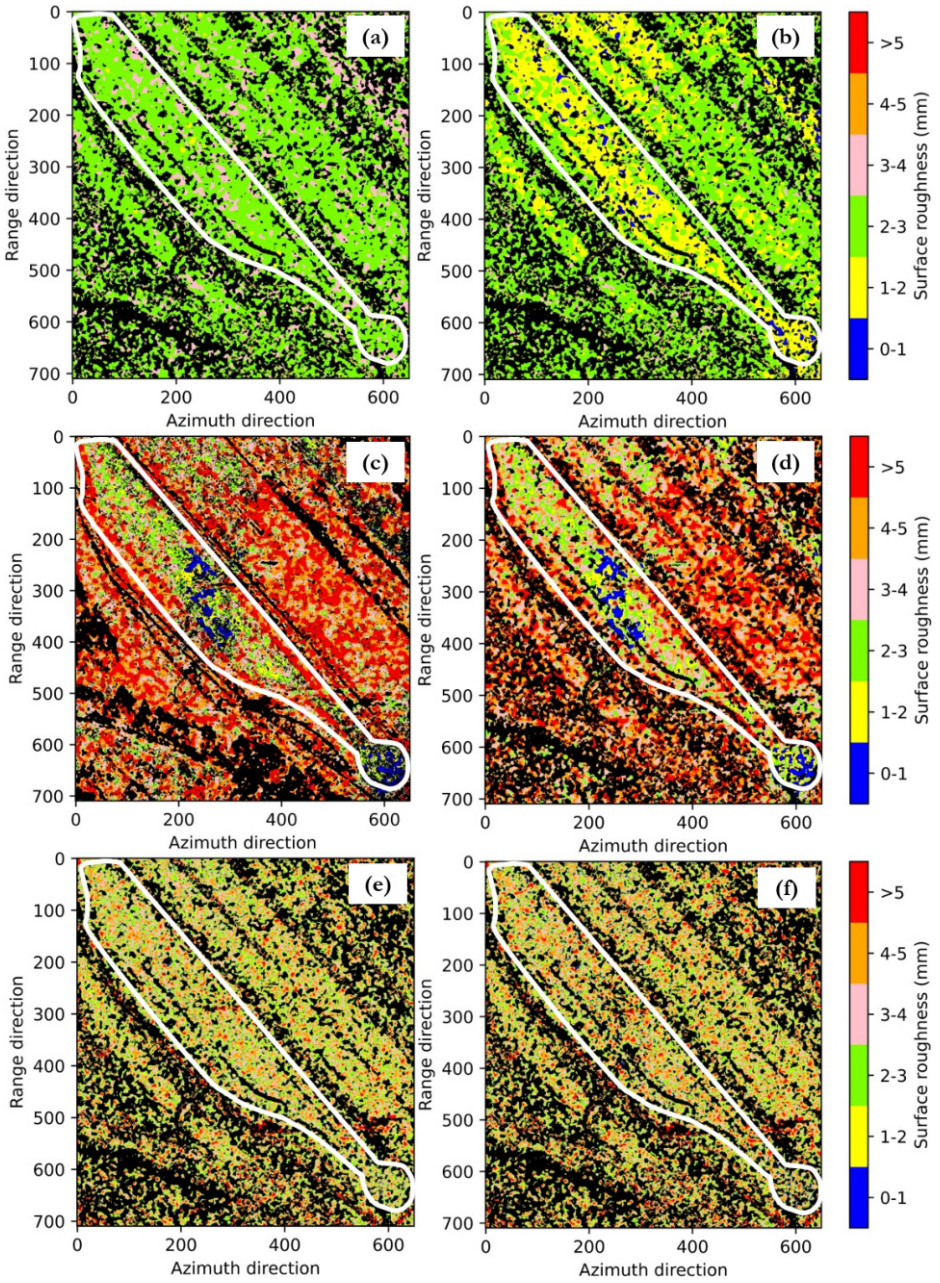

Figure 3.12: h_{rms} images. (a) h_{rms} image generated using the anisotropy method before additive noise removal. (b) h_{rms} image generated using the anisotropy method after additive noise removal. (c) h_{rms} image generated using the coherency matrix method before additive noise removal. (d) h_{rms} image generated using the coherency matrix method after additive noise removal. (e) h_{rms} image generated using the Oh 2004 model before additive noise removal. (f) h_{rms} image generated using the Oh 2004 model after additive noise removal.

The surface roughness images generated using the anisotropy method, coherency matrix method and the Oh 2004 model for the duraBASt test site and the adjacent motorway are shown in Figure 3.12. For the purpose of easier interpretation, the duraBASt test site is highlighted with a white border in all images. Figure 3.12(a) shows the surface roughness image generated using the anisotropy method without additive noise removal. Subsequent application of the anisotropy method after removing additive noise is shown in Figure 3.12(b). A comparison with the GE image in Figure 3.11 reveals that both results from the anisotropy method, even after noise removal, fail to effectively differentiate between smooth and rough road sections. Figure 3.12(c) and Figure 3.12(d) exhibit surface roughness images from the coherency matrix method before and after additive noise removal, respectively. The coherency matrix method is also unable to distinguish between smooth and rough road sections both before and after noise removal. Similarly, Figure 3.12(e) and Figure 3.12(f) illustrate surface roughness results using the Oh 2004 model before and after additive noise removal, respectively, demonstrating the model's inability to differentiate road surface conditions.

Figure 3.13 shows the surface roughness images generated using the Dubois model and the newly developed semi-empirical model for the duraBASt test site and the adjacent motorway. The Dubois model's surface roughness images, showcased in Figures 3.13(a) and (b) before and after additive noise reduction, exhibit minimal noticeable differences at this zoom level. Both images successfully identify surface roughness changes at the duraBASt test site and the motorway, as depicted in Figure 3.11. Figure 3.13(c) presents the surface roughness image from the new semi-empirical model before additive noise reduction. Comparing it with the GE image in Figure 3.11 and the Dubois model's results (Figures 3.13(a) and (b)) reveals that much smaller changes in the surface roughness variations at the duraBASt test site and also at the motorway are noticeable in the new model's result. Figure 3.13(d) illustrates the surface roughness image produced by the new model after additive noise reduction, showing a reduction in high surface value pixels with yellow colour compared to Figure 3.13(c). In summary, both the Dubois model and the new model demonstrated reliable surface roughness results, distinguishing them from the results generated using other models shown in Figure 3.12 that either produced noisy images or were unable to distinguish between smooth and rough road sections.

In Figure 3.14, the surface roughness (h_{rms}) values generated for the GT spots at the Kaufbeuren test site by different models are compared with the ground truth surface roughness (GT h_{rms}) values obtained by laser scanning (refer to Appendix A on pages 169 and 178 for more details on test site and GT data collection, respectively). The surface roughness plots were generated using the PS03, PS04, PS05, and PS12 datasets (cf. Table A.2 on page 174). Figure 3.14(a) shows the surface roughness plots for the GT h_{rms} values and the h_{rms} values estimated from the anisotropy method and coherency

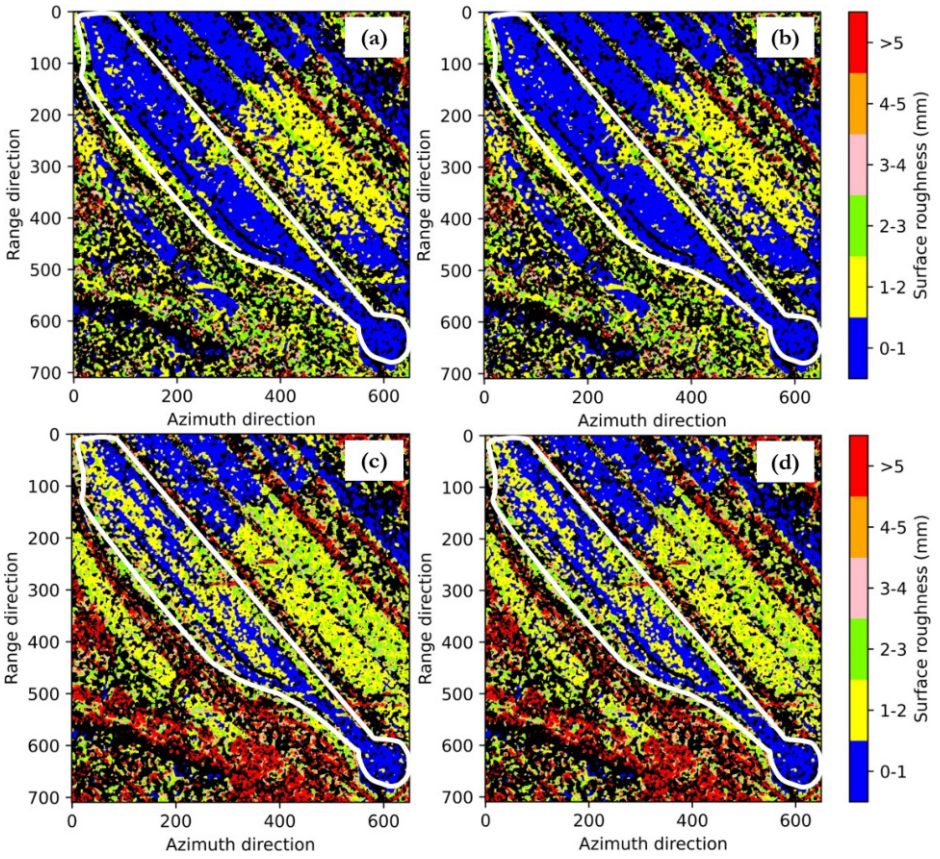

Figure 3.13: h_{rms} images. (a) h_{rms} image generated using the Dubois model before additive noise removal. (b) h_{rms} image generated using the Dubois model after additive noise removal. (c) h_{rms} image generated using the new model before additive noise removal. (d) h_{rms} image generated using the new model after additive noise removal.

matrix ($\boldsymbol{T}_3$) method. By analysing Figure 3.14(a), it can be seen that the h_{rms} values estimated by the anisotropy model at the smooth GT spots (low surface roughness spots) were highly overestimated and the model estimated h_{rms} values at the rough GT spots (high surface roughness spots) were underestimated. For the $\boldsymbol{T}_3$ matrix method, the h_{rms} values obtained at both the rough and smooth spots were highly overestimated. Table 3.2 shows the comparison between the GT h_{rms} values and the model-estimated h_{rms} values for the PS03 dataset. From Table 3.2, it can be found that the RMSE obtained for the anisotropy method is 0.88 mm and 1.99 mm for the $\boldsymbol{T}_3$ matrix method.

Figure 3.14(b) shows the surface roughness plots generated using the Oh 1992 and Oh 2004 models. By observing the plots, it can be understood that the h_{rms} values estimated by both the Oh 1992 and Oh 2004 models were overestimated at both the smooth and

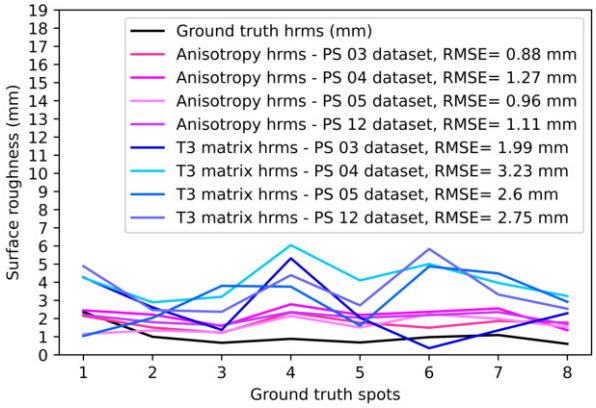

(a)

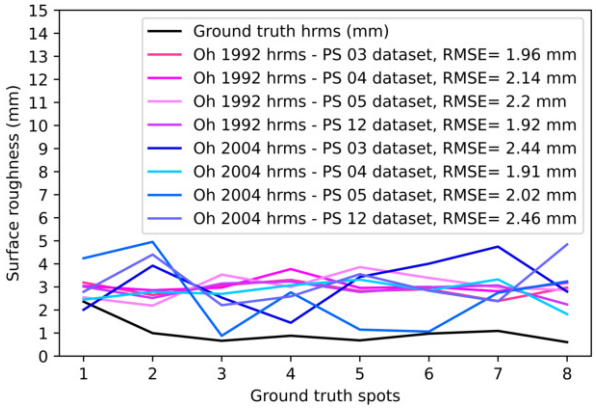

(b)

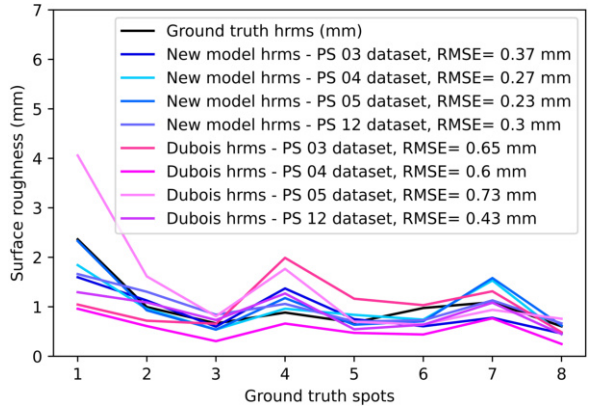

(c)

Figure 3.14: GT h_{rms} and model estimated surface roughness comparison plots. (a) anisotropy and coherency matrix method. (b) Oh 1992 and Oh 2004 method. (c) Dubois model and new model.

rough GT spots. From Table 3.2 it can also be seen that the RMSE obtained for the Oh 1992 model is 1.96 mm and 2.44 mm for the Oh 2004 model. From Figure 3.14(a) and Figure 3.14(b), it can be understood that the model estimated surface roughness plots are not correlated with the GT surface roughness plots.

By comparing the Dubois model estimated surface roughness plots with the GT h_{rms} plot it can be seen that some of the datasets show an underestimation at the GT spots and some other datasets show an overestimation (cf. Figure 3.14(c)). However, it can be seen that the plots are correlated and follow the same trend as the GT surface roughness plot. From Table 3.2, it can be seen that the RMSE obtained for the Dubois model using the PS03 dataset is 0.65 mm which is lower compared to the above-mentioned models. By comparing the surface roughness plots estimated using the new semi-empirical model with the GT h_{rms} plot, it can be seen that the deviations are the lowest between the plots. From Table 3.2 also, it can be seen that the RMSE obtained for the new model using the PS03 dataset is 0.37 mm, which is the lowest RMSE obtained from all the models. The PS03 dataset is used for the results shown in Table 3.2 because this dataset was not used for estimating the new model coefficients and can therefore be considered as a test dataset.

Table 3.2: Comparison of surface roughness results at GT spots obtained using different surface roughness estimation models.

GT spot	GT h_{rms} (mm)	Model estimated h_{rms} from PS03 dataset [mm]					
		Anisotropy method	Coherency matrix method	Oh 1992 model	Oh 2004 model	Dubois model	New model
1	2.36	2.14	4.27	3.19	2.01	1.05	1.60
2	0.99	1.50	2.61	2.65	3.92	0.72	1.12
3	0.66	1.22	1.38	3.06	2.54	0.66	0.60
4	0.88	2.33	5.32	3.31	1.45	1.99	1.37
5	0.68	1.78	2.04	2.82	3.43	1.16	0.74
6	0.98	1.50	0.37	2.90	4.01	1.03	0.61
7	1.09	1.86	1.35	2.39	4.75	1.31	0.78
8	0.61	1.79	2.29	2.97	2.80	0.49	0.46
RMSE (mm)		0.88	1.99	1.96	2.44	0.65	0.37

Figure 3.15 illustrates surface roughness error plots for both the Dubois model and the new semi-empirical model computed at the eight GT spots. These error plots are generated for the same datasets (PS03, PS04, PS05, and PS12) used for generating Figure 3.14(c). The surface roughness errors are determined by subtracting the GT h_{rms} values from the model-estimated h_{rms} values for each GT spot. The mean absolute error (MAE)

values for each dataset are also included in Figure 3.15. Analysing these error plots and MAE values allows a comparison of the performance of the Dubois model and the new semi-empirical model across multiple datasets, with the MAE values providing a quantitative assessment of the accuracy of each model w.r.t. the GT values.

The MAE is calculated as follows:

$$\text{MAE} = \frac{1}{n_{\text{GT spots}}} \sum_{i=1}^{n_{\text{GT spots}}} |h_{\text{rms}_i} - \text{GT } h_{\text{rms}_i}| \tag{3.20}$$

where $n_{\text{GT spots}}$ represents the number of GT spots, h_{rms_i} represents the model estimated h_{rms} value for each GT spot and GT h_{rms_i} is the GT h_{rms} value for each GT spot.

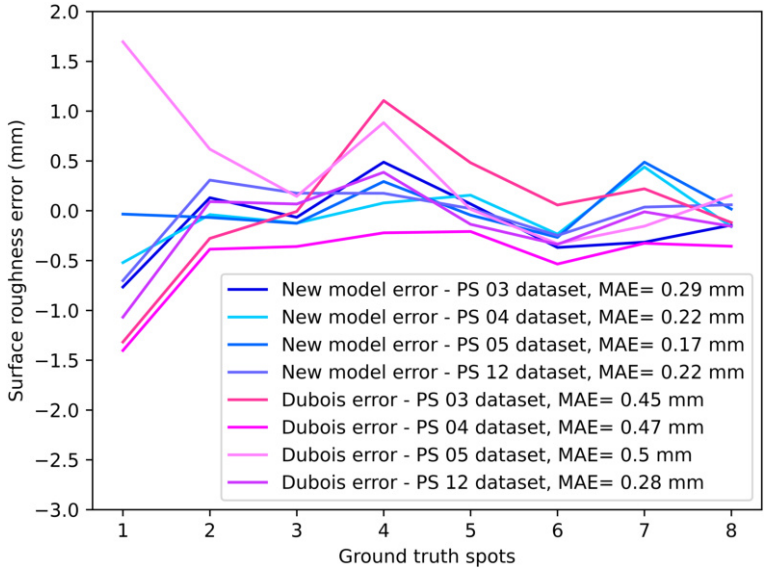

Figure 3.15: Surface roughness error plots for the Dubois model and the new model.

Comparing the error plots between the new model and the Dubois model shown in Figure 3.15, it is evident that the surface roughness errors are significantly reduced in the new model compared to the Dubois model. Specifically, examining the four error plots corresponding to each dataset for the Dubois model, it can be observed that the highest surface roughness error values are around approximately 1.70 mm and -1.40 mm. Positive error values denote an overestimation, while negative values indicate an underestimation of the h_{rms} values by the model. The highest MAE obtained for the Dubois model is 0.50 mm (PS05 dataset) and the lowest MAE is 0.28 mm (PS12 dataset), showing large variations between the datasets. Conversely, the highest surface

roughness error values for the new model are around 0.48 mm and -0.75 mm, indicating a significant reduction in both the overestimation and underestimation of the h_{rms} values. The highest MAE obtained for the new model is 0.29 mm (PS03 dataset) and the lowest is 0.17 mm (PS05 dataset), indicating lower MAE values compared to the Dubois model and more consistent h_{rms} estimation across the datasets. These findings underscore the superior performance of the new model over the Dubois model.

Table 3.3 illustrates a comparison between the GT h_{rms} values and those estimated using both the Dubois model and the new semi-empirical model for the PS03, PS04, PS05, and PS12 datasets (see Table A.2 on page 174). The PS04, PS05, and PS12 datasets were utilised to train the coefficients for the new model, while the PS03 dataset served as the testing dataset. The table presents the model-estimated h_{rms} values alongside the error values w.r.t. the GT h_{rms} value for each GT spot. Additionally, it provides the overall RMSE w.r.t. the GT h_{rms} values for each dataset. Upon examination of the table, it is evident that the Dubois model exhibits RMSE ranging from 0.43 mm (PS12 dataset) to 0.73 mm (PS05 dataset). Conversely, the new semi-empirical model demonstrates RMSE ranging from 0.23 mm (PS05 dataset) to 0.37 mm (PS03 dataset). In general, the errors obtained with the new model are significantly smaller compared to those of the Dubois model across all four datasets. Consequently, it can be summarised that the new semi-empirical model offers a superior estimate of road surface roughness than the Dubois model, both for the training and testing datasets.

Figure 3.16 illustrates the surface roughness error plots for the eight GT spots generated using the new model with the PS03 dataset (refer to Table A.2 on page 174), both with and without performing the additive noise subtraction pre-processing step (see section 3.2.1 on page 38). The magenta plot represents the error plot without additive noise subtraction, while the blue plot depicts the error plot with additive noise subtraction. Upon comparison, the plots exhibit close agreement, with only a slight performance enhancement observed with additive noise subtraction. This slight improvement is reflected in the MAE values, where the MAE value without additive noise subtraction is 0.31 mm, and with additive noise subtraction is 0.29 mm. This marginal difference can be attributed to the fact that most road pixels in the F-SAR datasets possess excellent SNR (above the minimum threshold of 5.98 dB required for the new model as discussed in section 3.2.2), resulting in minimal influence of additive noise on the co-polar σ^o backscatter values. However, it is advisable to perform additive noise subtraction whenever feasible, as it can reduce the likelihood of erroneous h_{rms} estimates, particularly in very smooth road regions with low SNR or in scenarios such as having shallow incidence angles or increased flight altitude of the F-SAR system, where SNR diminishes considerably.

Table 3.3: Comparison of the surface roughness results at the Kaufbeuren GT spots, obtained using the Dubois model and the new semi-empirical model for the PS03, PS04, PS05 and PS12 datasets.

GT Spot	GT h_{rms} (mm)	Dubois model								New semi-empirical model							
		PS03		PS04		PS05		PS12		PS03		PS04		PS05		PS12	
		h_{rms} (mm)	Error (mm)	h_{rms} (mm)	Error (mm)	h_{rms} (mm)	Error (mm)	h_{rms} (mm)	Error (mm)	h_{rms} (mm)	Error (mm)	h_{rms} (mm)	Error (mm)	h_{rms} (mm)	Error (mm)	h_{rms} (mm)	Error (mm)
1	2.36	1.05	-1.31	0.96	-1.40	4.06	1.70	1.29	-1.07	1.60	-0.76	1.84	-0.52	2.33	-0.03	1.66	-0.70
2	0.99	0.72	-0.24	0.61	-0.38	1.61	0.62	1.09	0.10	1.13	0.14	0.96	-0.03	0.93	-0.06	1.30	0.31
3	0.66	0.66	0.0	0.31	-0.35	0.81	0.15	0.73	0.07	0.60	-0.06	0.54	-0.12	0.54	-0.12	0.84	0.18
4	0.88	1.99	1.11	0.66	-0.22	1.77	0.89	1.27	0.39	1.37	0.49	0.96	0.08	1.17	0.29	1.05	0.17
5	0.68	1.16	0.48	0.47	-0.21	0.70	0.02	0.55	-0.13	0.75	0.07	0.83	0.15	0.64	-0.04	0.70	0.02
6	0.98	1.03	0.05	0.44	-0.54	0.64	-0.34	0.64	-0.34	0.61	-0.37	0.74	-0.24	0.71	-0.27	0.73	-0.25
7	1.09	1.31	0.22	0.78	-0.31	0.94	-0.15	1.08	-0.01	0.78	-0.31	1.53	0.44	1.58	0.49	1.12	0.03
8	0.61	0.49	-0.12	0.25	-0.36	0.76	0.15	0.45	-0.16	0.46	-0.15	0.45	-0.16	0.62	0.01	0.66	0.05
RMSE (mm)		0.65		0.60		0.73		0.43		0.37		0.27		0.23		0.30	

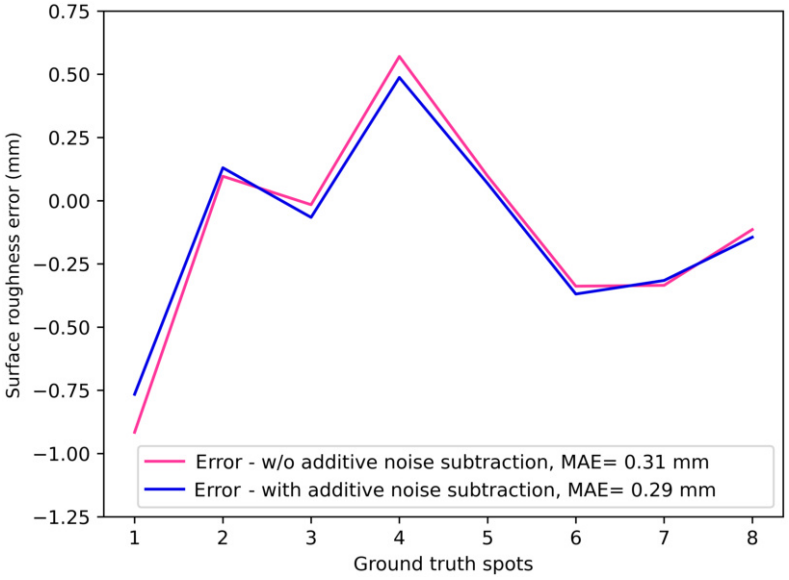

Figure 3.16: Comparison of surface roughness error plots generated by the new model using the PS03 dataset, with and without additive noise subtraction.

3.3.2 Performance Evaluation of the New Model

From the results discussed in the previous sub-section, it can be understood that the Dubois model and the new semi-empirical model performed better compared to the other models. However, the surface roughness values estimated by the Dubois model have an incidence angle dependency which led to the development of a new semi-empirical model based on the assumptions from the Dubois model.

Figure 3.17 shows the surface roughness image generated for the Kaufbeuren test site using the Dubois model. After geocoding, the image is visualised in GE, with the areas outside the runway, taxiway and parking areas removed. The F-SAR PS05 dataset, which has a flight track perpendicular to the Kaufbeuren runway (cf. Table A.2 on page 174 and Figure 3.2 on page 34), was used to generate the image. Consequently, one end of the runway falls in the near range, starting with an incidence angle of 32°, while the other end falls in the far range with an incidence angle ending at 55°. As explained in Appendix A on page 169, both ends of the runway are made of concrete, while the middle region is asphalt. However, it is clear from Figure 3.17 that the Dubois model has difficulty distinguishing between concrete and asphalt at near range. Both surfaces appear predominantly in blue, which indicates a similar surface roughness. On the other hand, the Dubois model can successfully distinguish between asphalt and concrete in the far range. Asphalt areas appear mostly in blue, while concrete areas are visible in green to red. The red colour corresponds to the concrete surface with repeated cuts at

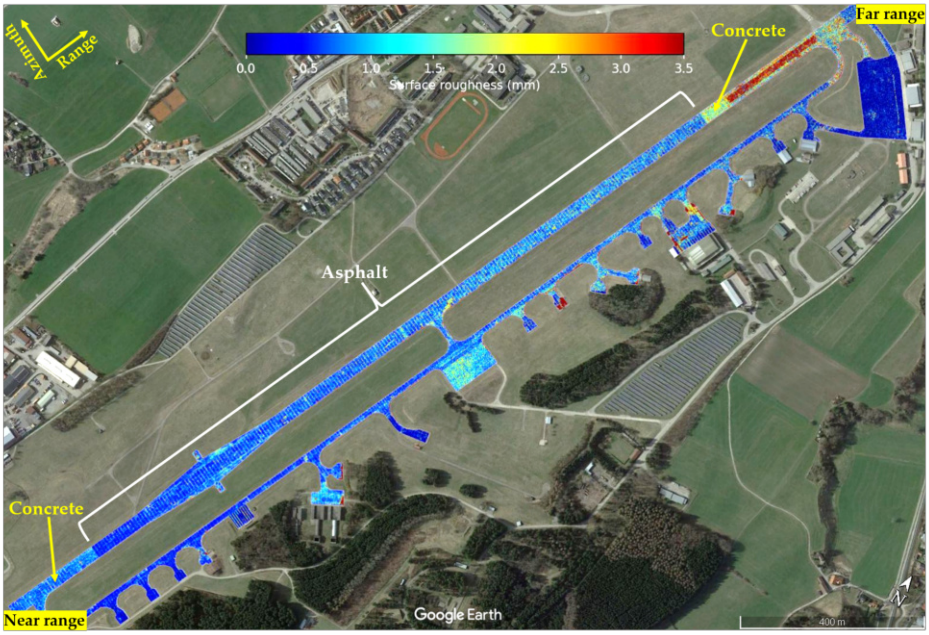

Figure 3.17: Surface roughness image for the Kaufbeuren test site generated using the Dubois model.

the end of the runway to facilitate aircraft braking (see GT spot 1 in Figure A.6 on page 179). In addition, an increase in surface roughness can be observed from near to far range for the asphalt regions. These observations indicate that the h_{rms} values estimated by the Dubois model have an incidence angle dependency, with a lower sensitivity to surface roughness at the near range.

Figure 3.18(a) shows the surface roughness image of the Kaufbeuren test site using the new model from the PS05 dataset, which is the same dataset used to generate the Dubois model result shown in Figure 3.17. A comparison between Figure 3.18(a) and Figure 3.17 reveals that in the surface roughness image generated using the new model, the concrete regions at both ends of the runway are showing a high value of surface roughness indicated by the cyan, green and yellow colours and the asphalt regions are showing a low value of surface roughness indicated by the blue colour. From this result, it can be clearly understood that the new model can distinguish between concrete and asphalt at both near range and far range which may also have different surface roughness. Furthermore, when looking at the asphalt regions from the near range to the far range, it can be seen that the influence of the incidence angle on the surface roughness variations has decreased significantly. Figure 3.18(b) shows the surface roughness image generated using the new model with the PS03 dataset, which was not included in the estimation of the model coefficients and has a different data acquisition geometry (refer

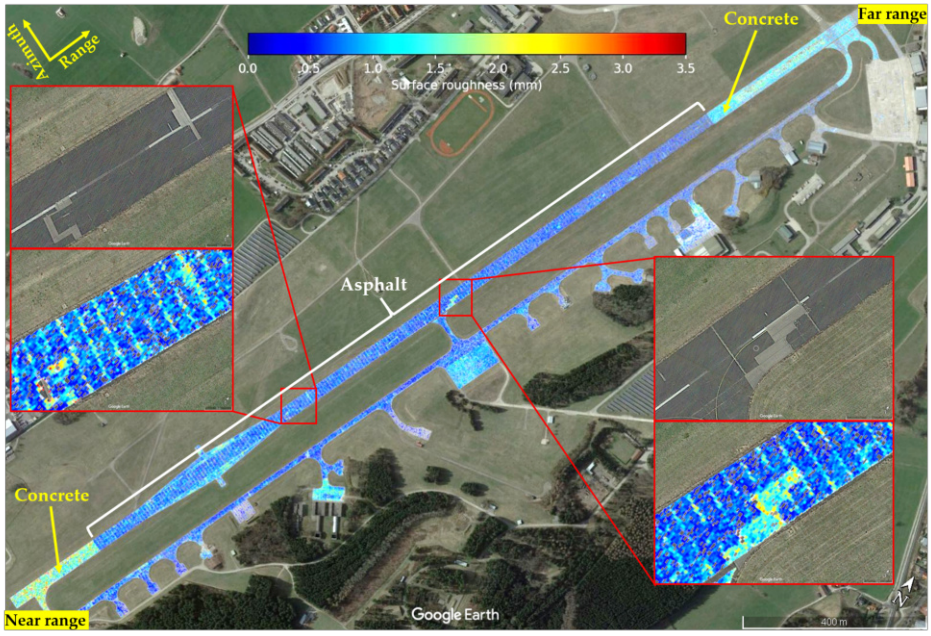

(a)

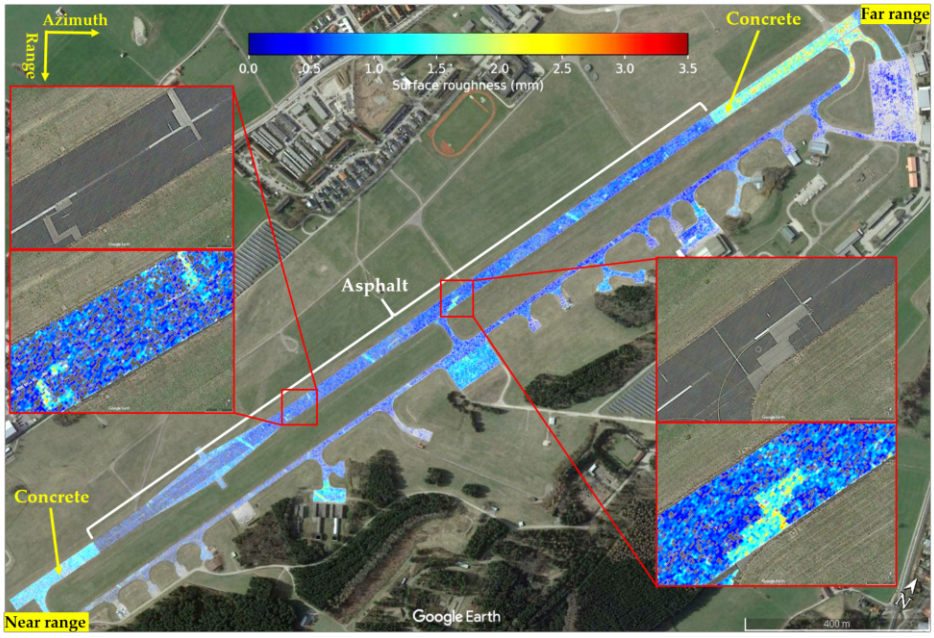

(b)

Figure 3.18: Surface roughness images for the Kaufbeuren test site generated with the new model, using (a) PS05 dataset, (b) PS03 dataset.

to Table A.2 on page 174). This dataset can therefore be considered as a testing dataset, and a comparison with Figure 3.18(a) shows a similar result, with asphalt appearing predominantly in blue and concrete in cyan to yellow colours. Therefore, it can be seen that the new model performs satisfactorily on both the training and testing datasets. A noticeable difference between Figures 3.18(a) and (b) is the presence of several high surface roughness cuts visible only in the zoomed views of Figure 3.18(a). These cuts, which appear across the runway at regular intervals, are due to the asphalt being laid in tiles with very small cuts between them. These small cuts are visible only in Figure 3.18(a) due to the perpendicular viewing (aspect) angle of the PS05 dataset w.r.t. the orientation of these cuts, which maximises backscatter from these cuts to the radar. In contrast, these cuts are not visible in Figure 3.18(b) due to the different viewing geometry (see the range direction arrows marked in both figures). In addition, these sections are very small in width and depth and therefore not visible in the GE optical images shown in the zoomed views.

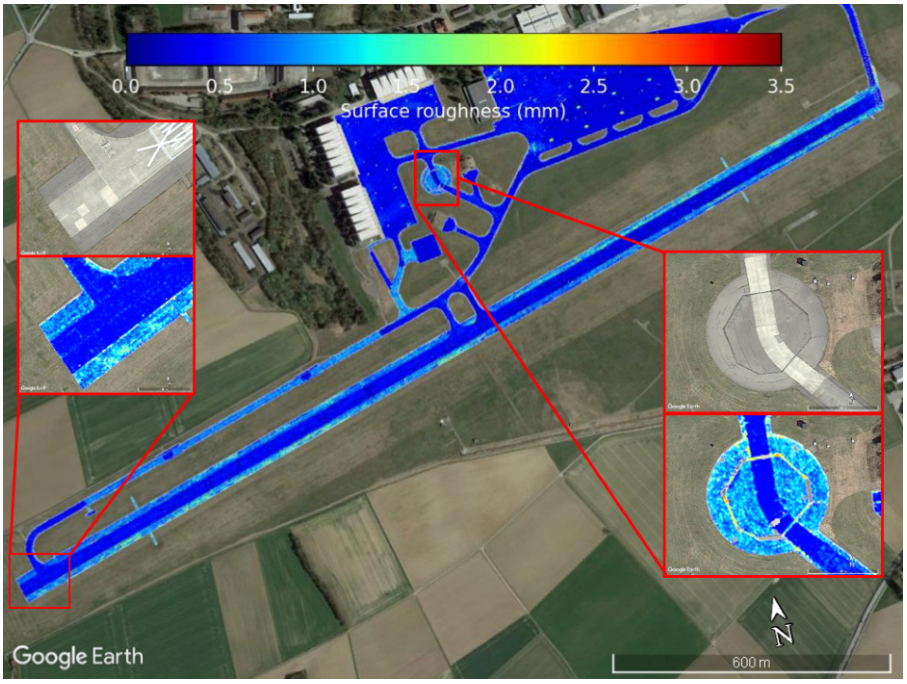

Figure 3.19: Surface roughness image generated for the Landsberg-Lech air base.

Figure 3.19 shows the surface roughness image overlaid on GE for the Landsberg-Lech airbase in Bavaria, Germany. By analysing the image, it can be seen that the central part of the runway is depicted in blue, indicating low h_{rms} values below 0.5 mm. In contrast, the outer shoulder areas of the runway are shown in cyan, which indicates an increased surface roughness in the order of 1.0 mm. The zoomed-in views in Figure 3.19 show

detailed images of the surface roughness together with GE optical images for a section of the runway and taxiway. When looking at the GE optical views, it is evident that the blue and cyan areas of surface roughness have different colours/appearances in the GE image, indicating the use of materials with different compositions in those areas, resulting in different surface roughness values.

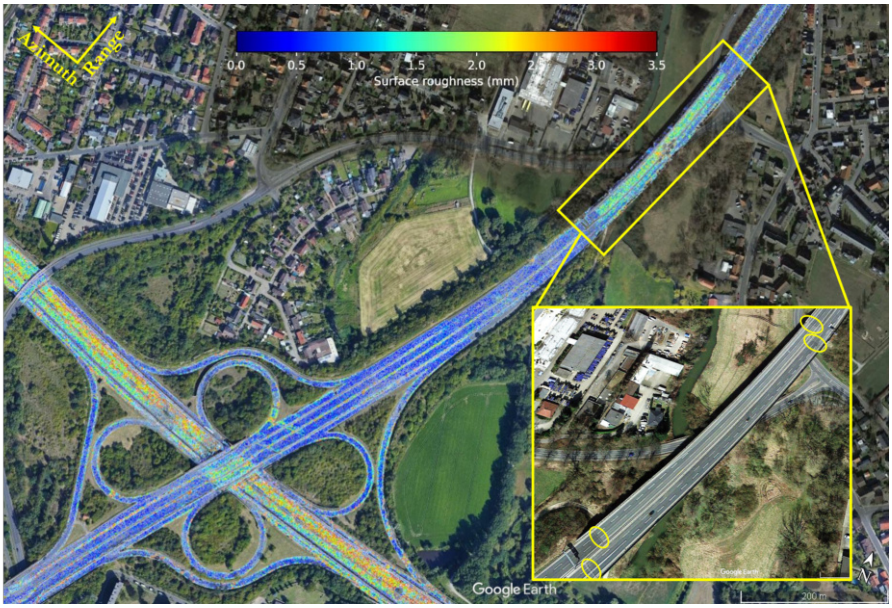

Figure 3.20: Road surface roughness image generated for the A2-A391 motorway crossing in Braunschweig.

The road surface roughness image for the A2-A391 motorway crossing in Braunschweig is shown in Figure 3.20. Here, the north-south motorway appears predominantly blue, indicating lower roughness, while the east-west motorway shows green to yellow colours, suggesting increased roughness. Similarly, a sharp increase in surface roughness can be seen at the top right end of the north-south motorway at the flyover. The zoomed-in GE view of this flyover also shows a sudden change in contrast at both ends of the flyover, denoted by the yellow ellipses, suggesting the use of different construction materials for the flyover as compared to the connecting roads.

Additionally, Figure 3.21 showcases the surface roughness image generated for a section of the A2 motorway in Braunschweig, incorporating a bridge. Analysis reveals a lower roughness level on the bridge and its westward connecting road, evident from the prevalence of blue colour, while the eastward connecting road displays cyan to green colours, indicating increased roughness. Consistent with previous observations, contrast changes in the GE image align with transitions in surface roughness. It is also interesting to note that the bridge appears slightly displaced into the river in the overlaid surface roughness

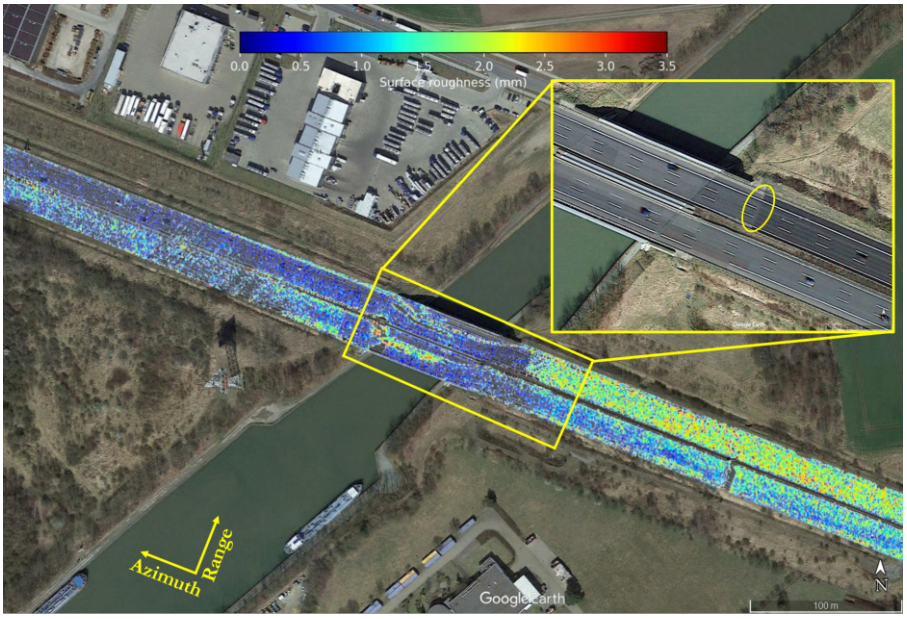

Figure 3.21: Road surface roughness image generated for a bridge on the A2 motorway in Braunschweig.

image, this is most likely due to elevation errors in the digital elevation model (DEM) used for SAR data focusing.

In both Figures 3.20 and 3.21, the east-west motorway appears noisy due to its alignment with the F-SAR system's azimuth/flight direction, which introduces distortions in the SAR image caused by moving vehicles. These distortions result from Doppler shifts in the backscattered signals generated by vehicles moving in the azimuth direction, leading to image smearing and positional displacement of the moving vehicles in the SAR image [26].

It is worth noting that the regions depicted in Figures 3.19, 3.20, and 3.21 were not the primary test sites of this study. Therefore, the results obtained in these areas demonstrate the efficiency of the new semi-empirical model and processing chain in accurately estimating road surface roughness across diverse regions, thereby facilitating the identification of areas with varying roughness and material compositions.

The surface roughness image in GeoTIFF format for the Kaufbeuren test site generated from the road surface roughness estimation processing chain is visualised in Figure 3.22. The GeoTIFF surface roughness image is a single-band representation containing surface roughness values estimated using the new semi-empirical model without any scaling applied. Each pixel representing the surface roughness values also has the latitude and

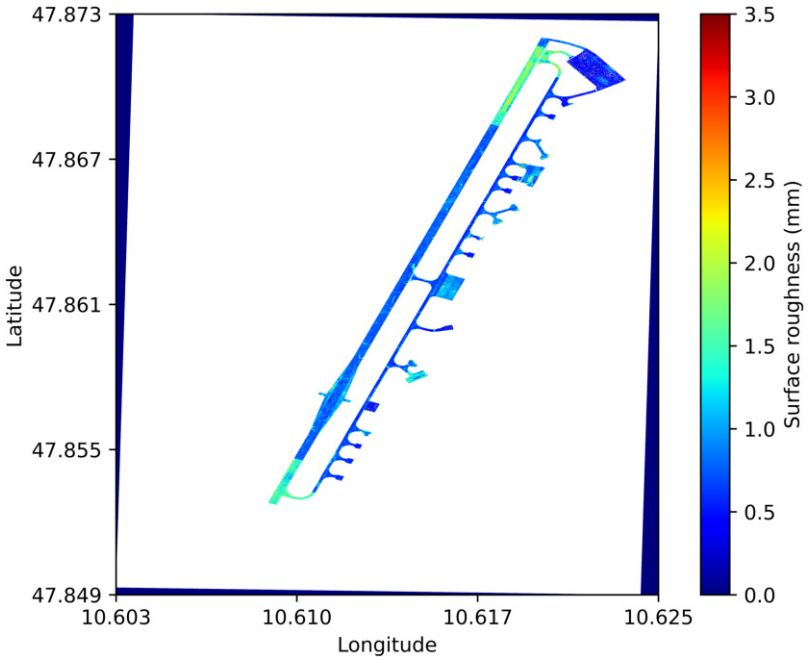

Figure 3.22: Visualisation of the GeoTIFF format surface roughness image generated for the Kaufbeuren test site.

longitude information, allowing precise location of surface roughness pixels on the ground (see x and y axes). The availability of road surface roughness results in GeoTIFF format ensures compatibility and integration with advanced GIS software, enhancing its utility for further analysis.

3.3.3 Influence of σ^o and SNR

As already discussed in section 3.2.2, an upper σ^o masking and a lower SNR masking are required to remove the unreliable and noisy h_{rms} values from the surface roughness images.

Figure 3.23 shows the surface roughness image generated using the new model for the Wolfsburg motorway intersection at Braunschweig, Germany, without performing σ^o and SNR masking. The zoomed view in the figure shows a portion of the motorway where a change in surface roughness can be observed. This sudden change in surface roughness at the motorway may be due to maintenance work done in that region. In the zoomed view, it can be seen that two red stripes are present across the road indicating high surface roughness values. These red stripes are caused by the strong backscatter signal from the overhead signboard present there and do not correspond to the actual

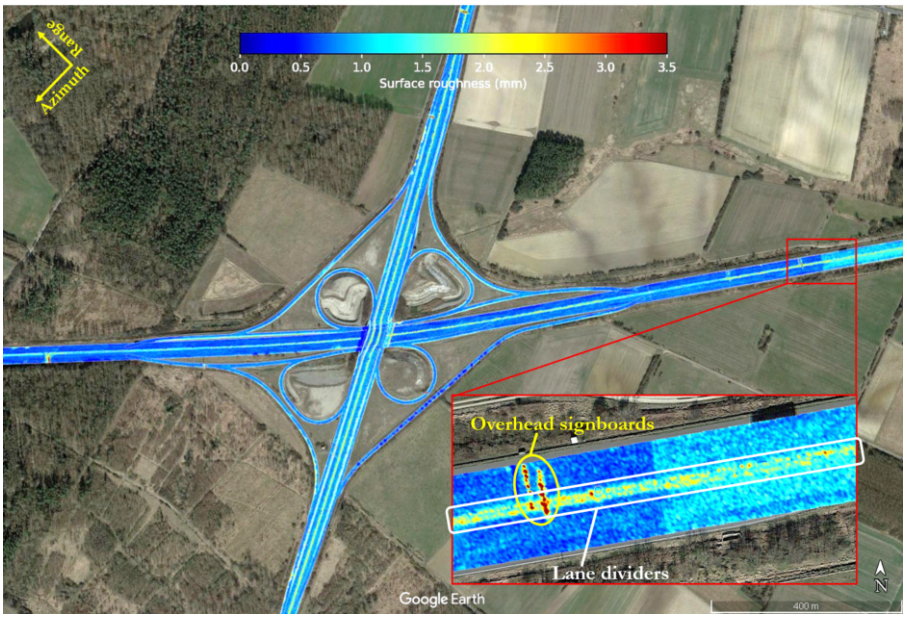

Figure 3.23: Surface roughness image of the Wolfsburg motorway intersection at Braunschweig without performing upper σ^o and lower SNR masking.

surface roughness of that location. Also, the green to yellow colours present between the two lanes of the motorway are caused due to the strong reflection from the lane dividers separating the two roads. An upper σ^o threshold masking can be done to remove this kind of anomaly from the surface roughness image.

Figure 3.24 shows the surface roughness image generated after performing the upper σ^o threshold masking. In Figure 3.24, all the pixels with σ^o values higher than -10.96 dB were masked out to remove strong reflections from signboards, lane dividers, etc. By comparing the zoomed view shown in Figure 3.24 with the zoomed view shown in Figure 3.23, it can be observed that the two red stripes present in Figure 3.23 due to the strong reflection from the signboards are not visible in Figure 3.24 after upper σ^o threshold masking. Also, it can be seen that the green to yellow colours present in between the lanes due to the reflection from the lane dividers are also removed in Figure 3.24. So, the upper σ^o masking technique is an effective way to mask out unreliable pixels from the surface roughness image caused due to strong reflecting targets. Even after upper σ^o threshold masking, the low SNR pixels can still lead to unreliable/noisy surface roughness values. So, all the pixels with SNR less than 5.98 dB were masked out from the surface roughness image. Figure 3.25 shows the surface roughness image after performing both upper σ^o threshold masking and lower SNR threshold masking. By comparing Figure 3.24 with Figure 3.25, it can be seen that some of the pixels corresponding to the blue colour got

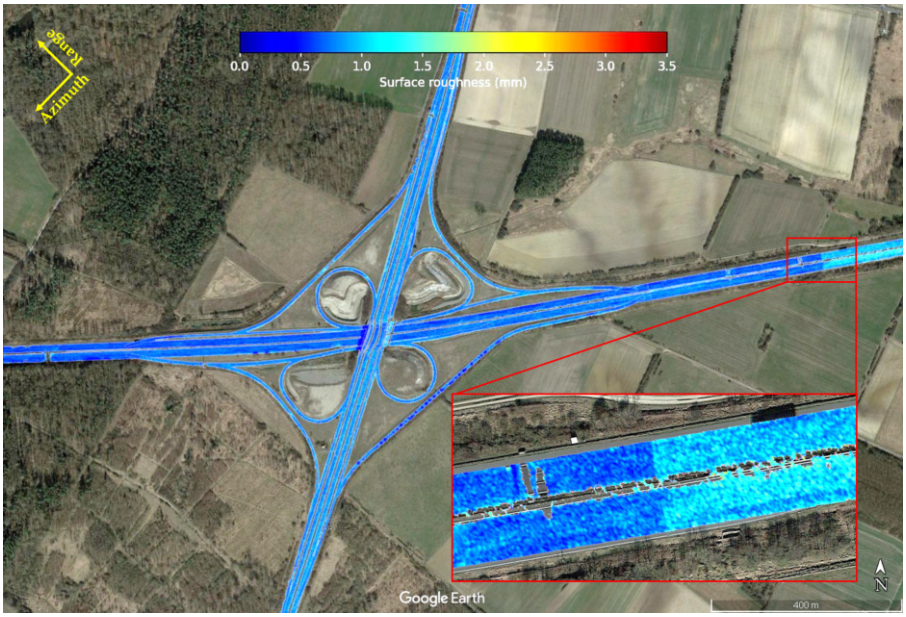

Figure 3.24: Surface roughness image of the Wolfsburg motorway intersection at Braunschweig after performing upper σ^o masking.

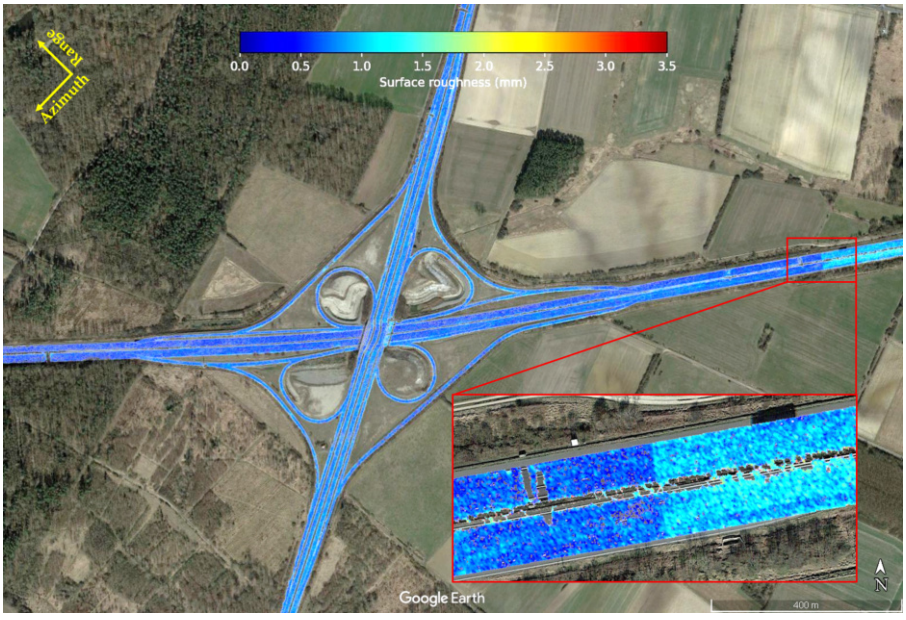

Figure 3.25: Surface roughness image of the Wolfsburg motorway intersection at Braunschweig after performing both upper σ^o and lower SNR masking.

removed in Figure 3.25. These pixels had an SNR of less than 5.98 dB. This is also visible in the surface roughness images shown for the Kaufbeuren test site in Figure 3.18. Both upper σ^o threshold masking and low SNR threshold masking can be applied together to minimise the unreliable and noisy h_{rms} values from the surface roughness images.

3.3.4 Multi-dataset Fusion

The surface roughness images generated from single datasets may have unreliable or missing h_{rms} values, which are affected by shadow areas, speckle, low SNR regions and incidence angles. Fusing surface roughness images from multiple individual datasets obtained with different data acquisition geometries into a single surface roughness image, using methods such as highest SNR and multi-dataset averaging (see section 3.2.2), help to mitigate these errors and produce a more robust single surface roughness image.

Figure 3.26 shows the fused surface roughness images generated using the highest SNR multi-dataset fusion method for the Kaufbeuren test site. Figure 3.26(a) depicts the fused surface roughness image generated using the PS02, PS03, PS04, PS05 and PS12 F-SAR datasets acquired at 3 km altitude (cf. Table A.2 on page 174), while Figure 3.26(b) displays the fused surface roughness image from the PS01, PS02, PS03 and PS04 F-SAR datasets acquired at 2.2 km altitude (cf. Table A.3 on page 175). By comparing the Figures 3.26(a) and (b) with the surface roughness images generated from single datasets (PS03 and PS05) shown in Figures 3.18(a) and (b), it can be observed that much finer details on the runway are visible in the surface roughness images generated using the highest SNR multi-dataset fusion method. More details of the runway, such as minor cuts and repair work, can be seen more clearly in the zoomed-in views in Figures 3.26(a) and (b) compared to the single dataset results. Furthermore, it can be seen that the missing pixels visible in Figures 3.18(a) and (b), which were caused by the upper σ^o and the lower SNR masking, were filled with valid h_{rms} values from other datasets in the two fused surface roughness images in Figures 3.26(a) and (b). However, the effect of local backscatter variations appears to be more dominant in the fused surface images generated by the highest SNR method leading to a more grainy/noisy appearance. These local backscatter variations may be due to the orientated features on the road surface, which can lead to high backscatter only from certain viewing (aspect) angles. The finer details are slightly more apparent in Figure 3.26(b) compared to Figure 3.26(a), which may be due to the lower flight altitude and higher SNR of the datasets used to generate Figure 3.26(b).

The fused surface roughness images produced through the multi-dataset averaging method are presented in Figure 3.27. Figure 3.27(a) is generated using the PS02, PS03, PS04, PS05 and PS12 F-SAR datasets acquired at 3 km altitude (cf. Table A.2 on page 174), while Figure 3.27(b) is from the PS01, PS02, PS03 and PS04 F-SAR datasets

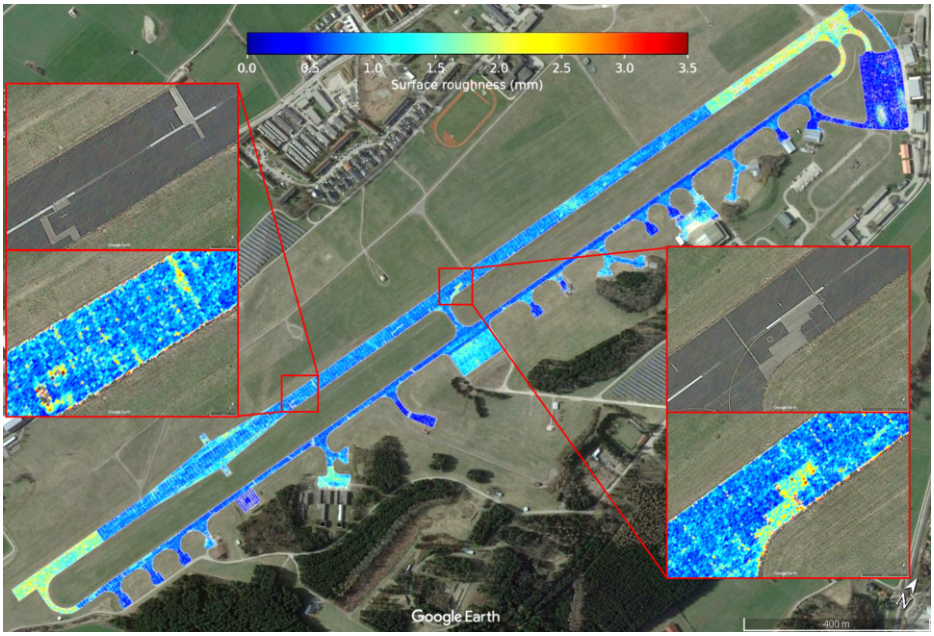

(a)

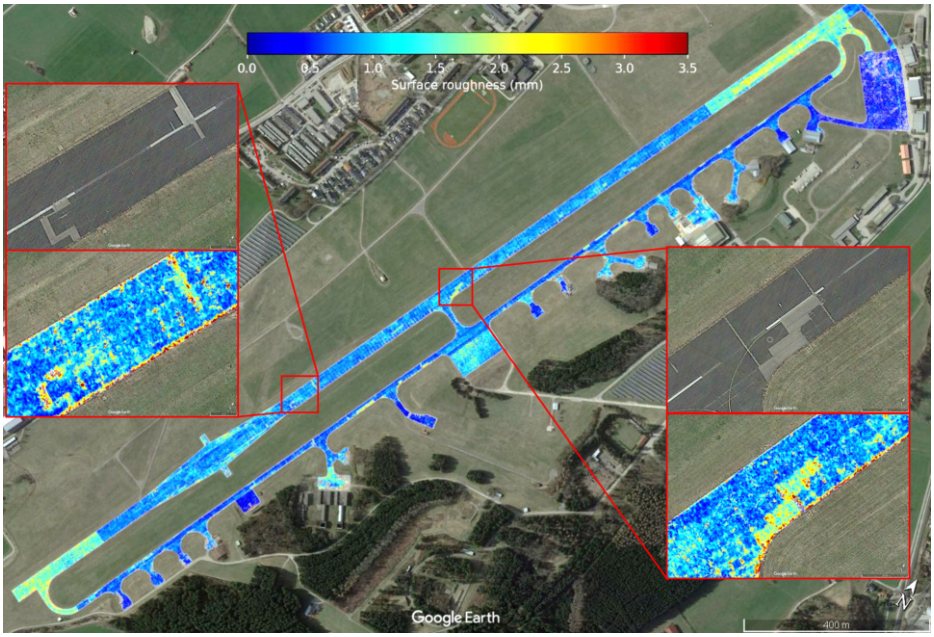

(b)

Figure 3.26: Comparison of fused surface roughness images for the Kaufbeuren test site generated using the highest SNR method from F-SAR data acquired at different altitudes. (a) Using the PS02, PS03, PS04, PS05 and PS12 F-SAR datasets acquired at 3 km altitude. (b) Using the PS01, PS02, PS03 and PS04 F-SAR datasets acquired at 2.2 km altitude.

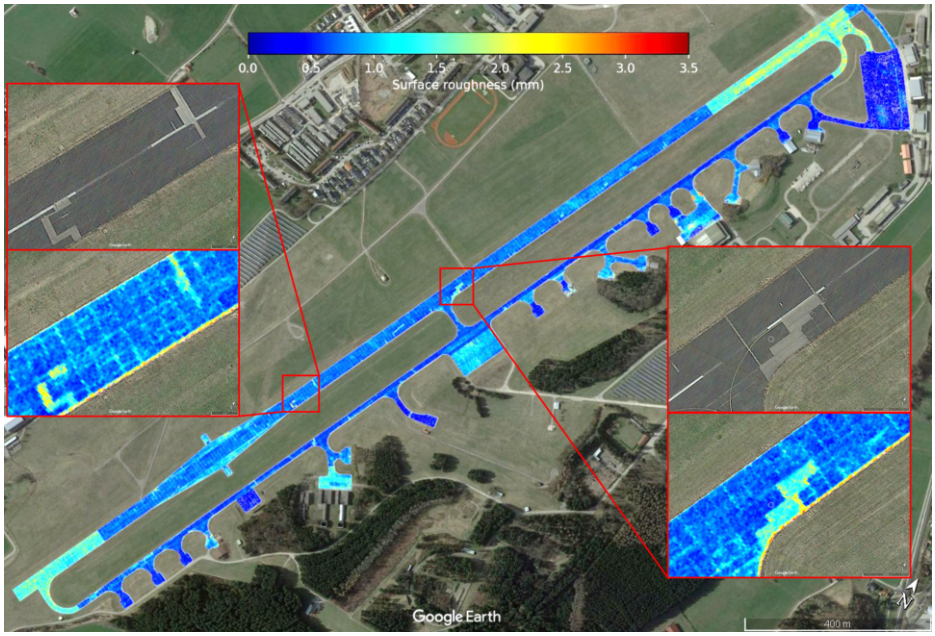

(a)

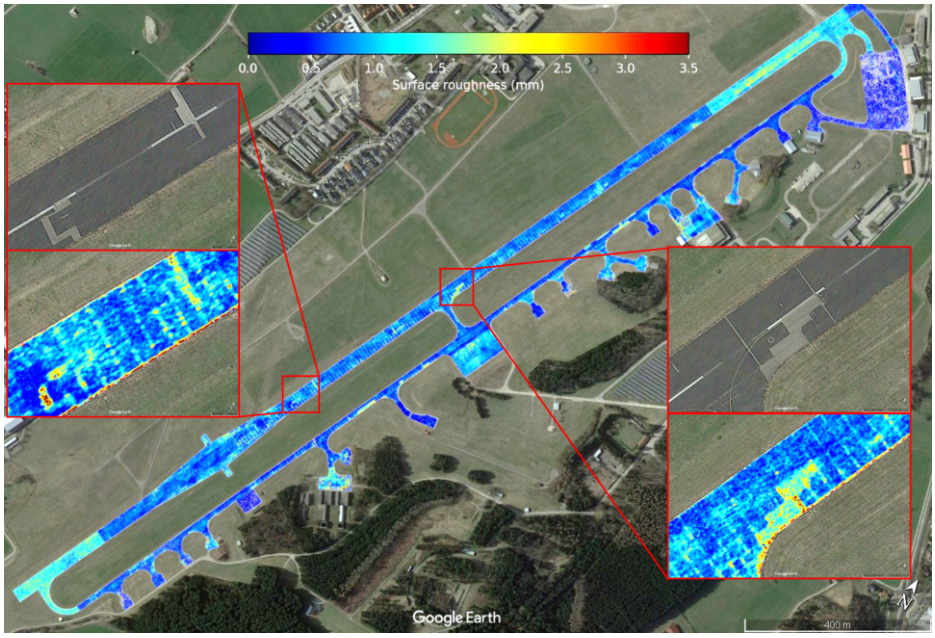

(b)

Figure 3.27: Comparison of fused surface roughness images for the Kaufbeuren test site generated using the multi-dataset averaging method from F-SAR data acquired at different altitudes. (a) Using the PS02, PS03, PS04, PS05 and PS12 F-SAR datasets acquired at 3 km altitude. (b) Using the PS01, PS02, PS03 and PS04 F-SAR datasets acquired at 2.2 km altitude.

acquired at 2.2 km altitude (cf. Table A.3 on page 175). A comparison with both Figures 3.18 and 3.26 reveals that the multi-dataset averaging images exhibit a smoother appearance compared to both the highest SNR method-based fused images and the surface roughness images from single datasets. Local variabilities present in Figures 3.18 and 3.26 are mitigated through this averaging process. In the zoomed views presented in Figure 3.27, the results are notably superior to those in Figures 3.18 and 3.26. The runway repair works are visible in cyan to red, while the surrounding regions predominantly appear in blue without significant variations. Finer details, including the smaller cuts on the runway, are visible in the multi-dataset averaged image, similar to the fused image based on the highest SNR method. The multi-dataset averaging process has also reduced the grainy appearance caused by the locally orientated features, and may also be due to the residual speckle in the surface roughness image. Similar to the highest SNR method-based fusion, finer details on the runway are more visible in the multi-dataset averaged image shown in Figure 3.27(b), as low altitude F-SAR datasets were used to generate this image.

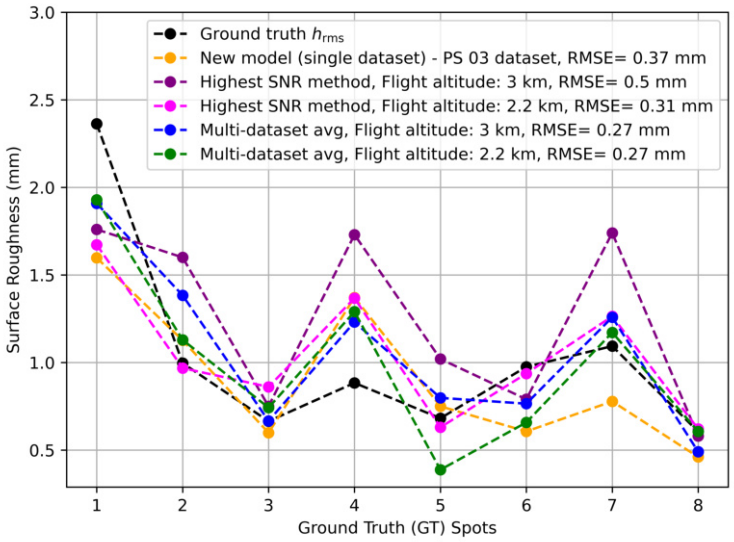

Figure 3.28: Comparison of h_{rms} plots from the highest SNR and multi-dataset averaging fusion methods with the GT h_{rms} plot and also with the h_{rms} plot from a single dataset.

Figure 3.28 presents a comparison among h_{rms} values obtained from the new semi-empirical model using a single dataset, the highest SNR fusion method, and the multi-dataset averaging fusion method, alongside the GT h_{rms} plot. The black plot shows the GT h_{rms} plot created for the eight GT spots at the Kaufbeuren test site. The orange plot shows the h_{rms} plot for the new semi-empirical model using the PS03 dataset (testing dataset) which is used to generate the surface roughness image shown in Figure 3.18

(b). A comparison of this plot with the GT h_{rms} plot shows a very good agreement and results in an RMSE of 0.37 mm.

The purple plot exhibits h_{rms} values estimated for the GT spots using the highest SNR multi-dataset fusion method with the PS02, PS03, PS04, PS05 and PS12 F-SAR datasets acquired at 3 km altitude (cf. Figure 3.26(a) and Table A.2 on page 174). Noticeable overestimation of h_{rms} values is evident, resulting in a higher RMSE of 0.50 mm compared to the single dataset RMSE of 0.37 mm. This overestimation is attributed to the increased sensitivity of the highest SNR method to speckle and local variations in datasets. Conversely, the magenta plot shows h_{rms} values using the highest SNR multi-dataset fusion method with the PS01, PS02, PS03 and PS04 F-SAR datasets acquired at 2.2 km altitude (cf. Figure 3.26(b) and Table A.3 on page 175). This plot exhibits a lower RMSE of 0.31, showcasing an improvement over the single dataset (orange plot). The deviation between the purple and magenta plots underscores the dependency of the highest SNR multi-dataset fusion method on data acquisition geometry, flight altitude and SNR.

The blue plot illustrates h_{rms} values generated by the multi-dataset averaging method using the PS02, PS03, PS04, PS05 and PS12 F-SAR datasets acquired at 3 km altitude (see Figure 3.27(a) and Table A.2 on page 174). This plot aligns well with the GT h_{rms} plot, exhibiting a lower RMSE of 0.27 mm. The green plot, depicting h_{rms} values generated by the multi-dataset averaging method using the PS01, PS02, PS03 and PS04 F-SAR datasets at 2.2 km altitude (see Figure 3.27(b) and Table A.3 on page 175), also demonstrates a lower RMSE of 0.27 mm with the GT h_{rms} plot. The blue and green plots suggest that the multi-dataset averaging method can offer reliable road surface roughness estimates and improve RMSE results without being influenced by data acquisition geometry and SNR, provided that individual surface roughness images used for multi-dataset averaging undergo upper σ^o and lower SNR thresholding to remove invalid and noisy h_{rms} values before averaging.

From Figures 3.26, 3.27 and 3.28, it can be summarised that the surface roughness images generated from the 3 km and 2.2 km altitude F-SAR datasets are nearly identical, with low RMSE values. This similarity is due to the significantly higher backscatter values in the co-polarisation channels of the F-SAR datasets at both altitudes, well above the system's NESZ (cf. Figure 3.1 on page 32), resulting in a very high SNR and minimal noise influence. Nonetheless, for road surface roughness estimation, it is generally advisable to use SAR datasets acquired at lower altitudes, as they provide a better SNR for road surfaces and may reveal finer details that might be less visible in higher-altitude datasets.

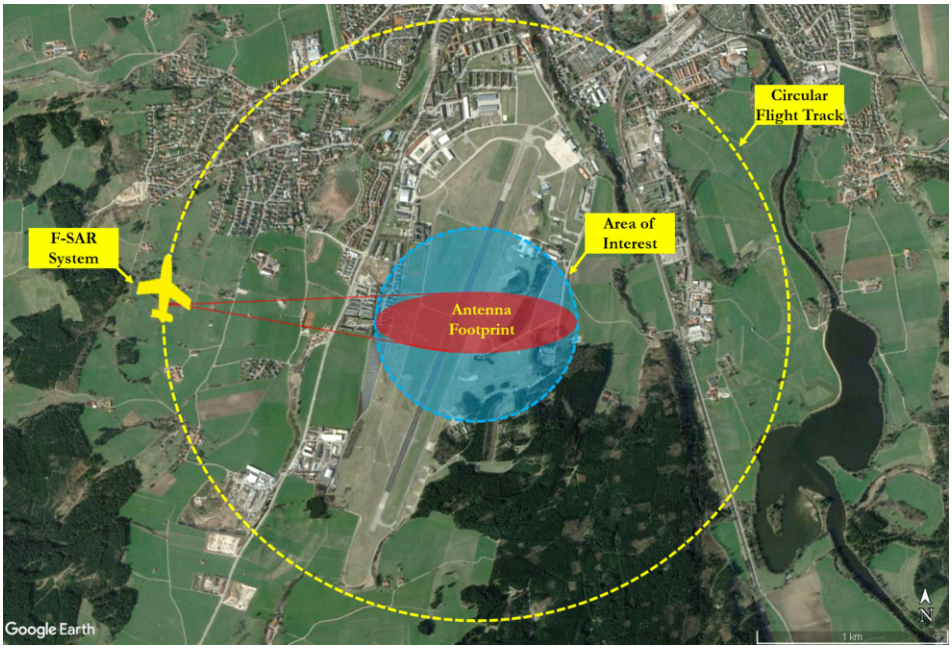

Figure 3.29: Circular SAR data acquisition geometry using F-SAR system.

3.3.5 Investigations using Circular SAR Data

The orientation of particles or grains within road construction materials like asphalt and concrete, influenced by the construction method, may introduce variability in road surface roughness estimates obtained from SAR datasets acquired along linear flight tracks. This is primarily due to the SAR antenna imaging the road surface from a specific aspect angle. Additionally, features such as cracks, cuts, and potholes can contribute to variations in roughness values when estimated from SAR datasets acquired from different sides of the road.

To explore the possibility of an aspect angle dependency in road surface roughness estimation, airborne circular SAR (CSAR) data can be used [84, 109, 147]. Figure 3.29 illustrates the CSAR data acquisition geometry using the F-SAR system, where the aircraft follows a circular flight track around the area of interest which needs to be imaged. This approach differs from the typical linear flight tracks depicted in Figure 3.2 on page 34. In CSAR, the same region is imaged at various aspect angles, generating multiple sub-aperture SAR datasets. For the specific CSAR dataset acquired over the Kaufbeuren test site utilised in this study (refer to Table A.3 on page 175), an azimuth integration angle of 5 degrees was chosen, resulting in a sub-aperture SAR image every 5 degrees around the complete 360-degree circular flight track. Therefore, a single CSAR dataset comprises 72 sub-aperture SAR images. It is essential to note that, compared to

the linear flight track F-SAR datasets in this study, the flight altitude during CSAR data acquisition was increased to 4 km due to operational constraints, potentially impacting the dataset's SNR performance negatively.

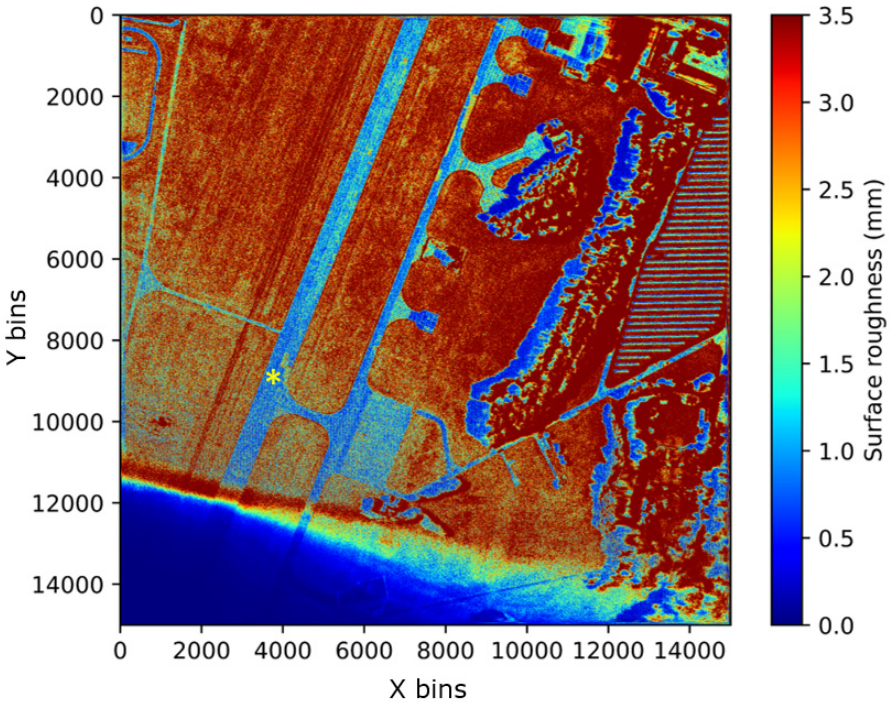

Figure 3.30: Fused surface roughness image for the Kaufbeuren test site generated from the CSAR dataset using the multi-dataset averaging method.

The 72 sub-aperture SAR images of the CSAR dataset were considered as individual SAR datasets and they were processed according to the algorithm and processing chain explained in section 3.2 to generate 72 surface roughness images using the new semi-empirical model. The fused surface roughness image obtained from these 72 images using the multi-dataset averaging method is shown in Figure 3.30. A comparison with surface roughness images obtained from linear F-SAR datasets (Figures 3.18, 3.26 and 3.27) shows significant noise in the fused CSAR roughness image, which distorts the finer details on the Kaufbeuren runway and parking areas. This noise can be attributed to the reduced SNR in the CSAR dataset, due to the increased flight altitude, as mentioned earlier. To investigate the variations in the h_{rms} and SNR values in the sub-aperture images, a 10 x 10 window was applied to a smooth asphalt area on the runway (area marked by the yellow '$*$' symbol in Figure 3.30). The mean h_{rms} values and SNR across all 72 sub-aperture images were then extracted for the pixels within this window.

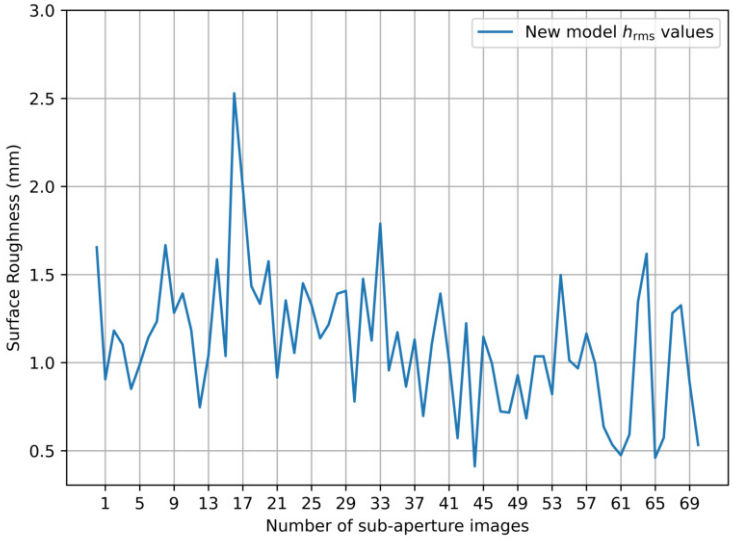

(a)

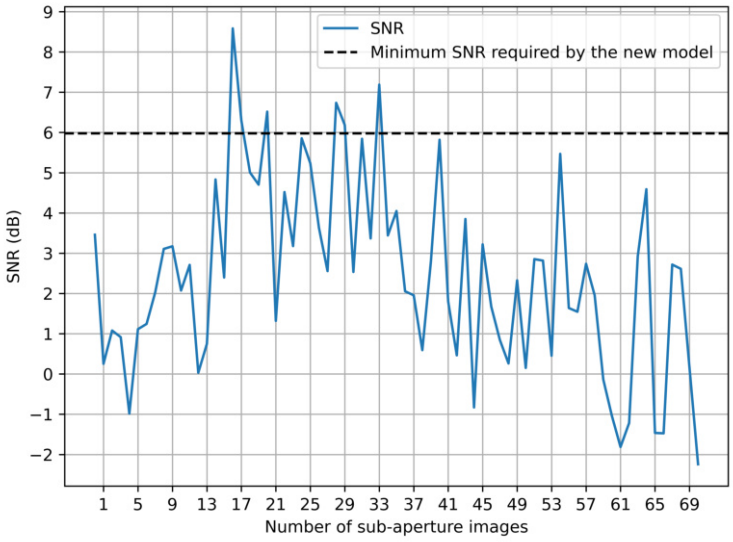

(b)

Figure 3.31: h_{rms} and SNR plots generated from the CSAR dataset across all the sub-aperture images for the area of the Kaufbeuren runway marked by the yellow '$*$' symbol in Figure 3.30. (a) h_{rms} plot. (b) SNR plot.

Figure 3.31 shows the h_{rms} and SNR plots for the smooth asphalt region within the aforementioned 10 x 10 window over the 72 sub-aperture images. When looking at the h_{rms} plot in Figure 3.31(a), it is clear that the plot exhibits significant noise, showing substantial h_{rms} variations from around 0.50 mm to 2.5 mm across the sub-aperture images. A reference to GT h_{rms} data in Table A.6 on page 180 shows an expected h_{rms} value of approximately 0.70 mm for a smooth asphalt surface. However, the model-estimated h_{rms} values from the CSAR dataset show an overestimation, which is clearly visible in Figure 3.31(a). Conversely, Figure 3.31(b) shows the SNR plot, which shows fluctuations from below -2 dB up to about 8.5 dB for different sub-aperture images. It should be noted here that the SNR for most sub-aperture images is below 5.98 dB, which is the minimum SNR threshold required for reliable h_{rms} estimation with the new semi-empirical model (see black dashed line in Figure 3.31(b)). Consequently, the two Figures 3.31(a) and (b) show that the SNR of the acquired CSAR dataset used for this investigation is insufficient for the road surface roughness estimation. Therefore, no conclusive findings on the possibility of an aspect angle dependency in the road surface roughness estimation can be derived from these datasets.

For future investigations, the use of an airborne SAR system with an electronically steerable antenna that can direct the antenna beam to a fixed point on the ground during the entire circular data acquisition flight path, in combination with a lower flight altitude to improve SNR, could provide better results.

3.4 Chapter Summary and Conclusion

In this chapter, a novel semi-empirical model for estimating road surface roughness from airborne X-band F-SAR datasets was presented. The model relies on co-polar σ^o backscatter and the local incidence angle (θ) images as input parameters. Experimental results from the Kaufbeuren, duraBASt and Braunschweig test sites demonstrated the superior performance of this model compared to state-of-the-art roughness estimation models and showed a close agreement with the ground truth data.

However, there are chances of getting low radar backscatter from road surfaces due to various reasons like specular reflections at very smooth regions, shallow incidence angles or increased flight altitude all of which can result in low SNR. Therefore, it is recommended to perform additive and multiplicative noise estimation and minimisation on the SAR datasets before using them for road surface roughness estimation. Furthermore, a post-processing step with an upper σ^o and a lower SNR thresholding procedure is essential to eliminate invalid and noisy surface roughness estimates.

This chapter also explored the potential of fusing multiple surface roughness images generated with the new model from datasets having different data acquisition geometries. This fusion, particularly through the multi-dataset averaging method, proved to be an

effective strategy for minimising errors arising from shadows, low SNR, speckle, oriented features on the road surface and different incidence/aspect angles.

Additionally, the integration of the road extraction and Google Earth visualisation techniques improved the interpretability of the surface roughness results by displaying surface roughness values that correspond exclusively to the road surfaces in Google Earth.

Finally, an attempt was made to investigate the possibility of an aspect angle dependency in road surface roughness estimation with the help of a circular SAR dataset, however, this approach faced challenges due to the very low SNR of the single CSAR dataset available for this study resulting from the higher flight altitude during data acquisition. Improved results can be expected with a CSAR dataset acquired using an airborne SAR system equipped with an electronically steerable antenna and higher SNR.

Based on the experimental findings presented in this chapter, it is advisable to use VV-polarised SAR data, preferably with steeper incidence angles in the 30 to 35 degrees range, for reliable road surface roughness estimation. Analysis of the PolSAR datasets in this chapter revealed that most road pixels in the VV-polarisation channel have an SNR above 5.98 dB, which is the minimum SNR required by the new semi-empirical model. Additionally, whenever possible, employing the multi-dataset averaging technique is recommended to minimise errors by fusing surface roughness estimates from multiple datasets.

4 Road Surface Roughness Estimation using Machine Learning Approaches

This chapter explores the application of machine learning-based models for road surface roughness estimation using high-resolution polarimetric SAR datasets. While the effectiveness of the newly developed semi-empirical model for road surface roughness estimation was presented in chapter 3, its usefulness is limited within the validity conditions of the model. Therefore, it is useful to investigate how well state-of-the-art machine learning-based models, that can learn and adapt to the statistics of the data [118], can estimate the road surface roughness. Parts of the contents presented in this chapter have already been published in [P5, P8] and also in the bachelor thesis [S2][1].

4.1 Machine Learning Models and Techniques

The machine learning-based models and techniques used later in road roughness estimation are comprehensively summarised in this section. The main concepts and assumptions of the Support Vector Regression (SVR), Decision Trees, Random Forest Regression (RFR) and Artificial Neural Networks (ANN) approaches are explained here. Given the limited availability of ground truth surface roughness data for training these models, methods like cross-validation and bagging are implemented in this study to avoid overfitting, which could otherwise compromise the reliability of the models in estimating the road surface roughness. The key principles of these techniques and their significance in connection with the road surface roughness estimation are also discussed in this section.

4.1.1 K-fold Cross Validation

In situations where the ground truth data are limited, as it is typically the case for road surface roughness estimation due to the difficulty in obtaining measurements from operational and busy roads, it becomes difficult to provide a validation set for evaluating the predictive performance of the model. This limitation can affect the effectiveness of the model and lead to potential overfitting and reduced reliability [55]. To mitigate this challenge, techniques such as cross-validation are used to increase reliability and minimise the variance of the results [66].

[1] The doctoral student (Arun Babu) supervised the bachelor student, and the cited bachelor thesis is mainly based on his ideas.

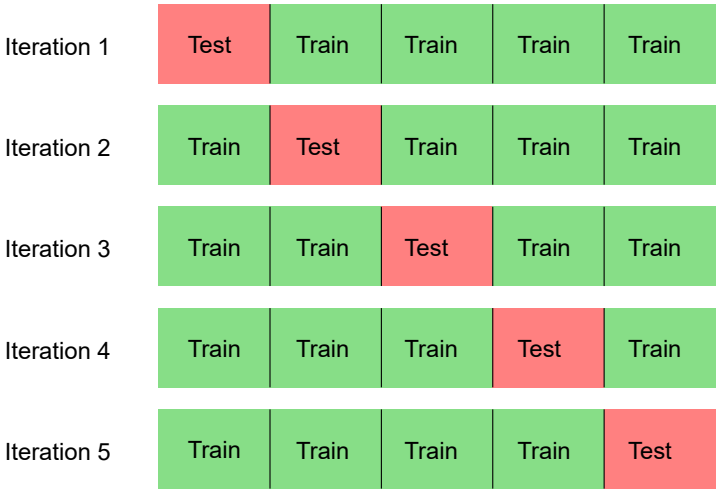

Figure 4.1: Scenario example for K-fold cross-validation in which $K = 5$.

The K-fold cross-validation technique uses part of the available data to fit the model and a different part to test it. The data is split into K pieces of approximately equal size. Figure 4.1 illustrates a scenario in which $K = 5$. For the k^{th} part, the model is fitted to the other $K - 1$ parts of the data and calculates the prediction error of the fitted model when predicting the k^{th} part of the data. This is done for $k = 1, 2, ..., K$ and the K estimates of prediction errors are combined.

4.1.2 Bagging

Another useful technique when less ground-truth data are available is bagging, which is a general-purpose procedure for reducing the variance of a statistical learning method. It basically consists of taking many training sets from the population, training a separate prediction model using each training set, and then averaging the resulting predictions. In other words, the bagging comprises computing $\hat{f}^1(x)$, $\hat{f}^2(x)$, ..., $\hat{f}^B(x)$ using B separate training sets, and average them in order to obtain a single low-variance statistical learning model, given by $\hat{f}_{\text{avg}}(x) = \frac{1}{B}\sum_{b=1}^{B}\hat{f}^b(x)$ [66]. This architecture is illustrated in Figure 4.2.

Bagging is particularly beneficial for decision trees as they are prone to high variance. In this technique, B regression trees are created using B bootstrap training sets and the predictions are averaged. These trees are grown deeply without clipping, resulting in high variance but low bias for each individual tree. By averaging these B trees, the variance is effectively reduced. Bagging has been shown to significantly improve accuracy by combining hundreds or even thousands of trees into a single uniform procedure.

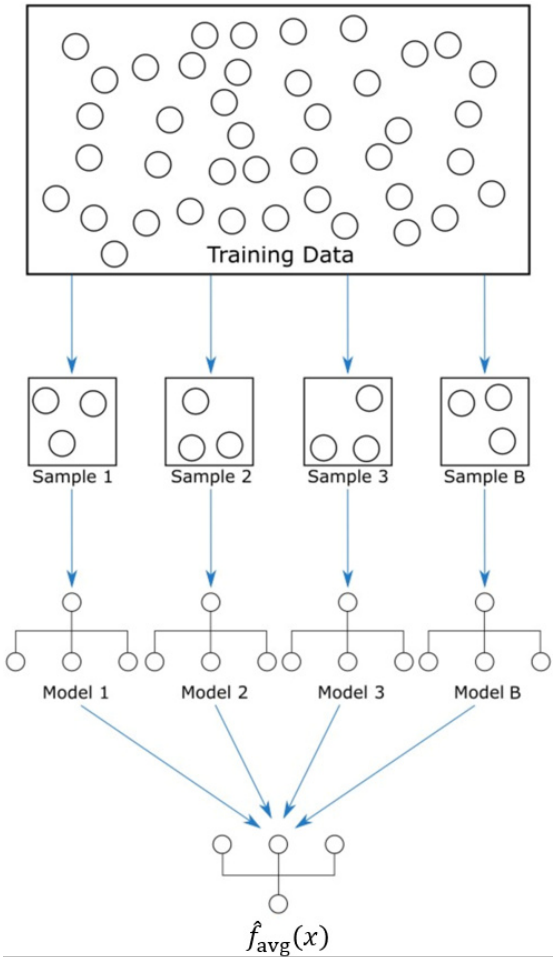

Figure 4.2: Scenario example illustrating the Bagging technique.

4.1.3 Support Vector Regression

A Support Vector Machine (SVM) is a powerful and versatile machine learning model, capable of performing linear or nonlinear classification, regression, and even outlier detection. This technique is an extension of the support vector classifier that results from enlarging the feature space using kernels, implicitly mapping their inputs into high-dimensional feature spaces [66]. The SVM can also be adapted to solve regression problems, in which case it is called Support Vector Regression (SVR). Essentially, it provides the flexibility to define how much error is acceptable in the model and it will find an appropriate line (or hyperplane in higher dimensions) to fit the data. In this study, the Radial Basis Function (RBF) kernel was adopted, which can be described by:

$$K(\boldsymbol{x}, \boldsymbol{x}') = e^{-\gamma\|\boldsymbol{x}-\boldsymbol{x}'\|} , \tag{4.1}$$

where $\|\boldsymbol{x} - \boldsymbol{x}'\|$ is the squared Euclidean distance between two feature vectors ($\boldsymbol{x}$ and $\boldsymbol{x}'$) and γ is a coefficient that defines how much influence a single training example has [55]. For this study, γ was set to $1/(n_{\text{features}}\sigma^2)$, in which σ^2 stands for the variance and n_{features} is the number of features in the model. Moreover, another important parameter for the SVR model is the regularisation parameter C, which is responsible for avoiding possible overfitting of the model. After testing several values, this parameter was set to $C = 1$ for this study.

4.1.4 Decision Trees

Decision Trees can also be applied to both regression and classification problems. Tree-based methods partition the feature space into a set of rectangles and then fit a simple model to each one. They are conceptually simple yet powerful. However, since isolated decision trees have a high variance, they typically are not competitive with the best-supervised learning approaches. For this reason, as already mentioned in section 4.1.2, decision trees are the ideal candidates for bagging [66], whose main idea is to average many noisy but relatively unbiased models, and therefore, reduce the variance.

4.1.5 Random Forest Regression

Random forest is known as an ensemble machine learning technique that involves the creation of hundreds of decision tree models. Essentially, the random forest algorithm takes advantage of the bagging technique, constructing multiples of individual decision trees for each sample and averaging the results, generating a final output with reduced variance. This way, it is possible to capture complex interaction structures in the data, and if grown sufficiently deep, have relatively low bias [55, 66]. However, to prevent the trees from being too deep and to avoid overfitting, the maximum depth for the Random Forest Regression (RFR) model was set to 5. Moreover, another relevant parameter in this model is the criterion (loss function) to be used during the training [66]. This parameter is responsible for measuring the quality of a split. For this work, the Mean Squared Error (MSE) was chosen, which is equal to variance reduction as a feature selection criterion.

4.1.6 Artificial Neural Network

The Artificial Neural Network (ANN), which applies both for regression and classification problems, is often represented by a network diagram as shown in Figure 4.3. The

basic idea behind this model is to extract linear combinations of the inputs as derived features and then model the target as a non-linear function of these resulting features [60]. For regression models, normally $K = 1$ and there is only one output unit Y_1 at the top. Derived features Z_m are created from linear combinations of the inputs X, and then the target Y_k is modelled as a function of linear combinations of the Z_m, as given by [66]:

$$\begin{aligned} Z_m &= \sigma\left(\alpha_{0m} + \alpha_m^T X\right),\ m = 1, ..., M, \\ T_k &= \beta_{0k} + \beta_k^T Z,\ k = 1, ..., K, \\ f_k\left(X\right) &= g_k\left(T\right),\ k = 1, ..., K \end{aligned} \tag{4.2}$$

where $Z = (Z_1, Z_2, ..., Z_M)$ represents the vector of derived features also known as hidden units, $T = (T_1, T_2, \dots, T_K)$ represents the vector of outputs of the hidden layer, and Y denotes the target variable. In the context of this neural network, Y typically comprises either the predicted values in regression tasks or the class probabilities in classification tasks. α_m and β_k denote the weights for the inputs X and for the hidden layers, respectively. The activation function $\sigma(v)$ is usually chosen to be the sigmoid function $\sigma(v) = 1/(1 + e^{-v})$ [55, 66]. In addition to the sigmoid function, there are also other activation functions broadly used in deep learning, such as logistic sigmoid, hyperbolic tangent (tanh), rectified linear units (ReLU), exponential linear unit (ELU), and scaled exponential linear unit (SELU) [60]. Finally, the output function $g_k(T)$ facilitates the final transformation of the hidden layer outputs T into the predicted values for the target variable Y. For regression problems, usually, the identity function $g_k(T) = T_k$ is adopted.

After testing several ANN architectures, as well as comparing the performance of different activation functions, the final architecture for this model was chosen, as shown in Figure 4.4. The final model is a Multi-Layer Perceptron (MLP), containing 2 hidden layers with 30 units each (without considering the bias unit). In addition, the first two layers used the Hyperbolic Tangent activation function, while the last layer used the linear function.

To evaluate the model's performance, the Root Mean Squared Error (RMSE) is used as a reference parameter:

$$\text{RMSE} = \sqrt{\frac{1}{n}\sum_{i=1}^{n}\left(\hat{y}_i - y_i\right)^2}\ . \tag{4.3}$$

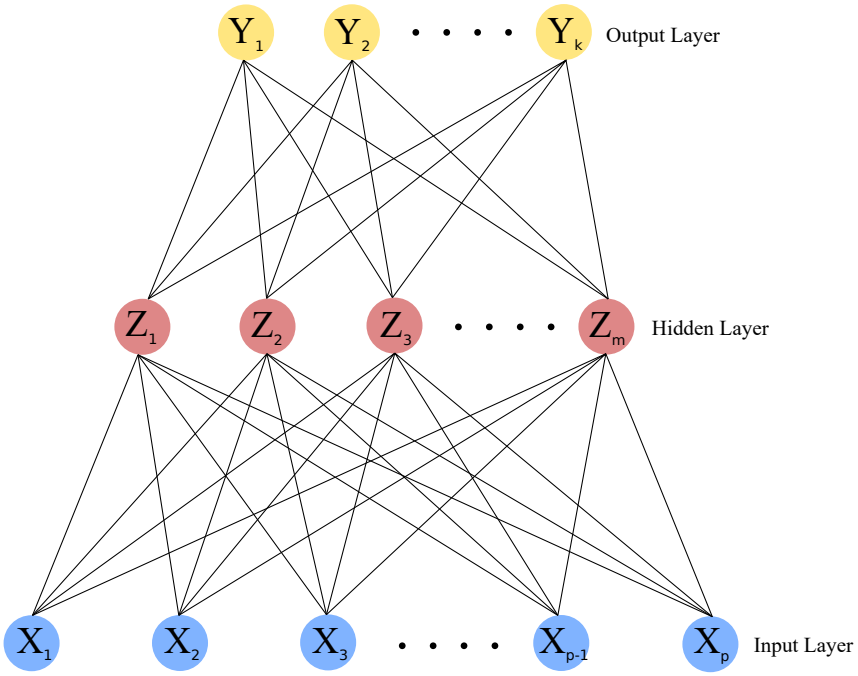

Figure 4.3: Example diagram of a single-hidden-layer neural network.

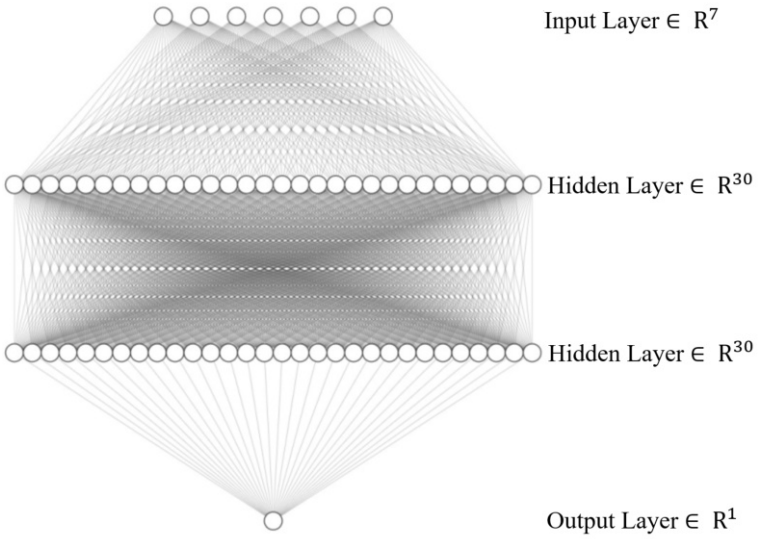

Figure 4.4: Multi-layer perceptron architecture chosen for the Artificial Neural Network model.

4.2 Structure of the Processing Chain

This section outlines the methodology employed for road surface roughness (h_{rms}) estimation using machine learning-based regression models with fully polarimetric airborne X-band F-SAR data. The PolSAR datasets must be pre-processed before they can be used for road surface roughness estimation. As already discussed in the previous chapter (refer to section 3.2.1 on page 38), these steps include the generation of the $\boldsymbol{T}_4$ matrix, the estimation and minimisation of additive noise, speckle filtering with the 3x3 refined Lee speckle filter, radiometric calibration and σ^o image generation.

4.2.1 Features Extraction and Data Preparation

After performing the pre-processing of the F-SAR datasets, the next step involves identifying features that are correlated with the ground-truth surface roughness (GT h_{rms}) values and can be used as inputs to machine learning-based regression models. For this purpose, a variety of disparity parameters, texture parameters, and polarimetric parameters were derived from the pre-processed F-SAR data, as shown in Table 4.1.

The texture parameters are calculated individually for each pixel, using a moving window of size 3 x 3. These features are shown in (4.4) to (4.7), where f_2, f_3, f_4, and f_7 represent contrast, correlation, homogeneity, and dissimilarity of a Gray Level Co-occurrence Matrix (GLCM), respectively [65, 127]. The GLCM, denoted as $\boldsymbol{P}$, is a matrix that represents the frequency of co-occurring intensity values of pixel pairs at a specific spatial relationship within the moving window. Each element $p(i,j)$ in $\boldsymbol{P}$ is computed by normalizing these frequencies to form a probability matrix. The parameters (μ_x, μ_y) and (σ_x, σ_y) are the mean and standard deviation of the marginal probability matrices obtained by summing the rows and columns of $\boldsymbol{P}$, respectively. The remaining parameters obtained from the GLCM do not indicate any correlation and are therefore discarded from further analyses.

$$f_2 = \sum_{i,j=0}^{N-1} \left[|i-j|^2 p\left(i,j\right) \right] \tag{4.4}$$

$$f_3 = \frac{\sum_i \sum_j \left(ij\right) p\left(i,j\right) - \mu_x \mu_y}{\sigma_x \sigma_y} \tag{4.5}$$

$$f_4 = \sum_i \sum_j \frac{1}{1+\left(i-j\right)^2} p\left(i,j\right) \tag{4.6}$$

$$f_7 = \sum_i \sum_j |i-j| p\left(i,j\right) \tag{4.7}$$

Table 4.1: List of the features extracted from the pre-processed F-SAR data.

Parameter	Description
σ^o	Calibrated σ^0 images for the HH and VV polarisations
θ	Local incidence angle during data acquisition
f_2 (Contrast)	A measure of local variation
f_3 (Correlation)	A measure of the linear dependency of gray levels of neighboring pixels
f_4 (Homogeneity)	A measure of local homogeneity
f_7 (Dissimilarity)	A measure of local dissimilarity
Mean	Average between neighboring pixels
Standard deviation	Standard deviation between neighboring pixels
Entropy	Measure of the randomness of the scattering
Anisotropy	Relation between the secondary scattering processes
α	Characterizes the scattering mechanism
β	Characterizes the dominant polarization

Besides that, the mean and the standard deviation of a 3 x 3 moving window over the HH and VV amplitude images are considered. At last, the parameters entropy (H), anisotropy (A), α, and β, obtained from the Cloude-Pottier Decomposition [37], are calculated.

In statistics, the two important correlation coefficients often used to measure the correlation between two variables are Pearson and Spearman [66]. Thus, after further analysis of the correlation of these variables, the parameters that do not present a direct correlation (Pearson $|r| \lesssim 0.3$) with the previously measured ground-truth surface roughness (GT h_{rms}) values are discarded. In addition, variables that show a high correlation (Spearman $|\rho| \gtrsim 0.7$) with other remaining variables are also removed, given that multicollinearity can compromise the performance of machine learning algorithms [10].

Likewise, the analysis of the NESZ presented in section 3.1 on page 31, which is a measure of the sensitivity of the SAR system to areas of low radar backscatter, showed that the data derived from the HV & VH channels are highly noisy, given that there is

only a tiny backscatter from these channels. Therefore, the anisotropy, entropy, alpha, and other similar parameters which require the cross-polarisation channels are discarded from further analysis. As a result, the relevant features that are used as input to the machine learning models are shown in Table 4.2.

Table 4.2: List of features selected as input to the machine learning regression models.

Parameter	Description
σ^0	Calibrated σ^0 images for the HH and VV polarisations
θ	Local Incidence angle during data acquisition
Mean	3x3 moving window average between neighbouring pixels of the HH and VV amplitude images
Standard deviation	3x3 moving window standard deviation between neighbouring pixels of the HH and VV amplitude images

Following the features selection, the 11 available F-SAR datasets (see Table A.2 on page 174) are divided into training and test datasets. In particular, 8 datasets are intended for training purposes, while the remaining 3 datasets are used for testing purposes. Subsequently, the features are scaled to ensure that features with different magnitudes do not influence or dominate the trained model. These scaled features are then used to train and test the machine learning-based regression models described in section 4.1 to predict h_{rms} values for the road surfaces. The block diagram of the processing chain used to train the machine learning-based models and to estimate the h_{rms} values is shown in Figure 4.5.

4.3 Experimental Results and Discussion

This section presents the road surface roughness results obtained using the machine learning-based regression models (SVR, RFR and ANN) for the Kaufbeuren, duraBASt and Braunschweig test sites. In the case of the Kaufbeuren test site , these results are compared with both the ground truth surface roughness (GT h_{rms}) values and also with the surface roughness results obtained from the new semi-empirical model. For the duraBASt and Braunschweig test sites, however, the results are compared exclusively with those from the new semi-empirical model, as no ground truth data are available. Further details on these test sites and the collection of ground-truth data are available in Appendix A on page 178.

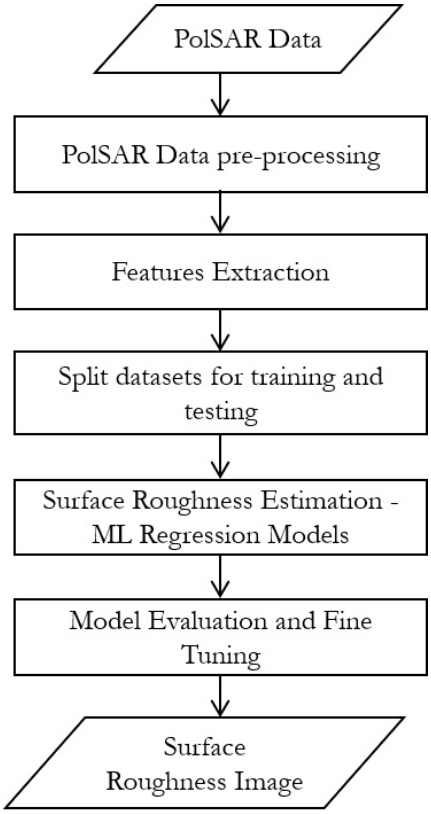

Figure 4.5: Block diagram of the processing chain used to train the machine learning-based models and to estimate the road surface roughness.

4.3.1 Kaufbeuren Test Site

After training the SVR, RFR, and ANN models with the eight training datasets, these models were then applied to the three testing datasets (PS03, PS11, PS14 datasets listed in Table A.2 on page 174) for calculating the road surface roughness (h_{rms}) values. For evaluating the performance of these models, the h_{rms} values were estimated for the GT spots. Then the RMSE between the model estimated h_{rms} and the GT h_{rms} values were calculated for both the training and testing datasets.

Figure 4.6 shows the RMSE values obtained for the SVR, RFR, and ANN models from the three testing datasets. For the PS03 dataset, which has a 45° flight track w.r.t. the Kaufbeuren runway, the RFR model has the lowest RMSE of 0.33 mm. The highest RMSE of 0.37 mm is observed for the SVR model. For the PS11 dataset, which was acquired with a flight track parallel to the runway and also with an incidence angle of approximately 39° at the runway, the RFR model has the lowest RMSE of 0.35 mm and

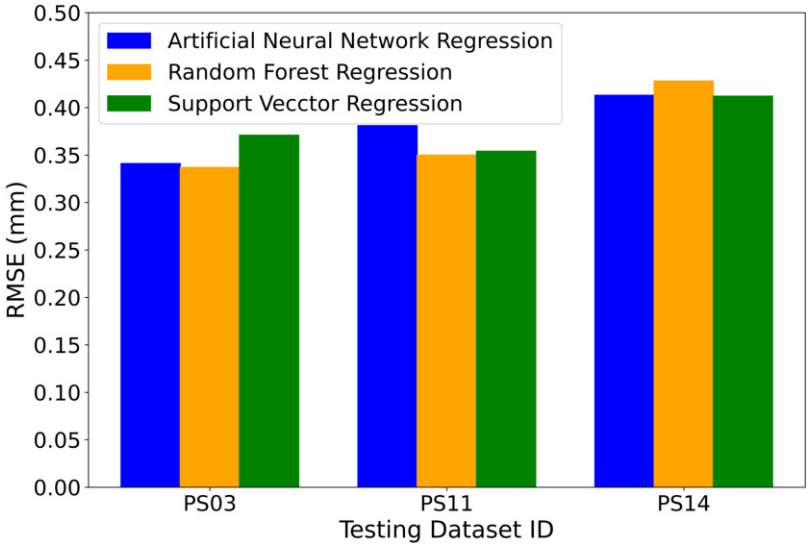

Figure 4.6: RMSE values estimated from the testing datasets for the machine learning models at the Kaufbeuren test site.

the highest RMSE of 0.38 mm is obtained for the ANN model. The PS14 dataset was also acquired with a flight track parallel to the runway and with an incidence angle of approximately 45° at the runway. For this dataset, the lowest RMSE of 0.41 mm was observed for the SVR model and the highest RMSE of 0.43 mm was observed for the RFR model.

From Figure 4.6, it can be seen that the RMSE for the models varies depending on the datasets. However, from all test datasets and models, it can be seen that the lowest RMSE is 0.33 mm and the highest RMSE is 0.43 mm, which is not a large variation. Table 4.3 summarises the mean RMSE values, by taking the mean from multiple datasets for both the training set and the testing set. It can be seen that for the training set, the lowest RMSE is 0.32 mm for the SVR model and the highest RMSE is 0.36 mm for the RFR model. In the case of the testing set, the lowest RMSE of 0.37 mm is obtained for the ANN model and the highest RMSE of 0.39 mm is obtained for both the SVR and RFR models. It can be seen from both Figure 4.6 and Table 4.3 that the RMSE variations for all the models are very low, which shows the consistency of the models in estimating the h_{rms} values.

Figure 4.7 and Figure 4.8 show the surface roughness (h_{rms}) images generated from the PS14 and PS03 test datasets, respectively. As mentioned before, the PS14 dataset was acquired with a flight track parallel to the runway with an incidence angle of approximately 45°, and the PS03 dataset was acquired with a 45° flight track w.r.t. the runway and the incidence angle varies from 29° to 55° from one end of the runway to the other

Table 4.3: Mean RMSE values for the GT spots at the Kaufbeuren test site.

Machine learning models	Mean RMSE training datasets (mm)	Mean RMSE testing datasets (mm)
Artificial Neural Network (ANN)	0.35	0.37
Support Vector Regression (SVR)	0.32	0.39
Random Forest Regression (RFR)	0.36	0.39

(cf. Table A.2 on page 174). Figures 4.7(a) and 4.8(a) were generated using the ANN model, Figures 4.7(b) and 4.8(b) using the SVR model. The RFR model results are shown in Figures 4.7(c) and 4.8(c). It is important to note that in these figures the areas outside the runway, taxiway, and parking space are not valid, but were not cut out since no geocoding was done.

Figure 4.8(d) shows the h_{rms} generated using the new semi-empirical model (refer to section 3.1 on page 31) for the PS03 dataset. In contrast to Figure 4.7 and Figure 4.8(a-c), this image was geocoded and had the irrelevant regions removed. By comparing all the h_{rms} images shown in Figure 4.7 and Figures 4.8(a-c) with Figure 4.8(d), it can be seen that the h_{rms} images generated by the ANN, SVR, and RFR models are matching with the h_{rms} image generated by the new semi-empirical model. In all the images, the asphalt regions appear primarily in blue colour indicating roughness values in the 0.5 to 1.0 mm range. The concrete regions at both ends of the runway appear in yellow colour indicating higher surface roughness in the 1.0 to 1.5 mm range. Also, the concrete areas with repeated cuts on the top end of the runway are appearing in green colour indicating higher roughness (1.5 to 2.0 mm range) compared to the other concrete regions without cuts. This is more evident in the PS03 dataset due to its 45° flight track to the runway which resulted in a higher backscattering from the cuts in the concrete. By further comparing the results with the GE image of the Kaufbeuren test site shown in Figure A.1 on page 170 and also with the information about the GT spots listed in Table A.6 on page 180, it can be observed that the ANN, SVR, and RFR models were able to distinguish the different compositions in the runway structure.

It is interesting to note that some areas of the taxiway, such as the region in the upper right corner in Figure 4.8(d), show colour differences compared to Figures 4.8(a)-(c). This mismatch arises from the h_{rms} values estimated for these regions by the new semi-empirical model, which were slightly less than 0.5 mm, resulting in a purple colour visualisation. In contrast, for the same region, the h_{rms} values estimated by the machine learning-based models were slightly above 0.5 mm, resulting in a blue colour visualisation.

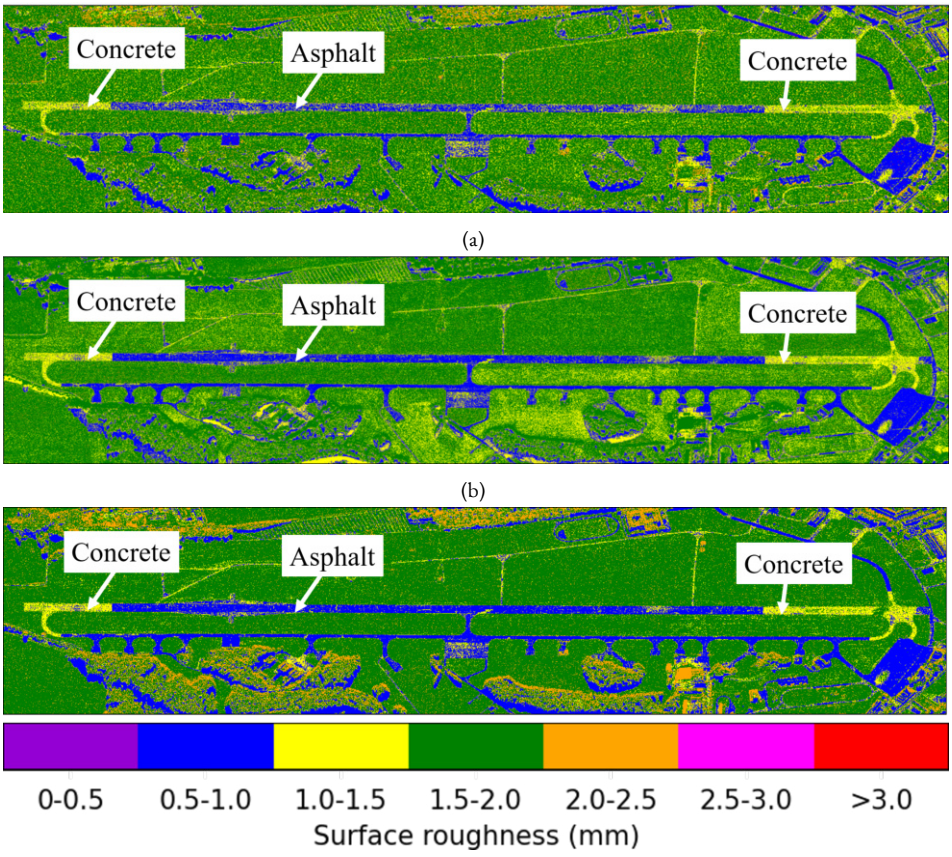

Figure 4.7: Surface roughness images for the Kaufbeuren test site generated using (a) artificial neural network, (b) support vector regression and (c) random forest regression with the PS14 testing dataset.

This discrepancy is attributed to the use of the discrete colour bar for visualisation of the surface roughness results.

Additionally, Table 4.4 lists the h_{rms} values estimated at each GT spot for the different models examined in this study. The obtained surface roughness from this investigation was calculated by taking the average of three test datasets. By comparing the results, it can be seen that the machine learning models were consistent with the new semi-empirical model, displaying similar results. Moreover, among the machine learning models, although the Random Forest Regression did not have the lowest RMSE value, it produced the best visually accurate results. In fact, this can be seen in the surface roughness images (Figure 4.7(c) and Figure 4.8(c), in which this model presented the lowest noise when compared to the others.

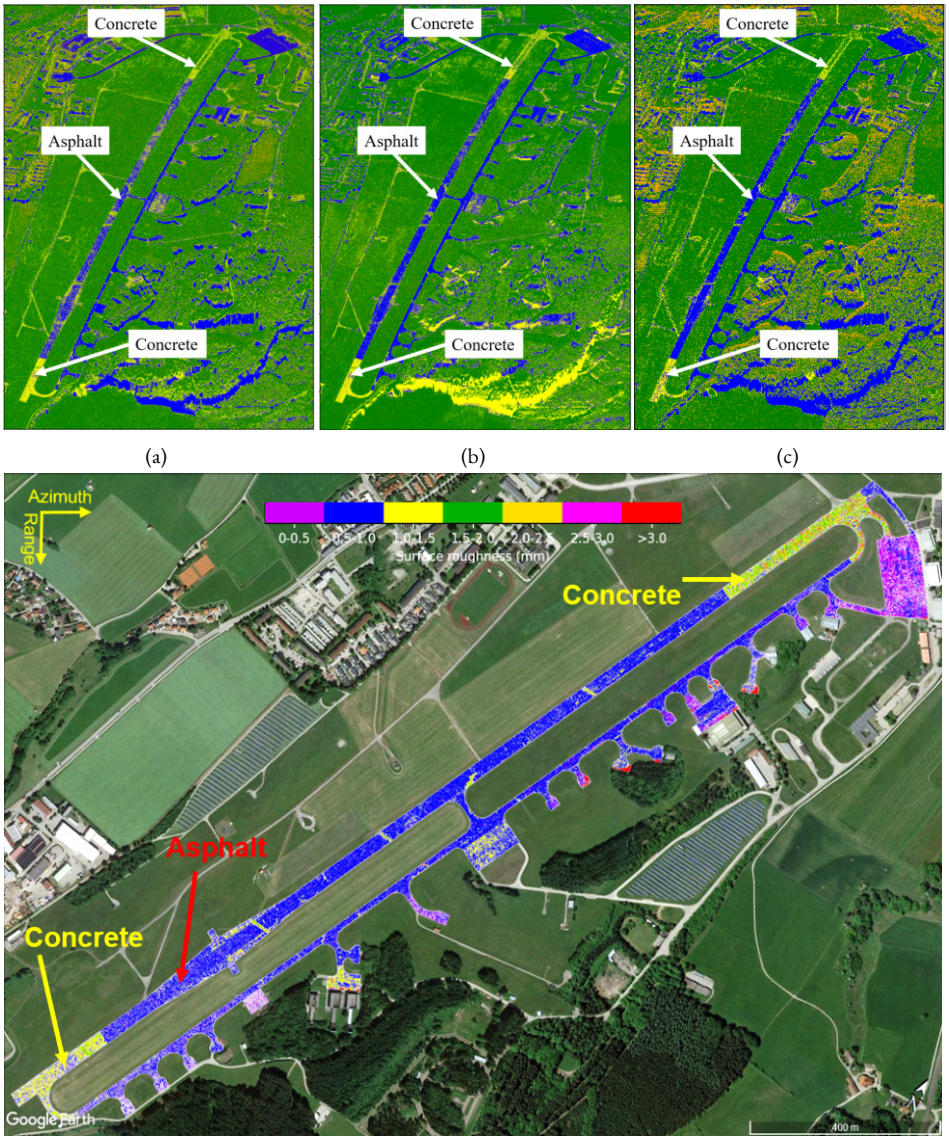

Figure 4.8: Surface roughness images for the Kaufbeuren test site generated using (a) artificial neural network, (b) support vector regression, (c) random forest regression (all in the slant range geometry without geocoding) and (d) new semi-empirical model with the PS03 testing dataset (geocoded and overlaid in GE).

Table 4.4: Comparison of surface roughness results at GT spots by averaging multiple datasets.

GT spot	GT h_{rms} (mm)	New Semi-empirical Model	ANN Model	SVR Model	RFR Model
1	2.36	1.78	1.50	1.42	1.37
2	0.99	1.14	1.09	1.05	1.10
3	0.66	0.60	0.69	0.68	0.72
4	0.88	1.40	1.29	1.32	1.26
5	0.68	0.80	1.00	0.89	0.77
6	0.98	0.79	0.93	0.82	0.79
7	1.09	1.28	1.30	1.31	1.21
8	0.61	0.59	0.65	0.69	0.72
RMSE (mm)		0.299	0.365	0.388	0.389

4.3.2 duraBASt Test Site

Likewise, the h_{rms} images generated using the ANN, SVR, and RFR models for the duraBASt test site are shown in Figure 4.9. The duraBASt test site is highlighted with a white border in Figures 4.9(a)-(d) and with a yellow border in Figure 4.9(e). This test site proved to be much noisier than the previous one. This happens because, unlike the previous test site, there is intense vehicle traffic in the region, which interferes with the data obtained by the SAR system. In the same way, the vegetation close to the highway also generates shadow regions harming performance of the models [111].

Nonetheless, it is still possible to compare the performance of the machine learning-based models with the new semi-empirical model. The h_{rms} images generated using the ANN, SVR, and RFR models are shown in Figures 4.9(a), (b), and (c), respectively. Figure 4.9(d) shows the h_{rms} image generated using the new semi-empirical model. It can be seen that the surface roughness results estimated by the ANN, SVR, and RFR models are matching with the new semi-empirical model result. The smooth areas on the duraBASt test site are appearing in blue colour indicating low surface roughness and the rougher regions are appearing in yellow colour indicating higher values of surface roughness. In addition, a sudden change in surface roughness can be noticed in the nearby highway indicated by the colour change from blue to yellow and green, which is probably due to a different material composition. In fact, also the GE image in Figure

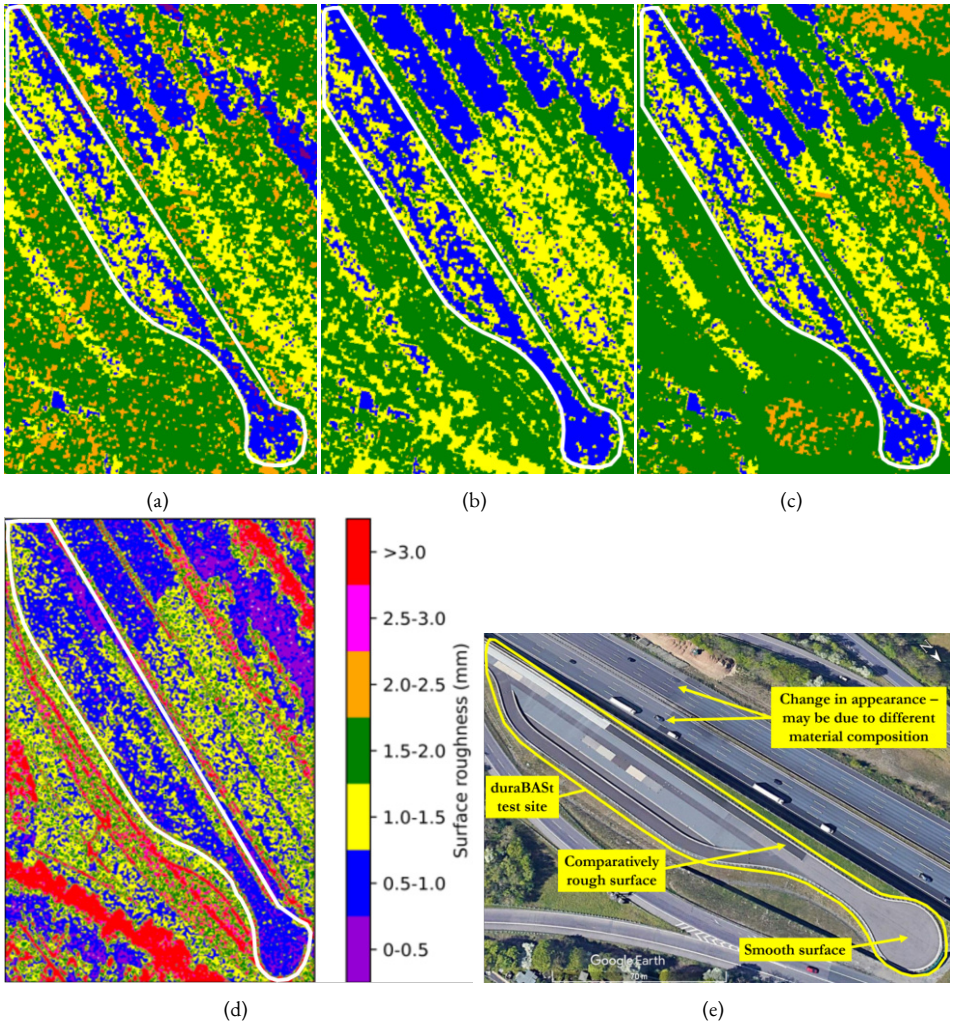

Figure 4.9: Surface roughness results for the duraBASt test site (white and yellow border), with results obtained using (a) artificial neural network, (b) support vector regression, (c) random forest regression, and (d) new semi-empirical models. (e) Corresponding Google-Earth image.

4.9(e) shows a change in the appearance of the road surface in the smooth and rough regions both on the duraBASt test site and on the highway.

It is important to note that the red regions visible outside the road surfaces in Figure 4.9(d) are predominantly displayed in green in Figures 4.9(a)-(c). This suggests a distinct and relatively lower estimation of surface roughness by the machine learning-based models compared to the new semi-empirical model for these regions. The reason behind this is that both the machine learning-based models and the new semi-empirical model were exclusively trained for road surfaces. Consequently, the h_{rms} values estimated by these models beyond the road surfaces can vary between models and are invalid and need to be discarded.

4.3.3 Braunschweig Test Site

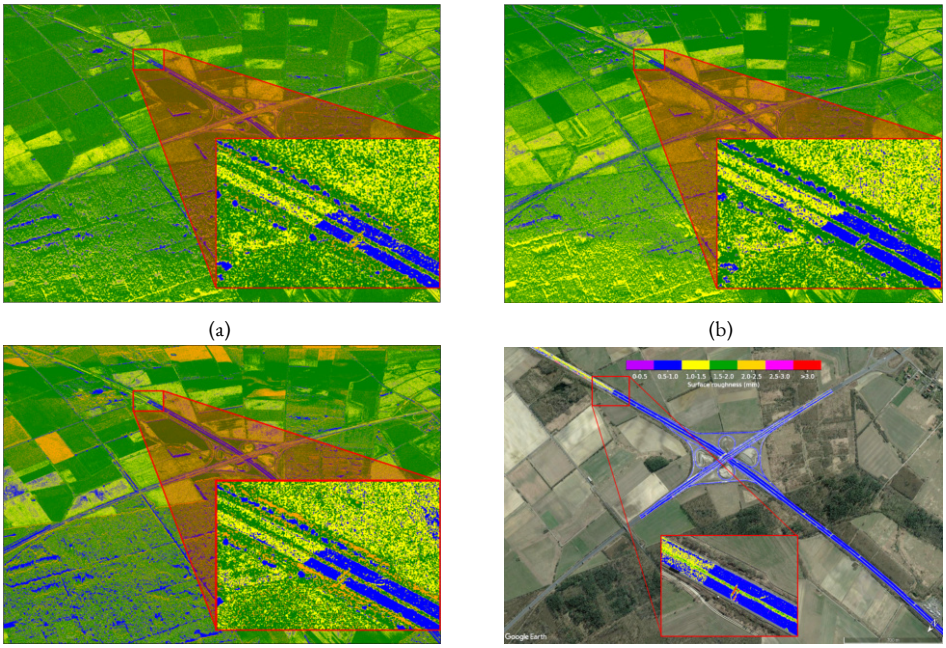

Figure 4.10: Surface roughness image generated for the Wolfsburg motorway intersection at Braunschweig using (a) artificial neural network, (b) support vector regression, (c) random forest regression and (d) new semi-empirical models.

Figures 4.10(a-c) show the surface roughness images generated using the ANN, SVR and RFR models for the Braunschweig test site. Specifically, Figure 4.10(a) shows the h_{rms} image generated with the ANN model, Figure 4.10(b) shows the h_{rms} image from the SVR model, and Figure 4.10(c) illustrates the estimated h_{rms} image from the RFR model.

Notably, most parts of the motorway appear in blue, indicating h_{rms} values in the 0.5 mm to 1.0 mm range. However, in the zoomed view area, a clear transition from blue to yellow can be observed, indicating increased surface roughness in the 1.0 mm to 1.5 mm range. This sharp change indicates a possible variation in road construction materials during a maintenance operation and underlines the ability of the ANN, SVR and RFR models to recognise different road materials with varying roughness. Furthermore, the results of the machine learning model are consistent with the new semi-empirical model, as shown in Figure 4.10(d).

4.4 Chapter Summary

This chapter presented a novel machine learning-based approach for road surface roughness estimation using a fully polarimetric airborne SAR system. For this purpose, three different machine learning models, namely support vector regression (SVR), random forest regression (RFR) and artificial neural network (ANN)-based regression, were investigated. To overcome the challenge of limited ground truth (GT) data for training, bagging and cross-validation techniques were used to prevent overfitting.

Experimental road surface roughness results of the SVR, RFR and ANN models using airborne F-SAR datasets collected over the Kaufbeuren, duraBASt and Braunschweig test sites showed good agreement with both the new semi-empirical model results discussed in chapter 3 and GT h_{rms} data. While all models had similar RMSE values compared to the GT data, the results of the RFR model appeared to be visually superior due to its less noisy appearance.

It is worth noting that the new semi-empirical model still gives slightly better results, and is also more computationally efficient and faster compared to machine learning-based models. However, the performance of the semi-empirical model is limited to the validity conditions assumed during its development. On the other hand, machine learning models can adapt to variations in data and environments. Therefore, the new semi-empirical model can be a good option for road surface roughness estimation when the input data satisfy the model's validity conditions requiring $h_{\text{rms}} < 12.43$ mm for X-band and $\theta > 30^o$, with a preference for incidence angles less than 35° for ensuring high SNR. In other situations, especially when datasets with $\theta < 30^o$ need to be used, machine learning-based models may be more suitable for reliable road surface roughness estimation.

5 Road Surface Roughness Estimation using Spaceborne SAR

5.1 Need for Spaceborne SAR-based Road Condition Monitoring

The chapters 3 and 4 emphasised the potential of airborne SAR systems, particularly the fully polarimetric X-band F-SAR system, for estimating road surface roughness using the new semi-empirical model and machine learning-based regression models. However, airborne SAR systems face constraints such as high operational costs, the need for precise flight planning and limited coverage, which makes them unsuitable for periodic global-scale road surface roughness estimation.

To address these limitations, spaceborne SAR systems emerge as a promising alternative. These systems enable cost-effective, repetitive data acquisition across any global location. In contrast to airborne SAR systems, state-of-the-art spaceborne SAR systems in general need to be operated in spotlight mode for achieving a comparably high spatial resolution as airborne SAR systems, but this generally limits them to a smaller scene size per acquisition. Moreover, the lower SNR of the spaceborne SAR datasets due to the higher platform altitude increases the challenge of utilising spaceborne SAR datasets for low SNR applications such as road roughness estimation. A future high-resolution wide-swath (HRWS) spaceborne SAR system is needed to overcome these limitations.

This chapter explores the potential of high-resolution X-band spaceborne SAR data acquired by the TerraSAR-X (TS-X) satellite of Germany for road surface roughness estimation. The Kaufbeuren and Braunschweig test sites utilised for the airborne SAR-based investigations were also used for this study and the TS-X datasets were acquired over these test sites. Further details about these test sites and an overview of the TS-X system can be found in Appendix A on pages 169 and 175, respectively. The use of spaceborne SAR datasets acquired in X-band allows for a direct comparison of road surface roughness results with those obtained from the airborne X-band F-SAR system discussed in chapters 3 and 4. Parts of the contents discussed in this chapter have already been published in [P6, P7] and also in the master thesis [S1][1].

[1] The doctoral student (Arun Babu) supervised the master student, and the cited master thesis is mainly based on his ideas.

5.2 Selection of Spaceborne SAR Imaging Mode

The TS-X satellite operates in several imaging modes, with higher spatial resolutions available in the staring spotlight (ST), high-resolution spotlight (HS), and stripmap (SM) modes (refer to Table A.4 on page 177). These modes provide different spatial resolutions, with ST offering the highest resolution of approximately 0.24 x 0.60 m (azimuth x range). HS mode offers a spatial resolution of 1.1 x 1.2 m, while SM mode provides a spatial resolution of 3.3 x 1.2 m. Additionally, each mode has different swath coverages, with ST covering approximately 3.7 x 4 km, HS covering 5 x 10 km, and SM covering 50 x 30 km (azimuth x range).

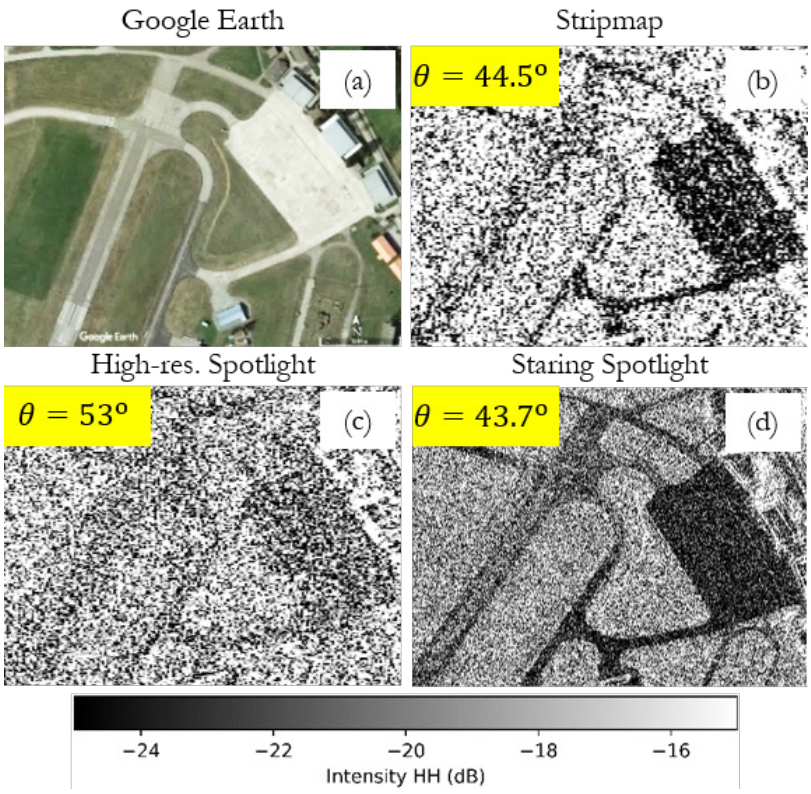

Figure 5.1: Comparison of TS-X imaging modes. (a) GE image of the Kaufbeuren runway. TS-X intensity images in (b) SM, (c) HS, and (d) ST modes.

Figure 5.1(a) illustrates a Google Earth (GE) image depicting a section of the Kaufbeuren runway. Correspondingly, Figures 5.1(b), (c), and (d) showcase TS-X HH polarised intensity images of the same runway segment, captured in SM, HS, and ST imaging modes, respectively. The SM and ST images have a scene centre incidence angle of approximately 44 degrees, while the HS image has a scene centre incidence angle of 53

degrees (an HS mode dataset with a similar incidence angle range to SM and ST images was unavailable from the TS-X archive). Upon comparing the TS-X intensity images with the GE image, it becomes evident that SAR backscatter variations from the runway, attributable to changes in runway construction materials, are distinguishable only in the ST mode intensity image due to its highest spatial resolution. The runway itself is less distinguishable in the SM and HS mode intensity images. The HS mode image appears to be of inferior quality compared to the SM mode image due to its shallower incidence angle of 53 degrees, resulting in a significantly degraded SNR. Consequently, it can be inferred from Figure 5.1 that only TS-X datasets acquired in ST imaging mode are suitable for road surface roughness estimation. Several TS-X ST mode datasets were taken from the archive and also newly acquired for road surface roughness estimation across the Kaufbeuren and Braunschweig test sites, with their details provided in Table A.5 on page 178.

5.3 Structure of the Processing Chain

The methodology adopted to estimate the road surface roughness using the TS-X ST mode datasets is discussed in this section. The block diagram of the processing chain is shown in Figure 5.2.

5.3.1 Radiometric Calibration and Multilooking

The first step of road surface roughness estimation utilising TS-X data involves pre-processing the TS-X ST mode data for using them as input for the surface roughness estimation model. The pre-processing of the data starts by performing the radiometric calibration to generate the calibrated σ^o backscatter image and it is carried out as follows [6]:

$$\sigma^o = (k_s * |\mathrm{DN}|^2 - \mathrm{NEBN}) * \sin\theta \tag{5.1}$$

where k_s is the calibration and processor scaling factor, DN values are the pixel intensity values, NEBN represents the noise equivalent beta nought values and θ is the local incidence angle. The σ^o values are estimated on a pixel-by-pixel basis and the NEBN values, which are a measure of the system noise, are estimated and subtracted at this stage to minimise the additive noise present in the data [6, P6].

The NEBN values for a TS-X dataset can be calculated using the information available in the annotation file delivered with the datasets. Within the annotation file, NEBN is expressed in the form of polynomials, which are scaled with the calibration and processor scaling factor (k_s). These polynomials describe the noise power as a function of range

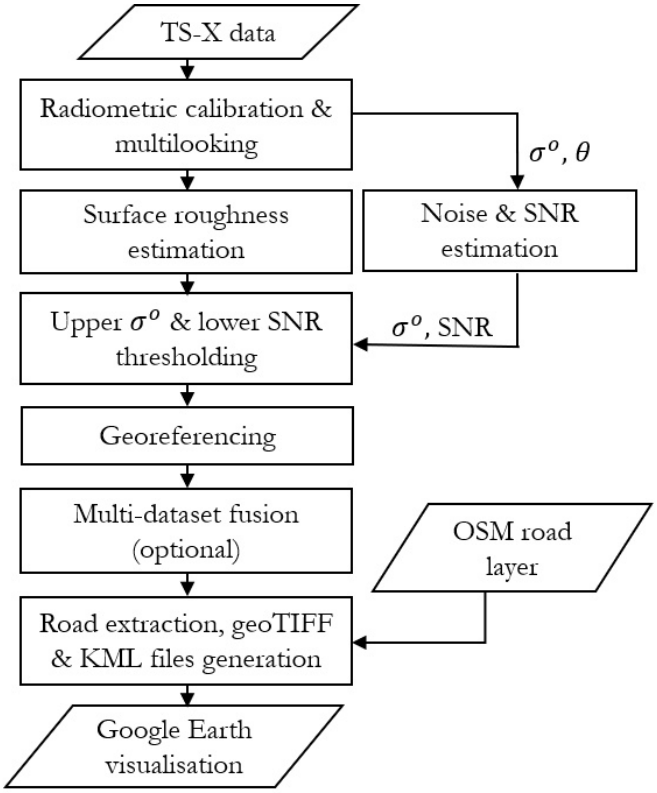

Figure 5.2: Block diagram of the processing chain used for road surface roughness estimation using TS-X ST mode data.

time, spanning from near range to far range, and are determined at various azimuth positions (azimuth time) of the TS-X satellite during data acquisition.

Figure 5.3 illustrates an example where the NEBN is calculated at three azimuth positions: the initial measurement at the beginning of data acquisition, the second measurement midway through data acquisition, and the final measurement at the end of data acquisition. Each noise polynomial for a specific range position at any of the azimuth positions of the TS-X system can be expressed as follows:

$$\mathrm{NEBN} = k_s \cdot \sum_{i=0}^{deg} coeff_i \cdot (\tau - \tau_{\mathrm{ref}})^i \quad , \tau \in \lfloor \tau_{\mathrm{min}}, \tau_{\mathrm{max}} \rfloor \, , \tag{5.2}$$

where deg denotes the degree of the noise polynomial, while $coeff$ stands for the coefficients of the noise polynomial. τ_{ref} represents the reference point in the range direction, whereas τ_{min} and τ_{max} indicate the minimum validity range point (near range) and the

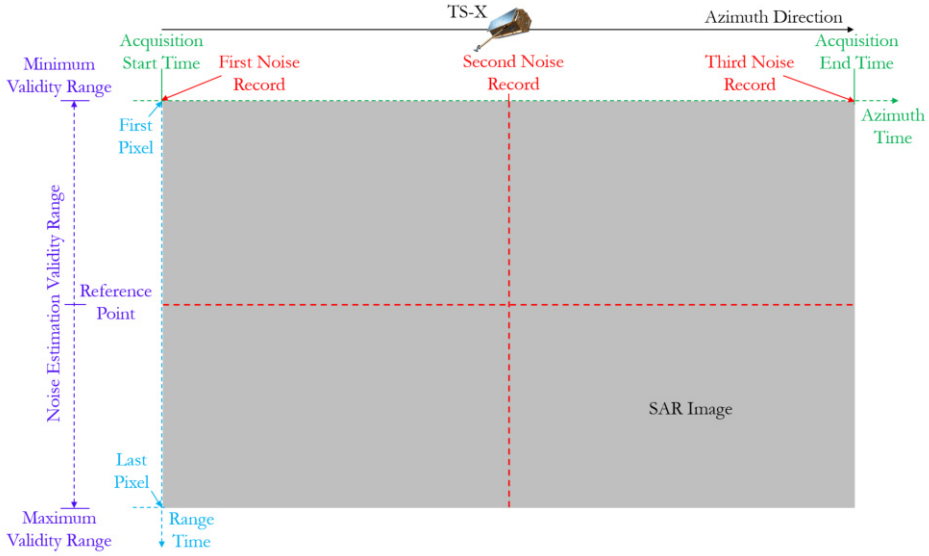

Figure 5.3: Illustration of the noise (NEBN) estimation.

maximum validity range point (far range), respectively, where the NEBN measurement remains valid.

Thus, in the scenario depicted in Figure 5.3, NEBN values are estimated for all pixels in the range direction between the first pixel (τ_{min}) and the last pixel (τ_{max}) for the three azimuth positions. Linear interpolation is used to estimate NEBN values between these three azimuth positions, resulting in an NEBN image with dimensions matching those of the SAR image. Pixel-wise subtraction of these NEBN values is performed during radiometric calibration (as in (5.1)) to generate the σ^o backscatter image with minimised additive noise.

After radiometric calibration and NEBN subtraction, spatial domain multilooking is applied to the σ^o backscatter image. Spatial domain multilooking is used to reduce speckle in the data while increasing the SNR, but at the cost of degradation in spatial resolution. This degradation of spatial resolution in multilooking results from the spatial averaging of neighbouring pixels in both the range and azimuth directions. To achieve this, a sliding window is used to perform spatial averaging over all pixels of the input image, where the window size is determined based on the smallest multilooking factors required in the azimuth and range directions to produce approximately square pixels [29].

Given the different spatial resolutions of the TS-X ST mode datasets in azimuth and range directions (see Table A.4 on page 177), distinct multilooking factors are selected

in these directions for performing the spatial domain multilooking. For example, a sliding window size of 5x1 (azimuth x range) is selected for the ST mode dataset with an incidence angle of 43.7 degrees (cf. Figure 5.1(d)). Following the multilooking, the σ^o image and the local incidence angle (θ) image are provided as inputs to the road surface roughness estimation model.

5.3.2 Adaptation of the New Semi-empirical Model for Spaceborne SAR Case

The new semi-empirical model presented in chapter 3 for road surface roughness using airborne X-band F-SAR datasets has been adapted to make it compatible with the TS-X ST-mode datasets for reliable road surface roughness estimation.

Since the TS-X ST-mode datasets have different characteristics as they are single-polarised with coarser spatial resolution compared to the fully polarimetric F-SAR datasets, a new set of model coefficients (δ, β, and ε) needs to be derived for fitting the new semi-empirical model expressed in (3.2) on page 33. Using TS-X ST mode datasets, these coefficients are determined by a least square-based curve fitting algorithm. This procedure uses TS-X σ^o values for the HH or VV polarisations, corresponding θ values and GT h_{rms} values from the eight GT spots (cf. Table A.6 on page 180).

A unique aspect of this adaptation is the possibility to include the reliable h_{rms} values derived from F-SAR datasets using the original version of the semi-empirical model as additional secondary ground truth surface roughness values. Consequently, the multi-dataset averaged F-SAR h_{rms} values with the lowest RMSE of 0.30 mm (see Figures 3.27 and 3.28 on pages 68 and 69, respectively) were used as secondary GT h_{rms} values.

For the extraction of h_{rms} values from the F-SAR surface roughness image, a random path along the Kaufbeuren runway was plotted on GE, covering both asphalt and concrete surfaces (a portion of this path is shown in Figure 5.4). Approximately 100 locations along this path were selected and the h_{rms} values at these locations were extracted from the geocoded multi-dataset averaged F-SAR surface roughness image covering the entire length of the runway, using the coordinates of these 100 points obtained from GE. Corresponding σ^o values for HH or VV polarisations and θ values for these 100 points were also extracted from TS-X datasets. These values, together with the actual eight GT h_{rms} values and the TS-X σ^o and θ values for these eight GT points, were passed into a least square-based curve fitting algorithm for estimating the model coefficients δ, β and ε. The model coefficients were estimated separately for HH and VV polarisations and their values are listed in Table 5.1. As the scattering assumptions remain unchanged in the adapted model, the validity conditions are the same as those of the original model ($ks < 2.5$ and $\theta > 30^o$) [P6].

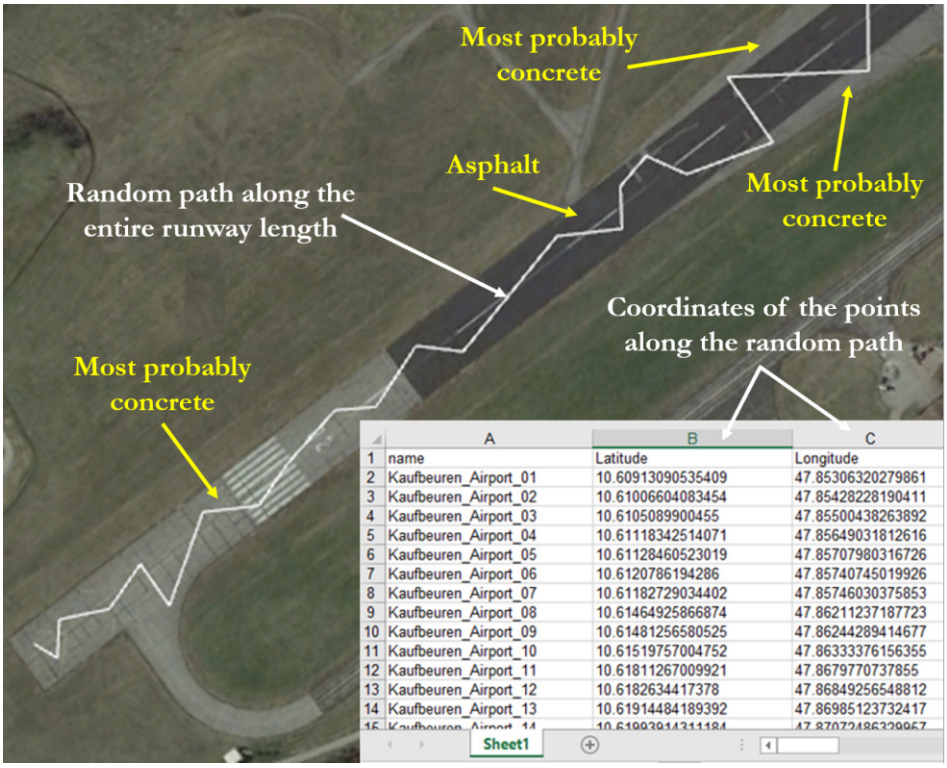

	A	B	C
1	name	Latitude	Longitude
2	Kaufbeuren_Airport_01	10.60913090535409	47.85306320279861
3	Kaufbeuren_Airport_02	10.61006604083454	47.85428228190411
4	Kaufbeuren_Airport_03	10.6105089900455	47.85500438263892
5	Kaufbeuren_Airport_04	10.61118342514071	47.85649031812616
6	Kaufbeuren_Airport_05	10.61128460523019	47.85707980316726
7	Kaufbeuren_Airport_06	10.6120786194286	47.85740745019926
8	Kaufbeuren_Airport_07	10.61182729034402	47.85746030375853
9	Kaufbeuren_Airport_08	10.61464925866874	47.86211237187723
10	Kaufbeuren_Airport_09	10.61481256580525	47.86244289414677
11	Kaufbeuren_Airport_10	10.61519757004752	47.86333376156355
12	Kaufbeuren_Airport_11	10.61811267009921	47.8679770737855
13	Kaufbeuren_Airport_12	10.6182634417378	47.86849256548812
14	Kaufbeuren_Airport_13	10.61914484189392	47.86985123732417

Figure 5.4: A portion of the random path drawn along the Kaufbeuren runway on GE for extracting h_{rms} values from the F-SAR surface roughness image.

Table 5.1: Model coefficients estimated for the TS-X ST mode data.

Model Coefficients	Polarisation	
	HH	VV
δ	0.16373946	0.17887929
β	-0.10682052	-3.95021343
ε	1.99490104	3.38223192

5.3.3 Upper σ^o and Lower SNR Thresholding

Similar to the case of airborne SAR data presented in section 3.2.2 on page 42, the surface roughness (h_{rms}) values obtained from the TS-X datasets using the adapted semi-empirical model need to be upper σ^o and lower SNR thresholded to remove the

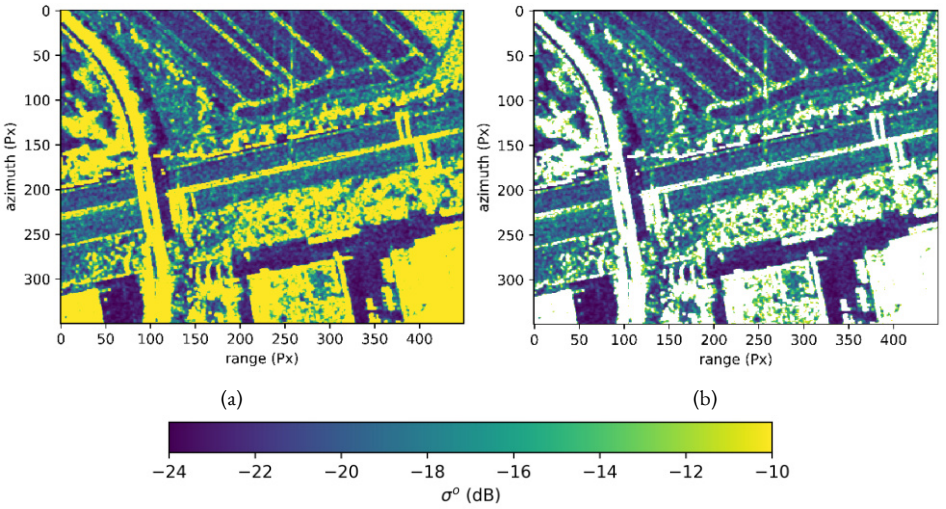

Figure 5.5: TS-X ST σ^o images for a motorway section at the Braunschweig test site. (a) without upper σ^o thresholding and (b) after masking out all the pixels with σ^o values above -10 dB (masked out pixels in white colour).

invalid high h_{rms} values and the unreliable noisy h_{rms} values, respectively, from the final surface roughness image [P4].

In the case of the TS-X data, Figure 5.5(a) shows the σ^o image for a motorway section at the Braunschweig test site. Figure 5.5(b) shows the σ^o image of the same region after masking out pixels with σ^o values higher than -10 dB. A comparison between these two figures shows that all pixels of the road surface have σ^o values below -10 dB. Conversely, σ^o values above -10 dB on the road surface come from strong backscatter sources such as overhead signboards and flyover walls that are not related to the road surface. Consequently, during the upper σ^o thresholding process, all h_{rms} pixels corresponding to σ^o values above -10 dB are masked from the final h_{rms} image, effectively removing high and invalid h_{rms} estimates [P6].

In order to perform the lower SNR thresholding, the SNR of the TS-X datasets must first be estimated. The SNR estimation procedure for the TS-X datasets is as follows [51]:

$$\text{SNR} = \frac{\sigma^o - \text{NESZ}}{\text{NESZ}}, \tag{5.3}$$

where NESZ represents the noise equivalent sigma zero, and it can be estimated from the available noise equivalent beta nought (NEBN) values as $\text{NESZ} = \text{NEBN} \cdot \sin\theta$ [6].

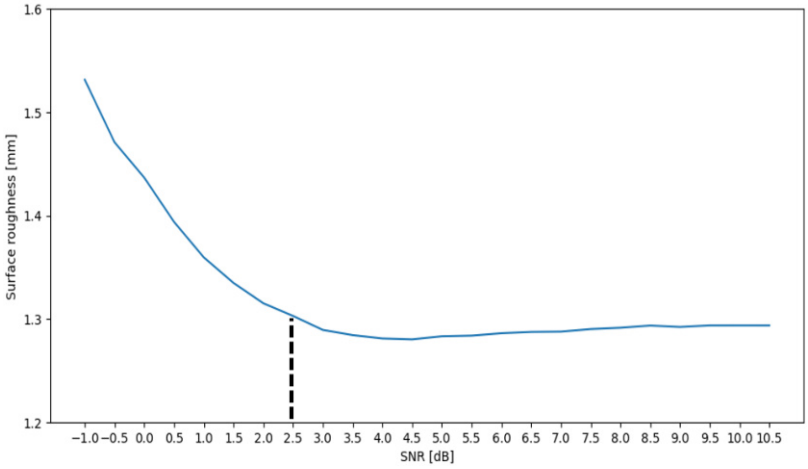

Figure 5.6: Surface roughness (h_{rms}) vs. SNR plot for lower SNR threshold estimation.

After estimating the SNR of the TS-X dataset, an area on the Kaufbeuren runway with high SNR was selected. Starting from this current SNR value, the SNR was then reduced by gradually adding random Gaussian noise to the data. For each SNR level, the h_{rms} value was also calculated and an SNR vs. h_{rms} plot was created.

Figure 5.6 shows the h_{rms} vs. SNR plot. From the plot, it can be seen that the SNR has been varied from the original value of 10.5 dB down to -1 dB. The h_{rms} value remains almost stable at 1.3 mm until the SNR reaches a lower value of 2.5 dB. Below the SNR value of 2.5 dB, a steep increase in h_{rms} is observed. Based on this observation, all pixels with SNR below 2.5 dB were masked out from the final surface roughness image to improve the credibility of the results.

5.3.4 Geocoding, Multi-dataset Fusion, Road Extraction and Google Earth Visualisation

After implementing the upper σ^o and lower SNR thresholding on the h_{rms} values estimated from the TS-X datasets, the subsequent post-processing steps, including geocoding, multi-dataset fusion, road extraction and Google Earth (GE) visualisation, were performed in a manner consistent with the procedures applied for the airborne F-SAR case (as described in section 3.2.2 on page 42).

In the geocoding step, the surface roughness images derived from the TS-X datasets are re-projected from the slant-range coordinate system to the geographic coordinate system. Subsequently, the fusion of multiple datasets is performed using either the highest SNR method or the multi-dataset averaging method (cf. section 3.2.2 on page 42), which is

applied only when surface roughness images from multiple TS-X datasets with different acquisition geometries and incidence angles are available.

In the final step, road sections are extracted from the resulting h_{rms} images using the Open Street Map (OSM) road layer (cf. section 3.2.2 on page 47). Keyhole Markup Language (KML) files are created to enable the visualisation of road surface roughness images in GE. In addition, GeoTIFF images are created to ensure compatibility for various investigations and visualisations with state-of-the-art GIS (Geographic Information System) software (cf. Figure 5.13) [P6].

5.4 Experimental Results and Discussion

This section presents the experimental road surface results from the TS-X ST mode datasets for the Kaufbeuren and Braunschweig test sites, which were obtained using the processing chain described in the previous section.

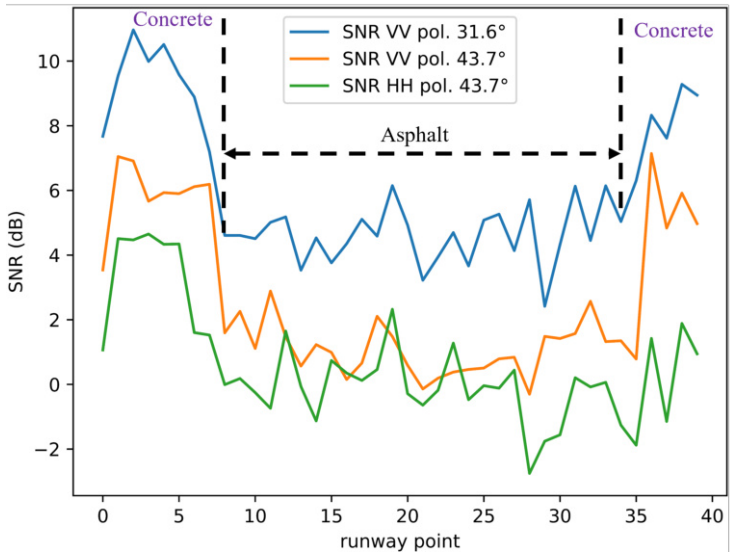

Figure 5.7: SNR plot for the Kaufbeuren runway.

Figure 5.7 shows SNR plots created for the Kaufbeuren runway, showing the SNR values at 40 randomly selected positions along the entire length of the runway. These plots comprise various datasets with different incidence angles and polarisations. The analysis of Figure 5.7 shows that the concrete surface has a higher SNR compared to the asphalt surface. This observation indicates that the concrete surface has a rougher texture, resulting in a stronger backscatter signal. It is noteworthy that the HH polarisation dataset has the lowest SNR, especially in the asphalt regions, making it unsuitable for

accurate road surface roughness estimation. In contrast, the VV polarisation data have a significantly higher SNR, with the VV dataset at an incidence angle of 31.6^o having the highest SNR among the other shown datasets. Consequently, VV polarisation datasets with incidence angles between 30 and 35 degrees are particularly suitable for an accurate road surface roughness TS-X estimation. This selection ensures an SNR of at least 2.5 dB in both concrete and asphalt areas, which is also consistent with the validity conditions of the roughness estimation model, which requires incidence angles greater than 30 degrees (cf. section 3.1 on page 31).

Figure 5.8 presents the surface roughness (h_{rms}) images of a section of the Kaufbeuren runway. After road extraction and KML file creation, the images were overlaid on GE. In Figure 5.8(a), the GE image shows the runway with areas of asphalt, smooth concrete, and rough concrete with repeated cuts. The h_{rms} image in Figure 5.8(b) is estimated using the F-SAR dataset (resolution: approximately 25 x 25 cm). Comparing Figure 5.8(b) with Figure 5.8(a), asphalt areas appear blue indicating low h_{rms} values, while concrete areas appear rougher and are indicated by cyan. Concrete areas with repeated cuts exhibit the highest roughness level, represented by yellow. Figure 5.8(c) displays the h_{rms} image generated using the TS-X HH polarisation dataset. Most pixels from asphalt and smooth concrete areas are masked out due to an SNR lower than the 2.5 dB threshold. In Figure 5.8(d), the shown h_{rms} image was estimated using the TS-X VV polarisation dataset. Figure 5.8(d) has more valid pixels compared to Figure 5.8(c) due to the higher SNR provided by the VV polarisation dataset. Asphalt areas are indicated by blue, while smooth concrete areas appear rougher in cyan. The concrete areas with cuts have the highest roughness level, represented by yellow with a value of approximately 2.25 mm. These findings align with the h_{rms} results from the F-SAR dataset in Figure 5.8(b). Figures 5.8(e) and (f) show the h_{rms} images obtained by fusing multiple datasets using the highest SNR method and the multi-dataset averaging method, respectively. The fusion involves all three VV-polarised TS-X datasets acquired over the Kaufbeuren test site listed in Table A.5 on page 178. In both images, asphalt areas are represented in blue to cyan colours and smooth concrete areas appear entirely in cyan. Figure 5.8(e) exhibits more yellow pixels in the concrete area with cuts compared to Figure 5.8(f), indicating a higher level of surface roughness. In both cases, the results closely agree with the F-SAR results.

Figure 5.9 shows the comparison of h_{rms} plots from TS-X and F-SAR datasets with the GT h_{rms} plot. The black plot shows the GT h_{rms} values for the eight GT spots, while the blue plot shows the estimated h_{rms} values for the GT spots from the F-SAR dataset. Although the blue plot correlates with the GT h_{rms} plot, over- and underestimations are evident for some GT spots. Overall, the plots have an RMSE of 0.30 mm. The green plot represents h_{rms} values estimated using the VV polarised TS-X dataset with an incidence angle of 31.6 degrees, which closely matches the GT h_{rms} plot with an RMSE of 0.32

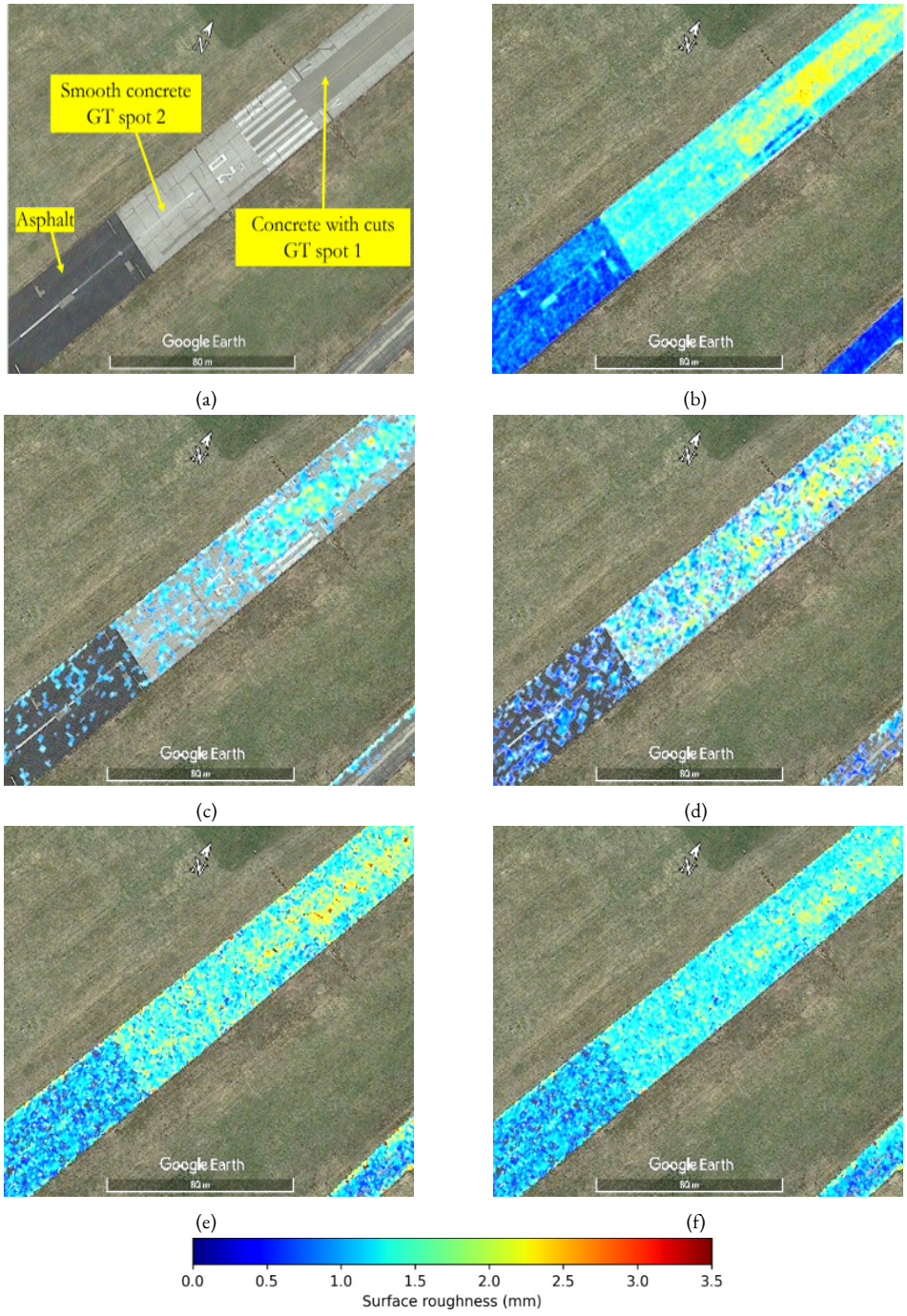

Figure 5.8: Images of the Kaufbeuren runway. (a) GE image. h_{rms} images from (b) F-SAR, (c) TS-X HH pol, (d) TS-X VV pol, multi-dataset fusion using (e) highest SNR method and using (f) multi-dataset averaging method.

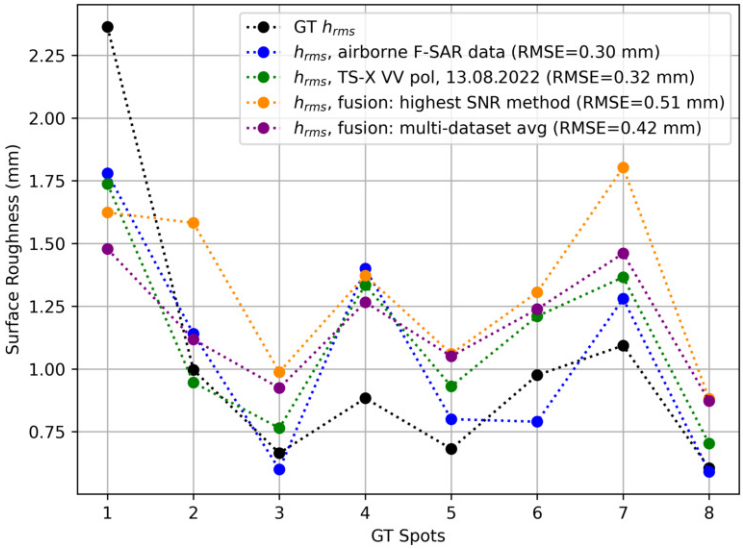

Figure 5.9: Comparison of h_{rms} plots generated using the TS-X data with the GT h_{rms} plot.

mm. It should be noted that this dataset was used to estimate the model coefficients and the F-SAR h_{rms} data with an RMSE of 0.30 mm were used as additional reference data. Therefore, the RMSE of the TS-X roughness data cannot be smaller than 0.30 mm. The orange plot generated by the multi-dataset fusion using the highest SNR method shows an overestimation of the h_{rms} values resulting in the highest RMSE of 0.51 mm, which is probably due to the sensitivity to local backscatter variations. The purple plot, produced by the multi-dataset averaging fusion method, has an RMSE of 0.42 mm with the GT h_{rms} plot. In short, Figure 5.9 indicates that the TS-X VV polarised datasets can reliably estimate the h_{rms} values with a comparable RMSE to the F-SAR and GT data.

The combined h_{rms} images generated for the entire Kaufbeuren test site using the multi-dataset averaging method are shown in Figure 5.10. Figure 5.10(a) shows the h_{rms} image from the F-SAR datasets, while Figure 5.10(b) shows the h_{rms} image from the TS-X datasets. Both images show a higher surface roughness in the concrete areas at both ends of the runway compared to the asphalt areas between them. In addition, the images identify repair works carried out on the runway, especially in the zoomed-in views, where these areas show a significant increase in surface roughness, probably due to the use of materials with different compositions during the maintenance activities. The very small cuts on the runway are most noticeable in Figure 5.10(a), which is due to the very high spatial resolution of the F-SAR datasets (25 cm). Despite the relatively low number of valid pixels in Figure 5.10(b), which is a consequence of the lower SNR of the TS-X datasets compared to Figure 5.10(a), the h_{rms} values estimated with the F-SAR and TS-X datasets are in the similar range, showing the consistency between them.

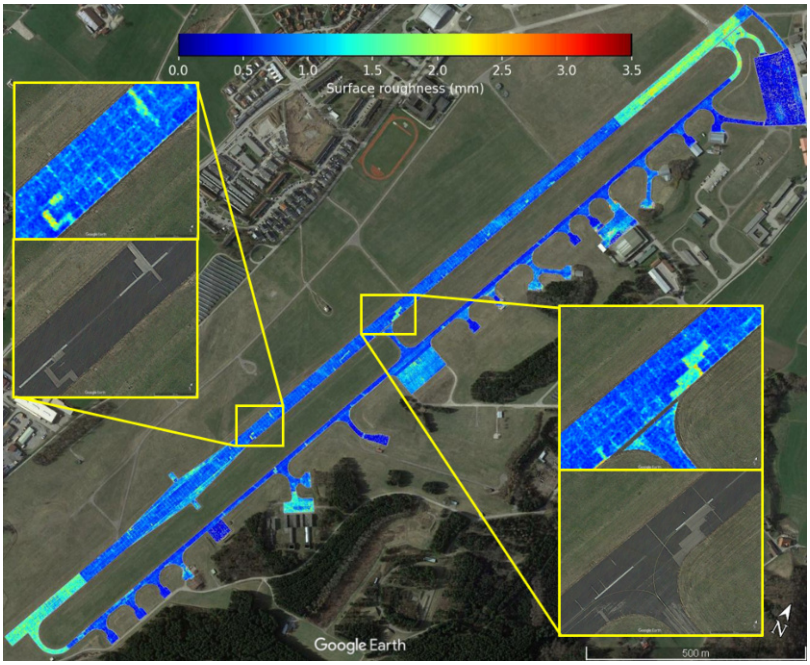

(a)

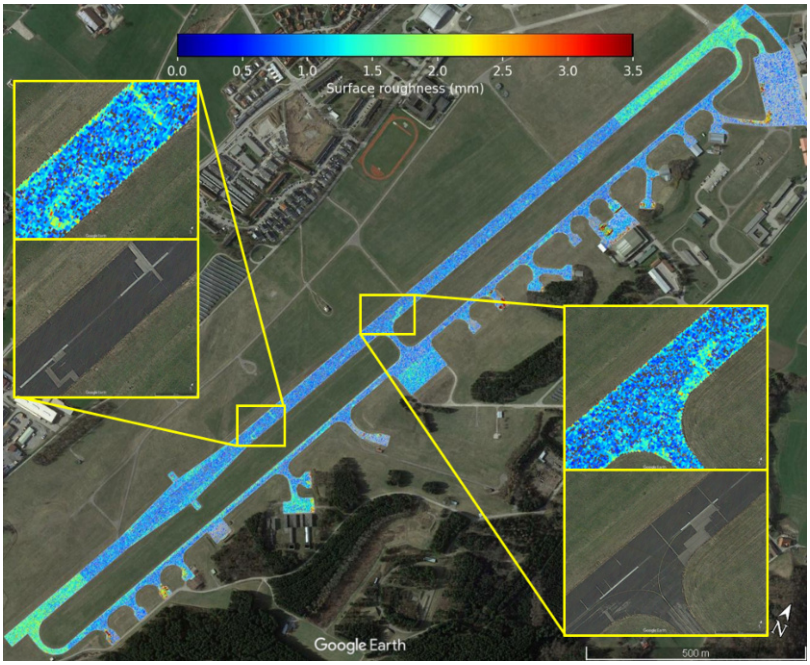

(b)

Figure 5.10: Fused h_{rms} images for the Kaufbeuren test site, generated using the multi-dataset averaging method from (a) F-SAR and (b) TS-X datasets.

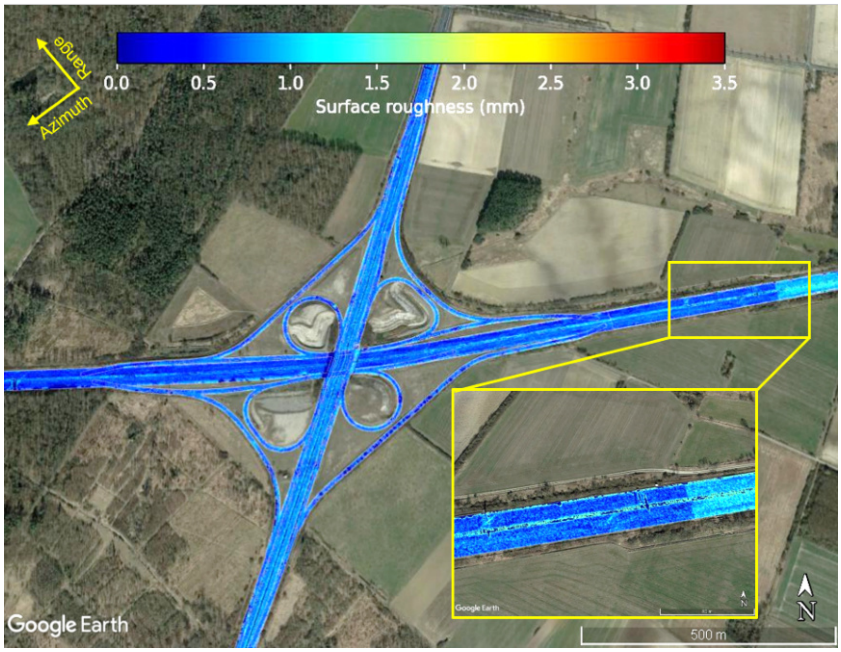

(a)

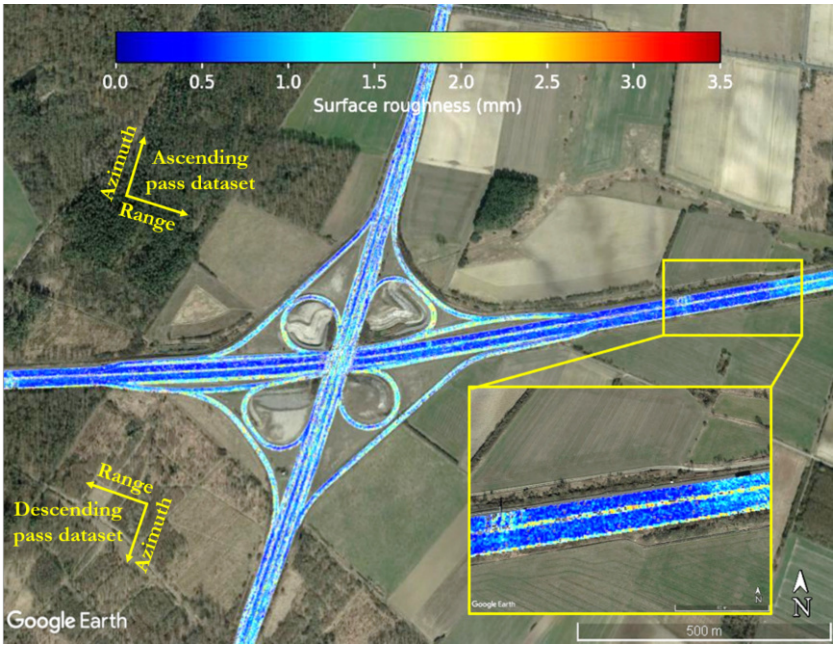

(b)

Figure 5.11: h_{rms} images for the Braunschweig test site, generated using (a) a single F-SAR dataset and (b) by multi-dataset averaging two TS-X datasets with incidence angles of 25.5 and 26.5 degrees. The approximate flight tracks for the TS-X datasets are indicated w.r.t. the geographical north.

Figure 5.11 shows a comparative evaluation of the h_{rms} images generated for the Wolfsburg motorway intersection using F-SAR and TS-X datasets. Figure 5.11(a) shows the h_{rms} image derived from a single F-SAR dataset, while Figure 5.11(b) shows the fused h_{rms} image generated using the multi-dataset averaging method with the two VV-polarised TS-X datasets acquired over the Braunschweig test site listed in Table A.5 on page 178. Both images were generated after performing upper σ^o and lower SNR thresholding to remove invalid and noisy pixels. In both visualisations, the motorway extending in the east-west direction appears predominantly in blue, which indicates a uniform road surface roughness. Towards the eastern end of the motorway, however, a shift to cyan can be seen, indicating a sudden change in the road surface roughness. This could be due to different construction materials or maintenance measures in this region and is consistent with the observations in the GE image shown in Figure A.3 on page 171 and also in the h_{rms} images shown in both Figures 3.23 and 4.10 on pages 64 and 93, respectively. The high level of agreement between the F-SAR and TS-X h_{rms} results for the east-west motorway is evident.

Conversely, the h_{rms} results derived from the TS-X datasets for the north-south motorway show increased noise compared to the F-SAR result. This noise is because the north-south direction coincides with the azimuth direction of the TS-X satellite in its sun-synchronous dusk-dawn orbit with an inclination of 97°, as shown by the yellow-coloured azimuth and range direction arrows for both ascending and descending passes in Figure 5.11(b). The movement of vehicles in the azimuth direction generates disturbances in the SAR image. In contrast, the h_{rms} result obtained from the F-SAR dataset for the north-south motorway remains consistently smooth and matches the surface roughness values observed for the east-west motorway (shown in blue). This is because the north-south motorway is not aligned with the azimuth/flight direction of the F-SAR system during data collection, as indicated by the azimuth and range direction arrows in Figure 5.11(a). To ensure reliable estimates of surface roughness for north-south orientated roads with the TS-X satellite, data acquisition should therefore ideally take place during low-traffic periods. Furthermore, the four loop-shaped and the 45°-oriented narrow motorway link roads exhibit increased and noisy surface roughness values in the TS-X result compared to the F-SAR result. This discrepancy is attributed to two factors. First, the TS-X dataset suffers from slight geocoding offsets, particularly for the four loop roads with elevation changes. These offsets result in high h_{rms} values from areas outside the road boundaries being mapped onto the roads while performing road extraction and GE visualisation. This issue arises from the use of a basic geocoding approach that does not account for elevation variations. Second, for the narrow 45°-oriented roads, double-bounce scattering caused by metallic fences and nearby trees further contributes to increased surface roughness values in the TS-X-derived h_{rms} image.

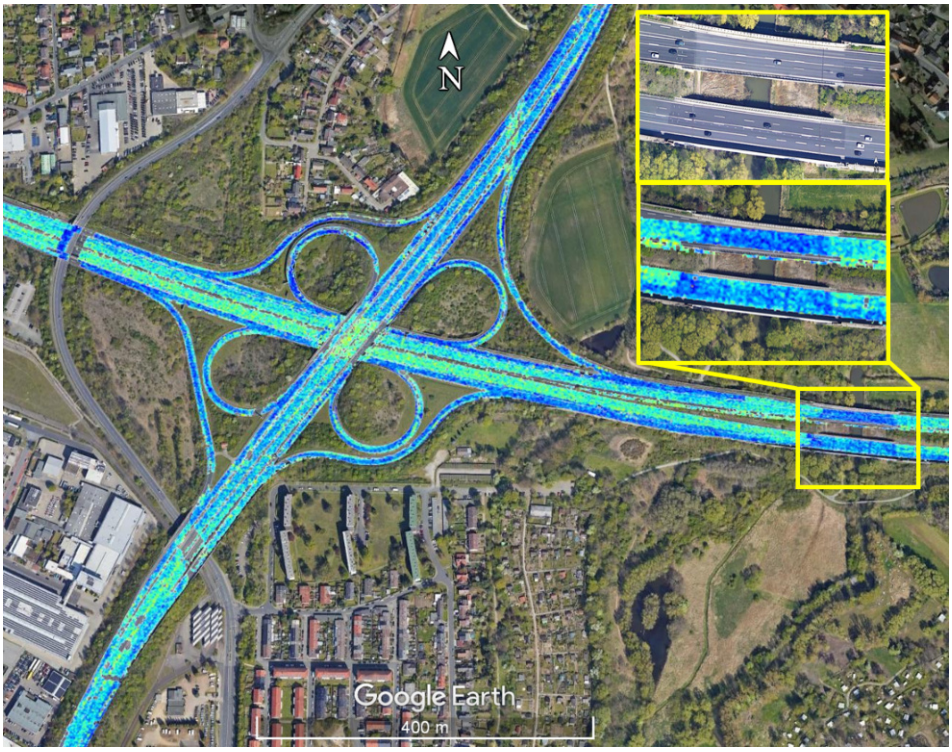

Figure 5.12: h_{rms} image from a TS-X HH polarised dataset for the A2-A391 motorway crossing in Braunschweig.

The road surface roughness image for the A2-A391 motorway crossing in Braunschweig generated using the TS-X HH polarised dataset is shown in Figure 5.12. Although this region is not one of the primary test sites considered for this study, the estimation of road surface roughness for this motorway crossing is conducted to assess the adapted semi-empirical model and processing chain's suitability for estimating road surface roughness of any roads of interest using the TS-X ST mode datasets. Due to the unavailability of VV polarised datasets, a HH polarised dataset is used for this example. The lower SNR thresholding is not applied to this image due to the low SNR of the HH polarised dataset for roads. As a result, the absolute values of h_{rms} are less accurate. However, qualitative comparisons of h_{rms} values can still be made. The south-north highway exhibits a lower h_{rms} (blueish colour) compared to the west-east highway, which shows a higher h_{rms} (primarily cyan). Zooming in on the bridge of the west-east highway reveals a lower h_{rms} (blue) compared to the connecting roads at either end of the bridge (cyan). This suggests a sharp change in h_{rms}, potentially due to the use of materials with lower surface roughness for bridge construction (see GE image in zoomed view).

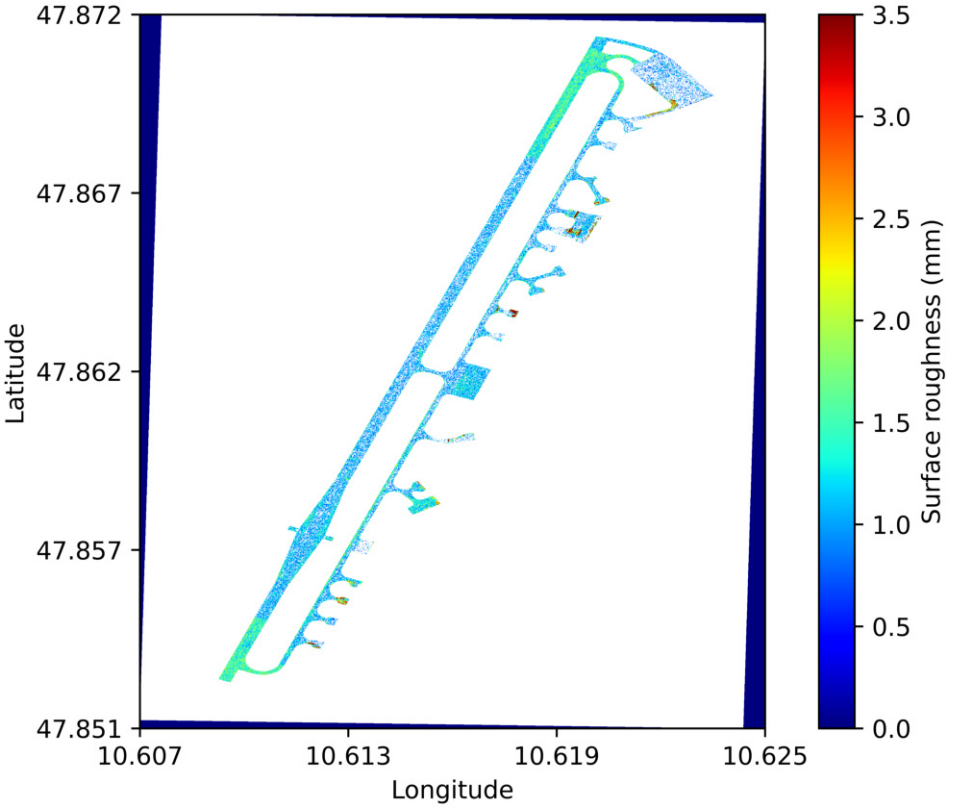

Figure 5.13: Visualisation of the GeoTIFF format multi-dataset averaged surface roughness image generated for the Kaufbeuren test site using the TS-X ST mode datasets.

The multi-dataset averaged surface roughness image in GeoTIFF format for the Kaufbeuren test site generated from the road surface roughness estimation processing chain is visualised in Figure 5.13. As already explained and visualised for the airborne SAR case in chapter 3 on page 63, the GeoTIFF surface roughness image is a single-band representation containing surface roughness values estimated using the adapted semi-empirical model without any scaling applied. Each pixel representing the surface roughness values also has the latitude and longitude information, allowing precise location of surface roughness pixels on the ground (see x and y axes). The availability of road surface roughness results in GeoTIFF format ensures compatibility and integration with advanced GIS software, enhancing its utility for further analysis.

5.5 Chapter Summary

This chapter introduced an innovative approach for assessing the road surface roughness utilising high-resolution spaceborne SAR datasets. Using the TS-X data acquired over the Kaufbeuren and Braunschweig test sites, it was found that the TS-X datasets acquired in Staring Spotlight (ST) mode were necessary for this investigation, as road surfaces were only clearly visible in ST mode. However, this high spatial resolution came at the cost of reduced swath and single polarisation channel operation in the case of the TS-X system. A future high-resolution wide-swath (HRWS) spaceborne SAR system with a bandwidth of up to 1200 MHz and an improved NESZ can have the potential to overcome these limitations and provide a better estimate of road surface roughness. The large bandwidth of 1200 MHz allows for finer spatial resolution, which is crucial for accurately detecting and mapping small-scale features on the road surface.

The staring spotlight TS-X datasets used in the study demonstrated notable sensitivity to surface variations, highlighting their potential for estimating large-scale road surface roughness (h_{rms}). The h_{rms} results obtained using the adapted semi-empirical model exhibited good agreement with both the F-SAR results (refer to chapters 3 and 4 for more details) and GT data. Nevertheless, the low SNR of the TS-X data, especially for the HH-polarised datasets, posed a serious challenge for road roughness estimation.

The most suitable TS-X datasets for road surface roughness estimation were the VV-polarised TS-X datasets acquired in ST mode with incidence angles in the range of 30 to 35 degrees. This choice was based on the fact that the highest possible spatial resolution could be achieved through the use of the ST mode and a steeper incidence angle, and VV polarisation ensured higher SNR, both of which were essential for reliable h_{rms} estimation. Post-processing of the h_{rms} images by applying upper σ^o and lower SNR thresholds is essential to eliminate invalid h_{rms} values. Additionally, the fusion of h_{rms} images generated from multiple datasets with different incidence angles and acquisition geometries can be performed using the multi-dataset averaging technique to improve the quality of the results. Road extraction and Google Earth visualisation approaches can help significantly in the interpretation of the results, as seen for the airborne F-SAR case in chapter 3 on page 59.

6 Cracks Detection and Road Width Estimation using Airborne SAR

This chapter focuses on methods for detecting cracks on road surfaces, estimating their orientation, and determining road width using airborne SAR data. The first section examines how the flight heading angle of the airborne SAR data, acquired along linear flight paths, affects cracks detection due to the oriented line-like nature of cracks. The second section discusses the various methods investigated for cracks detection using airborne SAR data and compares the results. The method developed for the cracks orientation estimation is presented in the third section of this chapter. Additionally, this chapter addresses the estimation of road width based on the observed differences in SAR backscatter or surface roughness values between the road surface and surrounding regions, with sharp changes occurring at the road boundaries. High-resolution airborne X-band SAR datasets acquired with the F-SAR system (cf. Table A.2 on page 174) are used for the investigations presented in this chapter.

6.1 Flight Heading Angle Dependency on Cracks Detection

Since road surface cracks are oriented line-like features, the flight heading angle of the airborne SAR system greatly influences their visibility in the acquired datasets. Figure 6.1 shows an illustration demonstrating the flight heading angle dependency on the backscatter response from a road crack.

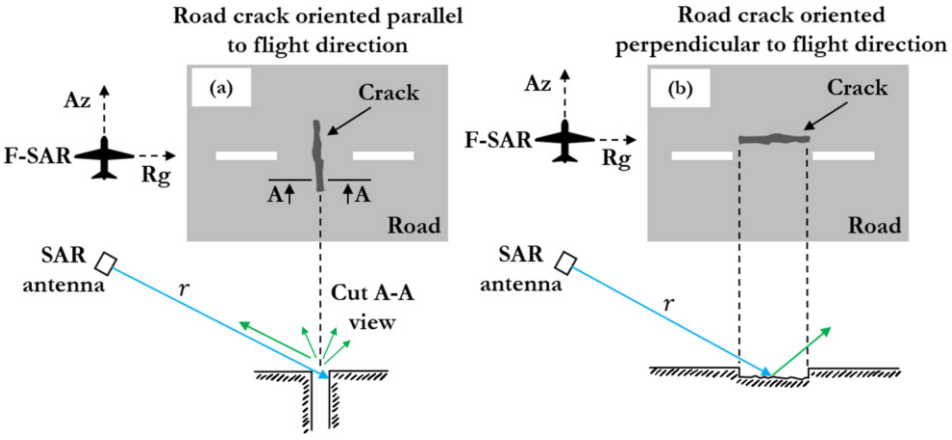

Figure 6.1: Illustration of the flight heading angle dependency on the backscatter response from a road crack.

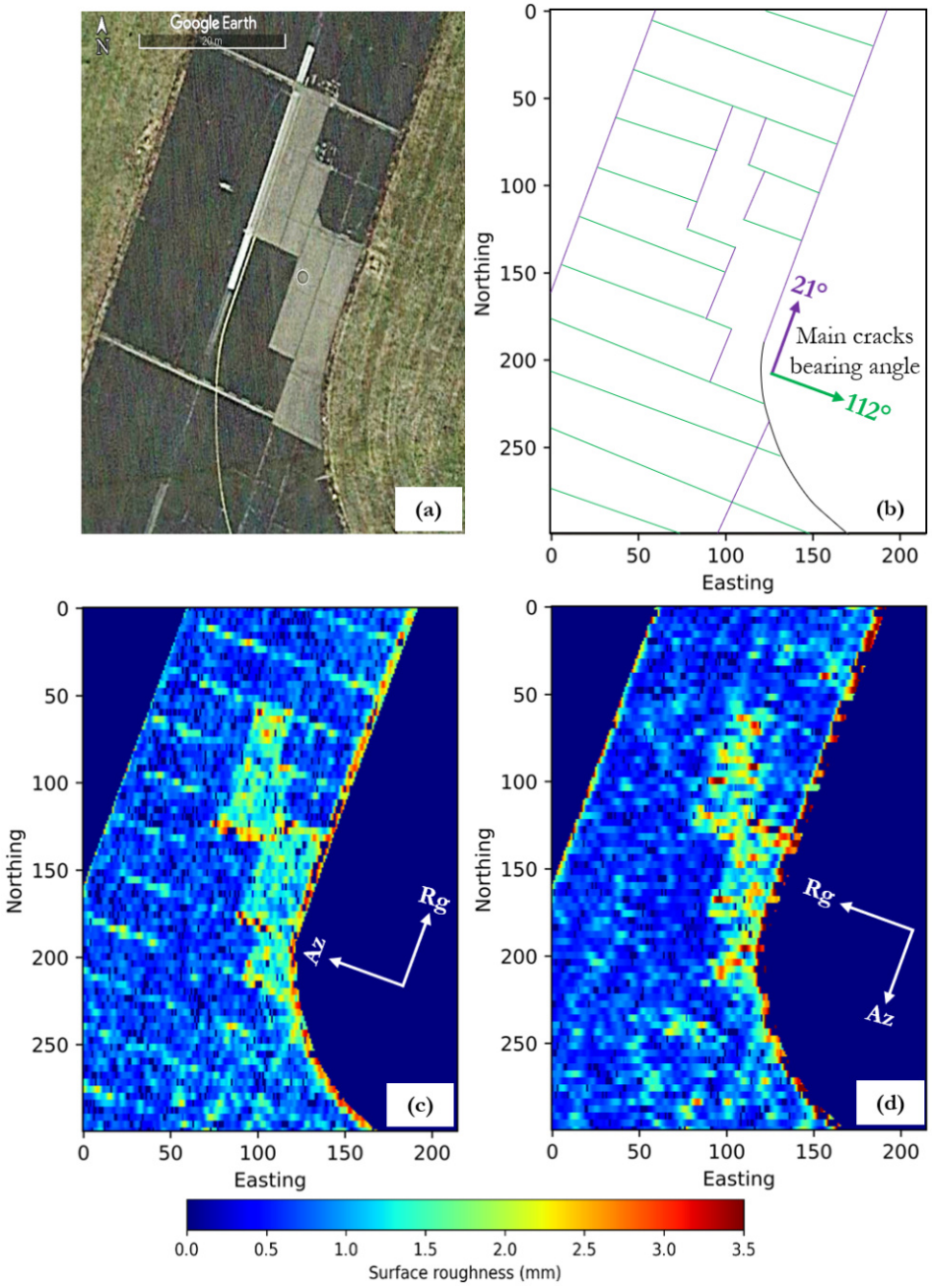

Figure 6.2: Images of a section of the Kaufbeuren runway illustrating how the flight heading angle affects the crack visibility in airborne SAR datasets. (a) GE image. (b) Cracks assumed to be present on the runway. Surface roughness images generated using the (c) PS05 and (d) PS04 F-SAR datasets.

Figure 6.1(a) illustrates the data acquisition geometry for the F-SAR system when a road crack is oriented parallel to the flight direction. In this scenario, the SAR antenna, mounted on the side of the aircraft fuselage, illuminates the entire length of the crack from a direction perpendicular to the crack's orientation, resulting in a maximum backscatter response from the crack edges. Therefore, it is expected that the cracks are most visible in SAR images when the flight path is aligned with their orientation. In contrast, as shown in Figure 6.1(b), if the flight direction is perpendicular or at an oblique angle to the crack, the radar signal cannot illuminate the entire length of the crack. Instead, most of the transmitted signal undergoes specular reflection from the inside of the crack instead of being backscattered from the crack edges. This leads to a reduced backscatter response and diminished visibility of the cracks in SAR images, potentially causing an underestimation of the severity of the cracks.

Figure 6.2(a) presents a Google Earth (GE) image of a section of the Kaufbeuren runway, where small cuts and repair patches are present. Figure 6.2(b) illustrates the main cracks assumed to be present in this section (info. from ground truth data and Google Earth), with purple lines indicating cracks aligned with the runway and green lines indicating cracks perpendicular to it. The green lines mostly represent small cuts on the runway. This study uses the bearing angle measured w.r.t. true north to estimate the orientation of these cracks. The purple and green cracks have bearing angles of approximately 21 degrees and 112 degrees, respectively. Figure 6.2(c) displays the surface roughness (h_{rms}) image for this runway section, generated using the F-SAR PS05 dataset (cf. Table A.2, page 174). Here, the flight path is parallel to the small cuts, resulting in strong backscattering and making these cuts visible as regions of high surface roughness. Conversely, Figure 6.2(d) shows the h_{rms} image from the PS04 dataset (cf. Table A.2, page 174), where the flight path is perpendicular to the small cuts, rendering them invisible. This demonstrates that the flight heading angle significantly affects the detectability of cracks in airborne SAR data, confirming the backscattering assumptions based on crack orientation shown in Figure 6.1. Thus, the flight heading angle is crucial for cracks detection, and the airborne SAR data should be acquired with a flight track parallel to the orientation of the cracks of interest to ensure their visibility.

6.2 Investigation on Cracks Detection Methods

This section presents the potential methods investigated for cracks detection using the airborne F-SAR datasets.

Figure 6.3 presents a generalised block diagram of the cracks detection and orientation estimation methodology. The input for the cracks detection algorithms is either a SAR backscatter image or a surface roughness image generated from the F-SAR data. The output from the cracks detection step serves as the input for the cracks orientation

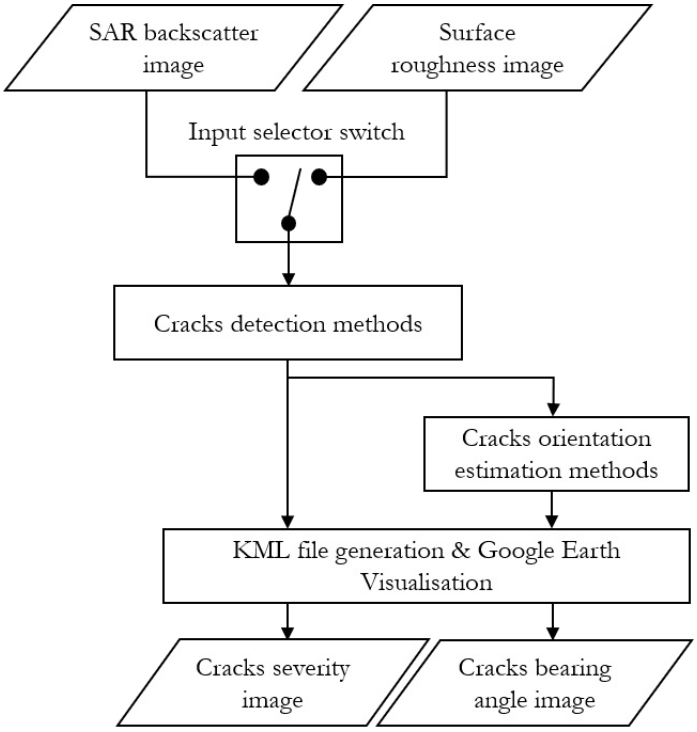

Figure 6.3: Generalised block diagram illustrating the cracks detection and orientation estimation methodology.

estimation method. Finally, KML files are generated to visualise the cracks detection results in terms of crack severity and the cracks orientation results in terms of bearing angle in GE.

The cracks detection methods investigated in the following sub-sections use the Canny edge detector, stationary wavelet transform (SWT), Radon transform, and a combination of adaptive thresholding with the Radon transform. Among these four methods, the best-performing one will then be used in the final processing chain.

6.2.1 Cracks Detection using Canny Edge Detector

One simple and well known method to detect oriented line-like structures in digital images is the edge detector. Among the various edge detectors available, this investigation employs the Canny edge detector [30]. This highly effective algorithm involves several steps: smoothing the image with a Gaussian filter to reduce noise, calculating intensity gradients to identify edges, applying non-maximum suppression to thin the edges, and using double thresholding to differentiate between strong and weak edges. Finally, edge

tracking by hysteresis connects weak edges to strong ones [94]. Known for its accuracy and ability to detect fine details while minimising noise, the Canny edge detector is a promising candidate for detecting road cracks in SAR images.

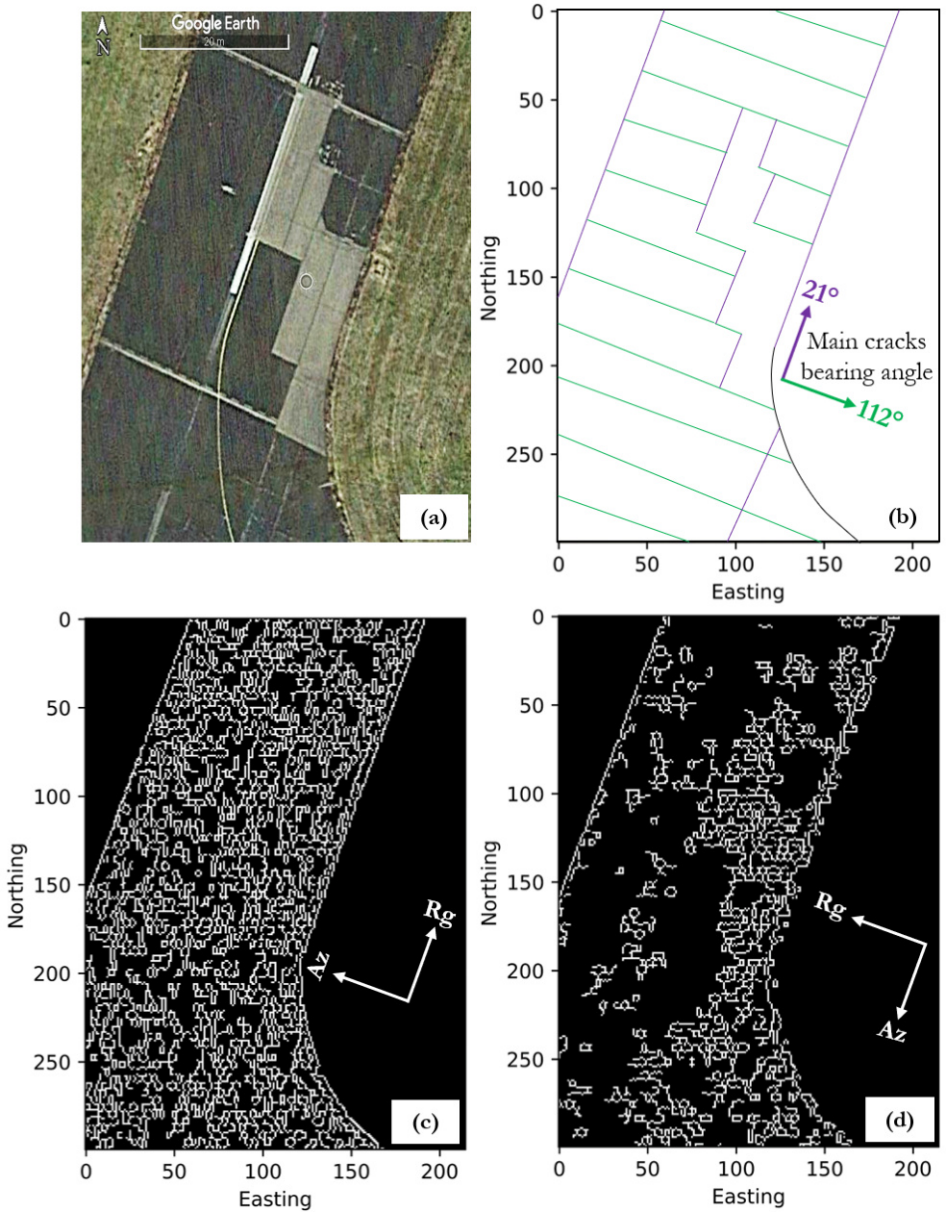

Figure 6.4: Images of a section of the Kaufbeuren runway illustrating the Canny edge detector results. (a) GE image. (b) Assumed cracks image. Canny edge detector outputs generated using the (c) PS05 and (d) PS04 F-SAR datasets.

Figure 6.4 displays the results of the Canny edge detector applied to a section of the Kaufbeuren runway using the h_{rms} images as input. Specifically, Figure 6.4(a) presents a GE image of a section of the Kaufbeuren runway, where small cuts and repair patches are present. Figure 6.4(b) illustrates the main cracks assumed to be present in this section. Figure 6.4(c) shows results from the PS05 dataset, and Figure 6.4(d) shows results from the PS04 dataset. When comparing these results with the GE image and the assumed cracks image of the same region, it is evident that the Canny edge detector fails to identify the cracks on the road surface most likely because of the noisy input data. This suggests that the edge detection methods are not suitable for detecting road cracks from the available X-band airborne F-SAR datasets used for this study, at least not without sophisticated pre-processing of the input data.

6.2.2 Stationary Wavelet Transform-based Cracks Detection

The stationary wavelet transform (SWT) is a powerful signal-processing technique for analyzing signals in both time and frequency domains. It decomposes a signal into various frequency components, each representing a different scale or level of detail [41]. Wavelets, the core concept of SWT, are small, localised functions that can be scaled and shifted to analyse different aspects of a signal, making SWT particularly suitable for detecting localised features [1]. This makes it useful in fields such as image processing [42], signal denoising [80] and pattern recognition [15].

Unlike traditional Fourier analysis, which decomposes signals into sinusoidal basis functions, wavelet analysis uses wavelets that are localised in both time and frequency domains. This allows it to capture transient and non-stationary features [1, 124]. For example, the Haar wavelet, characterised by its step-like waveform, is often used for its simplicity and effectiveness in detecting abrupt changes in signals. Mathematically, the Haar wavelet function ($\psi(t)$) can be represented as follows [8]:

$$\psi(t) = \begin{cases} 1 & \text{for } 0 \leq t < \frac{1}{2} \\ -1 & \text{for } \frac{1}{2} \leq t < 1 \\ 0 & \text{otherwise} \end{cases} \tag{6.1}$$

Other wavelets, such as Daubechies, Coiflets, and Symlets, have unique properties suited for different signal analysis types [126].

In wavelet analysis, the scale determines the level of details captured. Smaller scales capture fine details, while larger scales capture broader features. The decomposition process involves applying low-pass and high-pass filters to the signal, producing approximation (low-frequency) and detail (high-frequency) coefficients. These coefficients represent the signal's energy across different frequency bands and orientations. Approximation

coefficients capture the overall trend, while detail coefficients capture localised details. In image processing applications, these detail coefficients can correspond to different directional features, such as horizontal, vertical, or diagonal edges and can be used for applications like edge detection and texture analysis [41].

One significant advantage of SWT is its effectiveness in noise suppression. By decomposing a signal into multiple scales, noise at different frequencies can be isolated and filtered out without significantly affecting the underlying signal [80].

For cracks detection, the SWT analyses signals from sensors or imaging techniques to identify local discontinuities or structural abnormalities. Decomposing the signal into different scales and frequencies enhances crack visibility while suppressing noise, improving detection accuracy. SWT also extracts orientation information while preserving spatial localisation.

In cracks detection using airborne F-SAR data, the process involves two steps: cracks enhancement and cracks detection. First, SWT is applied to geocoded F-SAR σ^o backscatter images to enhance cracks detectability. Then, a thresholding algorithm is applied to the cracks enhanced SWT output image to detect and classify the cracks.

1. **Cracks Enhancement Procedure:** The block diagram for the cracks enhancement procedure using SWT is shown in Figure 6.5. The input is a geocoded σ^o backscatter image (either co-polar or cross-polar), with non-road regions masked out using OSM road layers (cf. section 3.2.2, page 47). The Haar wavelet, known for detecting abrupt changes, is applied for SWT across three scales. Scale 1 is the most sensitive, focusing on cracks detection and localisation but exhibiting high noise, while Scales 2 and 3 offer better noise reduction with less precise cracks localisation. At each scale, detail coefficients (high-pass filter outputs) labelled H, V, and D are extracted, representing horizontal, vertical, and diagonal features, respectively. An element-wise maximum operation on these coefficients creates 'Max_i' images, consolidating information from all directions. This process is repeated for all scales, resulting in Max_1, Max_2, and Max_3 images. Finally, the element-wise product of these three 'Max_i' images is computed, enhancing cracks, suppressing noise, and eliminating small isolated discontinuities, yielding the geocoded cracks-enhanced (GCE) image.

   Figure 6.6 illustrates the cracks enhancement results for a section of the Kaufbeuren runway. Specifically, Figure 6.6(a) shows the assumed cracks image, Figure 6.6(b) presents the σ^o_{VV} backscatter image used as input, and Figure 6.6(c) displays the GCE image. The σ^o_{VV} backscatter image is preferred for this analysis because it has higher backscatter compared to the HH polarisation and in the case of cross-polarisation (HV and VH) channels, the backscatter values for the road

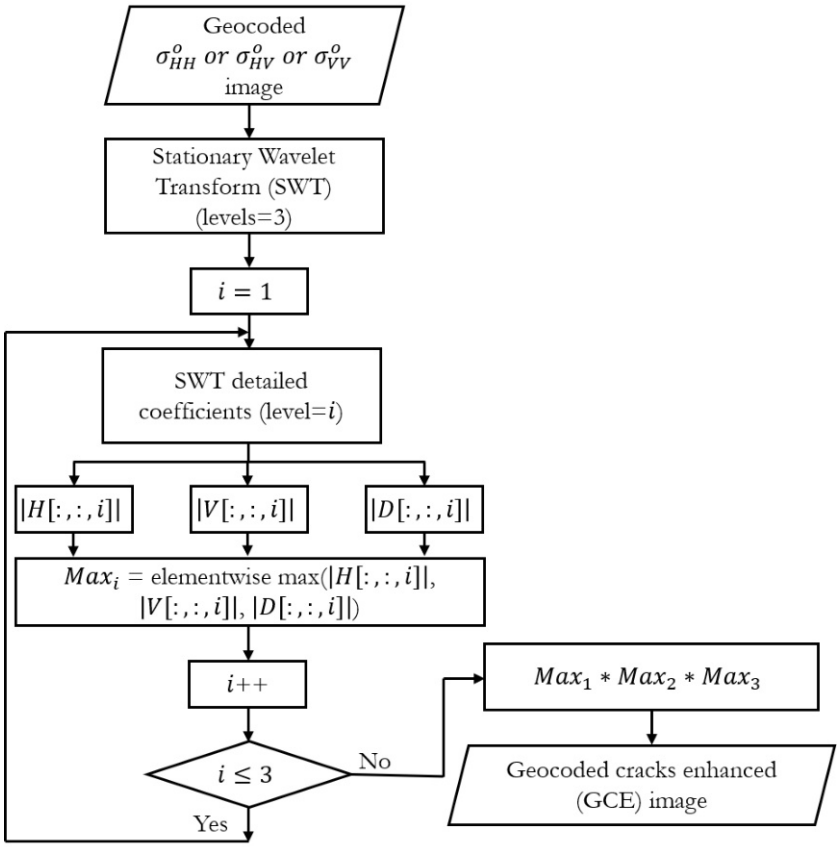

Figure 6.5: Cracks enhancement procedure using the SWT.

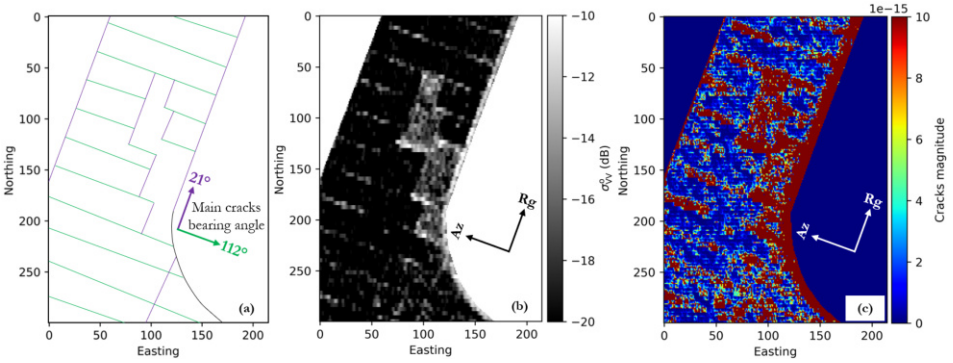

Figure 6.6: Cracks enhancement results for a section of the Kaufbeuren runway generated using the SWT-based method. (a) Assumed cracks image. (b) σ^o_{VV} backscatter image generated from the PS05 F-SAR dataset. (c) Geocoded cracks-enhanced image.

surfaces are lower than the NESZ, making them unsuitable for the cracks detection investigations (see σ^o vs NESZ plot in Figure 3.1 on page 32). Comparing the GCE image with the assumed cracks image and the σ^o_{VV} backscatter image reveals that all cuts visible in the σ^o_{VV} backscatter image are enhanced and more clearly visible in the GCE image. However, a drawback of this approach is that the cracks are spread out in the width direction, resulting from less precise crack localisation at higher scales. Additionally, the rectangular concrete repair patches on the runway, which have higher backscatter values than the surrounding asphalt regions, are also enhanced. This enhancement can falsely lead to these regions being detected as large cracks in subsequent steps.

2. **Cracks Detection and Classification:** The next step involves detecting and classifying cracks using the Otsu automatic thresholding algorithm. This method selects an optimal threshold to distinguish between foreground (cracks) and background (non-cracks) regions by maximising between-class variance and minimising intra-class variance. The Otsu thresholding algorithm is particularly effective for images with bimodal histograms, making it well-suited for tasks such as object detection and segmentation [59]. Figure 6.7 shows the block diagram of the cracks detection and classification methodology.

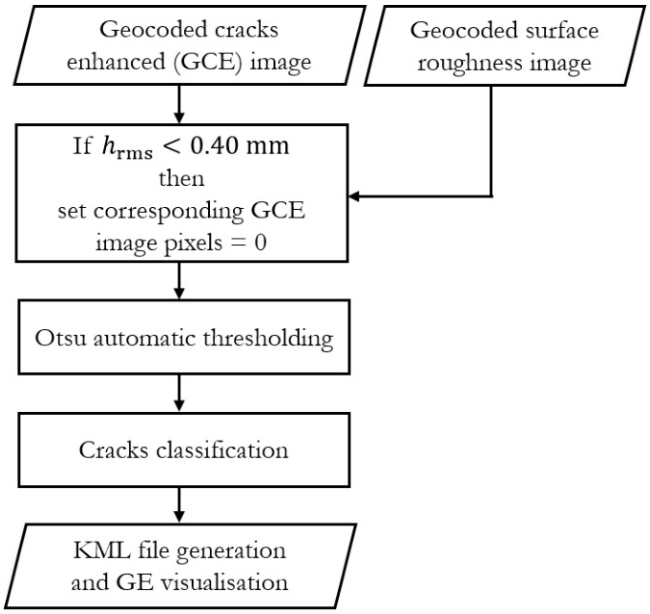

Figure 6.7: Cracks detection and classification procedure after cracks enhancement using the SWT.

Before applying the Otsu automatic thresholding algorithm to the GCE image, a pre-processing step sets pixels with surface roughness (h_{rms}) values below 0.40

mm to zero, assuming that such smooth areas are free of cracks. This procedure uses the geocoded surface roughness image as an additional input to improve the thresholding performance. The modified GCE image is then subjected to the Otsu thresholding procedure to determine the optimal threshold for separating cracks from non-crack regions.

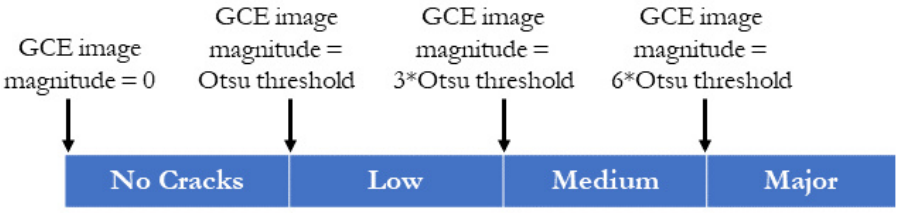

Figure 6.8: Cracks classification according to severity - the thresholds for each class were estimated empirically.

The resulting threshold is then used to categorise the cracks into low, medium, and major severity classes through empirical adjustment. This involves using a trial and error method, where multiplied values of the Otsu threshold serve as thresholds for each class. The classified cracks are visually compared with those in the GE optical image, and the thresholds are fine-tuned to match the observed crack severity. In the GCE image, pixels below the Otsu threshold are classified as non-crack regions, those between the threshold and three times its value as low-severity cracks, those between three and six times as medium-severity cracks, and those above six times as major cracks. This classification scheme is illustrated in Figure 6.8.

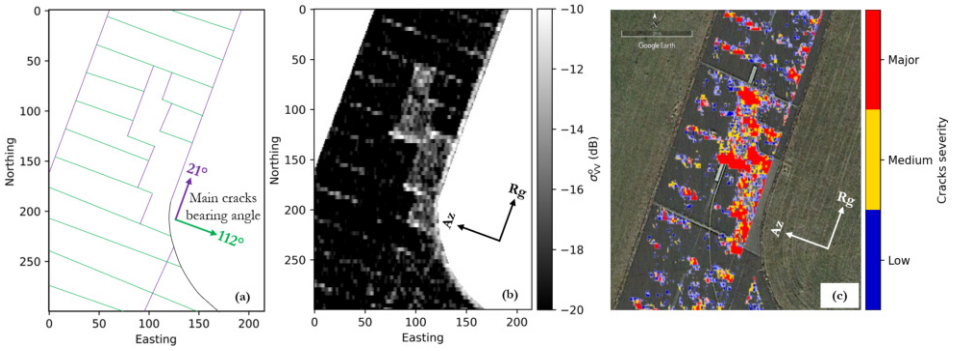

Figure 6.9: Cracks detection and classification results for a section of the Kaufbeuren runway. (a) Assumed cracks image. (b) σ^o_{VV} backscatter image generated from the PS05 F-SAR dataset. (c) Cracks detection and classification image obtained from the SWT-based method.

Figure 6.9(c) shows the cracks detection and classification results generated using the SWT-based method overlaid in GE for a section of the Kaufbeuren runway.

In this image, dark blue represents low-severity cracks, yellow indicates medium severity, and red denotes major cracks. Comparing this with the assumed cracks and σ^{o}_{VV} backscatter images in Figures 6.9(a) and (b), it is evident that the SWT-based method accurately detects the small cuts on the runway as cracks, with some parts showing low severity and others showing major severity depending on the backscatter signal strength. However, the method falsely detects most areas of the smooth rectangular concrete repair patches as large cracks instead of just the edges. Therefore, while the SWT-based approach can detect road surface cracks, it is unreliable due to false crack detections in areas with increased backscatter from different road construction materials.

6.2.3 Radon Transform-based Cracks Detection

The Radon transform is an integral transform commonly used in fields such as medical imaging, including computer tomography (CT) and nuclear magnetic resonance (NMR) [40]. It works by calculating projections of an image along different angles centred around the centre of the image, resulting in a series of line integrals. These line integrals represent how the features of the image are distributed along certain directions, allowing for comprehensive analysis. By integrating along specific directions, the Radon transform creates a transformation space in which patterns related to specific features become clearer [76].

The Radon transform projects the two-dimensional image function $f(x, y)$ from the (x, y) plane into the (θ_{r}, s) plane using multiple line integrals. A graphical representation of this process is illustrated in Figure 6.10. In the figure, the Radon transform function $R(\theta_{\mathrm{r}}, s)$ is represented as the line integral of $f(x, y)$ along the straight line 'w'. Here, the straight line 'w' is parameterised by two variables: θ_{r}, the projection/rotation angle from the x axis, and s, the distance from the origin along the projection line. The Radon transform can be mathematically represented as follows [70]:

$$R(\theta_{\mathrm{r}}, s) = \int_{-\infty}^{\infty} \int_{-\infty}^{\infty} f(x, y)\delta(s - x\cos\theta_{\mathrm{r}} - y\sin\theta_{\mathrm{r}})\, dx\, dy \tag{6.2}$$

where, as already mentioned in the graphical representation, θ_{r} represents the projection/rotation angle, s is the distance from the origin along the projection line, and δ denotes the Dirac delta function.

The ability of the Radon transform to detect and extract information about oriented features from an image by capturing line integrals along different directions is used in this study to detect the cracks on the road surfaces and also to estimate their orientation [135]. The Radon transform is investigated in two ways for cracks detection: first, it

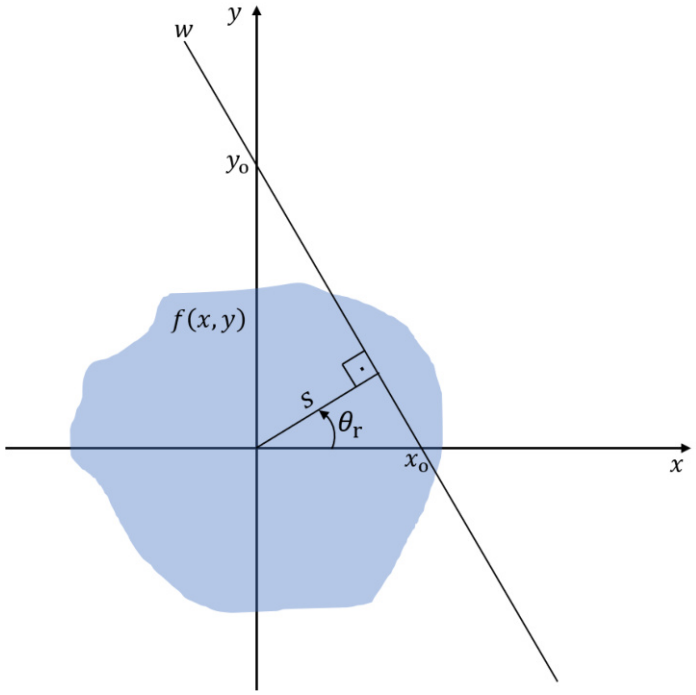

Figure 6.10: Graphical representation of the Radon transform.

is applied to simulated road cracks images, and second, a sliding window version of the Radon transform is applied to airborne F-SAR datasets. These investigations are detailed below:

1. **Investigations using simulated road cracks images:** To test the capability of the Radon transform to detect and estimate the orientation of the cracks on the road surface from SAR backscatter or surface roughness images, multiple 5x5 noisy images simulating road cracks with different orientations are generated. Each image contains random noise and a simulated line with a specified angle relative to the x-axis. These images simulate road cracks in SAR backscatter images with different orientations. The choice of the small 5x5 images is intentional because when applied to real SAR images for crack detection, the Radon transform has to be applied to small patches by using a sliding window. Therefore, it is important to determine whether the Radon transform can work effectively with a limited number of input pixels, such as the 25 pixels within a 5x5 window. In the case of F-SAR datasets with a spatial resolution of 0.25 cm used for this investigation, the 5x5 window covers an area of approximately 1.25 x 1.25 meters on the road surface.

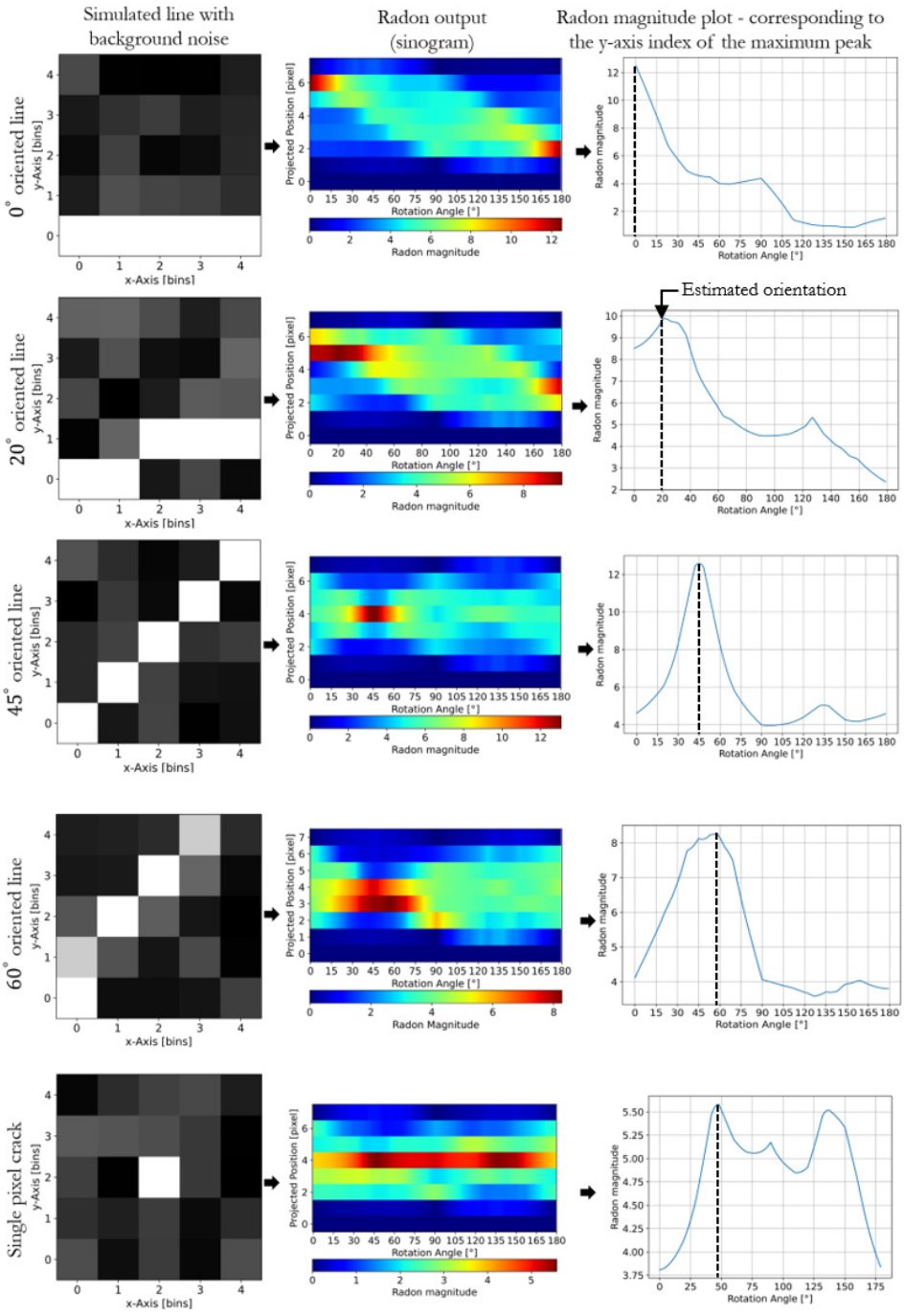

Figure 6.11: Cracks detection and orientation estimation results obtained using simulated lines with added background noise resembling cracks in a SAR backscatter image.

Figure 6.11 shows these simulated lines representing road cracks with orientations of 0, 20, 45 and 60 degrees. The Radon transform is then applied to each of these images, and the resulting Radon output is visualised in the form of a sinogram, which can also be seen in Figure 6.11. A sinogram provides a two-dimensional representation of the Radon output, showing the intensity of the line integrals of the image along different angles, w.r.t. a fixed axis (in this case the x-axis). The x-axis of the sinogram represents the Radon projection/rotation (θ_r) angle, while the y-axis indicates the distance from the origin along the projection line (s). Analysis of the sinograms shows that they have maximum Radon values at θ_r that match with the orientation angles of the simulated lines, in each case. In addition, the plots in Figure 6.11 show the Radon magnitude plots corresponding to the y-axis index of the sinogram at which the maximum value for the Radon transform is obtained. These plots also confirm that the maximum value for the Radon transform occurs when θ_r coincides with the orientation angle of the simulated line.

To understand the limitations of the Radon transform in detecting road cracks, an additional experiment was conducted to test the case when there is only a small crack present in the 5x5 image window, which covers only a single pixel. From this experiment shown in the last row of Figure 6.11, it can be seen that the Radon transform fails to detect the crack in this scenario and also shows incorrect orientation angle measurements. To summarise, for the Radon transform to be able to detect the crack and accurately estimate its orientation, the road crack in the 5x5 image should cover at least two pixels. However, if there are two or more separate small cracks within the 5x5 image, each occupying only a single pixel, then these cracks will be incorrectly detected by the Radon transform as a single crack with a wrong orientation angle.

From the investigations with the simulated cracks shown in Figure 6.11, it can be concluded that the Radon transform can accurately detect and estimate the orientation of cracks on a road surface from a noisy 5x5 image when there is only a single crack occupying at least two pixels.

2. **Direct application of windowed Radon transform on F-SAR generated surface roughness images:** A processing chain has been developed for detecting the cracks and estimating their orientation from the SAR data based on the above-discussed concept of utilising Radon maximum magnitudes and Radon rotation angles. The block diagram of this processing chain is shown in Figure 6.12.

   For this study, the geocoded surface roughness (h_{rms}) image obtained from the airborne F-SAR datasets is used as input for the Radon transform. It is chosen instead of using the σ^o backscatter image because the surface roughness image

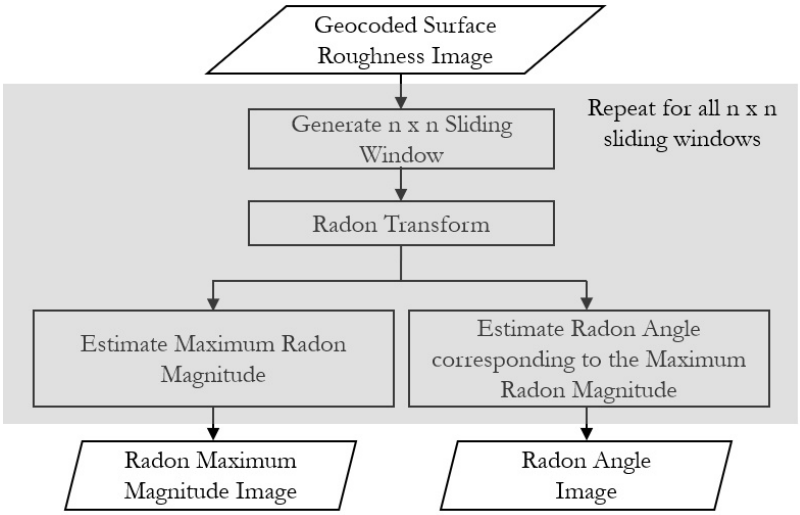

Figure 6.12: Block diagram for the cracks detection and orientation estimation using Radon transform.

shows a sharp increase in h_{rms} values at the cracked regions compared to the surrounding smooth road surfaces. This relative increase is more pronounced than what is observed in σ^o backscatter values, which can potentially improve the performance of the Radon transform in cracks detection and orientation estimation.

In Figure 6.11, it has already been shown that the Radon transform is capable of accurately detecting the cracks and also estimating their orientation from small 5x5 simulated noisy images. Therefore, in this processing chain, the Radon transform is iteratively applied over the large h_{rms} image by using a 5x5 sliding window. The use of a larger sliding window may overlap multiple cracks, leading to non-detection of smaller cracks and also producing a blurred Radon output image. Conversely, a very small window, like 3x3, lacks sufficient pixels for accurate crack orientation estimation. Therefore, the use of a 5x5 sliding window ensures an adequate number of pixels for the Radon transform, reducing the chances of overlooking smaller cracks near major ones. Also, the sliding window is moved across the input h_{rms} image in an overlapping manner, increasing the likelihood of detecting cracks that might be missed in the current position but detected in the next slightly shifted position of the sliding window.

In each sliding window, the maximum value computed by the Radon transform (indicative of a potential crack) and the Radon rotation angle (indicative of the crack orientation (θ_{r})) corresponding to this maximum value are recorded. This process generates the Radon maximum magnitude image and the Radon angle

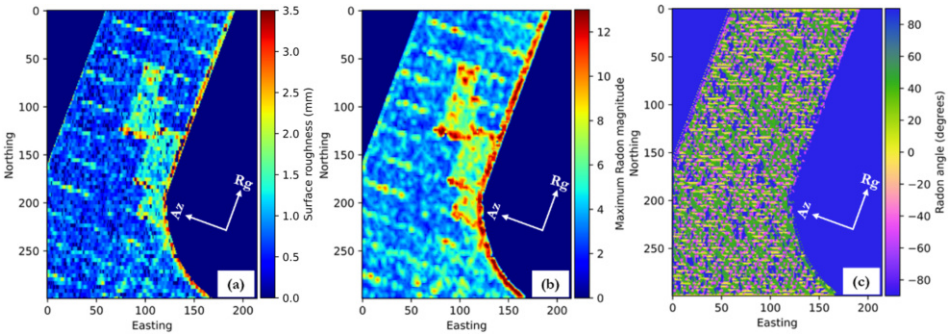

Figure 6.13: Images of a section of the Kaufbeuren runway illustrating the 5x5 Radon transform results. (a) h_{rms} image generated using the PS05 dataset. (b) Radon maximum magnitude image. (c) Radon angle image.

image after applying the sliding window Radon transform over the entire input image.

Figure 6.13 presents the results of applying the 5x5 sliding window Radon transform to the h_{rms} image of a section of the Kaufbeuren runway. Figure 6.13(a) displays the h_{rms} image generated from the PS05 dataset (cf. Table A.2 on page 174), where smooth areas of the road surface appear in blue, and regions with cracks or repair work are shown in cyan, indicating increased surface roughness. Figure 6.13(b) shows the Radon maximum magnitude image of the same region. In this image, severe cracks appear in red, and minor cracks range from cyan to yellow. However, maximum Radon magnitude values are present for all pixels, including smooth road regions, which are indicated by the blue pixels. Two rectangular patches on the runway, representing smooth areas with high surface roughness, are incorrectly identified as large cracks with high Radon magnitudes. Although the Radon transform enhances the cracks in the Radon maximum magnitude image due to line integration, when the Radon transform is applied directly to the h_{rms} image, the resulting Radon maximum magnitude image closely resembles the input h_{rms} image, but with scaled magnitude values. Furthermore, Figure 6.13(c) illustrates the Radon angle image corresponding to the maximum Radon magnitudes. This image also shows that there is always a Radon angle output for both cracked and smooth surfaces, resulting in a noisy appearance and providing limited useful information.

Therefore, it can be summarised that the application of the Radon transform directly on the SAR backscatter or h_{rms} images is not suitable for the reliable detection and orientation estimation of cracks on the road surface.

6.2.4 Cracks Detection with the Combined Use of Adaptive Thresholding and Radon Transform

Among the various cracks detection methods previously discussed in this section, it can be observed that the Radon transform enhances cracks visibility by integrating along their orientations (cf. Figure 6.13 on page 130) and also provides an accurate estimate of their orientation angle (cf. Figure 6.11 on page 127). However, the challenge arises when applying the Radon transform directly on the σ^{o} or h_{rms} images, as it produces Radon outputs for both cracked and smooth regions hindering the cracks detection process.

To address this challenge, pre-processing the input h_{rms} image can be performed to mask out smooth, non-cracked regions generating a binary cracks detection map image. This image can then be used to remove the h_{rms} values of the non-cracked regions from the h_{rms} image generating the cracks roughness image. This image contains the h_{rms} values only for the cracked regions and can then be used as input for the windowed Radon transform for estimating the crack severity and orientation. The methodology for performing the adaptive thresholding and Radon transform are explained below:

1. **Windowed adaptive thresholding algorithm for cracks detection:** An adaptive thresholding algorithm has been proposed that performs the above-mentioned pre-processing step on the input h_{rms} image thereby generating the binary cracks detection map image and the cracks roughness image. The block diagram of this thresholding algorithm is shown in Figure 6.14.

   Figure 6.14 illustrates the adaptive thresholding process applied locally to the input h_{rms} image using an n x n sliding window. For each window, the n x n h_{rms} values are first filtered with a median filter to reduce spikey noise that can interfere with accurate threshold estimation. Then, the mean and standard deviation of the filtered data are calculated, and the cracks detection threshold is determined as the sum of the mean and standard deviation within each sliding window as follows:

$$\text{Threshold} = \text{Mean} + \text{Standard Deviation} \tag{6.3}$$

   The center pixel within a sliding window is classified as a crack if it fulfils the following conditions: Its h_{rms} value is greater than or equal to the threshold value, its value is also greater than or equal to 1.2 mm (determined by trial and error approach), and the estimated mean value is greater than zero. Pixels that fulfil these criteria are assigned the value '1' in the binary crack detection map, which stands for cracks, while pixels that do not fulfil these criteria are assigned the value '0', which stands for smooth areas. The corresponding equation is given below:

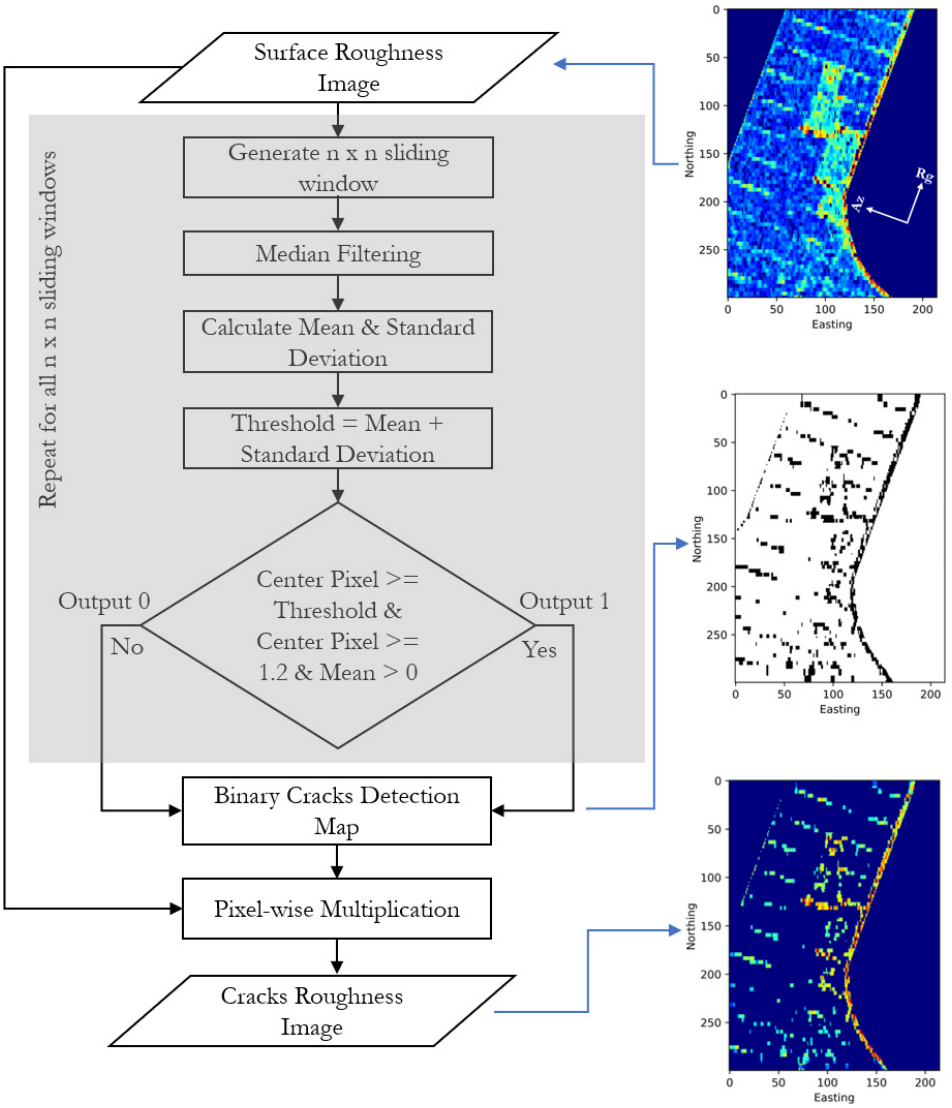

Figure 6.14: Block diagram of the windowed adaptive thresholding algorithm.

$$\text{Binary cracks detection output} = \begin{cases} 1 & \text{if center pixel } h_{\text{rms}} \text{ value} \geq \text{Threshold} \\ & \text{and center pixel } h_{\text{rms}} \text{ value} \geq 1.2 \\ & \text{and mean} > 0 \\ 0 & \text{otherwise} \end{cases} \tag{6.4}$$

The resulting binary cracks detection map is then multiplied pixel by pixel with the input h_{rms} image, keeping the h_{rms} values for cracked regions and setting the values in smooth regions to '0'. This resulting cracks roughness image is then used as input to the Radon transform for estimating the severity and orientation of the cracks.

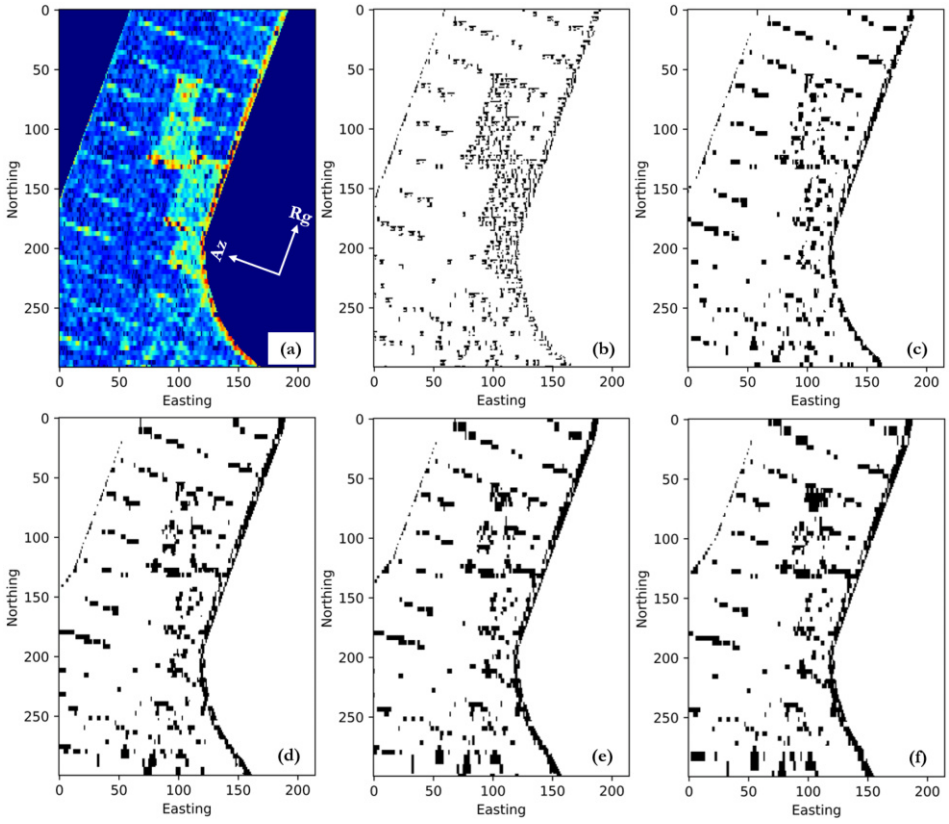

Figure 6.15: Windowed adaptive thresholding results for a section of the Kaufbeuren runway. (a) Surface roughness image generated using the PS05 dataset. Binary cracks detection maps generated using sliding window sizes of (b) 5x5, (c) 15x15, (d) 25x25, (e) 35x35, and (f) 45x45.

For performing the n x n adaptive thresholding algorithm, it is necessary to choose a suitable window size so that the cracks can be accurately detected. 5x5, 15x15, 25x25, 35x35 and 45x45 window sizes were evaluated in this study and the results are shown in Figure 6.15.

Figure 6.15(a) shows the h_{rms} image from the PS05 dataset, where smooth areas without cracks appear in blue, and regions with cracks range from cyan to red based on severity. Two rectangular repair patches appear predominantly in cyan due to higher surface roughness, despite being smooth and crack-free. Figures

6.15(b-f) present binary cracks detection maps generated by the adaptive thresholding algorithm with different sliding window sizes applied to the h_{rms} image in Figure 6.15(a). For smaller sliding window sizes of 5x5 and 15x15 (Figures 6.15(b) and (c)), many pixels in the smooth repair patches are incorrectly identified as cracks, which is likely due to not enough pixels being available for accurate threshold estimation. The 25x25 sliding window (Figure 6.15(d)) improves accuracy by correctly identifying the edges of the repair patches and reducing false crack detections within the smooth repair patches. Smaller cuts on the runway are also accurately recognised as cracks. Larger window sizes of 35x35 and 45x45 (Figures 6.15(e) and (f)) show no significant improvement over 25x25, with crack edges spreading to neighbouring pixels potentially enlarging smaller cracks. Considering these factors, the 25x25 sliding window is selected as the suitable window size for performing the adaptive thresholding.

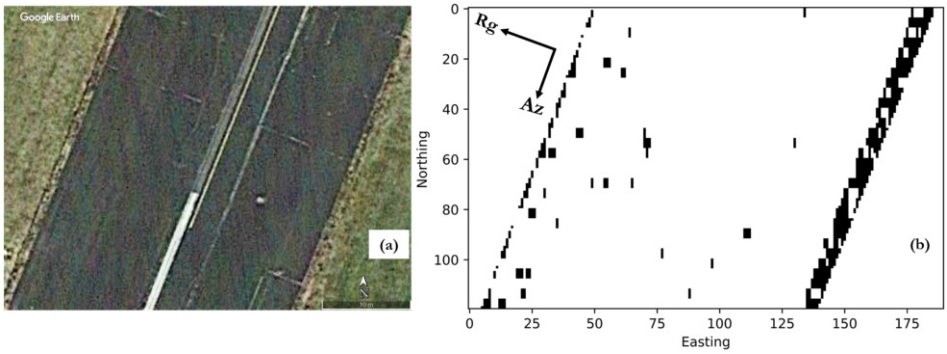

Figure 6.16: Windowed adaptive thresholding results for a smooth and almost cracks-free section of the Kaufbeuren runway. (a) GE image. (b) Binary cracks detection map generated using the PS04 dataset.

An investigation has been carried out to evaluate the performance of the adaptive thresholding algorithm in a smooth, crack-free area. Ideally, no false crack detections should occur in such a region. Figure 6.16(a) shows the GE image of a smooth, nearly crack-free section of the Kaufbeuren runway with only minor cuts present. The PS04 dataset (cf. Table A.2 on page 174) with a flight direction parallel to this runway was selected to minimise the visibility of these cuts in the h_{rms} image. Figure 6.16(b) shows the binary cracks detection map generated by applying the adaptive thresholding algorithm to this h_{rms} image. Analysing this image shows that only a few pixels are detected as cracks, while most of the image shows no cracks. These few detected cracks could be due to local backscatter variations in the PS04 dataset caused by oriented construction particles on the runway or by parts of the runway cuts that are still visible in the input h_{rms} image. Overall, this result indicates that the adaptive threshold algorithm effectively avoids false crack detections.

2. **Windowed Radon Transform for Cracks Severity Estimation:** The cracks roughness image obtained from the adaptive thresholding algorithm is used as input for the Radon transform to estimate the severity and orientation of cracks. A windowed Radon transform-based algorithm has been developed for this purpose, and its block diagram is shown in Figure 6.17.

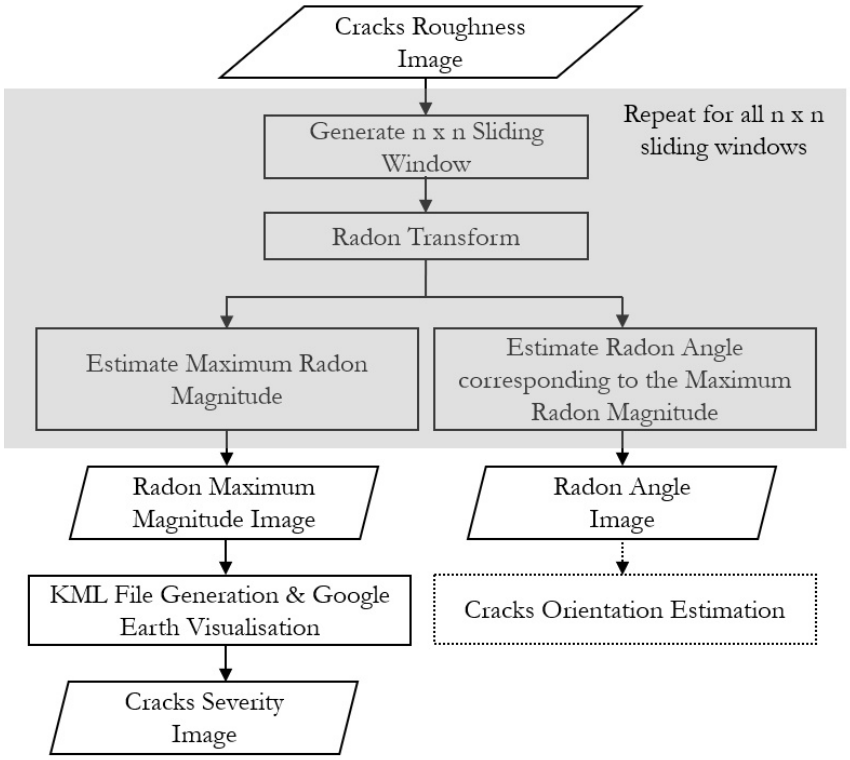

Figure 6.17: Block diagram of the windowed Radon transform used for estimating cracks severity from the cracks roughness image generated by the adaptive thresholding algorithm.

From Figure 6.17, it can be seen that similar to the direct application of the Radon transform on the surface roughness image discussed in section 6.2.3, in this case also, the Radon transform is applied in each sliding window. The maximum Radon magnitude and the corresponding angle value are estimated and recorded so that the maximum Radon magnitude and Radon angle images are obtained after processing all the sliding windows. The maximum Radon magnitude image is further processed for generating a KML file representing the crack severity image that can be visualised on GE. The Radon angle image serves as input for the cracks orientation estimation method, which is discussed later in section 6.3 on page 144.

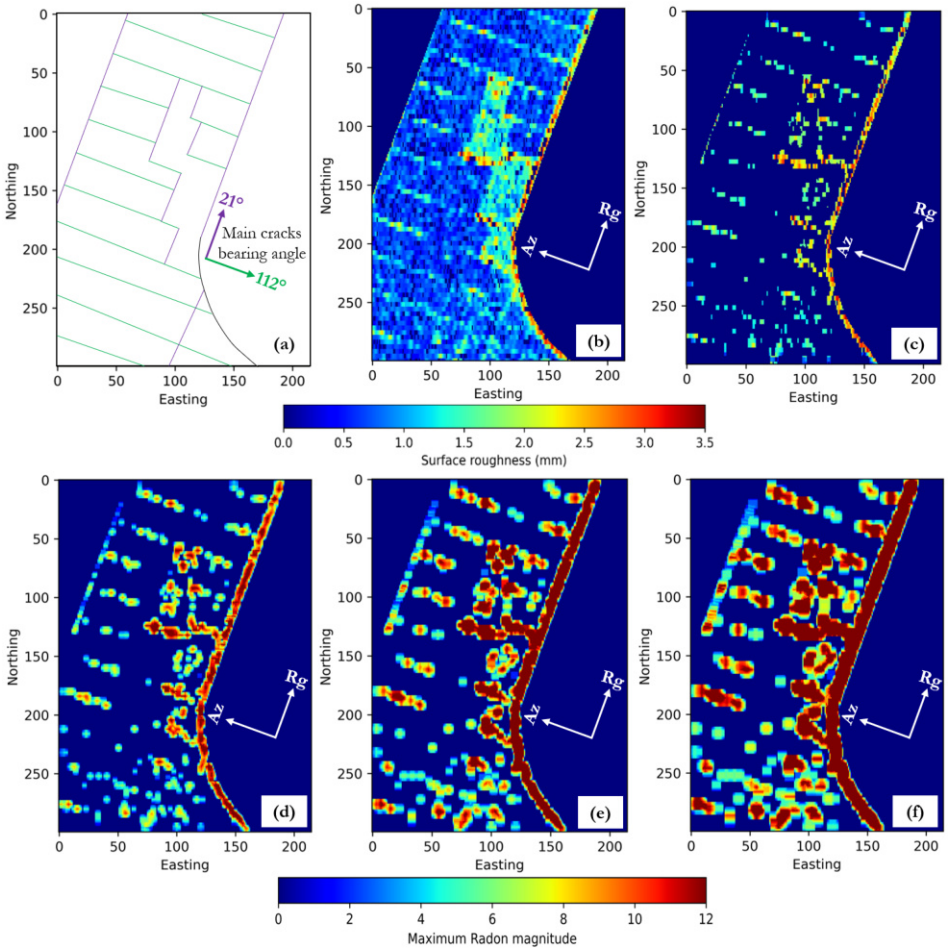

Figure 6.18: Windowed Radon transform results for a section of the Kaufbeuren runway. (a) Assumed cracks image. (b) Surface roughness image generated using the PS05 dataset. (c) Cracks roughness image obtained from the adaptive thresholding process. Radon maximum magnitude images generated using sliding window sizes of (d) 5x5, (e) 7x7, and (f) 9x9.

Similar to the adaptive thresholding algorithm, selecting the suitable window size is crucial for the windowed Radon transform. In this study, 5x5, 7x7, and 9x9 sliding window sizes were tested, and the results are presented in Figure 6.18. The experiment with different window sizes for the Radon transform is carried out for a section of the Kaufbeuren runway where small cuts and repair patches are present. Figure 6.18(a) illustrates the main cracks assumed to be present in this section. These cracks are visible as regions of high surface roughness in cyan to red colour in the surface roughness image generated from the PS05 F-SAR dataset (cf. Figure 6.18(b)). Figure 6.18(c) shows the cracks roughness image generated using

the adaptive thresholding method. By comparing the Figures 6.18(b) and (c), it can be seen that the cracks roughness image only contains the h_{rms} values for the cracks, with the smooth areas masked out. This image, as already mentioned before is used as input for the windowed Radon transform. The Radon maximum magnitude image generated with a 5x5 sliding window is shown in Figure 6.18(d). Comparing this image with the assumed cracks image in Figure 6.18(a) and the h_{rms} image in Figure 6.18(b), it becomes clear that most of the cracks present in this section of the Kaufbeuren runway can be recognised in the Radon maximum magnitude image. The small cuts present on the runway which are shown by the green coloured lines in Figure 6.18(a) appear mostly in cyan colour with only some red points indicating the low severity of these cuts. On the other hand, the edges of the rectangular repair patches appear in yellow to red colours indicating their high severity. This is because the concrete repair patches are expected to have a slightly raised surface compared to the surrounding asphalt regions which resembles large cracks. Figures 6.18(e) and (f) show Radon maximum magnitude images generated with 7x7 and 9x9 sliding windows, respectively. When comparing these images with Figure 6.18(d), no additional cracks can be found with larger windows. However, the detected cracks appear wider and more spread out, which can make it challenging for localisation on GE. Also, more cracks appear in red especially for the small cuts on the runway, indicating a higher severity, as more pixels along the cracks' orientation direction are available for integration during the Radon transform. Considering all these factors, the window size of 5x5 is selected for performing the Radon transform.

6.2.5 Cracks Detection Results and Discussion

This section presents the cracks detection results generated using the previously discussed methods with the airborne F-SAR data as input

Figure 6.19 shows the cracks detection results for the Kaufbeuren parking area where several cracks and potholes are present. The GE image in Figure 6.19(a) confirms the presence of these large cracks and potholes. Figure 6.19(b) illustrates the main directions of the cracks assumed to be present in the area. The cracks detection results presented in this figure were generated using the PS05 F-SAR dataset. Figure 6.19(c) presents the results from using the Canny edge detector. Comparing this image with the GE image and the assumed crack directions shows that the Canny edge detector identifies cracks in both smooth and cracked regions, making it unsuitable for this study. Figure 6.19(d) displays the results from the SWT-based detection method. This method accurately detects the major cracks visible in the GE image. However, the detected cracks appear larger than they are due to spatial averaging caused by using wavelets at multiple scales.

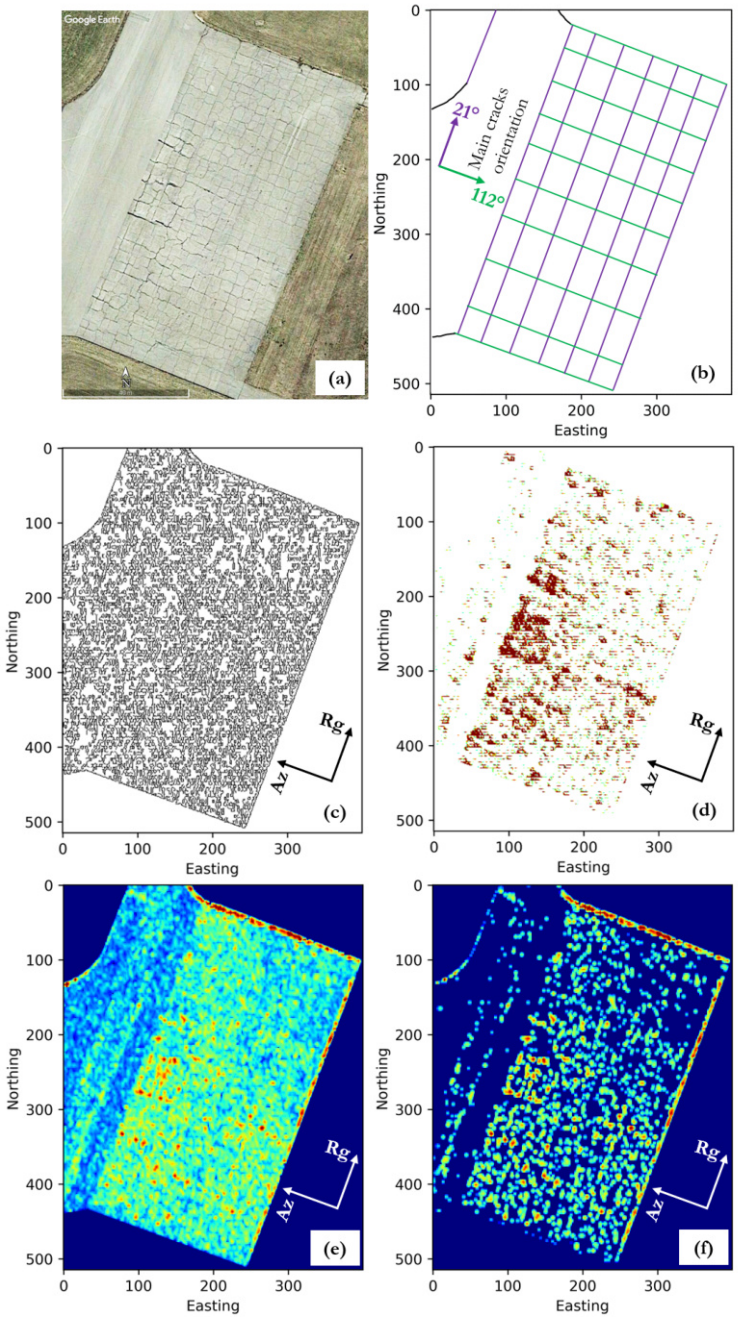

Figure 6.19: Cracks detection results for the Kaufbeuren parking area generated using the PS05 F-SAR dataset. (a) GE image. (b) Assumed cracks image. Cracks detection result generated using (c) Canny edge detector, (d) SWT-based method, (e) Radon transform-based method and (f) combination of adaptive thresholding and Radon transform.

Additionally, several cracks visible in the GE image are not detected because the SWT-based approach is sensitive only to horizontal, vertical, and diagonally oriented cracks, missing those with other orientations. Thus, the SWT-based method is not reliable for detecting road surface cracks. Figure 6.19(e) shows the results of applying the Radon transform directly to the surface roughness image. The cracks are clearly identified, with colours from cyan to red indicating their severity. However, since the Radon transform produces outputs for both cracked and non-cracked regions, it is not suitable for cracks detection. Finally, Figure 6.19(f) presents the results from combining an adaptive thresholding algorithm with the Radon transform. This approach accurately identifies most of the cracks visible in the GE image. Low-severity cracks appear in cyan, while major cracks range from yellow to red. The shape and orientation of the detected cracks also match those in the GE image. Therefore, among all the methods investigated, the combined use of the adaptive thresholding and the Radon transform provides the most reliable results for detecting cracks using X-band airborne F-SAR datasets.

The GE visualisation of the cracks detection results generated using the combined use of the adaptive thresholding and the Radon transform for the Kaufbeuren parking area is shown in Figure 6.20. Specifically, Figures 6.20(a), (c) and (e) show the surface roughness images used as input for performing the cracks detection generated from the PS05 dataset, multi-dataset averaging method and the highest SNR method, respectively, with corresponding cracks severity images shown in Figures 6.20(b), (d), and (f). In these cracks severity images, major cracks are highlighted in yellow to red, while minor cracks appear in cyan. The number of detected cracks varies among these images due to the dependency of cracks visibility on the flight heading angle, as discussed in section 6.1 on page 115. For example, Figure 6.20(b) shows more cracks detections from the PS05 dataset compared to Figure 6.20(d), which uses the multi-dataset averaged surface roughness image as input. The latter has fewer detected cracks because minor cracks visible only from certain flight angles are smoothed out when combining datasets with different headings using the multi-dataset averaging method (cf. Figure 6.20(c)). On the other hand, the cracks severity image shown in Figure 6.20(f), which utilises the surface roughness image generated by the highest SNR method, detects the highest number of cracks. This is due to the high sensitivity of the highest SNR method to local backscatter variations from oriented features on the road surface. However, this method also results in a grainy/noisy surface roughness image (Figure 6.20(e)), increasing the likelihood of false cracks detections and reducing reliability. Therefore, to achieve a comprehensive view of cracks with different orientations, it is recommended to generate multiple cracks severity images from individual SAR datasets acquired with different flight heading angles. Additionally, zoomed-in views of two sections of the parking area, marked as 'Detail 1' and 'Detail 2' in Figure 6.20(b), are provided in the following figures for a closer examination of the crack detection results.

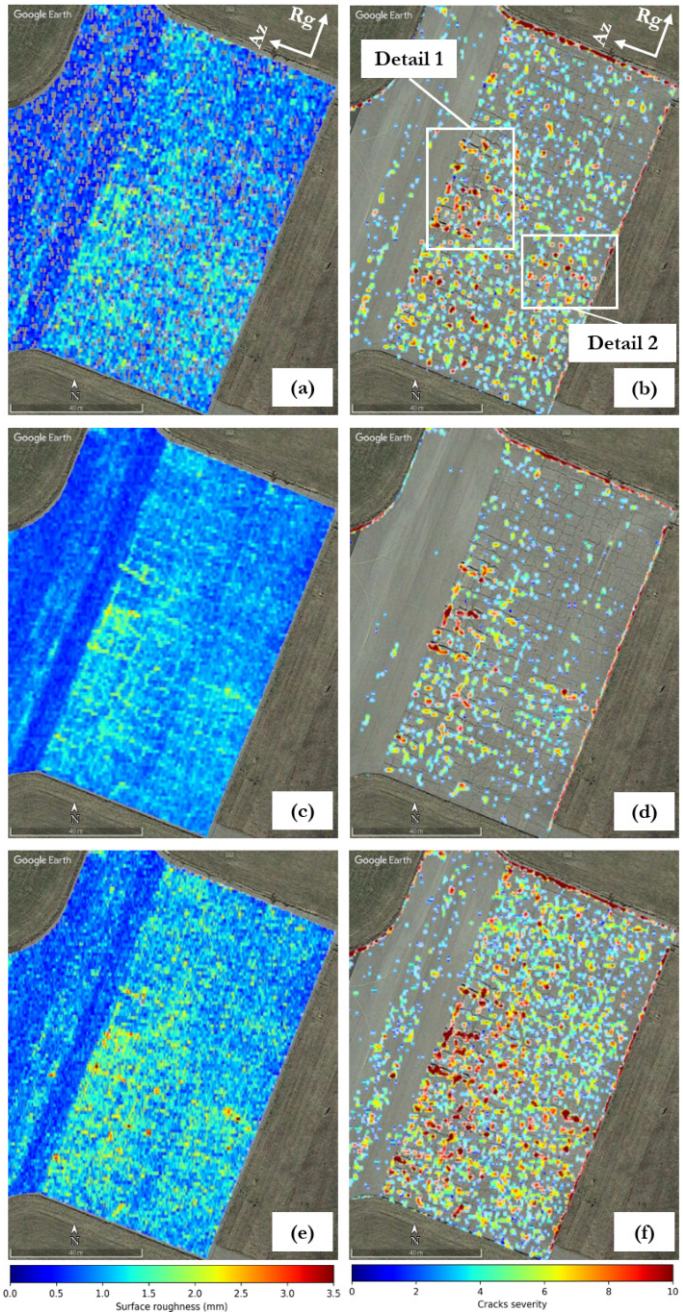

Figure 6.20: Cracks detection results generated using the combination of adaptive thresholding and Radon transform for the Kaufbeuren parking area. Surface roughness images used as input for cracks detection generated from (a) PS05 dataset, (c) multi-dataset averaging, and (e) highest SNR method. Corresponding cracks severity images generated from (b) PS05 dataset, (d) multi-dataset averaging, and (f) highest SNR method.

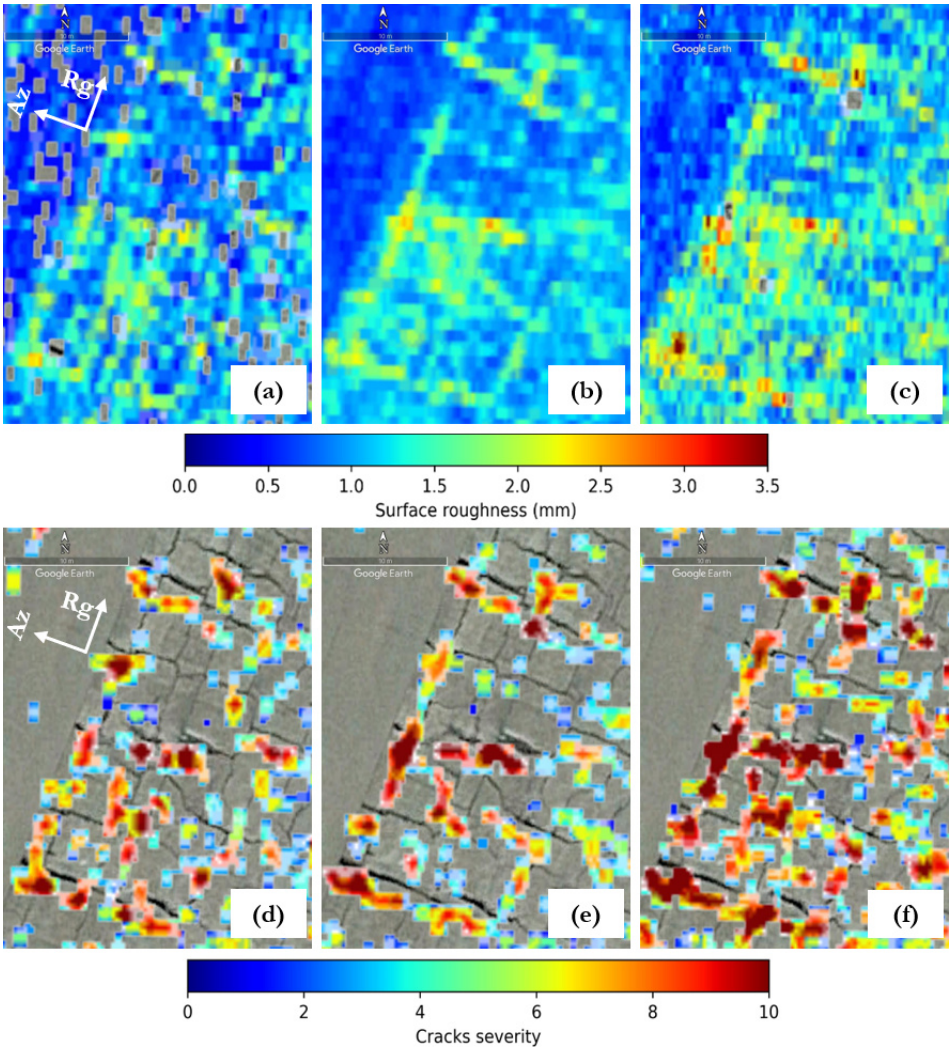

Figure 6.21: Cracks detection results generated using the combination of adaptive thresholding and Radon transform for the section of the Kaufbeuren parking area marked as 'Detail 1' in Figure 6.20(b). Surface roughness images used as input for cracks detection generated from (a) PS05 dataset, (b) multi-dataset averaging, and (c) highest SNR method. Corresponding cracks severity images generated from (d) PS05 dataset, (e) multi-dataset averaging, and (f) highest SNR method.

Figure 6.21 displays the cracks detection results for the section marked as 'Detail 1' in the Kaufbeuren parking area. Surface roughness images generated from the PS05 dataset, multi-dataset averaging, and highest SNR methods are shown in Figures 6.21(a), (b), and (c), respectively. The corresponding cracks severity images are presented in Figures 6.21(d), (e), and (f). By comparing these surface roughness images with the cracks

severity images, it is evident that cracks identifiable in the surface roughness images as regions with increased surface roughness values are accurately identified as cracks in the crack severity images. The detected cracks' locations and shapes closely match those visible in the underlying GE image. Large cracks are detected in yellow to red, indicating high severity, while smaller cracks are detected in cyan to green, indicating lower severity.

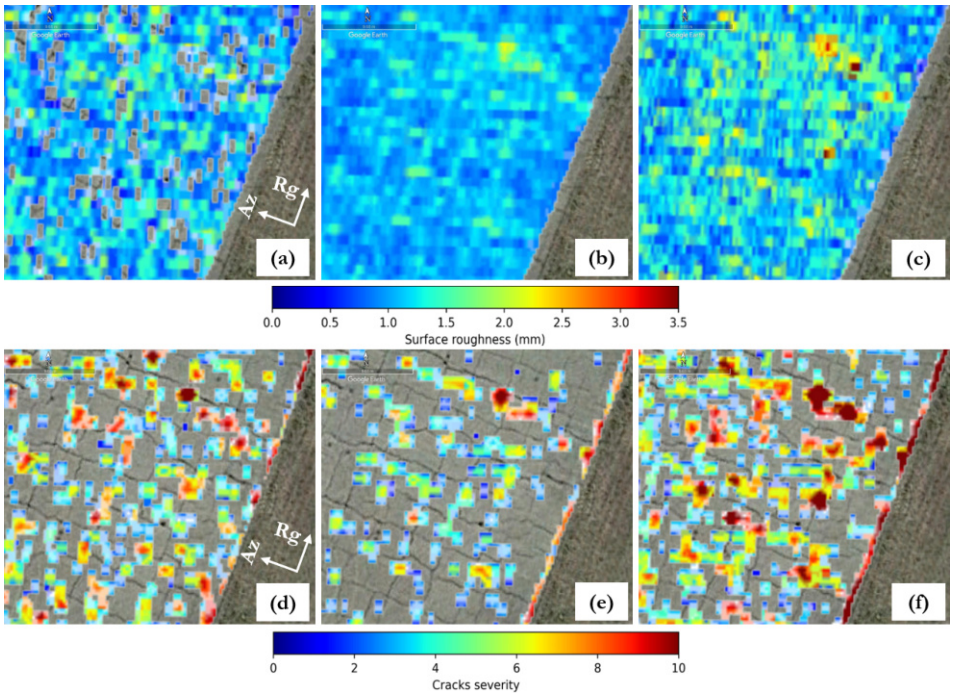

Figure 6.22: Cracks detection results generated using the combination of adaptive thresholding and Radon transform for the section of the Kaufbeuren parking area marked as 'Detail 2' in Figure 6.20(b). Surface roughness images used as input for cracks detection generated from (a) PS05 dataset, (b) multi-dataset averaging, and (c) highest SNR method. Corresponding cracks severity images generated from (d) PS05 dataset, (e) multi-dataset averaging, and (f) highest SNR method.

Similarly, Figure 6.22 presents the results for the area marked as 'Detail 2'. Here, the number of severe cracks detections is lower compared to 'Detail 1', which is consistent with the underlying GE image. The results shown in Figures 6.21 and 6.22 confirm that the cracks detected by the combined use of the adaptive thresholding and the Radon transform from the SAR images are indeed the actual cracks present on the road surface. The severity representation provides insights into the size of the cracks. A slight shift in the position of the detected cracks compared to their GE view can be attributed to inaccuracies in the digital elevation model (DEM) used for geocoding the SAR images.

Figure 6.23 presents the cracks severity image for the entire Kaufbeuren runway. This image was generated using the surface roughness image from the PS05 F-SAR dataset,

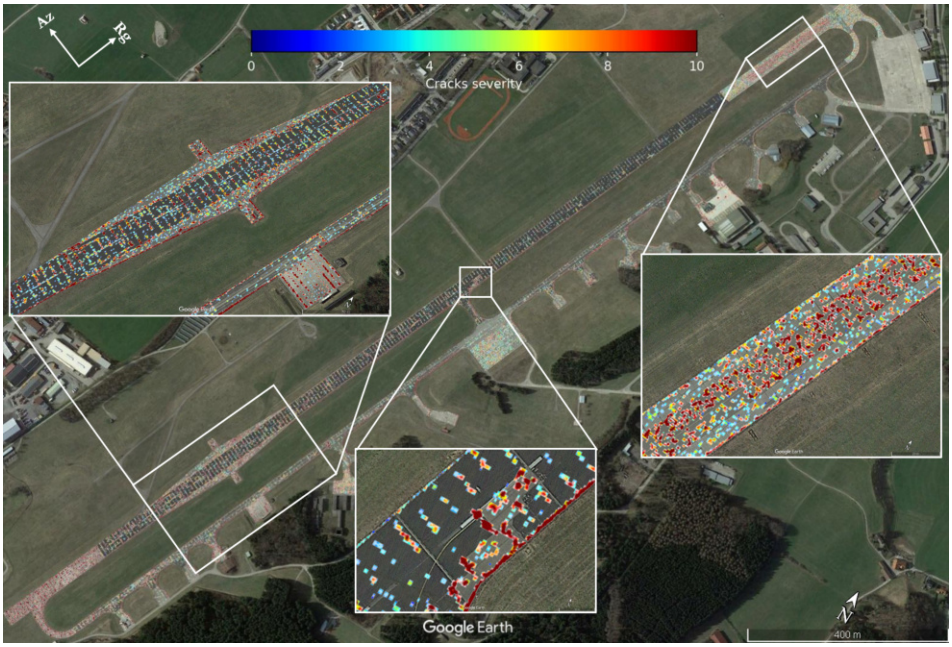

Figure 6.23: Google Earth visualisation of the cracks severity image generated using the combination of adaptive thresholding and Radon transform from the PS05 F-SAR dataset for the entire Kaufbeuren runway.

with the flight track oriented perpendicular to the runway (see azimuth and range direction arrows). The zoomed-in views in the figure reveal that small cuts on the runway, edges between concrete and asphalt regions, and areas with repeated cuts in the concrete at the top right end of the runway are accurately detected as cracks. The small cuts on the runway are mostly identified as low severity, while the concrete edges and repeated concrete cuts are detected with higher severity. Thus, it can be summarised that the combination of adaptive thresholding and the Radon transform is effective for detecting cracks and estimating their severity.

The cracks severity image for the Wolfsburg motorway intersection at Braunschweig is shown in Figure 6.24. This area features a very smooth road surface without any cracks. Additional details about this test site are provided in Appendix A.1.3 on page 170. By examining Figure 6.24, it is evident that only the road borders, flyover walls, and lane dividers are detected as cracks due to the increased backscatter from these materials. The road boundaries appear in cyan to red colours, while the lane dividers are mostly red, likely due to the very high backscattering from the metallic lane dividers. These high reflecting materials like lane dividers are detected because the surface roughness roughness image without performing upper σ^o and lower SNR masking (cf. Figure 3.23 on page 64) is used as input for generating the cracks severity image. No cracks

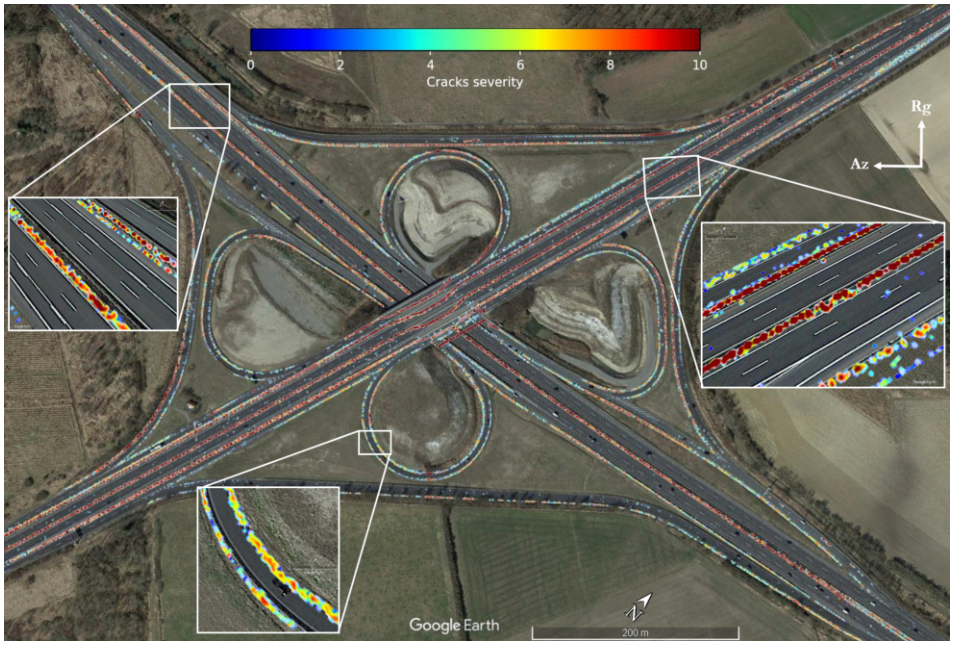

Figure 6.24: Google Earth visualisation of the cracks severity image generated using the combination of adaptive thresholding and Radon transform for the Wolfsburg motorway intersection at Braunschweig.

are detected on the road surface except for a few isolated blue pixels, which can be validated with the underlying GE view. This result demonstrates that the developed cracks detection algorithm, which combines adaptive thresholding and the Radon transform, is effective for real roads and does not produce a large number of false detections on smooth surfaces.

6.3 Investigation on Cracks Orientation Estimation

The investigations presented in section 6.2 of this chapter recommended the combined approach of using adaptive thresholding and Radon transform as the best choice for cracks detection and severity estimation. Also, it was shown that Radon transform is able to accurately estimate the orientation of cracks from simulated road cracks images (cf. Figure 6.11 on page 127). Therefore, the combined approach of using adaptive thresholding and Radon transform is further extended for estimating the orientation of the detected cracks from the X-band airborne F-SAR images.

The Radon angle image obtained as one of the outputs by performing the windowed Radon transform on the cracks roughness image as illustrated in the block diagram shown in Figure 6.17 on page 135 is used as input for the cracks orientation estimation.

The block diagram of the methodology adopted for the cracks orientation estimation is shown in Figure 6.25.

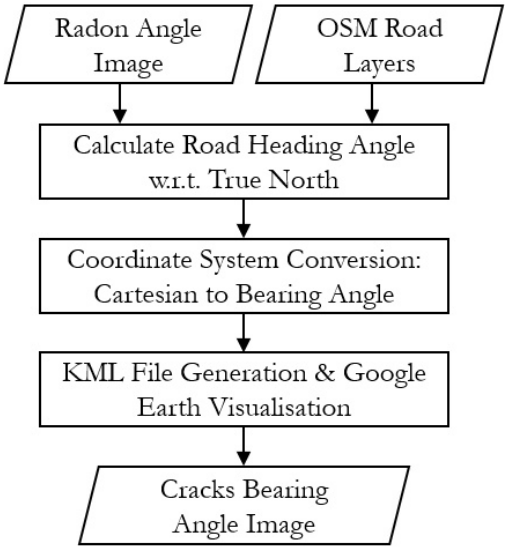

Figure 6.25: Block diagram of the methodology adopted for cracks orientation estimation.

The Radon angle image used as input for the cracks orientation estimation represents the orientation angles (θ_r) of the detected cracks in the Cartesian coordinate system measured w.r.t. the x-axis. However, for a more meaningful representation of their orientation, it is essential to measure the angles in the bearing angle (θ_b) coordinate system, where the angles are referenced to true north (cf. Figure 6.26). To achieve this, a coordinate system conversion is applied to the Radon angle image, resulting in the generation of the cracks bearing angle image. The coordinate system conversion is performed through the following steps:

$$\theta_b = (90^\circ - \theta_r - \theta_{road} - \theta_{decl}) \bmod 360^\circ \tag{6.5}$$

where θ_b denotes the bearing angle, θ_r is the Radon (orientation) angle of the cracks, θ_{road} represents the road angle, indicating the inclination of the road w.r.t. true north, determined using OSM data and θ_{decl} is the grid declination angle accounting for the difference between true north and universal transverse mercator (UTM) grid north [121]. θ_{decl} is included because the input h_{rms} image used for performing the Radon transform is geocoded into the UTM coordinate system. The integration of θ_{decl} into the equation ensures a precise adjustment of the bearing angle and compensates for the discrepancy between UTM north and true north. It is important to obtain θ_{decl} from reliable sources for the specific location and time of data acquisition.

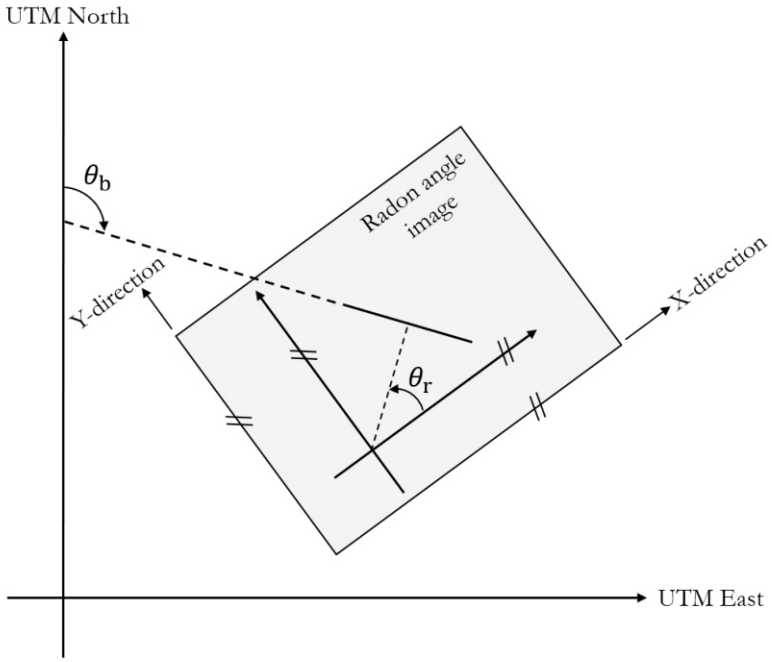

Figure 6.26: Visualisation of the coordinate system conversion - Radon angle (θ_r) to bearing angle (θ_b).

In OSM, road segments are represented as 'edges', which are essentially road lines connecting two end 'nodes' (vertices) [28], as shown in Figure 6.27.

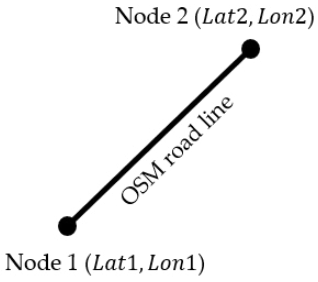

Figure 6.27: Road representation in OSM.

The road angle (θ_{road}) can be calculated using the following method:

$$\theta_{road} = \arctan\left(\frac{Y}{X}\right) \tag{6.6}$$

where Y and X are computed using the latitude ($Lat1$) and longitude ($Lon1$) of Node 1, and the latitude ($Lat2$) and longitude ($Lon2$) of Node 2. These nodes are adjacent nodes along the road centerline obtained from OSM.

The values for Y and X are calculated as follows:

$$Y = \sin(Lon2 - Lon1)\cos(Lat2) \tag{6.7}$$

$$X = \cos(Lat1)\sin(Lat2) - \sin(Lat1)\cos(Lat2)\cos(Lon2 - Lon1) \tag{6.8}$$

After performing the coordinate system conversion on the cracks Radon angle image, it is then further processed for generating a KML file representing the cracks bearing angle image that can be visualised on GE.

6.3.1 Cracks Orientation Estimation Results and Discussion

The cracks orientation estimation results estimated using the methodology discussed in the previous section are presented here.

Two regions of the Kaufbeuren airfield, as shown in Figure 6.28, are selected to analyse the cracks orientation estimation results. The first region is a section of the Kaufbeuren runway, featuring repair patches and small cuts (see Figure 6.28(a)), and the second region is the severely cracked parking area of the Kaufbeuren airfield (see Figure 6.28(c)). Both of these regions were previously shown in this chapter for the cracks severity estimation. Most cracks in these sections are found to have two orientations: longitudinal to the runway and transverse to the runway. The assumed cracks images in Figures 6.28(b) and (d) illustrate these main crack orientations, with purple lines indicating longitudinal cracks and green lines indicating transverse cracks. The actual bearing angles of these cracks, measured from GE, are 21 degrees for longitudinal cracks and 112 degrees for transverse cracks. These two bearing angles are considered the ground truth values for validating the cracks orientations estimated from the airborne F-SAR data presented in the following results.

Figure 6.29 displays the cracks orientation estimation results for the section of the Kaufbeuren runway with repair patches and small cuts. Surface roughness images generated from the PS05 dataset, multi-dataset averaging, and highest SNR methods are shown in Figures 6.29(a), (b), and (c), respectively. The corresponding cracks bearing angle images are presented in Figures 6.29(d), (e), and (f). By comparing these surface roughness images with the crack severity images, it is clear that regions with increased

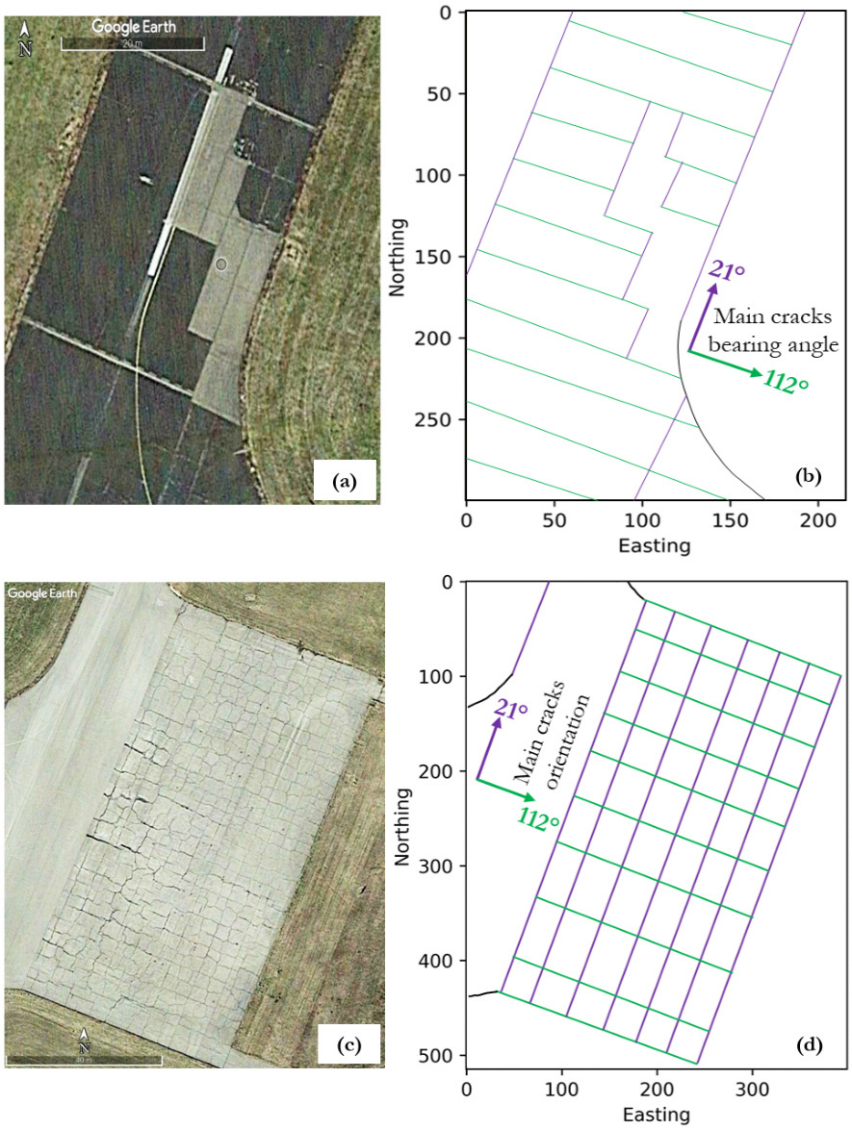

Figure 6.28: Regions of the Kaufbeuren airfield selected for analysing the cracks orientation estimation results. (a) GE image of a section of the Kaufbeuren runway where repair patches and small cuts are present and (b) shows the assumed cracks image for this section. (c) GE image of the Kaufbeuren parking area where severe cracks are present and (d) shows the assumed cracks image for this region.

surface roughness values correspond to cracks visible in the cracks bearing angle images. Cracks along the runway direction predominantly appear in purple, indicating a bearing angle of around 20 degrees, while cracks perpendicular to the runway appear in yellow to green, indicating a bearing angle of around 115 degrees. In all three images, the bearing

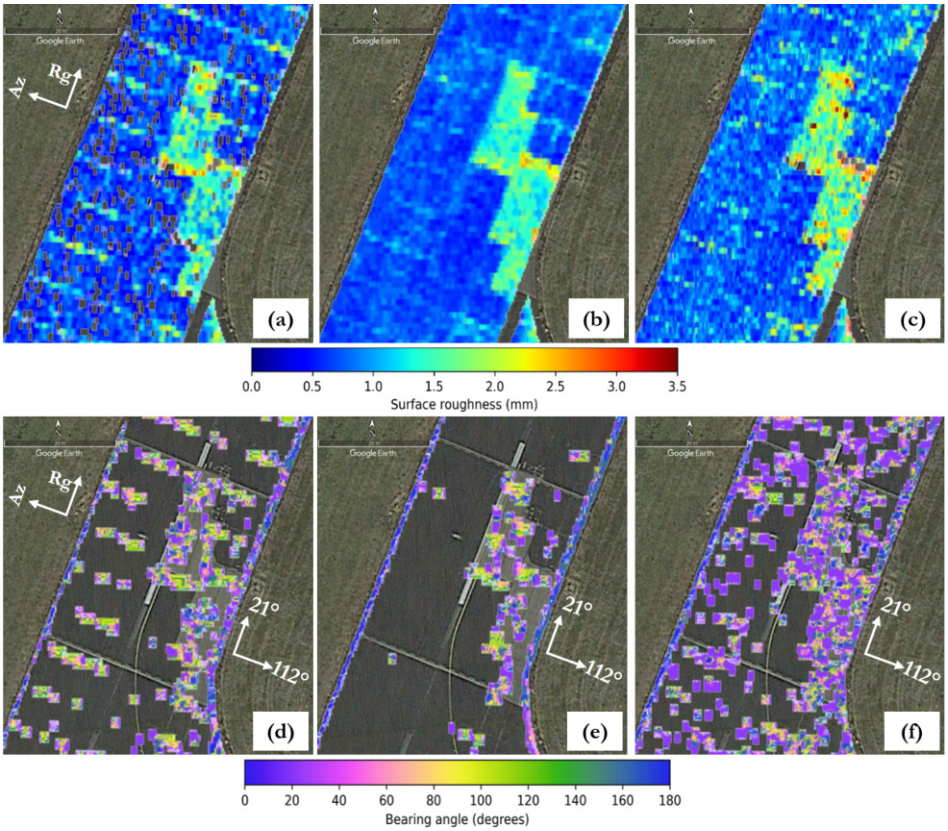

Figure 6.29: Cracks orientation estimation results for the section of the Kaufbeuren runway shown in Figure 6.28(a). Surface roughness images used as input for cracks orientation estimation generated from (a) PS05 dataset, (b) multi-dataset averaging, and (c) highest SNR method. Corresponding cracks bearing angle images generated from(d) PS05 dataset, (e) multi-dataset averaging, and (f) highest SNR method.

angles estimated by the Radon transform-based method closely match the actual bearing angles of the cracks measured from GE, as indicated by the white arrows. However, the number of detected cracks varies depending on the surface roughness image used as input. Fewer cracks are detected in the multi-dataset averaged image, while more false cracks are detected when the highest SNR fused surface roughness image is used as input. It is also noteworthy that the bearing angles of 0 degrees and 180 degrees represent the same orientation and are therefore displayed in the same colour (dark blue) using a cyclic colour map.

The histograms for these cracks bearing angle images are shown in Figure 6.30. Specifically, Figure 6.30(a) presents the histogram from the PS05 dataset, (b) from the multi-dataset averaging method, and (c) from the highest SNR method. All three histograms indicate that the dominant bearing angles are in the ranges of 20 to 30 degrees and 110

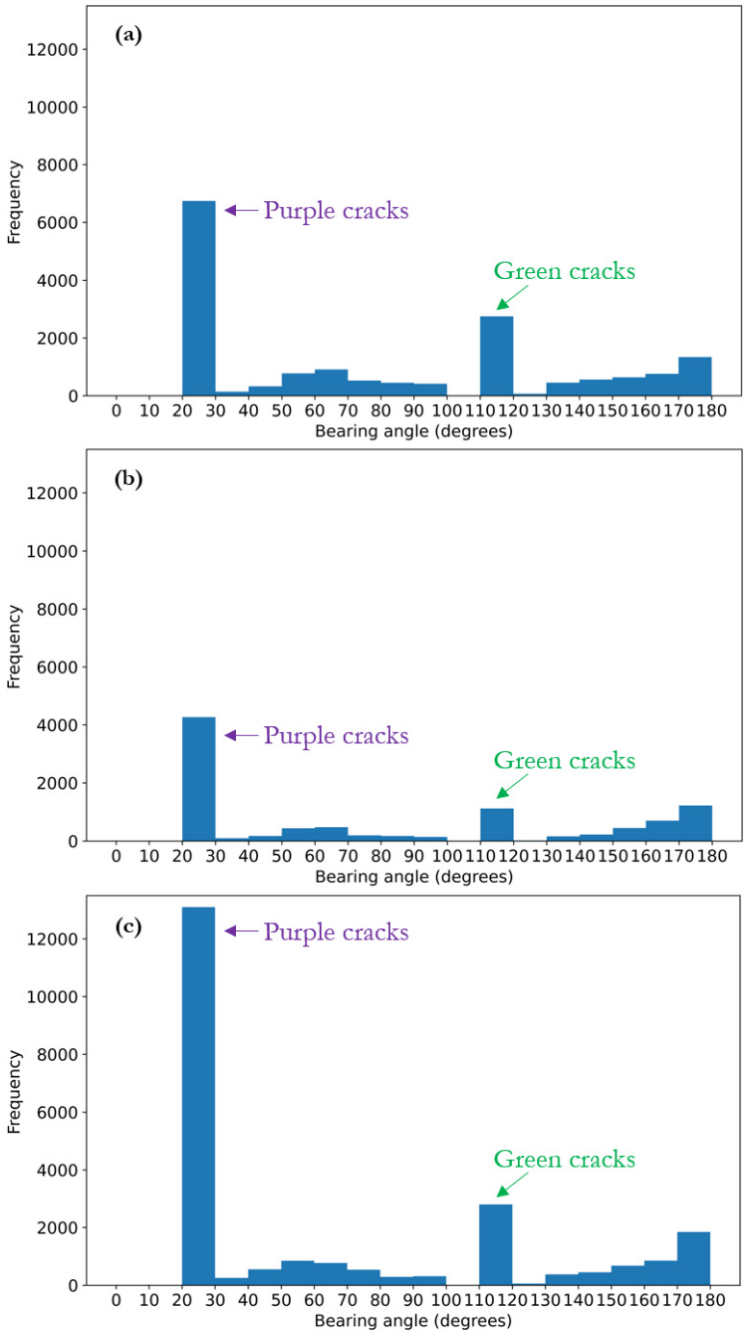

Figure 6.30: Histograms for the cracks bearing angle images shown in Figure 6.29. Generated from (a) PS05 dataset, (b) multi-dataset averaging, and (c) highest SNR method surface roughness images.

to 120 degrees. The 20 to 30 degrees range corresponds to the purple-coloured cracks, matching the GE-measured ground truth value of 21 degrees. The 110 to 120 degrees range corresponds to the green-coloured cracks, matching the ground truth value of 112 degrees. As previously discussed, the number of detected cracks varies depending on the surface roughness image used as input. Therefore, these histograms demonstrate that the cracks bearing angles estimated by the Radon transform-based method are in close agreement with the ground truth bearing angles measured from GE. It is important to note that the histograms are generated for bearing angles within the 0 to 180 degrees range. Bearing angles outside this range are wrapped into this range during histogram generation. This wrapping can be the reason for the higher pixel count in the 160 to 180 degrees range across all the histograms.

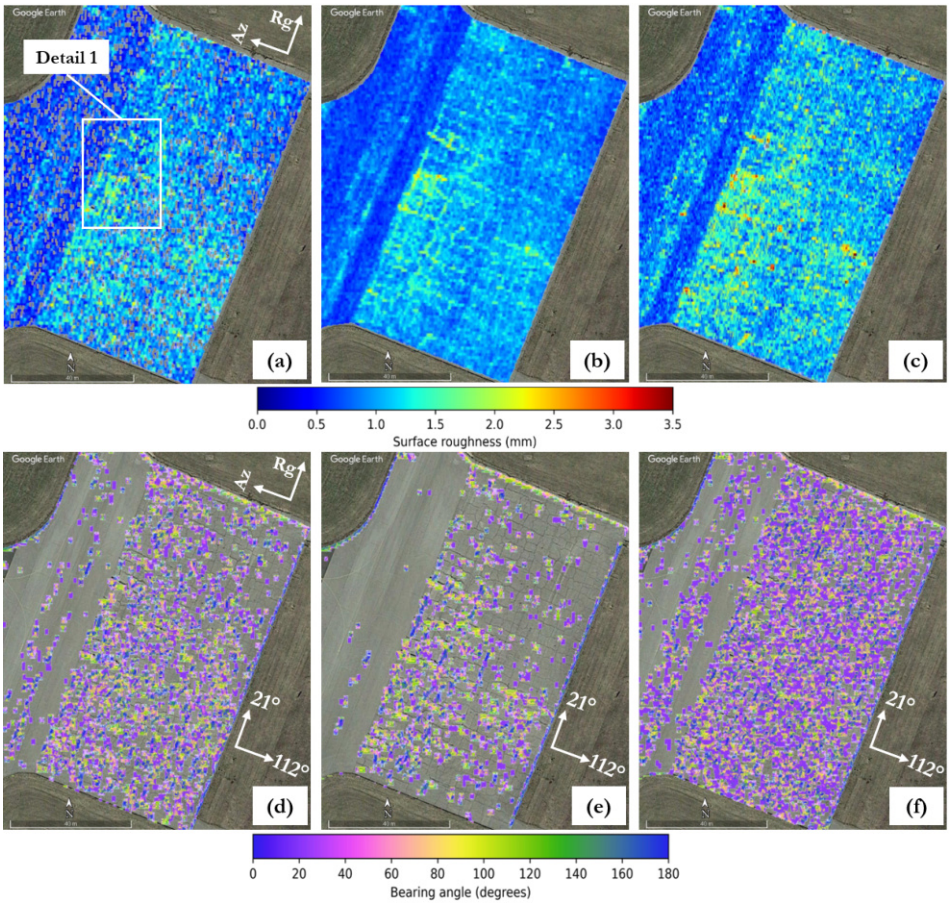

Figure 6.31: Cracks orientation estimation results for the Kaufbeuren parking area shown in Figure 6.28(c). Surface roughness images used as input for cracks orientation estimation generated from (a) PS05 dataset, (b) multi-dataset averaging, and (c) highest SNR method. Corresponding cracks bearing angle images generated from (d) PS05 dataset, (e) multi-dataset averaging, and (f) highest SNR method.

Figure 6.31 shows the cracks orientation estimation results for the Kaufbeuren parking area. Similar to Figure 6.29, Figures 6.31(a), (b), and (c) present the input surface roughness images generated from the PS05 dataset, multi-dataset averaging, and highest SNR methods, respectively. The corresponding cracks bearing angle images are displayed in Figures 6.31(d), (e), and (f). In these images, the detected cracks bearing angles predominantly appear in purple and green, indicating a close agreement with the GE-measured values (21 and 112 degrees). The results for a zoomed-in region of the parking area, marked as 'Detail 1' in Figure 6.31(a), are shown in Figure 6.32 for a closer examination of the cracks orientation estimation results for this parking area.

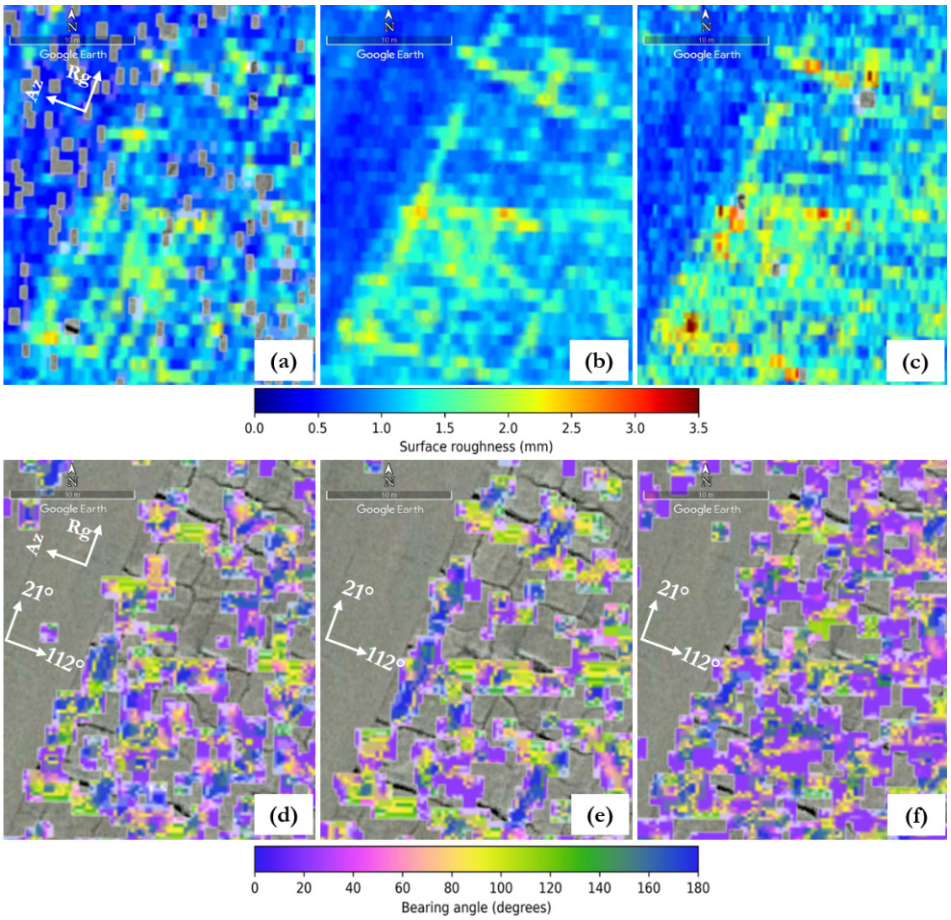

Figure 6.32: Cracks orientation estimation results generated for the section of the Kaufbeuren parking area marked as 'Detail 1' in Figure 6.31(a). Surface roughness images used as input for cracks orientation estimation generated from (a) PS05 dataset, (b) multi-dataset averaging, and (c) highest SNR method. Corresponding crack bearing angle images generated from (d) PS05 dataset, (e) multi-dataset averaging, and (f) highest SNR method.

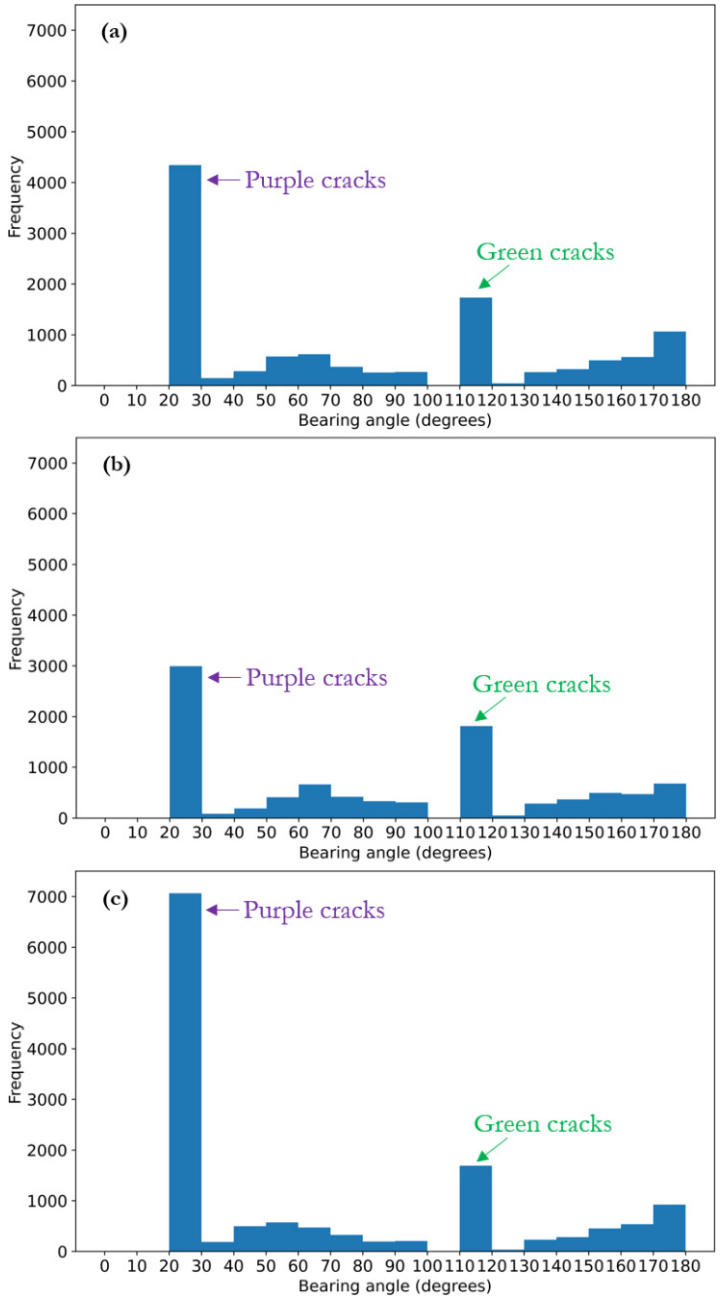

Figure 6.33: Histograms for the cracks bearing angle images shown in Figure 6.32. Generated from (a) PS05 dataset, (b) multi-dataset averaging, and (c) highest SNR method surface roughness images.

By analysing the cracks bearing angle images shown in Figure 6.32 for the section of the Kaufbeuren parking area marked as 'Detail 1', it can be observed that the dominant bearing angle for the cracks aligned in the north-east direction is around 20 degrees (purple), and the cracks aligned in the east-south direction have a dominant bearing angle of around 115 degrees (yellow to green). The location and shape of the cracks also match with the underlying GE optical view of these cracks. The main cracks visible in the GE image are accurately detected from the PS05 dataset while the number of detected cracks are less when the multi-dataset averaged surface roughness image is used as input. The cracks bearing angle image generated from the highest SNR fused surface roughness images shows a large number of cracks, which can be false cracks detections due to the grainy/noisy appearance of the surface roughness image. Therefore, the multi-dataset averaged and the highest SNR method based surface roughness images are not recommended for cracks detection and orientation estimation. The best approach will be to generate multiple cracks bearing angle images from individual SAR datasets having different flight heading angles.

Figure 6.33 shows the histograms for the cracks bearing angle images discussed in Figure 6.32. These histograms reveal that the dominant bearing angles fall within the 20 to 30 degrees (purple cracks) and 110 to 120 degrees (yellow to green cracks) ranges, which closely match the GE-measured bearing angles of 21 and 112 degrees, respectively. Thus, it can be concluded that the combined adaptive thresholding and Radon transform-based method is a reliable approach for estimating the orientation of cracks on the road surface. Similar to Figure 6.30, the histograms presented in this figure are also limited to bearing angles within the 0 to 180 degrees range, with values outside this range wrapped back into it. This wrapping likely accounts for the higher pixel count in the 160 to 180 degrees range.

Understanding the orientation of the cracks can aid in determining the causes of their formation and facilitate corrective measures. For example, longitudinal cracks, shown in purple, are aligned with the runway and are most likely caused by large tensile stresses developing near the tyre shoulders [101]. Transverse cracks, on the other hand, which are shown in yellow to green, are perpendicular to the runway and are caused mainly by factors such as soil settlement/shrinkage, improper joint spacing and freeze-thaw cycles during winter [31, 148].

However, it is important to note that the cracks detection, severity and orientation estimation results presented in this chapter were validated only w.r.t. the cracks visible in GE. Further comparisons and validations are required using very high-resolution optical photos such as those acquired with drone cameras. A flight campaign has been planned for this purpose, which is scheduled to take place in 2025.

6.4 Road Width Estimation

The road surface roughness images typically have h_{rms} values between 0 and 2 mm for the road surfaces, while regions outside the roads may have significantly higher or different h_{rms} values. This study utilises the abrupt change in h_{rms} values at the road boundaries to develop a method for road width estimation. The road width estimation results are intended as a byproduct of the cracks detection and orientation results.

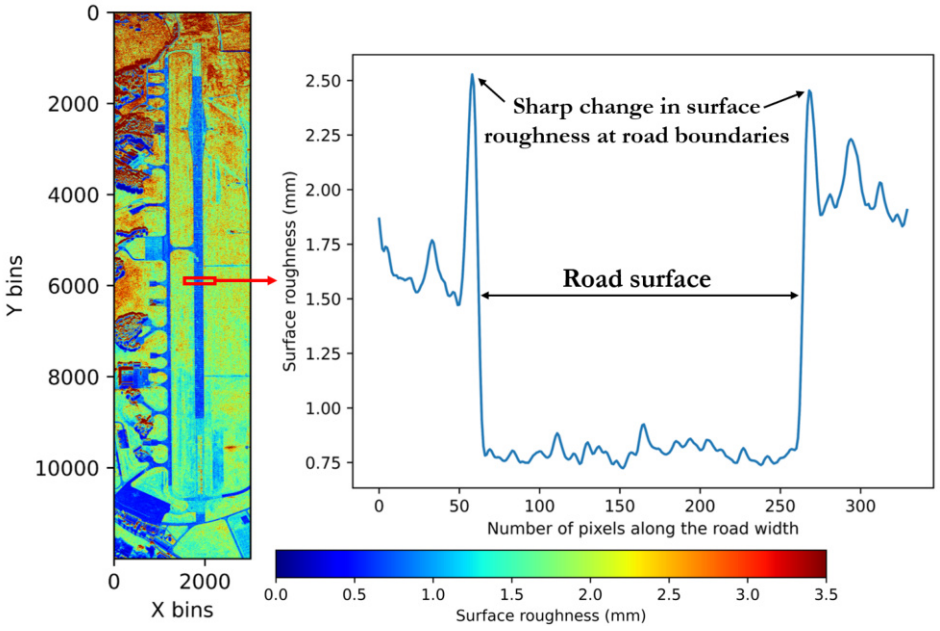

Figure 6.34: Basic concept of the road width estimation method.

The basic concept involved in the road width estimation method used in this study is illustrated in Figure 6.34. In this figure, the surface roughness image created for the Kaufbeuren runway is shown together with a surface roughness plot for a small section of the runway indicated using the red rectangle along the runway width (in transverse direction). When analysing the surface roughness plot, it becomes clear that the runway surface has low h_{rms} values below 1.0 mm, with a sharp increase in h_{rms} values up to 2.50 mm at the runway boundaries. By identifying these boundary/change points on both sides of the road surface where this abrupt increase in h_{rms} values occurs, the road width can be estimated. The block diagram of the processing chain developed based on this concept for road width estimation using the airborne F-SAR datasets is shown in Figure 6.35.

In this processing chain, the geocoded road surface roughness image and the OSM road layers are used as inputs for the road width estimation. After determining the geographic

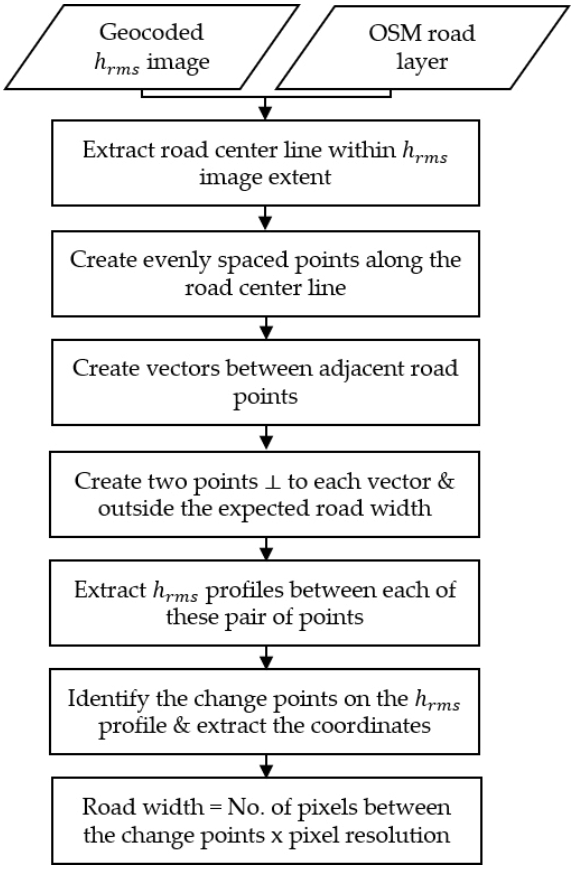

Figure 6.35: Block diagram of the processing chain adopted for road width estimation.

extent of the geocoded surface roughness image, the road centreline is extracted for the target roads within this geographic extent. Figure 6.27 on page 146 illustrates the representation of roads by a centre line between two endpoints. Along this extracted road centreline, evenly spaced points are generated at regular intervals (e.g. every 10 metres) for several estimates of the road width. Several vectors are then created between these neighbouring road points. It is important to note that these vectors run along the road centreline, and points perpendicular to these vectors are required to estimate the road width.

For each vector, two points are created that are perpendicular to the vector and outside the plausible road width. The next step is to extract surface roughness profiles (h_{rms}) between each pair of these perpendicular points. The analysis of each extracted h_{rms} profile is crucial to identify change points where h_{rms} values undergo abrupt changes. These identified change points for each h_{rms} profile serve as road boundary points

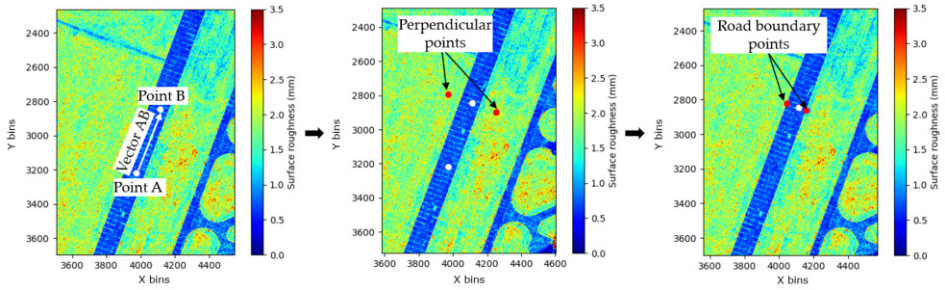

Figure 6.36: Graphical representation of the road width estimation methodology.

whose coordinates are extracted. The road width is then calculated by multiplying the number of pixels between each pair of change points by the spatial resolution of the input road surface roughness image. A KML file is then created to visualise the road width measurements in GE. A graphical representation of the road width estimation methodology is shown in Figure 6.36.

6.4.1 Road Width Estimation Results and Discussion

This section discusses the experimental road width estimation results generated from the X-band airborne F-SAR datasets.

Figure 6.37 shows the road width measurements for the Kaufbeuren runway visualised in GE using the geocoded surface roughness images from F-SAR datasets. The white dots automatically overlaid in GE correspond to the measured road widths for specific sections of the runway, and clicking on each dot shows the corresponding measured road width value. The comparison in Figure 6.37 shows that the road width measured with the F-SAR dataset is 29 m for a specific section of the Kaufbeuren runway, which closely matches the actual value of 29.41 m measured with GE. This indicates a good agreement between the road widths estimated by F-SAR and the actual values on the ground. The surface roughness profile shown in the figure refers to the section of the runway marked by the yellow line in the GE image. The examination of this profile shows higher roughness values outside the runway, with clear spikes at the boundaries of the runway. These change points, which correspond to an abrupt increase in surface roughness, were used to determine the road width as shown in the GE image.

The road width measurements for Apfeltranger road near the Kaufbeuren test site are shown in Figure 6.38(a). This road is a single-lane tertiary road. Similar to Figure 6.37, the white dots shown in GE correspond to the measured road widths for specific sections of the road surface, and clicking on each dot displays the corresponding measured road width value. It can be seen that the road width measured with the airborne F-SAR

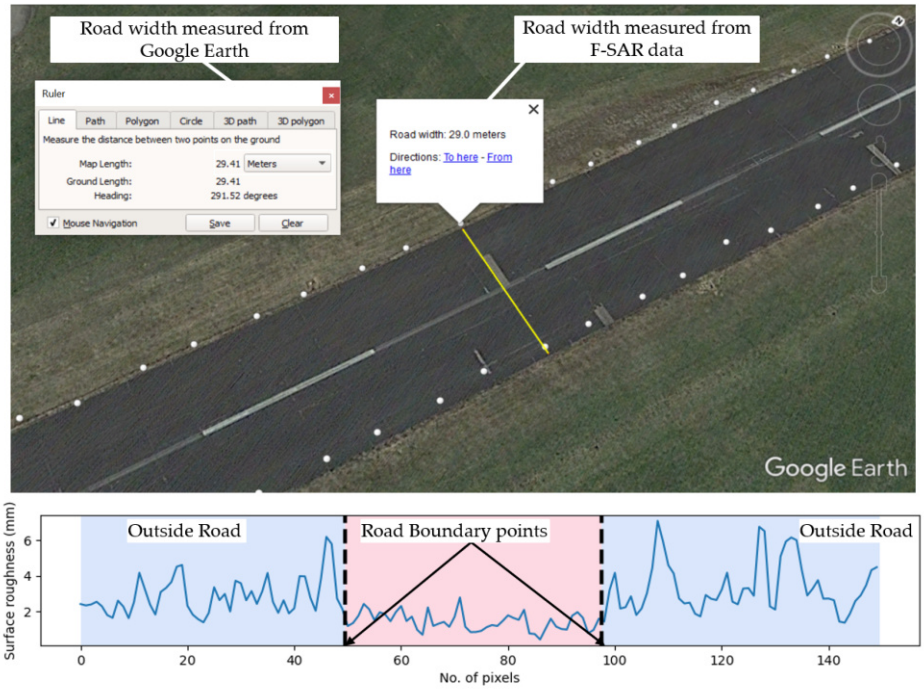

Figure 6.37: Road width estimation results for the Kaufbeuren runway visualised in GE.

dataset for this road surface is 6 m and the road width measured with GE for the same region indicated by the yellow line is 6.34 m, demonstrating close agreement with each other. Figure 6.38(b) shows the surface roughness image of the same section of the Apfeltranger road overlaid in GE. From this figure, it can be seen that the road width points are generated exactly at the road boundaries where the sharp change in surface roughness occurs demonstrating the capability of the road width estimation algorithm in estimating the surface roughness change points.

From both Figures 6.37 and 6.38, it can be summarised that the proposed road width estimation method can provide reliable road width measurements with the airborne F-SAR datasets for both wide runways and single lane narrow tertiary roads. However, it can be observed in both figures that the white dots representing the measured road widths do not perfectly align with the road boundaries visible in the underlying GE image. This discrepancy arises primarily from slight geocoding offsets in the surface roughness images generated from the F-SAR data, which serve as input to the processing chain. Additionally, some white dots exhibit further offsets relative to their neighbouring points, likely caused by fluctuations in the surface roughness profile, which can result in minor offsets (a few pixels) in detecting the boundary points. Further investigations

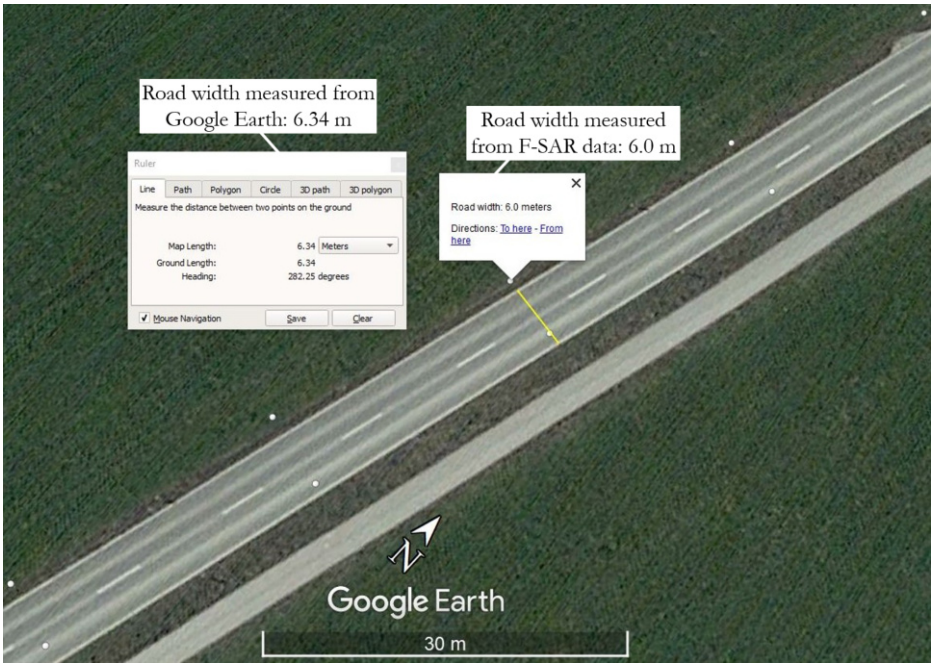

(a)

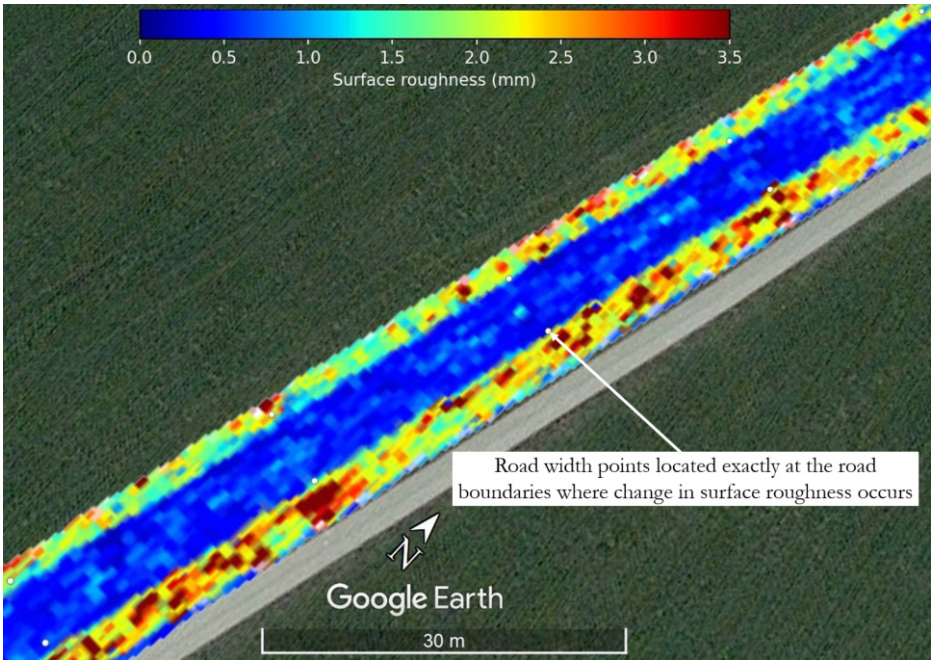

(b)

Figure 6.38: Road width estimation results for the Apfeltranger road near the Kaufbeuren test site visualised in GE. (a) Road width points. (b) Surface roughness image.

are needed to fine-tune the robustness of this method and to extend the scope of this processing chain to more complex scenarios such as multi-lane roads, intersections, etc.

6.5 Chapter Summary

In this chapter, methodologies for detecting cracks and estimating their orientation on road surfaces, as well as a method for estimating road width, are presented. All the analyses for this chapter were done using the fully polarimetric X-band airborne F-SAR datasets.

Analysis of the surface roughness images from various F-SAR datasets showed that crack visibility in SAR images depends on the flight heading angle due to the oriented nature of cracks. Therefore, the flight heading angle for cracks detection and orientation estimation should be chosen based on the orientation of the cracks of interest, such as longitudinal or transverse cracks. SAR data acquisition with a flight track parallel to the cracks orientation ensures the best visibility of the crack in the SAR backscatter and surface roughness images.

The investigations with the Canny edge detector and the stationary wavelet transform (SWT) showed that these methods are not suitable for reliable cracks detection using the X-band airborne F-SAR data used in this study. While the Radon transform showed promising results for estimating crack severity and orientation on simulated SAR images, it has a significant limitation: it generates outputs for all pixels, regardless of whether they correspond to cracked or smooth surfaces. This makes the Radon transform unsuitable for direct application on σ^o backscatter or surface roughness images.

To solve this problem, a combined approach of an adaptive thresholding algorithm and the Radon transform was proposed. The adaptive thresholding algorithm detects cracks in F-SAR surface roughness images, while the Radon transform estimates the severity and orientation of these cracks. This combined approach outperformed previous methods, with results visually validated using cracks visible on GE. The Radon magnitude values were used to colour-code the detected cracks showing their severity from minor to severe, and the estimated orientation angles closely agreed with the measurements from GE.

Fused surface roughness images produced by multi-dataset averaging or highest SNR methods are not ideal for cracks detection, as they may either miss smaller cracks or produce many false detections. The most effective input for accurate cracks detection and orientation estimation is a surface roughness image generated from a single F-SAR dataset. However, cracks with certain orientations might be undetected if they are not well-visible in this single dataset. To address this limitation, it is recommended to generate multiple cracks detection and orientation estimation results using several F-SAR datasets acquired with different flight heading angles. Specifically, using at least

two flight heading angles: one parallel and one perpendicular to the road. This will help in detecting both longitudinal and transverse cracks, which are common on road surfaces.

Additionally, a method for estimating road width based on surface roughness change point detection was developed, yielding results closely aligned with measurements from GE. All the results, including crack severity, orientation estimation and road width estimation, were visualised in GE, providing a user-friendly way to interpret the results without the need for expertise in SAR data analysis.

7 Discussion and Outlook

This chapter provides an overview of the results presented in this doctoral thesis and provides an outlook for future research activities in the field of road condition monitoring using airborne and spaceborne SAR systems.

7.1 Discussion

This doctoral thesis focused on the development of algorithms for road condition monitoring using focused SAR images acquired by high-resolution airborne and spaceborne SAR systems. Within the scope of this research, processing chains were developed for estimating the road surface roughness using both airborne and spaceborne SAR systems. Furthermore, processing chains were developed for detecting cracks on the road surfaces, determining the orientation of these cracks and estimating the width of roads of interest.

In Chapter 1, the importance of maintaining an optimal level of road surface roughness, insights into the formation of cracks and potholes, and a brief discussion of the safety issues caused by these parameters were discussed. This chapter also explored the state-of-the-art technologies currently in use for road surface condition monitoring using survey vehicles and the drawbacks associated with them, including the difficulty in performing nationwide monitoring, labour and cost intensiveness, and time-consuming processes. Since SAR backscatter signals are sensitive to surface roughness and dielectric changes, it is considered a suitable candidate for large-scale road condition monitoring. The principles of SAR systems and the state-of-the-art roughness estimation models developed for SAR systems were discussed in detail in Chapter 2.

When analysing fully polarimetric airborne X-band SAR data for road condition monitoring, in particular the data acquired using DLR's F-SAR system, cross-polarisation (HV and VH) channels exhibited an SNR below the noise floor (NESZ) of the SAR system, rendering them unsuitable. Existing roughness estimation models, reliant on these channels and also designed for soil roughness, were thus found to be ineffective for road surfaces. Chapter 3 introduced a new semi-empirical roughness model tailored for airborne X-band SAR data, utilising only co-polarisation channels (HH and VV) for road surface roughness estimation. This model demonstrated superior performance compared to the state-of-the-art roughness estimation models. It achieved an RMSE of approximately 0.37 mm with the ground truth surface roughness data, effectively discerning variations in surface roughness. Incorporating upper σ^o and lower SNR thresholding techniques in the processing chain eliminated invalid surface roughness

estimates. Fusion of surface roughness images from multiple datasets using the multi-dataset averaging technique minimised errors due to incidence and flight heading angle variations, low SNR, and shadow regions, improving the RMSE to 0.27 mm. However, this model is valid only under specified validity conditions: incidence angles greater than 30 degrees and surface roughness values less than 12.43 mm for the X-band SAR system. Furthermore, it is recommended to use SAR datasets acquired in VV polarisation with steeper incidence angles ranging from 30 to 35 degrees for reliable road roughness estimation, ensuring the highest possible SNR within the validity range of the model.

Machine learning-based regression models were then evaluated for road surface roughness estimation. The support vector regression (SVR), random forest regression (RFR) and artificial neural network (ANN) models discussed in Chapter 4 provided results that were consistent with both the new semi-empirical model and the ground truth surface roughness data. The highest RMSE observed for these models with the ground truth data was 0.39 mm, indicating a comparable performance to the new semi-empirical model. However, a major challenge lies in the limited ground truth data available for training these machine learning-based models. Techniques such as bagging and cross-validation can mitigate this problem up to some extent by preventing overfitting during model training. However, it is worth noting that the new semi-empirical model still gives slightly better results, and is also more computationally efficient and faster compared to the machine learning-based models. Therefore, the use of machine learning-based models is only recommended for scenarios where the new semi-empirical model is less reliable, e.g., when it operates outside its validity conditions. Consequently, the new semi-empirical model is a good option for road surface roughness estimation when the input data meet its validity conditions, while in other situations machine learning-based models may be more suitable for better road surface roughness estimation.

Chapter 5 presents investigations into road surface roughness estimation using spaceborne SAR systems. The analysis, conducted with the X-band data acquired by the TerraSAR-X (TS-X) satellite, revealed challenges such as reduced SNR compared to airborne SAR systems due to increased platform height. Techniques like additive noise minimisation and multilooking were employed to enhance the SNR. The new semi-empirical model, initially developed for airborne SAR, was adapted for spaceborne SAR data, characterised by coarser spatial resolution and lower SNR. Results from this adapted model exhibited good agreement with airborne SAR results and ground truth values, demonstrating an RMSE of approximately 0.32 mm. Notably, X-band spaceborne SAR in staring spotlight (ST) mode and VV polarisation with 30 to 35-degree incidence angles proved most suitable for road surface roughness estimation. The ST-imaging mode offered the highest spatial resolution, while VV polarisation with steeper incidence angles provided the necessary SNR. Challenges in road condition monitoring with state-of-the-art spaceborne SAR systems includes reduced swath and

single polarisation operation in ST mode, along with difficulties in estimating road surface roughness for north-south oriented roads during busy traffic times due to vehicle movement in the azimuth direction of the SAR system in the sun-synchronous orbit.

Investigations on cracks detection, orientation estimation and road width estimation are discussed in Chapter 6. Analysis of multiple road surface roughness images from various F-SAR datasets revealed that cracks visibility in SAR images depends on the flight heading angle, necessitating the selection of flight heading angle based on the orientation of the cracks of interest. Investigations with the Canny edge detector and the stationary wavelet transform (SWT) demonstrated their ineffectiveness for reliable crack detection. The Radon transform showed promising results, however, it provided estimates for all pixels regardless of whether they were cracked or not. To solve this issue, a combined approach using an adaptive thresholding algorithm and the Radon transform was proposed, which successfully detected cracks and estimated their severity and orientation, with results validated using GE. Additionally, the road width estimation results obtained by detecting sharp changes in surface roughness values at the road boundaries also showed good agreement with the GE measurements.

Results for road surface roughness, crack detection, orientation estimation, and road width estimation were geocoded and overlaid on GE for enhanced visualisation and interpretation. This representation is expected to aid road maintenance authorities in pinpointing issues on specific road sections without requiring SAR expertise.

The presented results confirm that this doctoral thesis has effectively fulfilled its research objectives. Through the development of algorithms and processing chains, it has enabled the estimation of road surface roughness utilising both DLR's airborne X-band F-SAR and Germany's spaceborne TS-X systems. Moreover, methodologies for detecting cracks, estimating orientation, and determining road width using the airborne X-band F-SAR system have been devised.

7.2 Future Work and Outlook

The following research concepts are proposed for the further advancement in the field of road condition monitoring using airborne and spaceborne SAR systems:

1. **International Roughness Index (IRI) Estimation:** The IRI is a widely used measure to assess the unevenness of road surfaces. It is determined by analysing the longitudinal profile of road surfaces and is used by highway authorities worldwide as a functional indicator of the flatness of roads, a crucial aspect that affects driving comfort and safety. Roads are often categorised based on their IRI measurements.

To estimate the IRI with SAR systems, a very-high resolution digital elevation model (DEM) generated from interferometric SAR data can be used. The DEM can, for example, be produced by using the interferometric X-band SAR data from DLR's F-SAR system. This radar-derived DEM facilitates the extraction of both the longitudinal and, with high-resolution data, even the transversal profiles of the road surface, enabling the accurate estimation of IRI values.

2. **Clustering of the Cracks Detected on the Road Surface:** The cracks detection method presented in Chapter 6 of this thesis, works on a pixel-by-pixel basis. As a next step, it is recommended to cluster these identified cracks pixels.

   Clustering these cracks pixels after detection improves the ability to recognise spatial patterns and distributions, providing a more comprehensive understanding of the cracks severity and damage extent. In addition, clustering facilitates the extraction of key features such as cracks length, size and shape, which are critical for developing accurate predictive models and prioritising maintenance actions. The Density-based Spatial Clustering of Applications with Noise (DBSCAN) algorithm and machine learning-based clustering algorithms can be considered as potential candidates for this purpose.

3. **Advancement of the Road Width Estimation Method:** The road width estimation method discussed in Chapter 6, which is based on the detection of change points in surface roughness values, is currently limited to simple situations such as a single road. It is not suitable for more complex scenarios with multiple parallel roads, intersections etc. One approach to extend the applicability to these complex scenarios could be to collect additional data from OSM. Even though road width information is generally not available in OSM, details such as the type of roads, the number of lanes, information about road intersections, etc. can be obtained from OSM. This additional information could then be used to customise the search criteria or conditions for identifying the change points of the surface roughness values.

4. **Airborne Polarimetric Ka-band SAR for Road Condition Monitoring:** A very-high resolution airborne SAR system operating in the Ka-band is expected to exhibit increased sensitivity to road surface roughness and damages, such as cracks and potholes. This increased sensitivity is attributed to its smaller wavelength, approximately 1 cm, in contrast to the X-band SAR system used in this thesis, which has a wavelength of approximately 3 cm.

   The use of a Ka-band SAR system is anticipated to result in higher backscattering from even minor undulations at the millimetre level on the road surface, enhancing the capability of the SAR system in capturing fine road surface details.

Additionally, there is potential for utilising the Ka-band SAR system for estimating the IRI parameter. An airborne polarimetric Ka-band SAR of this kind is currently under development at DLR.

5. **Future High Resolution Wide Swath (HRWS) Spaceborne SAR System for Road Condition Monitoring:** Chapter 5 highlighted the challenges of assessing road surface roughness with spaceborne SAR. These challenges arise from the low SNR and the requirement to operate state-of-the-art SAR systems such as TerraSAR-X in high-resolution imaging modes such as ST mode, which limits data acquisition to a single polarisation and reduces the swath coverage.

   Looking forward, the development of a future high-resolution wide-swath (HRWS) spaceborne SAR system with a bandwidth of up to 1200 MHz and an improved noise equivalent sigma zero (NESZ) holds promise for improving the accuracy of road surface roughness estimation.

Appendix

A Overview of Test Sites and Data Collection Activities

A.1 Test Sites

To investigate the potential of SAR to reliably estimate road surface roughness as well as to detect cracks and potholes and thereby obtain information about the overall condition of the road surface, test sites with surfaces made of typical road construction materials with different surface roughness values, such as concrete, asphalt or comparable materials, as well as some unrepaired sections with cracks and potholes are needed. For this study, three such test sites were identified whose surfaces consist of materials with different surface roughness, namely the Kaufbeuren airfield, duraBASt and Braunschweig test sites. In addition, Kaufbeuren airfield has some sections with cracks and potholes. The following sub-sections explain the details of the individual test sites.

A.1.1 Kaufbeuren Airfield Test Site

The Kaufbeuren airfield, situated in Bavaria, Germany, is a former military airfield featuring runways, taxiways, and parking areas. As a decommissioned facility, it lacks regular maintenance, resulting in the presence of rough and cracked surfaces. Figure A.1 displays the Google Earth (GE) image of this test site.

A close examination of Figure A.1 shows that the two ends of the runway are most likely made of concrete, as indicated by the yellow rectangles, while the section in between is asphalt. The photo on the top left of Figure A.1 shows an area that is most likely made of concrete, with both smooth concrete and concrete areas with repeated cuts. Similarly, the photo on the bottom right of Figure A.1 shows an asphalt area in the centre of the runway where repair work has been carried out using a rougher material, which may most likely be concrete. The presence of various surface types, including smooth, rough, and cracked surfaces composed of different materials, makes Kaufbeuren airfield an ideal test site for this study [P4, P6, P8]. Furthermore, ground truth (GT) surface roughness values (GT h_{rms}) were collected at this test site, which are used to train the new semi-empirical and machine learning models and also to validate the road surface roughness results estimated using these models. Further details regarding the GT data collection process are discussed in sub-section A.4 of this Appendix. In addition, the SAR datasets obtained over this test site were used for crack and pothole detection leveraging the presence of the severe cracks and potholes present here.

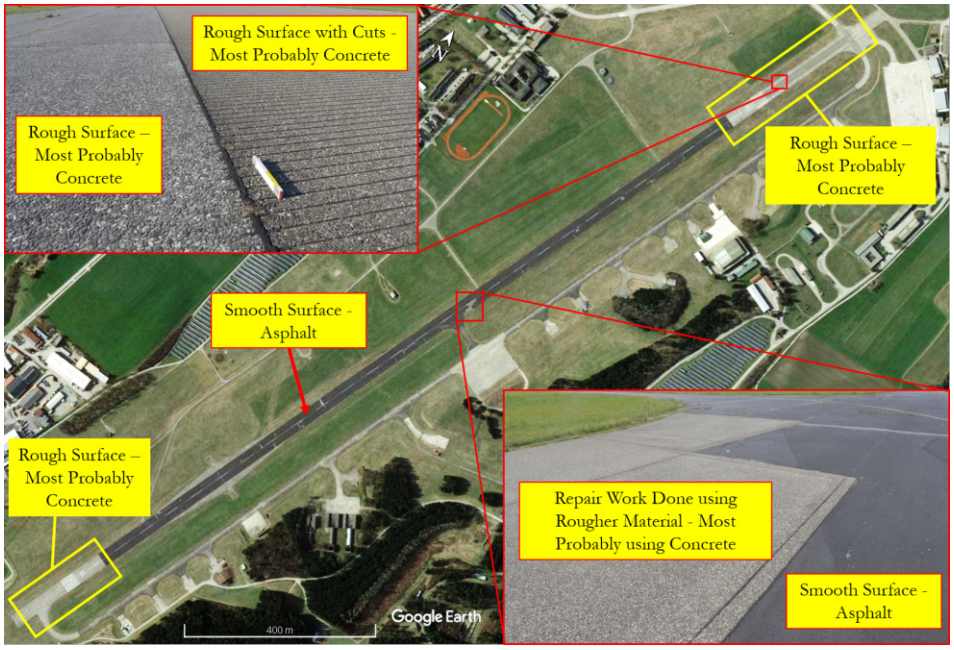

Figure A.1: Kaufbeuren airfield test site.

A.1.2 duraBASt Test Site

The "Demonstrations-, Untersuchungs- und Referenzareal der BASt (duraBASt)" test site, situated near the Cologne-East motorway intersection in Germany, is managed by the Federal Highway Research Institute, known as "Bundesanstalt für Straßenwesen (BASt)". Figure A.2 displays the GE image of the Cologne motorway intersection and the duraBASt test site. The duraBASt area, depicted within the yellow ellipse in the zoomed view, exhibits varied colours in the GE image due to the use of diverse construction materials with differing surface roughness values. This characteristic makes the site suitable for this study [P4, P8].

A.1.3 Braunschweig Test Site

The third test site is the Wolfsburg motorway intersection in Braunschweig, Germany, chosen for its long motorway stretch without disturbances from trees or buildings. Figure A.3 displays the GE image of this location. While the GE image suggests a relatively uniform road surface roughness for most of the test site, a noticeable change in the colour shade at the right end indicates potential repair work using asphalt with a different material composition, suggesting a variation in surface roughness in this region [P4, P8].

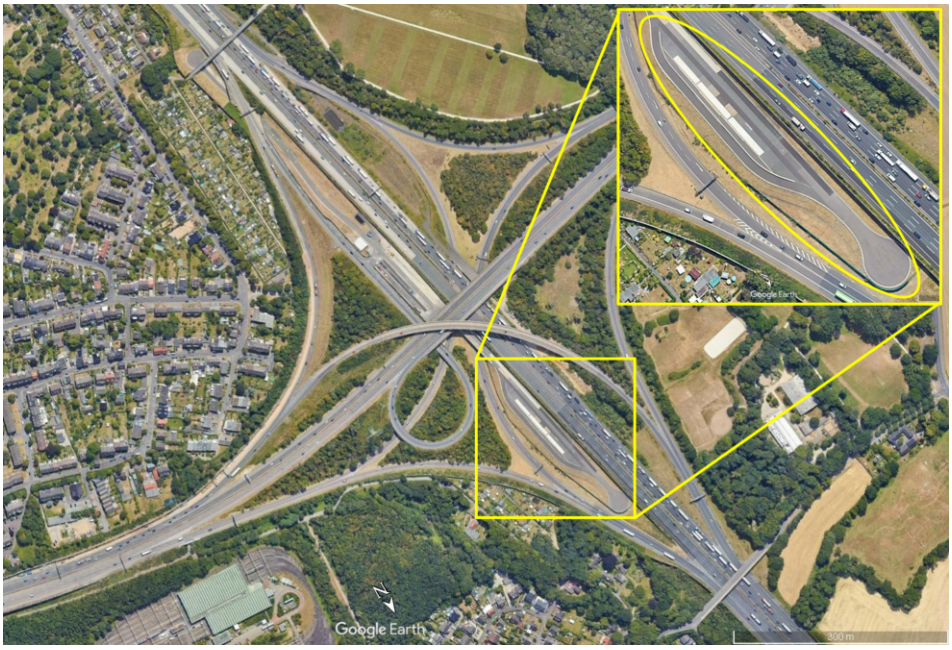

Figure A.2: duraBASt test site.

Figure A.3: Braunschweig test site.

A.2 F-SAR System and Data Acquisition

The high-resolution fully polarimetric SAR data acquired with the airborne F-SAR (Flugzeug-SAR) system of the German Aerospace Center (DLR) over the test sites Kaufbeuren, duraBASt and Braunschweig are used for this study. An overview of the F-SAR system and information about the datasets acquired over the test sites are discussed in the following sub-sections.

A.2.1 Overview of the F-SAR System

The F-SAR system, developed and operated by DLR's Microwaves and Radar Institute, is one of the most advanced airborne SAR systems capable of performing interferometric and polarimetric imaging in various frequency bands [113]. It is the successor to the former E-SAR (Experimental SAR) system developed and operated by DLR [119]. The F-SAR system was developed using commercial, off-the-shelf hardware components. The antennas for the different frequency bands were developed at DLR. The platform used for the F-SAR system is a Dornier DO 228-212 (D-CFFU) aircraft (cf. Figure A.4) [114].

Figure A.4: DLR research aircraft Dornier DO 228-212 equipped with the F-SAR system. The highlighted detail shows the antenna carrier mounted on the fuselage.

The F-SAR system is capable of acquiring fully polarimetric SAR data in the X, C, S, L and P frequency bands, with the added capability of simultaneous data acquisition in different frequency bands. The antenna mount for the X, C, S and L-bands is installed in the fuselage of the aircraft on the right side and carries three X-band, one C-band, two S-band and one L-band planar antennas (see zoomed view in Figure A.4), and the

P-band antenna is mounted under the aircraft body. Antenna pairs X1, X2 and S1, S2 can be used for cross-track interferometric (XTI) data acquisition in X-band and S-band, respectively. Antenna pair X2, X3 for X-band can be used for along-track interferometric (ATI) data acquisitions. The main technical parameters of the F-SAR system are listed in Table A.1 [113, 114].

Table A.1: Technical parameters of the F-SAR system in different frequency bands [113, 114].

Band	X	C	S	L	P
Frequency [GHz]	9.60	5.30	3.25	1.325	0.35
Bandwidth [MHz]	760	400	300	150	100
Pulse Repetition Frequency (PRF) [kHz]	5	5	5	10	12
Transmit Power [kW]	2.50	2.20	2.20	0.70	0.70
Range Resolution [m]	0.2	0.4	0.5	1.0	1.5
Azimuth Resolution [m]	0.2	0.3	0.35	0.4	1.5
Channels	4	2	2	2	2
Polarisation	Fully polarimetric (Quad-Pol)				
Swath Width [km]	12.5 (at max. bandwidth and max.) flight altitude				

A.2.2 F-SAR Datasets used for this Study

The choice of SAR parameters is an important decision that affects the accuracy and effectiveness of road surface roughness estimation and also the detection of cracks and potholes. The road surface, which is inherently smooth and has millimetre-scale surface irregularities, when observed with SAR sensors at different wavelengths, shows an interesting phenomenon. As the wavelength increases compared to the surface irregularities, the surface appears smoother and smoother due to the increased specular reflection that redirects the transmitted electromagnetic (EM) signals away from the radar, resulting in less backscatter and a lower signal-to-noise ratio (SNR). On the other hand, the same surface appears rougher to a SAR system operating at a shorter wavelength, resulting in more backscatter towards the SAR antenna and thus a higher SNR [140]. Therefore, the shortest available wavelength should be used to ensure the most accurate estimation of road surface roughness and the detection of very fine road details. In the case of the F-SAR system, this is the X-band with a wavelength of about 3 cm. In addition, the spatial resolution of the SAR system plays a critical role in identifying fine road surface features, and F-SAR offers the highest possible spatial resolution in the X-band with

an azimuth and range resolution of 0.2 m (cf. Table A.1) [75]. Considering all these factors, the fully polarimetric F-SAR datasets acquired in X-band are the best available choice for road surface roughness estimation and for cracks and potholes detection.

The Kaufbeuren airfield was selected as the primary test site for this study because of the availability of the long runway and taxiway without vehicle traffic, which also provided the opportunity to collect ground truth surface roughness data. For the road condition monitoring, the data acquisition should be done on dry days to avoid any backscatter variations due to rain water filling the voids or cracks on the road surface. Two flight campaigns were conducted at the Kaufbeuren airfield test site to acquire the high-resolution X-band F-SAR datasets. Multiple datasets were acquired with different incidence angles and aspect angles w.r.t. the Kaufbeuren runway to understand the effects of incidence angle and look direction changes in the road surface roughness estimation and also in the detectability of cracks and potholes. The first flight campaign was conducted on 04th September 2020 with the aircraft flown at an altitude of approximately 3 km. The details about the acquired datasets are given in Table A.2.

Table A.2: F-SAR data sets acquired over Kaufbeuren airfield during the first flight campaign.

Dataset ID	Incidence angle at the runway	Flight track w.r.t. runway	Flight heading angle
PS02	23° to 51°	45°	91.18°
PS03	29° to 55°	45°	91.20°
PS04	30° approx.	Parallel	201.71°
PS05	32° to 55°	Across	291.69°
PS06	32° approx.	Parallel	21.70°
PS08	35° approx.	Parallel	201.72°
PS10	34° approx.	Parallel	21.70°
PS11	39° approx.	Parallel	201.71°
PS12	40° approx.	Parallel	21.70°
PS13	45° approx.	Parallel	201.72°
PS14	45° approx.	Parallel	21.70°

Table A.3: F-SAR datasets acquired over Kaufbeuren airfield during the second flight campaign.

Dataset ID	Incidence angle at the runway	Flight track w.r.t. runway	Flight heading angle	Flight altitude
PS01	11° to 57°	Across	111.87°	2.2 km
PS02	22° to 60°	Across	291.87°	
PS03	36° to 40°	Parallel approx.	201.83°	
PS04	37° approx.	Parallel	21.81°	
PS05	40° to 50° approx.	Circular	0 to 360°	4.4 km

In the second flight campaign, both linear and circular flight paths were used. The linear flight paths were flown on 31st May 2022, and this time the flight altitude was lowered to about 2.2 km to test whether this could improve the SNR of the cross-polarisation channels (HV and VH). The circular SAR (CSAR) datasets were acquired on 08th June 2022 to test the dependency of the aspect angle on the road surface roughness estimation. However, in the case of the CSAR datasets, the flight altitude was increased to 4.4 km due to operational constraints for circular flight path. Table A.3 shows the information about the acquired datasets.

In addition, several F-SAR datasets were collected from the duraBASt and Braunschweig test sites to test the applicability of the methods developed in this study on real roads. The flight campaign at the duraBASt test site was conducted on 10th September 2019 and the flight campaign at the Braunschweig test site was conducted on 31st August 2020.

A.3 TerraSAR-X System and Data Acquisition

This study also investigated the possibility of estimating road surface roughness using spaceborne SAR data. For this purpose, the high-resolution data acquired by the German satellite TerraSAR-X (TS-X) and its twin satellite TanDEM-X (TD-X) over the test sites Kaufbeuren and Braunschweig were utilised. The following sub-sections provide an overview of the TS-X system as well as information about the TS-X datasets used for this study.

A.3.1 Overview of the TS-X System

The TS-X and TD-X satellites were developed by Airbus Defense and Space (former EADS Astrium) and operated by DLR in the framework of a Public Private Partnership (PPP). The TS-X satellite was launched in June 2007 and the TD-X satellite was launched

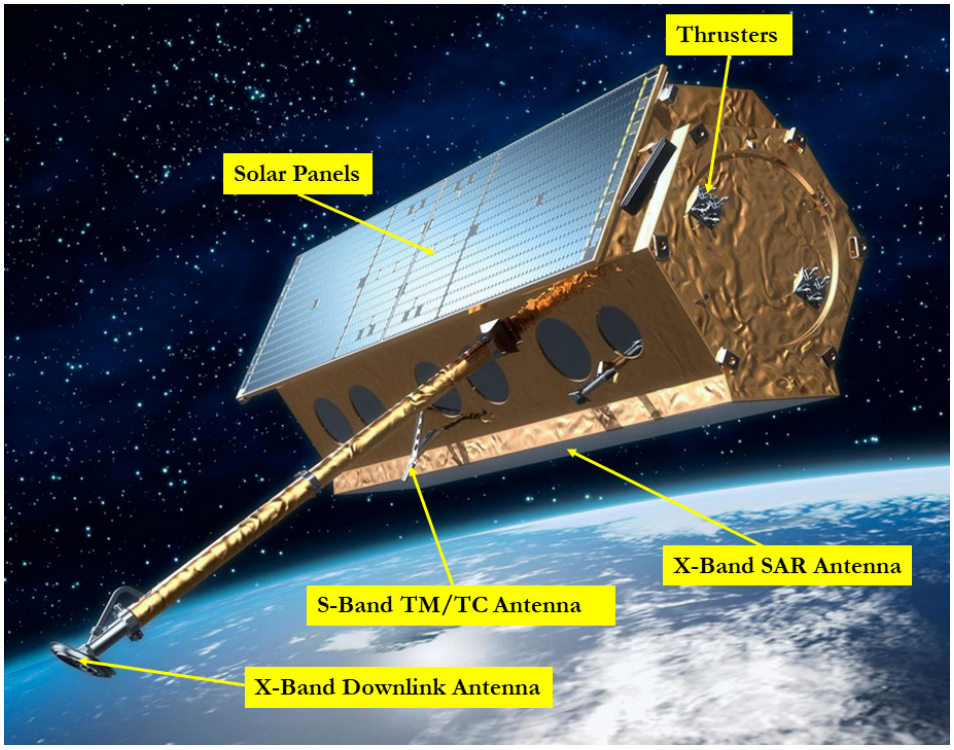

Figure A.5: Artistic illustration of the TerraSAR-X satellite with main components marked.

in June 2010. Both satellites are flying in a close helix formation in a sun-synchronous repeat orbit with the major aim to perform single pass interferometry to generate a high-resolution digital elevation model (DEM) [18]. Since both satellites are identical, no distinction is made between them in this study, instead, they are collectively referred to as the TS-X system.

The TS-X system operates in X-band, with a centre frequency of 9.65 GHz. It employs a right-looking, active electronically steerable phased array antenna with a maximum chirp bandwidth of up to 300 MHz. The system supports both single and dual polarised data acquisitions, depending on the selected imaging mode [100]. The spatial resolution and the extent of the swath covered by the TS-X system also vary according to the imaging mode chosen [7, P6]. Information about the available imaging modes and their corresponding data acquisition parameters are given in Table A.4.

Table A.4: TerraSAR-X imaging modes.

Imaging Mode	Swath Coverage (Azimuth x Range) [km]	Spatial Resolution (Azimuth x Range) [m]	Polarisation	Incidence Angle [^{o}]
Staring SpotLight (ST)	3.7 x 4	0.24 x 0.6	Single HH or VV	20-45
HighRes SpotLight (HS)	5 x 10	1.1 x 1.2	Single HH or VV	20-55
		2.2 x 1.2	Dual HH and VV	
SpotLight (SL)	10 x 10	1.7 x 1.2	Single HH or VV	20-55
		3.4 x 1.2	Dual HH and VV	
StripMap (SM)	50 x 30	3.3 x 1.2	Single HH or VV	20-45
	50 x 15	6.6 x 1.2	Dual HH and VV, HH and HV or VV and VH	
ScanSAR (SC)	150 x 100	18.5 x 1.2	Single HH or VV	20-45
Wide ScanSAR (WS)	200 x 270	40 x (1.7-3.3)	Single HH , HV, VH or VV	15.6-49

A.3.2 TS-X Datasets used for this Study

In this study, mainly X-band datasets acquired by the TS-X satellite in staring spotlight (ST) imaging mode were used to investigate the feasibility of global road condition monitoring using spaceborne SAR. The choice of ST mode is to achieve the best possible spatial resolution, which is approximately 0.24 x 0.60 m (azimuth x range) and a swath coverage of 3.7 x 4 km in azimuth and range directions, respectively (cf. Table A.4) [7, P6]. Details of the datasets acquired over the Kaufbeuren and Braunschweig test areas are listed in Table A.5.

Table A.5: TS-X datasets acquired in staring spotlight (ST) mode.

Test site	Date of acquisition	Polarisation	Incidence angle at the runway
Kaufbeuren	16.03.2014	HH	43.7°
Kaufbeuren	13.08.2022	VV	31.6°
Kaufbeuren	23.09.2022	VV	43.7°
Kaufbeuren	29.09.2022	VV	31.0°
Braunschweig	14.02.2023	VV	26.5°
Braunschweig	21.02.2023	VV	25.5°

A.4 Ground Truth Surface Roughness Data Collection

A ground truth (GT) surface roughness (GT h_{rms}) data collection activity was performed on 3rd September 2020 at the Kaufbeuren airfield test site to validate the surface roughness values (h_{rms}) estimated from the F-SAR and TS-X datasets using state-of-the-art roughness estimation models as well as to develop and train new models. Similar to the SAR data collection, the GT data collection were also performed on a dry, sunny day to avoid any measurement errors. Eight locations on the runway and taxiway in Kaufbeuren, each with an area of 1 m^2, were identified for the GT h_{rms} data collection. The photos and locations of these GT spots are shown in Figure A.6. From the photos it can be seen that GT data were collected from different surface types, i.e., smooth, rough and cracked surfaces as well as surfaces with different material compositions.

A handheld laser scanner with the capability to measure vertical surface undulations with a micrometre level accuracy was used to scan each of the GT spots. Figure A.7(a) shows the laser scanning process at GT spot 1. The output of the laser scanner is an "xyz" file in which the x and y values represent the row and column coordinates of the measurement points within each GT spot and the z values represent the corresponding surface undulation value for each measurement point. The surface undulation image generated for GT-spot 1 is shown in Figure A.7(b). This spot is most probably a concrete area with repeated cuts, which can be clearly seen in the surface undulation image. A single GT h_{rms} value was then generated for each GT spot from the surface undulation values using (2.11) given on page 22. All information on the individual GT spots, including the calculated GT h_{rms} values , can be found in Table A.6.

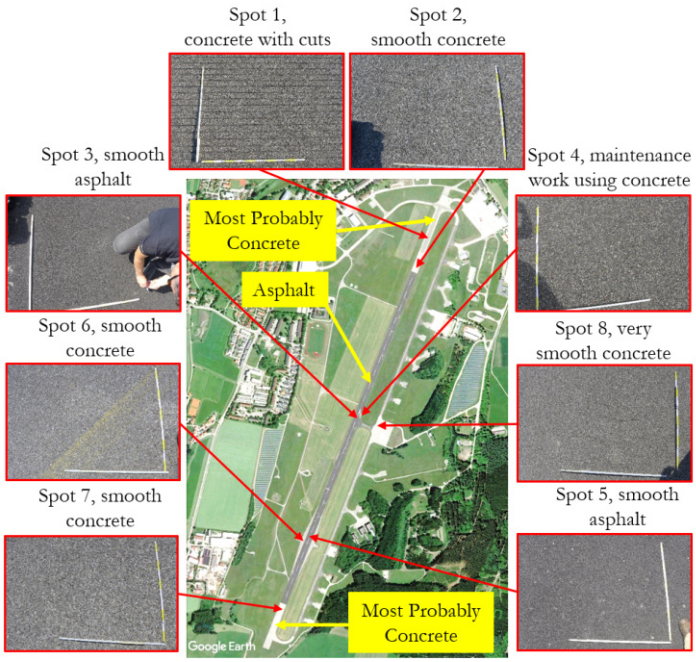

Figure A.6: Photos and locations of the ground truth spots at Kaufbeuren airfield.

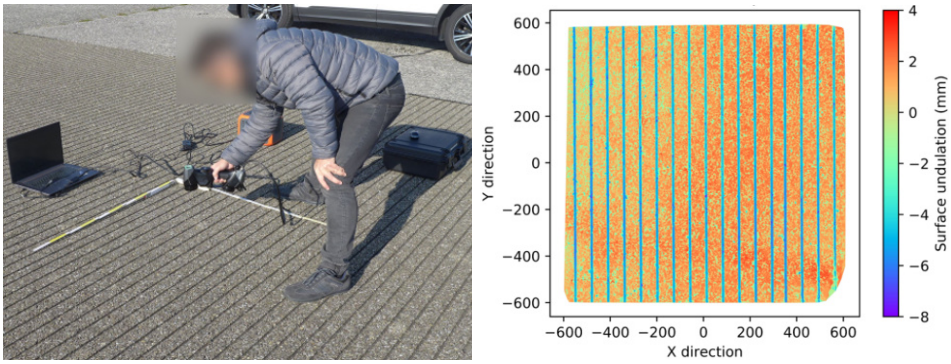

(a) (b)

Figure A.7: (a) GT data collection process. (b) Surface undulation image for GT spot 1, which is the only spot that contains repeated cuts.

Table A.6: Information about the ground truth spots, each with a dimension of 1 m x 1 m.

GT spot	Latitude (°)	Longitude (°)	Surface undulation (mm)		GT h_{rms} (mm)	Characteristics
			Min	Max		
1	47.87000278950265	10.61914390509984	-7.09	2.73	2.36	Concrete area with repeated cuts
2	47.86848751709891	10.61825671660665	-3.00	2.27	0.99	Smooth concrete area
3	47.86231983316981	10.61474126700445	-2.53	1.70	0.66	Smooth asphalt area
4	47.86230525205922	10.61480184484127	-4.34	1.66	0.88	Smooth area - repair work done most probably using concrete
5	47.857180781816	10.61153339982374	-2.45	2.26	0.68	Smooth asphalt area
6	47.85721718838993	10.61139022882151	-4.14	2.01	0.98	Smooth concrete area
7	47.85446597169599	10.61009957476967	-3.03	2.62	1.09	Smooth concrete area
8	47.86190571408042	10.61604281732041	-2.38	1.91	0.61	Concrete, very smooth

Bibliography

[1] Abramovich, F.; Bailey, T. C.; Sapatinas, T.: Wavelet analysis and its statistical applications. In: *Journal of the Royal Statistical Society: Series D (The Statistician)* 49.1 (2000), 1–29.

[2] Acosta, M.; Kanarachos, S.; Blundell, M.: Road Friction Virtual Sensing: A Review of Estimation Techniques with Emphasis on Low Excitation Approaches. In: *Applied Sciences* 7.12 (2017).

[3] Afridi, M. A.; Erlingsson, S.; Sjögren, L.: Municipal street maintenance challenges and management practices in Sweden. In: *Frontiers in Built Environment* 9 (2023).

[4] Ager, T. P.: An introduction to synthetic aperture radar imaging. In: *Oceanography* 26.2 (2013), 20–33.

[5] Agrawal, R.; Chhadva, Y.; Addagarla, S.; Chaudhari, S.: *Road Surface Classification and Subsequent Pothole Detection Using Deep Learning*. In: *2021 2nd International Conference for Emerging Technology (INCET)*. 2021, 1–6.

[6] Airbus Defence and Space: Radiometric Calibration of TerraSAR-X Data. 2014.

[7] Airbus Defence and Space: TerraSAR-X Image Product Guide. 2015.

[8] Akujuobi, C. M.: *Wavelets and wavelet transform systems and their applications*. Springer, 2022.

[9] Ali, H.; Sritharan, V.; Hariharan, M.; Zaaba, S. K.; Elshaikh, M.: *Feature extraction using Radon transform and Discrete Wavelet Transform for facial emotion recognition*. In: *2016 2nd IEEE International Symposium on Robotics and Manufacturing Automation (ROMA)*. 2016, 1–5.

[10] Alin, A.: Multicollinearity. In: *WIREs Computational Statistics* 2.3 (2010), 370–374.

[11] Alshammari, S.; Gebre-Amlak, H.; Ayinala, K.; Song, S.; Choi, B.-Y.: *Optimizing City's Service Routes for Road Repairs*. In: *2020 IEEE International Smart Cities Conference (ISC2)*. 2020, 1–8.

[12] Arabani, M.; Mirabdolazimi, S.; Sasani, A.: The effect of waste tire thread mesh on the dynamic behaviour of asphalt mixtures. In: *Construction and Building Materials* 24.6 (2010), 1060–1068.

[13] Arabzadeh, A.; Guler, M.: Thermal fatigue behavior of asphalt concrete: A laboratory-based investigation approach. In: *International Journal of Fatigue* 121 (2019), 229–236.

[14] Argenti, F.; Lapini, A.; Bianchi, T.; Alparone, L.: A tutorial on speckle reduction in synthetic aperture radar images. In: *IEEE Geoscience and remote sensing magazine* 1.3 (2013), 6–35.

[15] Asgari, S.; Mehrnia, A.; Moussavi, M.: Automatic detection of atrial fibrillation using stationary wavelet transform and support vector machine. In: *Computers in Biology and Medicine* 60 (2015), 132–142.

[16] Attoh-Okine, N.; Adarkwa, O.: *Pavement Condition Surveys – Overview of Current Practices*. Tech. rep. Delaware Center for Transportation, 2013.

[17] Babu, A.; Kumar, S.: SBAS interferometric analysis for volcanic eruption of Hawaii island. In: *Journal of Volcanology and Geothermal Research* 370 (2019), 31–50.

[18] Bachmann, M.; Zink, M.: *The TanDEM-X Mission — Bi-static SAR for a global DEM*. In: *2011 3rd International Asia-Pacific Conference on Synthetic Aperture Radar (APSAR)*. 2011, 1–4.

[19] Baghdadi, N.; Bernier, M.; Gauthier, R.; Neeson, I.: Evaluation of C-band SAR data for wetlands mapping. In: *International Journal of Remote Sensing* 22.1 (2001), 71–88.

[20] Baghdadi, N.; Choker, M.; Zribi, M.; Hajj, M. E.; Paloscia, S.; Verhoest, N. E. C.; Lievens, H.; Baup, F.; Mattia, F.: A New Empirical Model for Radar Scattering from Bare Soil Surfaces. In: *Remote Sensing* 8.11 (2016).

[21] Baghdadi, N.; Dubois-Fernandez, P.; Dupuis, X.; Zribi, M.: Sensitivity of Main Polarimetric Parameters of Multifrequency Polarimetric SAR Data to Soil Moisture and Surface Roughness Over Bare Agricultural Soils. In: *IEEE Geoscience and Remote Sensing Letters* 10.4 (2013), 731–735.

[22] Baghdadi, N.; Holah, N.; Zribi, M.: Soil moisture estimation using multi-incidence and multi-polarization ASAR data. In: *International Journal of Remote Sensing* 27.10 (2006), 1907–1920.

[23] Bamler, R.: Principles Of Synthetic Aperture Radar. In: *Surveys in Geophysics* 21.2 (2000), 147–157.

[24] Bani Baker, M. I.; Abendeh, R. M.; Khasawneh, M. A.: Freeze and Thaw Effect on Asphalt Concrete Mixtures Modified with Natural Bentonite Clay. In: *Coatings* 12.11 (2022).

[25] Baumgartner, S. V.: *Circular and Polarimetric ISAR Imaging of Ships Using Airborne SAR Sensors*. In: *EUSAR 2018; 12th European Conference on Synthetic Aperture Radar*. 2018, 1–6.

[26] Baumgartner, S. V.; Krieger, G.: Chapter 18 - Multi-Channel SAR for Ground Moving Target Indication. In: *Academic Press Library in Signal Processing: Volume 2*. Ed. by Sidiropoulos, N. D.; Gini, F.; Chellappa, R.; Theodoridis, S. Vol. 2. Academic Press Library in Signal Processing. Elsevier, 2014, 911–986.

[27] Beauchemin, M.; Thomson, K. P.; Edwards, G.: Modelling forest stands with MIMICS: implications for calibration. In: *Canadian Journal of Remote Sensing* 21.4 (1995), 518–526.

[28] Boeing, G.: OSMnx: New methods for acquiring, constructing, analyzing, and visualizing complex street networks. In: *Computers, Environment and Urban Systems* 65 (2017), 126–139.

[29] Braun, A.; Veci, L.: Sentinel-1 Toolbox SAR Basics Tutorial. 2020.

[30] Canny, J.: A Computational Approach to Edge Detection. In: *IEEE Transactions on Pattern Analysis and Machine Intelligence* PAMI-8.6 (1986), 679–698.

[31] Cao, H.; Chen, T.; Zhu, H.; Ren, H.: Influence of Frequent Freezendash;Thaw Cycles on Performance of Asphalt Pavement in High-Cold and High-Altitude Areas. In: *Coatings* 12.6 (2022).

[32] Carrea, L.; Wanielik, G.: *Polarimetric SAR processing using the polar decomposition of the scattering matrix*. In: *IGARSS 2001. Scanning the Present and Resolving the Future. Proceedings. IEEE 2001 International Geoscience and Remote Sensing Symposium (Cat. No.01CH37217)*. Vol. 1. 2001, 363–365 vol.1.

[33] Chan, C. Y.; Huang, B.; Yan, X.; Richards, S.: Investigating effects of asphalt pavement conditions on traffic accidents in Tennessee based on the pavement management system (PMS). In: *Journal of Advanced Transportation* 44.3 (2010), 150–161.

[34] Chen, K.: *Principles of Synthetic Aperture Radar Imaging: A System Simulation Approach*. Signal and Image Processing of Earth Observations. CRC Press, 2016.

[35] Chen, K.; Wu, T.-D.; Tsang, L.; Li, Q.; Shi, J.; Fung, A.: Emission of rough surfaces calculated by the integral equation method with comparison to three-dimensional moment method simulations. In: *IEEE Transactions on Geoscience and Remote Sensing* 41.1 (2003), 90–101.

[36] Choker, M.; Baghdadi, N.; Zribi, M.; El Hajj, M.; Paloscia, S.; Verhoest, N. E. C.; Lievens, H.; Mattia, F.: Evaluation of the Oh, Dubois and IEM Backscatter Models Using a Large Dataset of SAR Data and Experimental Soil Measurements. In: *Water* 9.1 (2017).

[37] Cloude, S.; Pottier, E.: A review of target decomposition theorems in radar polarimetry. In: *IEEE Transactions on Geoscience and Remote Sensing* 34.2 (1996), 498–518.

[38] Cumming, I.; Wong, F.: *Digital Processing of Synthetic Aperture Radar Data: Algorithms and Implementation*. Artech House remote sensing library. Artech House, 2005.

[39] Curlander, J.; McDonough, R.: *Synthetic Aperture Radar: Systems and Signal Processing*. Wiley Series in Remote Sensing and Image Processing. Wiley, 1992.

[40] Deans, S. R.: *The Radon transform and some of its applications*. Courier Corporation, 2007.

[41] Demirel, H.; Anbarjafari, G.: IMAGE Resolution Enhancement by Using Discrete and Stationary Wavelet Decomposition. In: *IEEE Transactions on Image Processing* 20.5 (2011), 1458–1460.

[42] Demirel, H.; Anbarjafari, G.: IMAGE Resolution Enhancement by Using Discrete and Stationary Wavelet Decomposition. In: *IEEE Transactions on Image Processing* 20.5 (2011), 1458–1460.

[43] Department of Transport and Main Roads: *Pavement Rehabilitation Manual*. Tech. rep. Queensland Government, 2019.

[44] Do, M.-T.; Cerezo, V.: Road surface texture and skid resistance. In: *Surface Topography: Metrology and Properties* 3.4 (2015).

[45] Doerry, A. W.: *SAR data collection and processing requirements for high quality coherent change detection*. Tech. rep. Sandia National Laboratories, 2008.

[46] Doerry, A. W.; Bickel, D. L.: *Stripmap SAR Data Collection Geometry on a Round Earth*. Tech. rep. Sandia National Laboratories, 2020.

[47] Douidar, I.; Safy, M.; Saleh, A.: *Parametric evaluation of PRF availability for a space borne SAR*. In: *2017 International Conference on Control, Automation and Diagnosis (ICCAD)*. 2017, 287–291.

[48] Dubois, P.; Zyl, J. van; Engman, T.: Measuring soil moisture with imaging radars. In: *IEEE Transactions on Geoscience and Remote Sensing* 33.4 (1995), 915–926.

[49] Dubois-Fernandez, P. C.; Souyris, J.-C.; Angelliaume, S.; Garestier, F.: The Compact Polarimetry Alternative for Spaceborne SAR at Low Frequency. In: *IEEE Transactions on Geoscience and Remote Sensing* 46.10 (2008), 3208–3222.

[50] Espeseth, M. M.; Skrunes, S.; Brekke, C.; Johansson, M.: *The impact of additive noise on polarimetric radarsat-2 data covering oil slicks*. In: *IGARSS 2019-2019 IEEE International Geoscience and Remote Sensing Symposium*. IEEE. 2019, 5756–5759.

[51] Espeseth, M. M.; Brekke, C.; Jones, C. E.; Holt, B.; Freeman, A.: The Impact of System Noise in Polarimetric SAR Imagery on Oil Spill Observations. In: *IEEE Transactions on Geoscience and Remote Sensing* 58.6 (2020), 4194–4214.

[52] Fa, W.; Wieczorek, M. A.; Heggy, E.: Modeling polarimetric radar scattering from the lunar surface: Study on the effect of physical properties of the regolith layer. In: *Journal of Geophysical Research: Planets* 116.E3 (2011).

[53] Frolova, O.; Salaiová, B.: Analysis of Road Cover Roughness on "Control" Road Section with Crumb Tire Rubber. In: *Procedia Engineering* 190 (2017). Structural and Physical Aspects of Construction Engineering, 589–596.

[54] Fung, A.: *Microwave Scattering and Emission Models and Their Applications*. Artech House remote sensing library. Artech House, 1994.

[55] Geron, A.: *Hands-on machine learning with scikit-learn, keras, and TensorFlow*. 2nd ed. Sebastopol, CA: O'Reilly Media, 2019.

[56] Ghandour, R.; Victorino, A.; Doumiati, M.; Charara, A.: *Tire/road friction coefficient estimation applied to road safety*. In: *18th Mediterranean Conference on Control and Automation, MED'10*. 2010, 1485–1490.

[57] Gierull, C. H.; Cerutti-Maori, D.; Ender, J.: Ground moving target indication with tandem satellite constellations. In: *IEEE Geoscience and Remote Sensing Letters* 5.4 (2008), 710–714.

[58] Goel, K.; Gonzalez, F. R.; Adam, N.; Duro, J.; Gaset, M.: *Thermal dilation monitoring of complex urban infrastructure using high resolution SAR data*. In: *2014 IEEE Geoscience and Remote Sensing Symposium*. 2014, 954–957.

[59] Goh, T. Y.; Basah, S. N.; Yazid, H.; Aziz Safar, M. J.; Ahmad Saad, F. S.: Performance analysis of image thresholding: Otsu technique. In: *Measurement* 114 (2018), 298–307.

[60] Goodfellow, I.; Bengio, Y.; Courville, A.: *Deep Learning*. Adaptive Computation and Machine Learning series. London, England: MIT Press, 2016.

[61] Greenberg, J. D.; Logsdon, M. G.; Franklin, J. F.: Introduction to geographic information systems (GIS). In: *Learning landscape ecology: a practical guide to concepts and techniques*. Springer, 2002, 17–31.

[62] Grégoire, C.; Wielen, A. V. d.; Geem, C. V.; Drevet, J.-P.: *Methodologies for the Use of Ground-Penetrating Radar in Road Condition Surveys*. Tech. rep. Belgian Road Research Centre, 2016.

[63] Hajnsek, I.; Papathanassiou, K.; Cloude, S.: *Removal of additive noise in polarimetric eigenvalue processing*. In: *IGARSS 2001. Scanning the Present and Resolving the Future. Proceedings. IEEE 2001 International Geoscience and Remote Sensing Symposium (Cat. No. 01CH37217)*. Vol. 6. IEEE. 2001, 2778–2780.

[64] Hajnsek, I.: Inversion of Surface Parameters Using Polarimetric SAR. PhD thesis. Friedrich Schiller University Jena, 2001.

[65] Haralick, R. M.; Shanmugam, K.; Dinstein, I.: Textural Features for Image Classification. In: *IEEE Transactions on Systems, Man, and Cybernetics* SMC-3.6 (1973), 610–621.

[66] Hastie, T.; Tibshirani, R.; Friedman, J.: *The Elements of Statistical Learning*. 2009.

[67] Hershfield, D. M.: Freeze-Thaw Cycles, Potholes, and the Winter of 1977–78. In: *Journal of Applied Meteorology (1962-1982)* 18.8 (1979), 1003–1007.

[68] Hettiarachchi, C.; Yuan, J.; Amirkhanian, S.; Xiao, F.: Measurement of pavement unevenness and evaluation through the IRI parameter – An overview. In: *Measurement* 206 (2023), 112284.

[69] Hofmockel, J.; Masino, J.; Thumm, J.; Sax, E.; Gauterin, F.: Multiple vehicle fusion for a robust road condition estimation based on vehicle sensors and data mining. In: *Cogent Engineering* 5.1 (2018). Ed. by Chadli, M.

[70] Hong, L.; Salari, E.; Chou, E.: *Pavement information system: Detection, classification and evaluation*. In: *2010 IEEE International Conference on Electro/Information Technology*. 2010, 1–5.

[71] Hooper, A.; Bekaert, D.; Spaans, K.; Arıkan, M.: Recent advances in SAR interferometry time series analysis for measuring crustal deformation. In: *Tectonophysics* 514-517 (2012), 1–13.

[72] Hoskera, A. K.; Nico, G.; Irshad Ahmed, M.; Whitbread, A.: Accuracies of Soil Moisture Estimations Using a Semi-Empirical Model over Bare Soil Agricultural Croplands from Sentinel-1 SAR Data. In: *Remote Sensing* 12.10 (2020).

[73] Ilie, G.-A.: *Spaceborne SAR Tomography: Application in Urban Environment*. Tech. rep. INP - Grenoble, France, 2011.

[74] Jagdhuber, T.: Soil Parameter Retrieval under Vegetation Cover Using SAR Polarimetry. PhD thesis. University of Potsdam, 2012.

[75] Keller, M.; Fischer, J.; Jager, M.: *DLR's Airborne SAR F-SAR Product Description*. Tech. rep. Microwaves and Radar Institute, German Aerospace Center, Oberpfaffenhofen, 2019.

[76] Kelley, B.; Madisetti, V.: The fast discrete Radon transform. I. Theory. In: *IEEE Transactions on Image Processing* 2.3 (1993), 382–400.

[77] Khoshnevis, S. A.; Ghorshi, S.: A tutorial on tomographic synthetic aperture radar methods. In: *SN Applied Sciences* 2.9 (2020), 1504.

[78] Kobayashi, T.; Nadai, A.; Umehara, T.; Satake, M.; Matsuoka, T.; Uratsuka, S.; Sawada, H.; Mitsuzuka, N.; Wakabayashi, H.; Hiuri, T.: *Forest monitoring in northern Japan with an airborne high-resolution SAR*. In: *IGARSS 2000. IEEE 2000 International Geoscience and Remote Sensing Symposium. Taking the Pulse of the Planet: The Role of Remote Sensing in Managing the Environment. Proceedings (Cat. No.00CH37120)*. 2000, 408–410 vol.1.

[79] Kropáč, O.; Múčka, P.: Be careful when using the International Roughness Index as an indicator of road unevenness. In: *Journal of Sound and Vibration* 287.4 (2005), 989–1003.

[80] Kumar, A.; Tomar, H.; Mehla, V. K.; Komaragiri, R.; Kumar, M.: Stationary wavelet transform based ECG signal denoising method. In: *ISA Transactions* 114 (2021), 251–262.

[81] Laurent, J.; Lefebvre, D.; Samson, E.: *Development of a new 3D transverse laser profiling system for the automatic measurement of road cracks*. In: *Symposium on Pavement Surface Characteristics, 6th, 2008, Portoroz, Slovenia*. 2008.

[82] Lavin, P.: *Asphalt pavements: a practical guide to design, production and maintenance for engineers and architects*. CRC Press, 2003.

[83] Li, Q.; Qiao, F.; Yu, L.: Impacts of pavement types on in-vehicle noise and human health. In: *Journal of the Air & Waste Management Association* 66.1 (2016), 87–96.

[84] Lin, Y.; Hong, W.; Tan, W.; Wang, Y.; Xiang, M.: *Airborne circular SAR imaging: Results at P-band*. In: *2012 IEEE International Geoscience and Remote Sensing Symposium*. 2012, 5594–5597.

[85] Liu, H.; Zhang, Z.; Guo, D.; Peng, L.; Bao, Z.; Han, W.: *Research progress on characteristic technique of pavement micro-texture and testing technology of pavement skid resistance at home and abroad*. In: *2011 International Conference on Remote Sensing, Environment and Transportation Engineering*. 2011, 4368–4372.

[86] Liu, P.; Ravee, V.; Wang, D.; Oeser, M.: Study of the influence of pavement unevenness on the mechanical response of asphalt pavement by means of the finite element method. In: *Journal of Traffic and Transportation Engineering (English Edition)* 5.3 (2018), 169–180.

[87] Longitudinal and transverse evenness. https://www.durabast.de/durabast/EN/Reference/LT/LT_node.html. Accessed: 2023-07-25. Federal Highway Research Institute (BASt), Germany.

[88] López-Martínez, C.; Pottier, E.: Basic Principles of SAR Polarimetry. In: *Polarimetric Synthetic Aperture Radar: Principles and Application*. Ed. by Hajnsek, I.; Desnos, Y.-L. Springer International Publishing, 2021, 1–58.

[89] Lu, Z.; Kwoun, O.; Rykhus, R.: Interferometric synthetic aperture radar (InSAR): its past, present and future. In: *Photogrammetric engineering and remote sensing* 73.3 (2007), 217.

[90] Ma, X.; Wu, P.; Wu, Y.; Shen, H.: A Review on Recent Developments in Fully Polarimetric SAR Image Despeckling. In: *IEEE Journal of Selected Topics in Applied Earth Observations and Remote Sensing* 11.3 (2018), 743–758.

[91] Masino, J.: *Road Condition Estimation with Data Mining Methods using Vehicle Based Sensors*. Karlsruhe: KIT Scientific Publishing, 2021, 234.

[92] Matijošius, J.; Vasiliauskas, A. V.; Vasilienė-Vasiliauskienė, V.; Krasodomskis, Ž.: The Assessment of Importance of the Factors that Predetermine the Quality of a Service of Transportation by Road Vehicles. In: *Procedia Engineering* 134 (2016), 422–429.

[93] Mattia, F. et al.: *Multi-Frequency Sar Data for Agriculture*. In: *IGARSS 2022 - 2022 IEEE International Geoscience and Remote Sensing Symposium*. 2022, 5176–5179.

[94] McIlhagga, W.: The Canny Edge Detector Revisited. In: *International Journal of Computer Vision* 91.3 (2011), 251–261.

[95] Meyer, F. J.; Ajadi, O. A.; Hoppe, E. J.: Studying the Applicability of X-Band SAR Data to the Network-Scale Mapping of Pavement Roughness on US Roads. In: *Remote Sensing* 12.9 (2020).

[96] Michelin: The Tyre Grip. Société de Technologie Michelin: Clermont-Ferrand, 2004.

[97] Mittermayer, J.; Wollstadt, S.; Prats-Iraola, P.; Scheiber, R.: The TerraSAR-X Staring Spotlight Mode Concept. In: *IEEE Transactions on Geoscience and Remote Sensing* 52.6 (2014), 3695–3706.

[98] Mooney, P.; Minghini, M., et al.: A review of OpenStreetMap data. In: *Mapping and the citizen sensor* (2017), 37–59.

[99] Moreira, A.; Prats-Iraola, P.; Younis, M.; Krieger, G.; Hajnsek, I.; Papathanassiou, K. P.: A tutorial on synthetic aperture radar. In: *IEEE Geoscience and Remote Sensing Magazine* 1.1 (2013), 6–43.

[100] Munder, J.; Miller, D.: *TerraSAR-X, German X-band remote sensing system*. In: *International Conference on Recent Advances in Space Technologies, 2003. RAST '03. Proceedings of*. 2003, 14–18.

[101] Myers, L. A.; Roque, R.; Ruth, B. E.; Drakos, C.: Measurement of Contact Stresses for Different Truck Tire Types To Evaluate Their Influence on Near-Surface Cracking and Rutting. In: *Transportation Research Record* 1655.1 (1999), 175–184.

[102] Oh, Y.; Sarabandi, K.; Ulaby, F.: An empirical model and an inversion technique for radar scattering from bare soil surfaces. In: *IEEE Transactions on Geoscience and Remote Sensing* 30.2 (1992), 370–381.

[103] Oh, Y.: Quantitative retrieval of soil moisture content and surface roughness from multipolarized radar observations of bare soil surfaces. In: *IEEE Transactions on Geoscience and Remote Sensing* 42.3 (2004), 596–601.

[104] Oliver, C.; Quegan, S.: *Understanding Synthetic Aperture Radar Images*. EngineeringPro collection. SciTech Publ., 2004.

[105] Ozden, A.; Faghri, A.; Li, M.; Tabrizi, K.: Evaluation of Synthetic Aperture Radar Satellite Remote Sensing for Pavement and Infrastructure Monitoring. In: *Procedia Engineering* 145 (2016). ICSDEC 2016 – Integrating Data Science, Construction and Sustainability, 752–759.

[106] Pan, Y.; Zhang, X.; Cervone, G.; Yang, L.: Detection of Asphalt Pavement Potholes and Cracks Based on the Unmanned Aerial Vehicle Multispectral Imagery. In: *IEEE Journal of Selected Topics in Applied Earth Observations and Remote Sensing* 11.10 (2018), 3701–3712.

[107] Parliament, E.; Internal Policies of the Union, D.-G. for; Stanghellini, A.; Frisoni, R.; Lidia, R.; Neri, J.; Sawicki, T.; Devenish, L.; Casullo, L.; Carl, S.; Vollath, C.; Silaghi, R.; Spano, F.; Dionori, F.: *EU road surfaces : economic and safety impact of the lack of regular road maintenance*. Publications Office, 2014.

[108] Pichierri, M.; Hajnsek, I.; Zwieback, S.; Rabus, B.: On the potential of Polarimetric SAR Interferometry to characterize the biomass, moisture and structure of agricultural crops at L-, C- and X-Bands. In: *Remote Sensing of Environment* 204 (2018), 596–616.

[109] Ponce, O.; Joerg, H.; Scheiber, R.; Prats, P.; Hajnsek, I.; Reigber, A.: *First study on holographic SAR tomography over agricultural crops at C-/X-band*. In: *2016 IEEE International Geoscience and Remote Sensing Symposium (IGARSS)*. 2016, 7403–7406.

[110] Radopoulou, S. C.; Brilakis, I.: Improving Road Asset Condition Monitoring. In: *Transportation Research Procedia* 14 (2016). Transport Research Arena TRA2016, 3004–3012.

[111] Raynal, A. M.; Bickel, D. L.: *Imaging radar performance analysis using product dark regions*. In: *Radar Sensor Technology XXII*. Ed. by Ranney, K. I.; Doerry, A. Vol. 10633. International Society for Optics and Photonics. SPIE, 2018, 319–329.

[112] Reamer, R. E.; Stockton, W.; Stromfors, R. D.: *New military uses for synthetic aperture radar (SAR)*. In: *Airborne Reconnaissance XVI*. Ed. by Augustyn, T. W.; Henkel, P. A. Vol. 1763. International Society for Optics and Photonics. SPIE, 1993, 113–119.

[113] Reigber, A.; Horn, R.; Nottensteiner, A.; Prats, P.; Scheiber, R.; Bethke, K.-H.; Baumgartner, S.: *Current status of DLR's new F-SAR sensor*. In: *8th European Conference on Synthetic Aperture Radar*. 2010, 1–4.

[114] Reigber, A.; Scheiber, R.; Jager, M.; Prats-Iraola, P.; Hajnsek, I.; Jagdhuber, T.; Papathanassiou, K. P.; Nannini, M.; Aguilera, E.; Baumgartner, S.; Horn, R.; Nottensteiner, A.; Moreira, A.: Very-High-Resolution Airborne Synthetic Aperture Radar Imaging: Signal Processing and Applications. In: *Proceedings of the IEEE* 101.3 (2013), 759–783.

[115] Ressel, R.; Singha, S.; Lehner, S.; Rösel, A.; Spreen, G.: Investigation into Different Polarimetric Features for Sea Ice Classification Using X-Band Synthetic Aperture Radar. In: *IEEE Journal of Selected Topics in Applied Earth Observations and Remote Sensing* 9.7 (2016), 3131–3143.

[116] Richards, J.: *Remote Sensing with Imaging Radar*. Signals and Communication Technology. Springer Berlin Heidelberg, 2009.

[117] Sahebi, M. R.; Angles, J.; Bonn, F.: A comparison of multi-polarization and multi-angular approaches for estimating bare soil surface roughness from spaceborne radar data. In: *Canadian Journal of Remote Sensing* 28.5 (2002), 641–652.

[118] Sarker, I. H.: Machine Learning: Algorithms, Real-World Applications and Research Directions. In: *SN Computer Science* 2.3 (2021).

[119] Scheiber, R.; Reigber, A.; Ulbricht, A.; Papathanassiou, K.; Horn, R.; Buckreuss, S.; Moreira, A.: *Overview of interferometric data acquisition and processing modes of the experimental airborne SAR system of DLR*. In: *IEEE 1999 International Geoscience and Remote Sensing Symposium. IGARSS'99 (Cat. No.99CH36293)*. Vol. 1. 1999, 35–37 vol.1.

[120] Schnebele, E.; Tanyu, B. F.; Cervone, G.; Waters, N.: Review of remote sensing methodologies for pavement management and assessment. In: *European Transport Research Review* 7.2 (2015), 7.

[121] Service, U. S. A. M.: *Grids and Magnetic Declinations*. 425. 1945.

[122] Shakya, A. K.; Ramola, A.; Kandwal, A.; Vidyarthi, A.: Soil moisture sensor for agricultural applications inspired from state of art study of surfaces scattering models semi-empirical soil moisture models. In: *Journal of the Saudi Society of Agricultural Sciences* 20.8 (2021), 559–572.

[123] Shen, Q.; Wang, H.; Shum, C. K.; Jiang, L.; Yang, B.; Zhang, C.; Dong, J.; Gao, F.; Lai, W.; Liu, T.: Soil Moisture Retrieval From Multipolarization SAR Data and Potential Hydrological Application. In: *IEEE Journal of Selected Topics in Applied Earth Observations and Remote Sensing* 16 (2023), 6531–6544.

[124] Silik, A.; Noori, M.; Altabey, W. A.; Ghiasi, R.; Wu, Z.: Comparative analysis of wavelet transform for time-frequency analysis and transient localization in structural health monitoring. In: *Structural Durability & Health Monitoring* 15.1 (2021), 1.

[125] Singh, P.; Shree, R.: Speckle noise: Modelling and implementation. In: *International Journal of Control Theory and Applications* 9.17 (2016), 8717–8727.

[126] Singh, R.; Vasquez, R. E.; Singh, R.: *Comparison of Daubechies, Coiflet, and Symlet for edge detection*. In: *Visual Information Processing VI*. Vol. 3074. SPIE. 1997, 151–159.

[127] Soh, L.-K.; Tsatsoulis, C.: Texture analysis of SAR sea ice imagery using gray level co-occurrence matrices. In: *IEEE Transactions on Geoscience and Remote Sensing* 37.2 (1999), 780–795.

[128] State Materials Office: *Flexible Pavement Condition Survey Handbook*. Tech. rep. Florida Department of Transportation, 2012.

[129] Suanpaga, W.; Yoshikazu, K.: Riding Quality Model for Asphalt Pavement Monitoring Using Phase Array Type L-band Synthetic Aperture Radar (PALSAR). In: *Remote Sensing* 2.11 (2010), 2531–2546.

[130] Tello, M.; Pardini, M.; Papathanassiou, K.; Fischer, R.: *Towards Forest Structure Characteristics Retrieval from SAR Tomographic Profiles*. In: *EUSAR 2014; 10th European Conference on Synthetic Aperture Radar*. 2014, 1–4.

[131] Ticconi, F.; Pulvirenti, L.; Pierdicca, N.: Electromagnetic Waves. In: ed. by Zhurbenko, V. InTech, 2011. Chap. Models for Scattering from Rough Surfaces.

[132] Tomiyasu, K.: Tutorial review of synthetic-aperture radar (SAR) with applications to imaging of the ocean surface. In: *Proceedings of the IEEE* 66.5 (1978), 563–583.

[133] Touzi, R.; Lopes, A.: The principle of speckle filtering in polarimetric SAR imagery. In: *IEEE Transactions on Geoscience and Remote Sensing* 32.5 (1994), 1110–1114.

[134] Trevett, J. W.: *Imaging radar for resources surveys*. Springer Science & Business Media, 2013.

[135] Trouvé, E.; Mauris, G.; Rudant, J.-P.; Tonyé, E., et al.: Detection of linear features in synthetic-aperture radar images by use of the localized Radon transform and prior information. In: *Applied optics* 43.2 (2004), 264–273.

[136] Tsokas, A.; Rysz, M.; Pardalos, P. M.; Dipple, K.: SAR data applications in earth observation: An overview. In: *Expert Systems with Applications* 205 (2022), 117342.

[137] Ulaby, F.; Long, D.; Michigan. Press, U. of: *Microwave Radar and Radiometric Remote Sensing*. University of Michigan Press, 2014.

[138] Vehmas, R.; Neuberger, N.: Inverse Synthetic Aperture Radar Imaging: A Historical Perspective and State-of-the-Art Survey. In: *IEEE Access* 9 (2021), 113917–113943.

[139] Verhoest, N. E.; Lievens, H.; Wagner, W.; Álvarez-Mozos, J.; Moran, M. S.; Mattia, F.: On the Soil Roughness Parameterization Problem in Soil Moisture Retrieval of Bare Surfaces from Synthetic Aperture Radar. In: *Sensors* 8.7 (2008), 4213–4248.

[140] Verma, A. K.; Nandan, R.; Verma, A.: Space-Borne-Synthetic Aperture Radar (SAR) System For Real Time Survilliances Of Earth Surface For Detection And Management Of Flood Disaster In Indian Sub-Continent. In: *Journal of Applied Mathematics and Computation* (2018), 166–177.

[141] Vries, F. P. de: *Speckle reduction in SAR Imagery by various multi-look techniques*. TNO-FEL, 1998.

[142] Woodhouse, I.: *Introduction to Microwave Remote Sensing*. CRC Press, 2017.

[143] Wriggers, P.; Reinelt, J.: Multi-scale approach for frictional contact of elastomers on rough rigid surfaces. In: *Computer Methods in Applied Mechanics and Engineering* 198.21 (2009). Advances in Simulation-Based Engineering Sciences – Honoring J. Tinsley Oden, 1996–2008.

[144] WSP Canada Limited: *Pavement Surface Condition Rating Manual*. Tech. rep. British Columbia Ministry of Transportation and Infrastructure Construction Maintenance Branch, 2020.

[145] Yommy, A. S.; Liu, R.; Wu, S.: *SAR image despeckling using refined Lee filter*. In: *2015 7th International Conference on Intelligent Human-Machine Systems and Cybernetics*. Vol. 2. IEEE. 2015, 260–265.

[146] Zhang, J.; Wang, M.; Wang, D.; Li, X.; Song, B.; Liu, P.: Feasibility study on measurement of a physiological index value with an electrocardiogram tester to evaluate the pavement evenness and driving comfort. In: *Measurement* 117 (2018), 1–7.

[147] Zhao, Y.; Lin, Y.; Wang, Y. P.; Hong, W.; Yu, L.: *Target multi-aspect scattering sensitivity feature extraction based on Circular-SAR*. In: *2016 IEEE International Geoscience and Remote Sensing Symposium (IGARSS)*. 2016, 2722–2725.

[148] Zhou, L.; Ni, F.; Zhao, Y.: Evaluation Method for Transverse Cracking in Asphalt Pavements on Freeways. In: *Transportation Research Record* 2153.1 (2010), 97–105.

Own publications referring to this work

[P1] Babu, A.; Baumgartner, S. V.: *Road Surface Quality Assessment Using Polarimetric Airborne SAR*. In: *2020 IEEE Radar Conference (RadarConf20)*. 2020, 1–5.

[P2] Babu, A.; Baumgartner, S. V.: *Road Surface Roughness Estimation Using Polarimetric SAR Data*. In: *2020 21st International Radar Symposium (IRS)*. 2020, 281–285.

[P3] Babu, A.; Baumgartner, S. V.; Krieger, G.: *Road Surface Condition Monitoring Using Fully Polarimetric Airborne SAR Data*. In: *EUSAR 2021; 13th European Conference on Synthetic Aperture Radar*. 2021, 1–6.

[P4] Babu, A.; Baumgartner, S. V.; Krieger, G.: Approaches for Road Surface Roughness Estimation Using Airborne Polarimetric SAR. In: *IEEE Journal of Selected Topics in Applied Earth Observations and Remote Sensing* 15 (2022), 3444–3462.

[P5] Babu, A.; Baumgartner, S. V.; Krieger, G.; Rischioni, L. G.: *Estimation of Road Surface Roughness Using Airborne Synthetic Aperture Radar*. In: *EUSAR 2022; 14th European Conference on Synthetic Aperture Radar*. 2022, 1–6.

[P6] Babu, A.; Gerber, D.; Baumgartner, S. V.; Krieger, G.: Road Surface Roughness Estimation Using Spaceborne Synthetic Aperture Radar. In: *IEEE Geoscience and Remote Sensing Letters* 20 (2023), 1–5.

[P7] Babu, A.; Gerber, D.; Baumgartner, S. V.; Krieger, G.: *Road Surface Roughness Assessment: A Spaceborne SAR-Based Approach*. In: *European Conference on Synthetic Aperture Radar (EUSAR)*. 2024.

[P8] Rischioni, L. G.; Babu, A.; Baumgartner, S. V.; Krieger, G.: Machine Learning Approaches for Road Condition Monitoring Using Synthetic Aperture Radar. In: *IEEE Journal of Selected Topics in Applied Earth Observations and Remote Sensing* 16 (2023), 3070–3082.

Academic supervisions

[S1] Gerber, D.: Road Surface Roughness Estimation With Spaceborne Synthetic Aperture Radar (SAR). MA thesis. Hochschule Kempten, 2022.

[S2] Rischioni, L. G.: Machine Learning Approaches For Road Condition Monitoring Using Synthetic Aperture Radar. BA thesis. Instituto Tecnológico de Aeronáutica (ITA), São José dos Campos, Brazil, 2022.